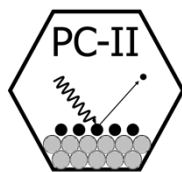


# Scanning Probe Studies of Porphyrins and Ionic Liquids on Metal Surfaces

Untersuchungen zur Adsorption von Porphyrinen und Ionischen Flüssigkeiten  
mit Rastertunnelmikroskopie und Rasterkraftmikroskopie

Der Naturwissenschaftlichen Fakultät  
der Friedrich-Alexander-Universität Erlangen-Nürnberg



zur Erlangung des  
Doktorgrades Dr. rer. nat.

vorgelegt von  
**Rajan Adhikari**  
aus Gorkha, Nepal



Als Dissertation genehmigt  
von der Naturwissenschaftlichen Fakultät  
der Friedrich-Alexander-Universität Erlangen-Nürnberg

Tag der mündlichen Prüfung:	24.11.2023
Vorsitzender des Promotionsorgans:	Prof. Dr. Svetlana Tsogoeva
Gutachter:	Prof. Dr. Hans-Peter Steinrück Prof. Dr. Christian Papp



“To my beloved mother *Saraswati Adhikari* and my beloved father *Tara Nath Adhikari*.”



# Contents

<b>Publications.....</b>	<b>iii</b>
<b>Abbreviations.....</b>	<b>v</b>
<b>1 Introduction .....</b>	<b>1</b>
<b>2 Methods and Experimental Set-up .....</b>	<b>4</b>
2.1 Brief Historical Path of Scanning Probe Microscopy (SPM).....	4
2.2 Scanning Tunneling Microscopy (STM).....	5
2.3 Non-contact Atomic Force Microscopy (nc-AFM).....	6
2.4 Experimental Set-up .....	8
2.4.1 UHV Chamber 1.....	8
2.4.2 UHV Chamber 2.....	9
2.5 Substrates: Ag(111), Cu(111), and Cu(110).....	10
2.6 Porphyrins .....	12
2.7 Ionic Liquids.....	15
<b>3 Literature Review.....</b>	<b>16</b>
3.1 Molecular Conformation and Self-assembly .....	16
3.2 Surface reactions: <i>In situ</i> Metalation and Dehydrogenation .....	18
<b>4 Results .....</b>	<b>21</b>
4.1 Cyano-Functionalized Porphyrins on Cu(111) [P1].....	21
4.2 Cyano-Functionalized Benzoporphyrin on Cu(111) [P2].....	25
4.3 Mixture of Benzoporphyrins on Ag(111), Cu(111), and Cu(110) [P4] .....	29
4.4 Ionic liquid [C <sub>1</sub> C <sub>1</sub> Im][Tf <sub>2</sub> N] on Cu(111) [P3] .....	38
<b>5 Conclusions .....</b>	<b>44</b>
<b>Acknowledgements.....</b>	<b>51</b>
<b>Bibliography .....</b>	<b>53</b>
<b>Appendix .....</b>	<b>61</b>
A1 List of STM/nc-AFM Raw Data File IDs .....	61
A2 List of Publications.....	62
Publication [P1].....	62
Publication [P2].....	96
Publication [P3].....	106
Publication [P4].....	138

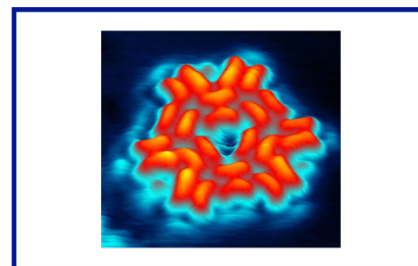


## Publications

This cumulative thesis is based on the following first-author publications [P1-P4]:

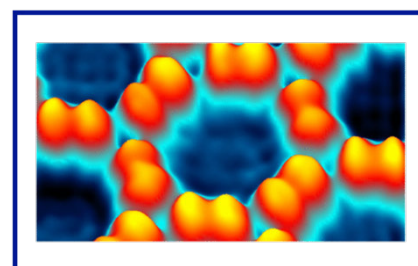
- [P1] Formation of Highly Ordered Molecular Porous 2D Networks from Cyano-Functionalized Porphyrins on Cu(111),** R. Adhikari, G. Sigleithmaier, M. Gurrath, M. Meusel, J. Kuliga, M. Lepper, H. Hölzel, N. Jux, B. Meyer, H.-P. Steinrück, and H. Marbach, *Chem. Eur. J.* **2020**, *26*, 13408; [10.1002/chem.202001980](https://doi.org/10.1002/chem.202001980)

Contribution: STM data evaluation, interpretation and writing of the manuscript was predominantly performed by R. Adhikari.



- [P2] Self-Assembled 2D-Coordination Kagome, Quadratic, and Close-Packed Hexagonal Lattices Formed from a Cyano-Functionalized Benzoporphyrin on Cu(111),** R. Adhikari, J. Kuliga, M. Ruppel, N. Jux, H. Marbach, and H.-P. Steinrück, *J. Phys. Chem. C* **2021**, *125*, 13, 7204–7212; [10.1021/acs.jpcc.1c00746](https://doi.org/10.1021/acs.jpcc.1c00746)

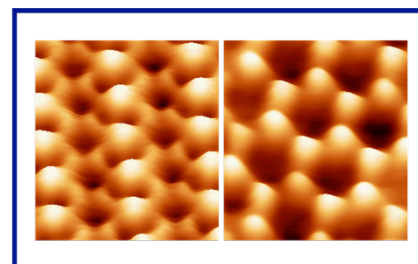
Contribution: STM data acquisition, evaluation, interpretation and writing of the manuscript was predominantly performed by R. Adhikari.



- [P3] Structure and Reactivity of the Ionic Liquid [C<sub>1</sub>C<sub>1</sub>Im][Tf<sub>2</sub>N] on Cu(111),** R. Adhikari<sup>#</sup>, S. Massicot<sup>#</sup>, L. Fromm, T. Talwar, A. Gezmis, M. Meusel, A. Bayer, S. Jaekel, F. Maier, A. Görling, and H.-P. Steinrück, *Top. Catal.* **2023**, 1-18; [10.1007/s11244-023-01801-y](https://doi.org/10.1007/s11244-023-01801-y)

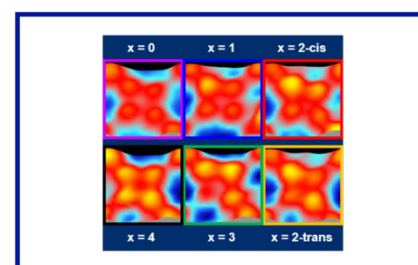
Contribution: Acquisition, evaluation, interpretation of the nc-AFM/STM data and writing of the corresponding part of the manuscript was predominantly performed by R. Adhikari.

<sup>#</sup>shared first-authorship



- [P4] Structure and Conformation of Individual Molecules upon Adsorption of a Mixture of Benzoporphyrins on Ag(111), Cu(111), and Cu(110) Surfaces,** R. Adhikari, J. Brox, S. Massicot, M. Ruppel, N. Jux, H. Marbach, and H.-P. Steinrück, *ChemPhysChem*, **2023**, e202300355; [10.1002/cphc.202300355](https://doi.org/10.1002/cphc.202300355)

Contribution: STM data acquisition, evaluation, interpretation and writing of the manuscript was predominantly performed by R. Adhikari.



Other publications, not used in this thesis but contributed to during this thesis work, are sorted by date:

- ⇒ **Conformation Controls Mobility: 2H-Tetranaphthylporphyrins on Cu(111)**, J. Kuliga, S. Massicot, R. Adhikari, M. Ruppel, N. Jux, H.-P. Steinrück, and H. Marbach, *ChemPhysChem*, **2020**, 21.5, 423-427.
- ⇒ **Metalation of 2HTCNPP on Ag(111) with Zn: Evidence for the Sitting atop Complex at Room Temperature**, J. Kuliga, R. C. de Campos Ferreira, R. Adhikari, S. Massicot, M. Lepper, H. Hölzel, N. Jux, H. Marbach, A. de Siervo, and H.-P. Steinrück, *ChemPhysChem*, **2021**, 22.4, 396-403.
- ⇒ **On the adsorption of different tetranaphthylporphyrins on Cu(111) and Ag(111)**, J. Brox, R. Adhikari, M. Shaker, M. Ruppel, N. Jux, H. Marbach, S. Jaekel, and H.-P. Steinrück, *Surface Science*, **2022**, 720, 122047.
- ⇒ **Adsorption and Thermal Evolution of [C<sub>1</sub>C<sub>1</sub>Im][Tf<sub>2</sub>N] on Pt(111)**, S. Massicot, A. Gezmis, T. Talwar, M. Meusel, S. Jaekel, R. Adhikari, L. Winter, C. C., Fernández, A. Bayer, F. Maier, and H.-P. Steinrück, *Phys. Chem. Chem. Phys.*, **2023**, 25.41, 27953-27966.

## Abbreviations

1D	one-dimensional
2D	two-dimensional
AFM	atomic force microscopy
DFT	density functional theory
fcc	face-centered cubic
FM	frequency modulation
FM-AFM	frequency modulation atomic force microscopy
ILs	ionic liquids
LEED	low-energy electron diffraction
ML	monolayer
nc-AFM	non-contact atomic force microscopy
NEXAFS	near edge x-ray absorption fine structure
PLL	phase-locked loop
PSD	position-sensitive detector
PVD	physical vapor deposition
QCM	quartz crystal microbalance
QMS	quadropole mass spectrometer
RT	room temperature
SCILL	solid catalyst with ionic liquid layer
SI	supporting information
SILP	supported ionic liquid phase
SPM	scanning probe microscopy
STM	scanning tunneling microscopy
STS	scanning tunneling spectroscopy
TPD	temperature-programmed desorption
UHV	ultra-high vacuum
VT	variable temperature
XPS	x-ray photoelectron spectroscopy



## 1 Introduction

As we continue to face global difficulties such as climate change, resource scarcity, and sustainability concerns, looking to nature for inspiration becomes even more important. By incorporating natural world concepts into our technical advances, we have the ability to build a more harmonious relationship between technology and the environment, leading to a more successful and sustainable future for society as a whole. Achieving the goal necessitates better understanding and optimization of key materials, products, or novel technical concepts. One promising path in this direction is the miniaturization of building blocks in areas such as catalysis, energy storage and conversion, or electronics, to name only a few (see [1-3] and references therein). Thus, the precise design and fabrication of functional materials at the molecular or atomic level have become significant challenges and prominent topics in both industry and scientific research [1]. Nanotechnology, which deals with materials and devices at the nanometre scale (from a few nm to  $< 100$  nm), has opened new avenues for developing materials with distinct properties and functionalities (see [4, 5] and references therein).

The primary goal of the nanotechnology miniaturization process is to increase the density of functional elements [6]. The most prominent illustration of the trend towards miniaturization is Moore's Law, which states that the number of transistors per area of integrated circuits doubles approximately every two years [7]. To maintain the trend of achieving and fabricating smaller devices, two ways come into play: the top-down approach and the bottom-up approach. In the top-down approach, larger structures are fabricated and then gradually reduced in size through photolithographic processes [8] or other techniques. In contrast, in the bottom-up approach, the fundamental building blocks are typically atoms or molecules. These building blocks are manipulated or self-assembled into larger structures or devices [2]. Indeed, large organic molecules have shown great potential for the formation of self-assembled nanostructures. These molecules possess unique electronic and chemical properties that can be fine-tuned over a wide range, making them excellent building blocks for nanotechnology applications [1, 5, 9]. Among the class of nitrogen-containing macrocycles, porphyrins are omnipresent in nature [10, 11] and are most exploited representatives, in part because of their significance to biology [12]. Examples are shown in Figure 1. Heme, characterized by the presence of an iron Fe (II) ion coordinated at the center of a macrocycle, facilitates oxygen transfer and storage in the lungs and cells of mammals. On the other hand, Chlorophyll *a* contains a magnesium Mg (II) ion at its core and plays a crucial role in capturing light for photosynthesis in plants [13].

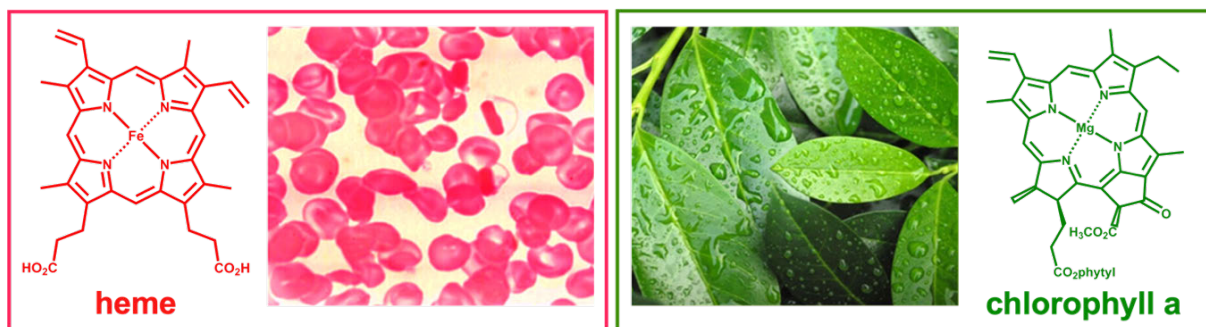


**Figure 1:** The two most prominent metalloporphyrins found in nature, heme and chlorophyll a. Modified image from reference [8] used with permission.

Clearly, the choice of metal center and/or different substituents significantly influences the functionalities of the porphyrin molecules. Hence, the vast diversity of porphyrins, with metal centers encompassing most elements of the periodic table, has led to a wide range of chemical and physical properties [14-20]. This variety makes porphyrins highly interesting and valuable for numerous applications. For example, in catalysis to reduce nitric oxide [21], or to synthesize cyclic carbonates from CO<sub>2</sub> [22], or in medical applications for photodynamic therapies [23, 24]. Besides that, they have found use in chemical sensors [25, 26], or in the development of cheap dye-sensitized solar cells on titania surfaces [27, 28], or in nanotechnology, to name only a few.

Ionic liquids (ILs), on the other hand, are a class of compounds with a low melting point that are composed entirely of molecular ions, solely cations and anions. Many ILs remain liquid below 100 °C, often at or even near room temperature (RT) [29-31]. Moreover, ionic liquids exhibit high thermal stability [32, 33], making them suitable for the use in catalysis [34, 35] and energy storage [36]. Further, by tailoring their properties with different functional groups, task-specific reaction media [37, 38] can be obtained. Due to their customizable physicochemical features, they are also used in other applications, such as lubrication [39, 40], sensors [41, 42], or in dye-sensitized solar cells [43, 44], to name only a few. Further, ILs initiated new concepts for catalysis: the supported ionic liquid phase (SILP) [45-47] and the solid catalyst with ionic liquid layer (SCILL) approaches [47, 48]. Moreover, due to their low vapor pressure properties [49], ILs can be used as a liquid phase under ultra-high vacuum (UHV) conditions, providing valuable insights into their adsorption behavior on solid surfaces at the molecular level [34, 50-55].

Their inherent flexibility, diverse functionality, and low vapor pressure make them ideal candidates for studying adsorption behavior on metal [14-16, 55] and oxide [56-61] surfaces using whole arsenal of surface science techniques (see [17, 51, 62] and references therein). In

particular, the combination of scanning tunneling microscopy (STM) and non-contact atomic force microscopy (nc-AFM) emerged as a powerful real space experimental technique to pave the way for the development of functional nanostructures and nanoscale devices with diverse functionalities and potential applications in various fields.

The objective of this thesis is to further advance the fundamental understanding of the adsorption behavior of various complex porphyrin derivatives and ILs on different surfaces at room temperature (RT) or below using experimental techniques like STM and nc-AFM. Specifically, the focus is on investigating the intramolecular conformation, intermolecular interactions, supramolecular arrangements, and on-surface reactions of functionalized tetraphenylporphyrins (TPPs) and simple ILs on surfaces. Ultimately, this information can be instrumental in driving innovation and development of molecular scale technologies or catalytic concepts with improved functionalities and tailored properties.

This thesis is a cumulative thesis based on four publications [P1-P4] in peer-reviewed scientific journals (see Appendix A2). The work was performed in collaboration with groups of Prof. Dr. Norbert Jux, Prof. Dr. Andreas Görling, and Prof. Dr. Bernd Meyer (all from FAU Erlangen-Nürnberg).

Chapter 2 briefly introduces the theories underlying the methods and experimental set-up, as well as the substrates, porphyrins, and ionic liquids investigated. Chapter 3 gives a brief overview of the central topic of the porphyrin literature relevant to this thesis and related publications. Chapter 4 briefly summarises the results of the publications [P1-P4]. Finally, the concluding Chapter 5 summarises the findings.

## 2 Methods and Experimental Set-up

*In the framework of this thesis, the primary experimental tools used to probe molecules and substrates at the molecular or atomic level were STM and nc-AFM. The fundamentals underlying these experimental techniques are introduced in this chapter. Furthermore, the systems investigated — single crystals, porphyrins, and ionic liquids — are outlined.*

### 2.1 Brief Historical Path of Scanning Probe Microscopy (SPM)

With the development of scanning tunneling microscope (STM) in 1981, Binnig and Rohrer (Nobel Prize in 1986) strongly pushed the field of nanotechnology [63]. It was the first instrument capable of imaging the surface features of a material in real space with atomic resolution [64].

Aside from the impressive simplicity of its concept, the STM has some limitations and challenges. The STM detects the current that flows between two conducting electrodes, a tip and a sample surface upon applying a voltage. It is therefore limited to conducting or semiconducting materials. In addition, due to the close proximity of the tip to the sample (usually  $< 1$  nm), extreme stability, shielding of sounds, and good vibrational isolation of the microscope are required, which frequently necessitates performing STM experiments under ultra-high vacuum (UHV) conditions.

It was discovered early on that there are significant local forces acting between the microscope tip and the sample. In 1986, Binnig, Quate, and Gerber invented the atomic force microscope (AFM) based on these forces [65]. The concept of using forces rather than current as the imaging signal made it possible to study nearly any surface. However, the AFM took about 15 years to achieve true atomic resolution [66].

In AFM, a tip is mounted at the end of a flexible cantilever that deflects (or bends) linearly with the applied force. Initially, the deflection was measured using an STM mounted on the cantilever's metalized backside. Later, optical [67] and piezoelectric [68] detecting methods were developed. AFM uses multiple operation modes depending on the application, which can be classified as contact (also denoted as static) or non-contact (also denoted as dynamic). In the contact mode, the tip is in contact with the surface and the force applied to the tip triggers a proportional static deflection of the cantilever. In contrast, in non-contact mode the cantilever is actuated close to its resonance frequency. The restoring force of the oscillation allows for stable operation (avoiding the jump-to-contact problem) at close tip-sample distances without physical contact. The resonance frequency of the cantilever is altered by the force between tip

and surface during approach. This frequency shift is the origin of the amplitude and frequency modulation mode of the non-contact AFM [65, 69].

In the attempt to achieve atomic resolution with AFM, various problems arose that slowed down progress compared to STM. Firstly, contact AFM could not attain full atomic resolution due to the greater contact area. Large oscillation amplitudes [70] were needed to solve the jump-to-contact (snap-in) problem in nc-AFM, which causes soft cantilevers to break at the surface. Large amplitude operation, on the other hand, was less sensitive to short-range forces (which cause atomic corrugation) interfering with long-range forces. This issue was avoided by using harder cantilevers. Besides, the non-exponential and non-monotonic force-distance relationship impeded the hunt of atomic resolution even more. Furthermore, nc-AFM necessitates multiple feedback circuits, requiring more sophisticated feedback electronics than STM. Nonetheless, nc-AFM was able to achieve atomic resolution on metals, semiconductors, and insulators over time. For a more detailed description of STM and AFM, the reader is referred to [71-74] and references therein.

Following the realization of STM and AFM, a wide range of alternative scanning probe-based techniques have been developed and are collectively referred to as “scanning probe microscopy” (see [75] and references therein). Many of these devices have found widespread use in both scientific research and industrial applications.

## 2.2 Scanning Tunneling Microscopy (STM)

The STM is based on the quantum mechanical tunneling effect [76]. Thereby, an electron with a specific kinetic energy has a finite probability of overcoming a potential barrier that it could classically not surmount. The tunneling particle is an electron whose wave function  $\Psi$  decays exponentially in the potential barrier, which is given by the vacuum gap between a conducting sample and a conducting tip. Thus, the probability density  $|\Psi^2|$  of finding an electron at a position behind the barrier is non-zero and allows for electron transmission. This phenomenon is referred to as tunneling. Such an effect enables STM to probe the surface topography or electronic structure of a flat sample surface using a sharp metallic conducting tip, which ideally is monoatomic. Most commonly, wires from tungsten or platinum-iridium (9:1) alloys are used for the tip, which is mounted on a piezoelectric control element that allows for a precise control in  $x$ ,  $y$ , and  $z$  directions. These precise movements are achieved using piezo actuators, which are based on the reverse piezoelectric effect, i.e., they convert electric signals into mechanical motion, typically from the sub Å range up to a few  $\mu\text{m}$  [77].

Upon applying a bias voltage  $U$ , the potential of tip and sample are shifted with respect to each other and a net tunneling current  $I$  of electrons from occupied sample to unoccupied tip states (or vice versa, depending on the bias polarity) is observed. In general, this phenomenon occurs when the distance  $d$  between tip and sample (potential barrier) is in the order of 1 nm or less. The tunneling current  $I$  decays exponentially with increasing tip-sample distance  $d$  and is represented by a simplified proportional equation [78].

$$I \propto U \cdot e^{-\frac{2d}{\hbar} \sqrt{2m_e\phi}} \quad 2.1$$

In Equation 2.1,  $\phi$  is the barrier height between tip and sample, which corresponds approximately to the average work function of tip and sample. Further,  $m_e$  is the electron mass and  $U$  is the applied bias voltage between tip and sample. After the tunneling contact is established, the tip scans over the surface in a raster-like fashion, line-by-line. Typically, two scanning modes are distinguished: constant current mode and constant height mode. In the commonly used constant current mode, the tip-sample distance  $d$  is adjusted to maintain a specific tunneling current, which can be set as an input for the  $z$  feedback loop. The imaging signal is represented by the topographic displacements caused by the  $z$  piezo. In constant height mode, the tip is scanned on a plane parallel to the surface without varying  $z$ . The imaging signal is then the tunneling current itself. The constant height option allows for faster scan speeds but needs the tip-sample junction to be extremely stable. This can be achieved through excellent vibrational dampening, low drift rates, and an atomically flat surface.

### 2.3 Non-contact Atomic Force Microscopy (nc-AFM)

Atomic force microscopy can be performed in different modes based on its dynamic and static characteristics and the type of interaction with the sample, which can be net repulsive or attractive [75]. Here, only the dynamic mode AFM in the attractive regime, also known as nc-AFM, will be discussed. In nc-AFM, a tip is connected to a driven oscillator, which ideally applies a force on it according to Hook's law  $F = -kz$ , where  $F$  is the spring force,  $k$  is the spring constant, and  $z$  is the displacement. As oscillators, micromachined Si cantilevers are commonly employed. Quartz crystal resonators, such as the qPlus [68] or KolibriSensor [79], have gained popularity due to their higher stiffness. The increased stiffness enables the steady operation of the resonator with small amplitudes, which improves sensitivity to short-range forces and compatibility with simultaneous STM operation. The spring constant  $k$ , resonance frequency  $f_0$ , and quality factor  $Q$  define the cantilever. Overall, the cantilever motion can be treated as a damped harmonic oscillator [72, 73].

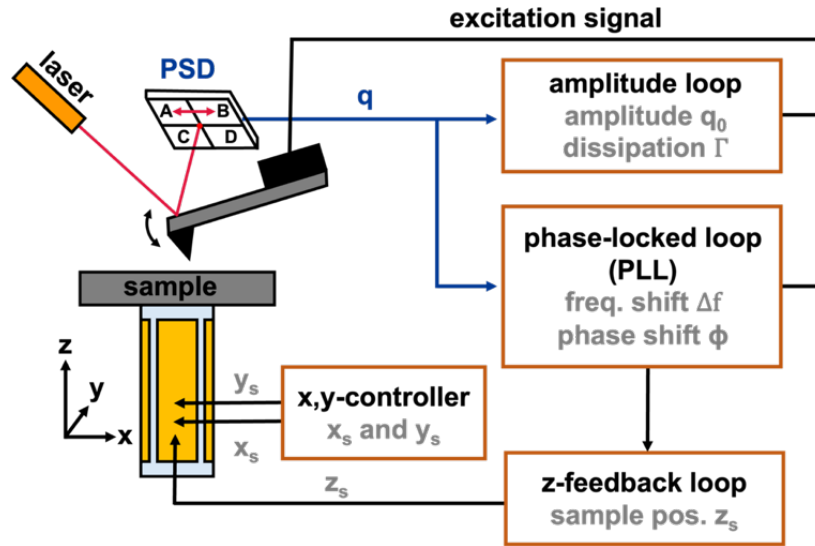


**Figure 2:** Schematic view of the frequency modulated AFM (FM-AFM) mode. A cantilever is forced to oscillate. The deflection  $q$  is detected via a position-sensitive detector (PSD). Piezo elements regulate the sample positions  $x_s$ ,  $y_s$ , and  $z_s$  with respect to the cantilever. In total, three feedback loops are used. The amplitude loop keeps the maximum deflection (amplitude) of the oscillating cantilever constant. The phase-locked loop (PLL) keeps the phase  $\phi$  between the vibrating cantilever and the excitation signal constant. The  $z$ -feedback loop keeps the frequency shift  $\Delta f$  between the cantilever's resonance frequency  $f_0$  and its eigenfrequency  $f$  constant by adjusting the sample position  $z_s$  using piezo elements.

In Figure 2, a feedback scheme for frequency modulation AFM (FM-AFM) [72, 73] is shown. The cantilever is excited to oscillate at its resonance frequency  $f_0$ . In this context, the cantilever is driven by a shaking piezo. The piezo vibrates at the cantilever's resonance frequency  $f_0$ , with a constant phase shift of  $\phi = \frac{\pi}{2}$  between the piezo and the cantilever. The laser beam is focused onto the back of the cantilever and then reflected onto a position-sensitive detector (PSD), where the cantilever deflection signal is detected. FM-AFM employs three feedback loops: the amplitude controller, the phase-locked loop (PLL), and the  $z$ -feedback loop. The oscillating cantilever's deflection signal  $q$  is routed to the PLL and the amplitude loop. The latter feedback loop described involves comparing the determined amplitude of the oscillating tip  $q_0$  with an externally provided reference value. The force used to excite the cantilever is then adjusted to match the cantilever's deflection amplitude  $q_0$  with the reference value. This feedback mechanism ensures that the cantilever's oscillation remains stable and at the desired amplitude. The dissipation  $\Gamma$  term represents the loss of kinetic energy per unit time in the oscillator, primarily caused by friction. While operating in UHV conditions, the cantilever dissipation is often quite low. Low dissipation is beneficial as it allows better sensitivity in detecting weak tip-sample forces and leads to sharper and more defined resonance peaks, resulting in higher imaging resolution. As the tip approaches the sample surface, the attractive interaction causes a resonance frequency shift towards lower frequencies. The tip-sample interaction becomes

repulsive very close to the surface, resulting in a positive frequency shift. To maintain a constant phase shift  $\phi$  between the oscillating cantilever and the excitation piezo element, a PLL is employed that modulates the frequency of the excitation signal. Furthermore, the PLL determines the resonance frequency  $f_0$  of the cantilever, which is subsequently sent to the z-feedback loop. In Equation 2.2, the frequency shift  $\Delta f$  characterizes the difference between the cantilever's resonance frequency  $f_0$  and its eigenfrequency  $f$  [80].

$$\Delta f = f - f_0 \quad 2.2$$

The z-feedback loop maintains the frequency shift  $\Delta f$  constant by adjusting the sample height  $z_s$  with piezo elements. As a result, the AFM controller can adjust the tip-sample distance by changing the z-feedback loop's reference value for the frequency shift  $\Delta f$ . So, this mode is known as FM-AFM. Further, the sample position can be adjusted along the lateral directions using  $x$ ,  $y$  controllers and additional piezo elements. This allows one to measure at multiple points on the sample, through scanning the surface. The acquired height signal  $z_s$  as a function of lateral position is referred to as a *topography*-related map.

### 2.4 Experimental Set-up

In order to study the adsorption behavior of complex porphyrin derivatives and ILs on different substrates, it is of utmost importance to keep the surface free from contaminations. Therefore, the sample preparation and all scanning probe microscopy (SPM) measurements presented in this work were performed under UHV conditions in two different chambers, hereafter referred to as Chamber 1 and 2. Both chambers contain an STM, and Chamber 2 is additionally equipped with a facility for AFM measurements.

#### 2.4.1 UHV Chamber 1

All experiments, sample preparations, and measurements on porphyrins were carried out in a two-chamber UHV system with a base pressure in the low  $10^{-10}$  mbar regime. To decouple against external low frequency vibrations, the entire system rests on three *Newport I-2000* laminar flow stabilizers (1.5 to 2.0 bar).

The home-built preparation chamber houses several sample preparation tools such as a *SPECS IQE11/12* sputter gun and electron bombardment (or radiative) heating from a filament of an Osram halogen light bulb (250 W) for cleaning and annealing the single crystals. For the deposition of organic molecules (porphyrin derivatives), a home-built 3-fold and a 1-fold Knudsen cell evaporator are used. Both evaporators can be individually pumped and separated

from the chamber by VAT gate valves, allowing for fast sample exchange without breaking the vacuum of the preparation chamber. A 3-fold *Omicron Focus EFM 3* electron beam evaporator is attached to the preparation chamber for deposition of different metals (Cu, Co, or Pd). In addition, a 1-fold *Omicron Focus EFM 3* electron beam evaporator is used in combination with a quartz crystal microbalance (*QCM, INFICON, SQM-160*) to ensure stable and reproducible evaporation rate for Co evaporation. Several gas inlets offer the possibility of dosing gases into the chambers. For sample characterization, it is armed with a *SPECS ErLEED* optic for low energy electron diffraction (LEED) and a *Pfeiffer HiQuad QMG700* ( $m/z = \text{max. } 2000$  atomic units) quadrupole mass spectrometer (QMS) for the detection of large organic molecules (porphyrin derivatives) and helium leak checks. In addition, the manipulator in the preparation chamber is equipped with a heating and cooling system and a temperature readout.

The analysis chamber houses a commercially available *RHK UHV VT STM 300* of the Besocke design (beetle type) [81]. The STM is operated with RHK SPM 100 electronics, which is connected to a PC for data acquisition via a digital interface. A *FEMTO DLPCA-200* variable gain, low noise current pre-amplifier is used to measure the low tunneling currents. Note that the current denoted in publications [P1-P2] have to be multiplied by a factor of 10 (due to different amplifier setting). This does not affect any of the conclusions. Radiative heating and a flow cryostat permit sample temperatures ranging from ca. 200 to 500 K. The load lock can be pumped separately and is separated from the analysis chamber by VAT gate valves, allowing for quick load exchange of samples and tips. The STM images were obtained with a manually cut Pt/Ir tip in constant current mode. The denoted bias voltage refers to voltage applied to the tip relative to the sample potential.

#### 2.4.2 UHV Chamber 2

Again, all experiments, sample preparations, and measurements on ILs were carried out in a two-chamber UHV system with a base pressure in the low  $10^{-11}$  mbar regime. To decouple the system from external low frequency vibrations, the entire UHV system rests on four tunable damping legs, and the AFM is additionally equipped with an eddy current damping mechanism. In this case, the base plate of the *VT AFM Q+ XA* is surrounded by a ring of copper plates that comes down between (permanent) magnets through a four-spring suspension system. The spring suspension system can be blocked to allow for tip or sample transfer.

The preparation chamber houses several sample preparation tools such as a *SPECS IQE11/35* sputter gun and electron bombardment heating for substrate cleaning and annealing. For the deposition of different ILs, two IL evaporators are used in combination with a quartz crystal

microbalance *PREVAC* (*QCM*, *TM13*, *TMC13*). The evaporator is built on a *Tectra KC3-BODY* with a customized head, and the construction details are accessible elsewhere [82]. Both evaporators can be pumped independently to avoid cross contamination and are decoupled from the chamber by VAT gate valves, allowing for quick sample exchange without breaking the vacuum of the preparation chamber. A 4-fold organic evaporator *OmniVac VE 300* is used for the deposition of organic molecules (porphyrin derivatives) and is currently dismantled. A 3-fold *Focus EFM 3T* electron beam evaporator is attached to the preparation chamber for the deposition of different metals (Fe, Co, or Pt). Several gas inlets offer the possibility of dosing gases into the chamber. In addition, an atomic hydrogen source *Focus EFM H* is equipped for dosing hydrogen. For sample characterization, the chamber is armed with a *Scienta Omicron SPECTALEED* optic for low energy electron diffraction (LEED) and a *Pfeiffer Vacuum (QMA 200, QME 220, QMG 220)* quadrupole mass spectrometer (QMS;  $m/z = \text{max. } 100$  atomic units) for residual gas analysis and helium leak checks. In addition, the manipulator in the preparation chamber is equipped with a heating and cooling system and a temperature readout. A separately pumped load lock chamber is connected to the preparation chamber via a VAT gate valve, allowing for quick load exchange of samples, tips, or cantilevers.

The analysis chamber houses a commercial *VT AFM Q+ XA*. STM or nc-AFM measurements were conducted using the *Scienta Omicron MATRIX* system that comprises software, computer hardware, and digital plus analog I/O electronics. The sample temperature can be varied using a built-in *PBN* heater and a bath cryostat. Using liquid nitrogen, a minimum substrate temperature of ca. 110 K is achieved, and it can be heated up to 500 K. A *Pt-100* sensor is used for temperature reading in analysis chamber. The STM images were obtained with a manually cut Pt/Ir tip in constant current mode. The denoted bias voltage refers to voltage applied to the tip relative to the sample potential. The AFM images were obtained in non-contact mode with silicon cantilevers in constant height mode. The instrument also involves a UHV suitcase for inter-chamber transfer of substrates, which can be attached to analysis chamber via a VAT gate valve.

The raw STM/nc-AFM images were processed using the WSxM software [83]. Moderate filtering (background subtraction, Gaussian smoothing) was applied for noise reduction.

### 2.5 Substrates: Ag(111), Cu(111), and Cu(110)

The adsorption behavior of porphyrin derivatives on Ag(111), Cu(111), and Cu(110) surfaces was investigated using STM in UHV Chamber 1, and the adsorption behavior of ILs on Cu(111) was probed using nc-AFM/STM in UHV Chamber 2.

To comprehend the adsorption and reaction behavior of large organic molecules or ILs on metallic substrates, a thorough knowledge of the atomic arrangement and electronic structure of the surface is required. Both silver and copper crystallize in the face-centered cube (fcc) lattice, as shown in Figure 3 (blue frame). The lattice constant of a silver crystal is  $a_{Ag} = 4.08 \text{ \AA}$ , hence the length of the unit cell vector on the  $\langle 111 \rangle$  surface is  $\frac{\sqrt{2}}{2} a_{Ag} = 2.89 \text{ \AA}$ . In contrast, the lattice constant of a copper crystal is  $a_{Cu} = 3.61 \text{ \AA}$ , hence  $\frac{\sqrt{2}}{2} a_{Cu} = 2.55 \text{ \AA}$ . Although both crystals exhibit same surface geometry, due to their different electronic structure the Cu substrate is more reactive surface than the Ag substrate. Because of the difference in reactivity, both surfaces are suitable candidates for studying the adsorption and reaction behavior of porphyrin derivatives or ILs. On the reactive Cu surface, the molecule-substrate interaction is expected to be stronger due to the strong interaction of the iminic nitrogen atoms of the porphyrin macrocycle, whereas on the rather inert Ag surface, molecule-molecule interactions dominate. Hence, it is possible to compare experiments performed on both surfaces to better understand how different functional groups influence the adsorption and reaction behavior of porphyrin derivatives. The Ag(111) crystal was purchased from Surface Preparation Laboratory, and the Cu(111) single crystal was purchased from MaTeck.

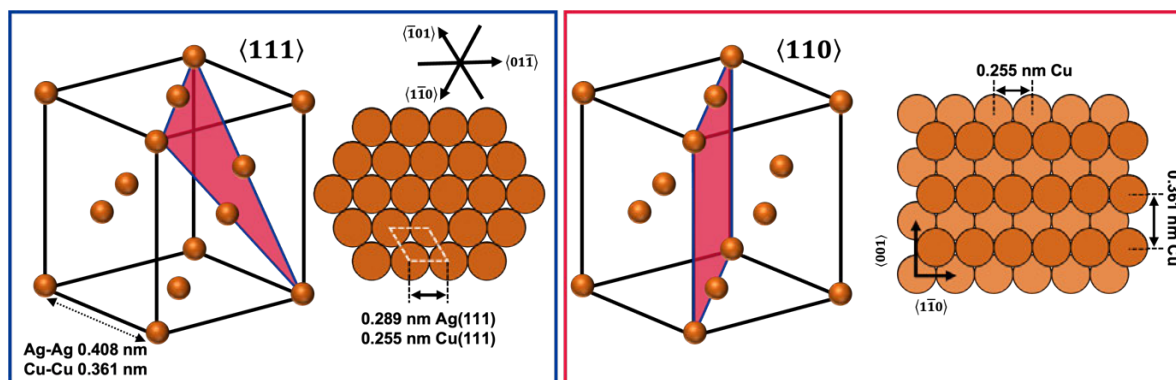


**Figure 3:** Surface phases ( $\langle 111 \rangle$  and  $\langle 110 \rangle$ ) indicated by shading (red) in the perspective view of the face-centered cubic (fcc) unit cell together with their top view of the atomic arrangement.

In addition, an experiment addressing the adsorption behavior of porphyrin derivatives was also carried out on Cu(110) surface. This surface is characterized by close-packed Cu rows along the  $\langle 1\bar{1}0 \rangle$  directions, resulting in a unidirectional corrugation. Its open structure is expected to make this surface more reactive than Ag(111) or Cu(111), and it was therefore chosen as a template substrate to study porphyrin derivatives. Figure 3 (red frame) shows the  $\langle 110 \rangle$  plane and the corresponding top view giving a next neighbor distance of  $2.55 \text{ \AA}$  and a row distance of  $3.61 \text{ \AA}$ . The Cu(110) single crystal was purchased from MaTeck. All Ag(111),

Cu(111), and Cu(110) single crystals have a specified purity of > 99.99 % and an alignment of <math>0.1^\circ</math> with respect to the nominal orientation.

In UHV Chamber 1, the single crystals are prepared by sequential cycles of  $\text{Ar}^+$  ion bombardment (600 or 700 eV, sample current between 5 to 12  $\mu\text{A}$  for 3 h) at an Ar background pressure of  $5.5 \times 10^{-5}$  mbar, followed by annealing at 850 K. The annealing step is done with a heating rate of 1 K/s to 850 K. This temperature is held for 10 minutes, followed by cooling down to RT at a rate of 1/3 K/s. This relatively slow preparation procedure leads to larger terraces and a lower number of steps. To avoid contaminating the sample surface with desorbing species from the manipulator during the annealing process for Cu(111) and Cu(110), the manipulator is cooled down and held at ca. 170 K.

In contrast, the preparation of Cu(111) in UHV Chamber 2 is slightly different. The Cu(111) surface is cleaned by sequential cycles of  $\text{Ar}^+$  ion bombardment (1 keV, sample current between 10 to 20  $\mu\text{A}$  for 1 h) at an Ar background pressure of  $5.5 \times 10^{-5}$  mbar, followed by annealing at 900 K for 10 minutes and cooling down to the desired temperatures ca. <math>160</math> K.

## 2.6 Porphyrins

Porphyrins are a class of heterocyclic molecules in which the parent macrocycle (porphin) is made up of four pyrrole rings connected by four methine bridges (i.e., at the position 5, 10, 15, 20) [84, 85]. Figure 4 shows the macrocycle's compliance with Hückel's criteria ( $4n + 2$ ) for aromaticity, emphasizing that porphyrins have highly conjugated  $\pi$ -electron system [86].

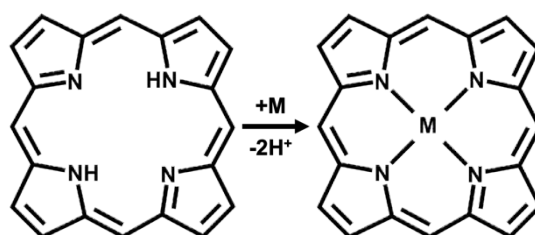


**Figure 4:** Schematic view of metal-free porphin (left) and the corresponding metalated species (right).

The system also exhibits a tautomerism [13, 87, 88] in which the two aminic hydrogen atoms (-NH-) can transfer intramolecularly to the adjacent iminic nitrogen atoms (=N-) on the surface, either by thermally induced self-transfer [89] or STM tip manipulation; this behavior can be imaged at cryogenic temperature of  $\sim 4$  K [90, 91]. In the adsorbed state, the proton exchange can be frozen, even at RT [92]. When the macrocycle is in the metal-free configuration (free-base porphyrin), it does not contain a metal ion (or atom) bound to the nitrogen atoms in the central cavity. As shown in Figure 4, the central cavity of macrocycle can coordinate a large

variety of metal atoms by removing off the hydrogen atoms, resulting in metalloporphyrins. In addition, a diverse range of porphyrin derivatives can be obtained by attaching functional end groups to different positions of the macrocycle, as depicted in Figure 5. Due to this complexity, the literature's nomenclature of porphyrins is often inconsistent. In order to characterize the porphyrins studied in this thesis, the following, most commonly used nomenclature will be adopted.

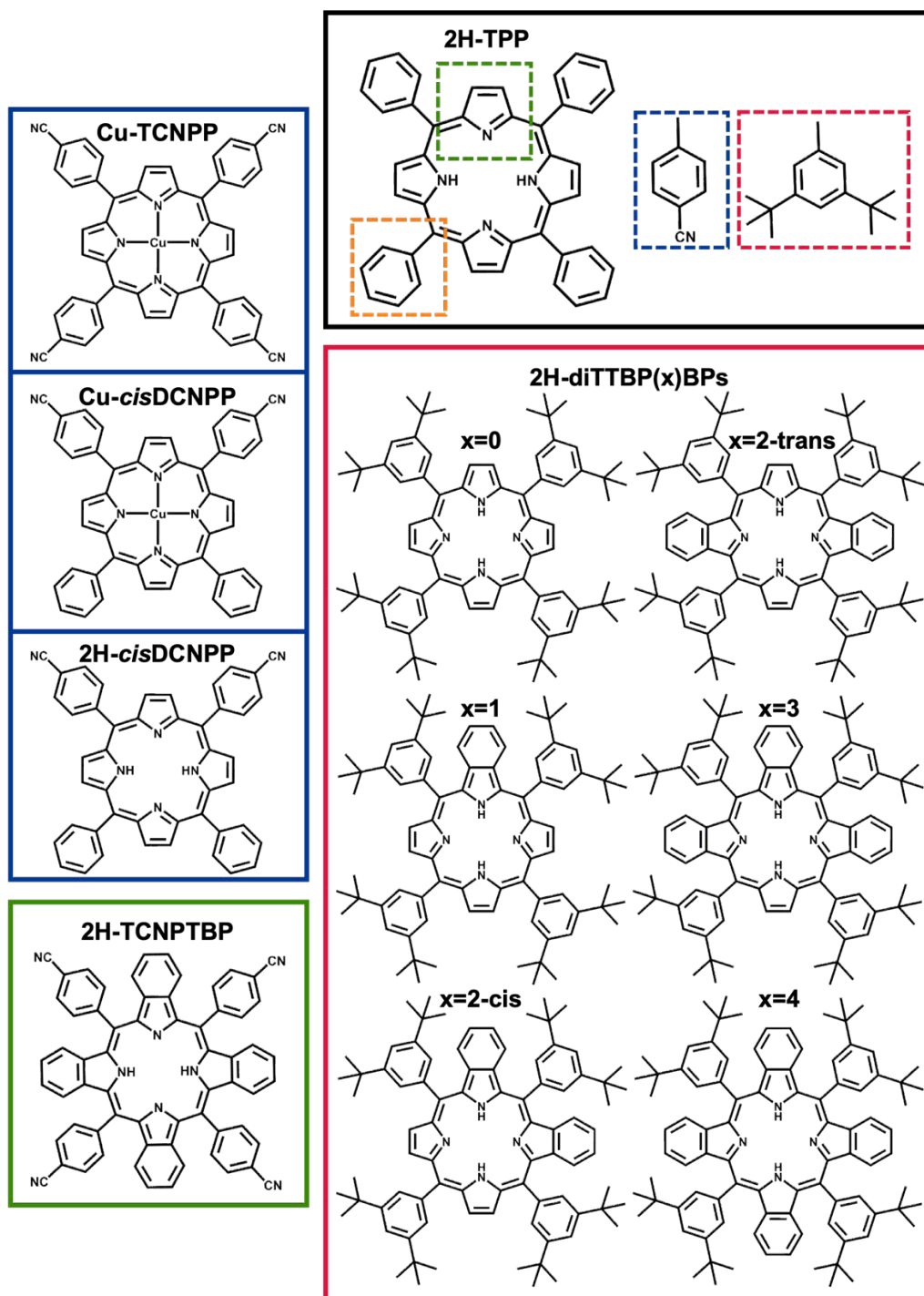


**Figure 5:** Schematic view of the porphyrin derivatives investigated in this thesis, namely Cu-TCNPP, Cu-cisDCNPP, 2H-cisDCNPP (blue solid frame), 2H-TCNPTBP (green solid frame), and 2H-diTTBP(x)BPs (red solid frame), along with 2H-TTP (black solid frame).

The porphyrin derivatives studied in this thesis are shown in Figure 5. The macrocycle can be functionalized in two different positions: Substituents bound to the carbon atom of the methine bridge are called *meso*-substituents (orange dashed frame), while substituents attached to the pyrrole rings are referred to as  $\beta$ -substituents (green dashed frame) [93]. All molecules in Figure 5 have phenyl legs substituted at each of the four *meso*-positions. As a result, these molecules are commonly referred to as *tetraphenylporphyrins*. The groups employed to further functionalize the porphyrins in *meso*-position are *para*-cyanophenyl (blue dashed frame) and (3, 5-di-*tert*-butyl)-phenyl (red dashed frame). The molecules depicted in the blue solid frame are referred to as *cyanoporphyrins* due to the functionalization with cyano groups at the *para*-positions of the *meso*-substituted phenyl legs. A fourfold functionalization directly at the  $\beta$ -position of the macrocycle (green and red solid frames) with benzene rings (isoindole groups) leads to the class of *tetrabenzoporphyrins* [94].

The chemical structure in Figure 6 suggests that the tetraphenylporphyrin exhibits a relatively flat intramolecular conformation. However, when molecules are adsorbed on a surface, the orientation of the individual groups within them deviates from this flat geometry due to steric hindrance. The macrocycle's conformation is represented by the twist angle  $\theta$ , which reflects the rotation around the  $\sigma$ -bonds, the tilt angle  $\phi$ , which corresponds to the inclination of the phenyl rings and macrocycle plane, and the angle  $\delta$ , which describes the tilting of the pyrrole rings relative to the macrocycle plane [95-99].

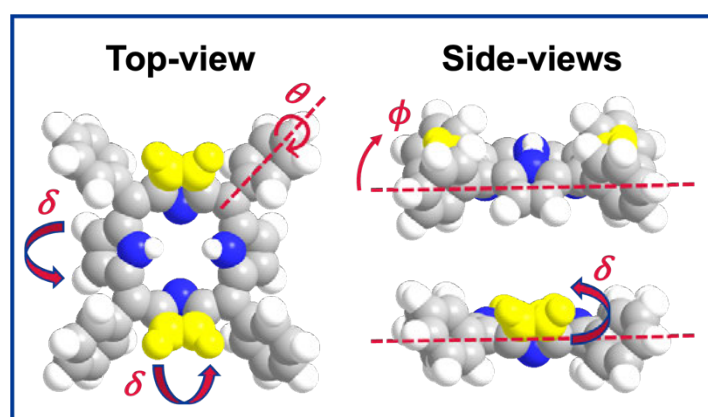


**Figure 6:** Top and side-views of space filling model of 2H-TPP illustrating macrocycle's conformational flexibility. The upward bent pyrrole groups are shown in yellow. The angle  $\delta$  refers to the tilting of the pyrrole groups out of the macrocycle plane. The angle  $\phi$  and  $\theta$  corresponds to the tilt and twist angle of the phenyl legs.

Figure 6 depicts an example of “saddle-shape” intramolecular conformation, in which two opposite pyrrole rings (yellow) are tilted upwards and the other two downwards, and the phenyl legs are twisted. In Chapter 4, the “saddle-shape” conformation as well as the novel adsorption

geometries “crown-shape” and “inverted” structure observed in this thesis are discussed in more detail.

In the framework of this thesis, a variety of metal-free and metalloporphyrin films were deposited by thermal sublimation from a home-built Kundsen cell [100] on Ag(111), Cu(111), and Cu(110) at RT. All porphyrin derivatives (or compounds) shown in Figure 5 were synthesized by the group of Prof. Dr. Norbert Jux from the Chair of Organic Chemistry II at the FAU Erlangen-Nürnberg.

## 2.7 Ionic Liquids

Ionic Liquids (ILs) are molten salts consisting solely of molecular ions (anions and cations) with a melting temperature below 100 °C and an exceptionally low vapor pressure [29-31, 34]. The low vapor pressure renders ILs vacuum stable and allows them to be used in the liquid phase under vacuum conditions. Their unique property profiles are determined by a complex combination of van der Waals, Coulomb, dipole, and hydrogen bonding interactions that are rarely found together in other materials (see [34] and references therein). By tailoring their properties with different functional groups or different anion-cation combinations, task-specific reaction media can be obtained [37, 38].

The most commonly used anions are fluorinated borane, phosphane, or methanesulfonate derivatives, or simply halogenides. Usual cations are imidazolium- and pyrrolidinium-based ions with one longer alkyl substituent and one methane group. Other common cations are quaternary ammonium ions or phosphonium ions [101, 102]. Figure 7 depicts the chemical and molecular structure of the ionic liquid  $[C_1C_1Im][Tf_2N]$  investigated in this thesis, which was deposited by physical vapor deposition (PVD) from a home-built Kundsen cell [82] on Cu(111) at different temperatures. It was synthesized under ultra-clean conditions by a procedure adapted from the literature described elsewhere [103].

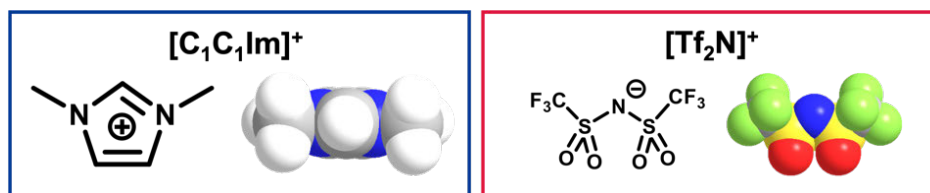


**Figure 7:** The chemical and molecular model of the ionic liquid  $[C_1C_1Im][Tf_2N]$ .

### 3 Literature Review

*This chapter will outline some key concepts and examples to describe the molecular conformation, self-assembly, and chemical surface reactions of porphyrins on different surfaces. These considerations are pertinent to the central theme of this thesis.*

#### 3.1 Molecular Conformation and Self-assembly

Molecular self-assembly is the spontaneous assembly of molecules under equilibrium conditions into structured, stable, non-covalently joined aggregates [104]. Self-assembly on metal surfaces is of particular interest since the confinement in two dimensions lowers the number of possible interaction motifs, and the local probe STM/AFM allows for real space examinations of the assembled networks. This enables a thorough understanding of the underlying mechanisms, particularly molecule-molecule and molecule-substrate interactions.

In this context, porphyrins belong to the most promising candidates, both as model systems and as useful molecular building blocks [14, 17, 105]. Moreover, they provide a diverse set of derivatives with tunable properties due to the availability of a large number of substituents plus different coordinated metal atoms at the core [105]. Porphyrins generally adsorb flat lying on metal substrates, driven by van der Waals forces, with the plane of the macrocycle parallel to the surface plane [105].

In a simplified picture, the intramolecular conformation of the adsorbed molecules reflects the interplay of molecule-molecule or molecule-substrate interactions. For the most exploited representative, the tetraphenylporphyrins, sterical hindrance of the 4-phenyl ligands at the *meso*-position does not allow for a completely flat adsorption geometry, but leads to a “saddle-shape” conformation on Au(111) and Ag(111) [14, 17, 105-107]. This indicates that by changing the molecular structure, the intramolecular conformation can be influenced. For example, by introducing a metal atom at the macrocycle core and four benzene rings (isoindole groups) at the  $\beta$ -position of macrocycle, a peculiar “crown-shape” structure was observed for Ni(II)-5, 10, 15, 20-tetraphenyltetrabenzoporphyrins (Ni-TPBP) on Cu(111) [108]. Moreover, a “bowl-like” structure was observed for 2H-5, 10, 15, 20-tetrakis(3,5-di-*tert*-butyl)-phenylporphyrins (2H-TTBPP) on Cu(111) by adding two bulky *tert*-butyl groups to the *meso*-phenyl groups [99]. However, the molecular structure is not only determined by the substituents but also by the macrocycle and its interaction with the surface. Jarvis et al. [109] studied 2H-tetra(4-bromophenyl) porphyrin (2H-Br<sub>4</sub>TPP) on Cu(111) using STM and DFT calculations. They proposed a “saddle-shape” conformation based on van der Waals

interactions (without strong chemical interactions) being the dominant molecule-substrate interactions. In contrast, in a similar system with 2H-TPP on Cu(111), Albrecht et al. [110] observed a different conformation, in which the two iminic nitrogen atoms of the pyrrole ring form a strong coordination with the underlying Cu substrate, yielding almost vertical pyrrole rings. This conformation differs from the “saddle-shape” or “crown-shape” and was called the “inverted” structure by Lepper et al. [111]. In fact, the different intramolecular conformations of porphyrins are linked to the different degree of interaction of iminic nitrogen atoms of the pyrrole or isoindole groups with the substrate atoms.

Further, the influence of the substituents linked to the porphyrin’s macrocycle is not only limited to its intramolecular conformation, but the substituents can also have a significant impact on the resulting supramolecular structure, making them a key element in self-assembly. For example, a slight change from 2H-tetraphenylporphyrin (2H-TPP) to 2H-tetraphenyl-tetrabenzoporphyrin (2H-TPTBP) with the addition of four isoindole (benzene rings) groups to the  $\beta$ -position of macrocycle not only changes the mobility of the molecules but also the self-assembly. For 2H-TPP, individually adsorbed molecules are observed on Cu(111) at low coverage, whereas 2H-TPTBP forms ordered islands [112]. Furthermore, the sole difference between 2H-TPP and 2H-tetrapyridylporphyrin (2H-TPyP) lies in the substitution of a single carbon atom within each phenyl group, which is replaced by a nitrogen atom in the *para*-position. As a result, 2H-TPP molecules form a long-range square arrangement on Ag(111) at RT [113], while 2H-TPyP molecules arrange in a different structure [114]. These examples illustrate that varying the porphyrin substituents is a successful route to control how these supramolecular nanostructures self-assemble. To understand this, it is also necessary to consider the underlying substrate’s influence on the adsorption behavior (see Figure 8).

Two distinct conformations of 2H-TPP are found on Ag(111) and Cu(111), which regulate its adsorption behavior. On Ag(111), 2H-TPP molecules at RT exhibit high mobility and form a long-range ordered structure with square unit cells due to weak molecule-substrate interaction with “saddle-shape” conformation stabilized by T-type interactions of the peripheral phenyl legs (see Figure 8, blue frame) [107]. In contrast, 2H-TPP on Cu(111) has strong interactions with surface atoms, resulting in its “inverted” structure, where it adsorbs individually along the high-symmetry crystallographic directions (white arrows in Figure 8, red frame), but without forming 2D islands [111, 115]. These examples reveal that the adsorption behavior of large organic molecules on well-defined single crystal surfaces is controlled by a complex interplay of molecule-molecule and molecule-substrate interactions.

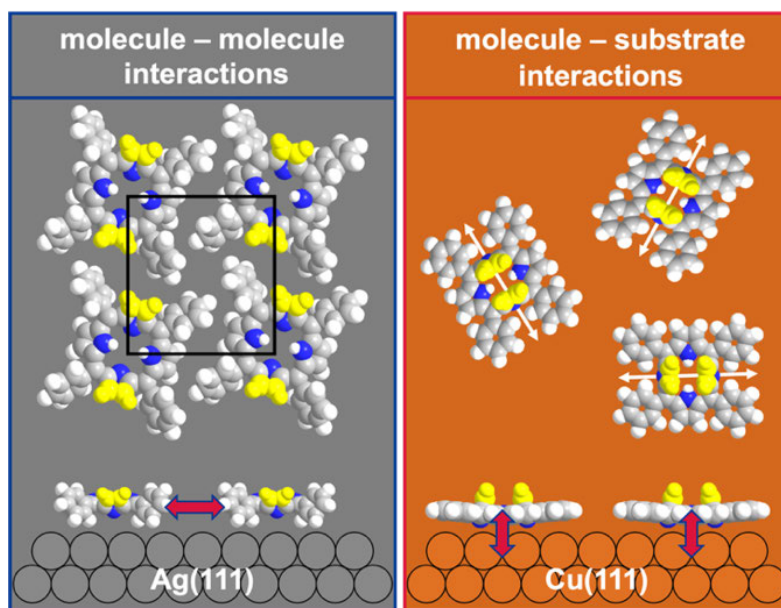


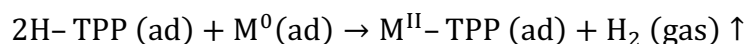
**Figure 8:** Example of 2H-TPP adsorption behavior on Ag(111) and Cu(111). Weak molecule-substrate interactions on Ag(111) result in 2D supramolecular arrangements via T-type interactions between neighboring porphyrins, which have a “saddle-shape” conformation (blue frame). Because of the strong molecule-substrate interaction on Cu(111), molecules adsorb individually and orient along the high-symmetry directions with an “inverted” conformation (white arrows in red frame).

So far, the supramolecular structure of porphyrins induced by non-covalent intermolecular interactions has been discussed. However, covalent intermolecular bonding can also create a supramolecular structure of porphyrins on surfaces. For bromine-functionalized porphyrins (Br<sub>4</sub>TPP) on Au(111), Grill et al. [116] demonstrated *in situ* (by thermal annealing) covalently linked networks via on-surface Ullmann-type coupling. Haq et al. [117, 118] demonstrated further *in situ* synthesis of supramolecular structures, revealing porphyrin linkage via C-Cu bond formation. In addition, a novel method to perturb supramolecular structures *in situ* is the addition of CN groups to the periphery of TPPs that promote different binding motifs, such as dipole-dipole interactions, H-bonds, or metal-organic bond formation (see [119, 120] and references therein).

### 3.2 Surface reactions: *In situ* Metalation and Dehydrogenation

The ability of the porphyrin macrocycle to coordinate a wide spectrum of metal atoms not only influences the electronic state but the inserted metal ion also acts as an active site, making it suited for use in surface science investigations [14-17, 21, 121-123]. For example, the *in situ* metalation of metal-free porphyrin (2H-TPP) with metal atoms from the substrate or by pre- or post-deposition of metal atoms has been well studied by STM, scanning tunneling spectroscopy (STS), AFM, X-ray photoelectron spectroscopy (XPS), and near edge X-ray absorption fine structure (NEXAFS). For pre- and post-deposition, the *in situ* metalation of 2H-TPP has

been shown to occur on Au(111) with Ni [124], on Ag(100) with Si [125] and on Ag(111) with Co [105, 126] and Cu [127, 128] at RT, or with Fe [129, 130], Zn [131, 132] or Ce [133] after moderate heating [16]. The work focused mostly on the chemical reactivity and the effect of reactant deposition order. The metalation reaction of 2H-TPP with different metal atoms, e.g., M = Cu, Co, Fe, to name only a few, can be written as:



Self-metalation was initially demonstrated for 2H-protoporphyrin IX (2H-PPIX) on Cu(110) and Cu(100) at RT [134]. The substrate's reactivity is important, as indicated by other observations of self-metalation of different porphyrins on Cu substrates [117, 127, 135] as well as on Fe(110) and Ni(111) [136]. In contrast, no self-metalation reaction was observed on relatively inert substrates such as Au or Ag. For 2H-TPP on Cu(111), Ditze et al. [137] investigated the metalation rate and corresponding activation energy of the self-metalation reaction by Arrhenius analysis at low coverage using STM at RT. Remarkably, not only the molecules metalate during this process, but also the adsorption behavior changes [138]. Further, Lepper et al. [139] evidenced that the self-metalation reaction of metal-free TPPs on Cu(111) systematically decreases with an increasing number of cyano substituents ( $n = 0, 1, 2,$  and  $4$ ) attached at the *para*-positions of the phenyl rings. In order to elucidate the mechanism of metal coordination on the porphyrin macrocycle, DFT calculations were performed on 2H-porphyrin in the gas phase [131]. A three-step reaction has been proposed: First, the reaction starts with the formation of an initial complex, in which the metal atom is coordinated by the intact unreduced porphyrin. In two subsequent steps, the pyrrolic hydrogen atoms are transferred to the metal atom, forming  $\text{H}_2$ , which is eventually released [131].

Further, a peculiar *in situ* on-surface reaction type is dehydrogenation that happens around 450 to 500 K. Using temperature-programmed desorption (TPD), supported by XPS and STM, Röckert et al. [140] identified three reactions for 2H-TPP on Cu(111): Metalation with Cu substrate atoms at 400 K, stepwise partial dehydrogenation at 450 K, and finally complete dehydrogenation (formation of new intramolecular C-C bonds between the pyrrole and the *meso*-phenyl groups) at 500 K [141]. A similar type of reaction has been observed for 2H-TPP on Ag(111), resulting in temperature-induced ring closure and a planar configuration [142]. Likewise, on-surface dehydrogenative coupling is not only confined to intramolecular C-C bond formation, but can also be used to cross-link other carbon-based compounds to porphyrins (see [143] and references therein). For example, He et al. [144] observed fused tetrapyrroles on

graphene edges by surface-assisted covalent coupling by heating porphin and graphene sheets on Ag(111) to 620 K.

To sum up, metalation of porphyrins happens at or slightly above RT, whereas dehydrogenation necessitates a higher heating temperature. Consequently, porphyrin properties, as well as molecule-molecule and molecule-substrate interactions, can be altered *in situ* using these reaction types, which is relevant to this work.

## 4 Results

*The work presented in this chapter has been published. Figures and texts are reprinted and modified. The part presented in this thesis is shortened compared to the original publication and focuses mainly on the adsorption behavior, molecular conformation, self-assembly, in situ metalation reaction, and dehydrogenation using STM, nc-AFM, and DFT calculations plus complementary XPS on single crystal metal surfaces. The published papers [P1-P4] are attached to the Appendix A2 and provide a detailed discussion of each system investigated.*

*The findings aim to understand the fundamental aspects of adsorption behavior as well as chemical interactions of porphyrin molecules (the central theme of this thesis) and ILs on metal surfaces, which is key for the advancement of various fields such as nanotechnology and catalysis. Here, porphyrin molecules and ILs deposited on a metal surface may either strongly interact with the substrate or move freely (due to high mobility resulting from low diffusion barriers) on the substrate to form well-ordered supramolecular structures. The outcomes are driven by the complex interplay of molecule-molecule or molecule-substrate interactions. In order to draw conclusions regarding the interplay of the interactions, the intramolecular conformation of molecules as well as their supramolecular order must be thoroughly investigated. Success hinges on the selection of molecular building blocks, reactivity and symmetry of underlying substrates, as well as activation conditions.*

### 4.1 Cyano-Functionalized Porphyrins on Cu(111) [P1]

The extensive investigation of 2H-TPP interaction on single crystal surfaces has established this system as a well-known reference system [15, 107, 110, 111, 115, 127, 129, 131, 137, 145]. On Cu(111) at RT, individual 2H-TPP were observed due to strong molecule-substrate interaction between the iminic nitrogen atoms of the porphyrin and the Cu atoms of the substrate [111, 115]. In contrast, on Ag(111) supramolecular structures of 2H-TPP are formed as a result of T-type intermolecular interactions between the peripheral phenyl substituents of neighboring molecules [107]. Due to the different interplay of interactions on the two different substrates, two different intramolecular conformations, namely “inverted” and “saddle-shape”, were observed on Cu(111) and Ag(111), respectively. This section focuses on the changes introduced by cyano groups ( $n = 2$ -*cis*, 4) at the *para*-position of the *meso*-substituted phenyl legs of tetraphenylporphyrins with and without a metal (Cu) center.

The adsorption behavior of three related cyano-functionalized tetraphenylporphyrin derivatives was investigated on Cu(111) by STM as a function of temperature combined with DFT

calculations. The goal was to identify the role of the cyano groups and the central Cu atom. Figure 5 (blue frame) in Section 2.6 depicts the chemical structures of these porphyrin derivatives: Cu-5,10,15,20-tetrakis-(*p*-cyano)-phenylporphyrin (Cu-TCNPP), Cu-*meso-cis*-di(*p*-cyano)-phenylporphyrin (Cu-*cis*DCNPP), and 2H-*meso-cis*-di(*p*-cyano)-phenylporphyrin (2H-*cis*DCNPP). Figure 9a-f (blue frame) depict STM images of sub-monolayer amounts of Cu-TCNPP deposited and measured on Cu(111) at RT. Cu-TCNPP, with four cyano groups, forms a 2D hexagonal honeycomb-type structure with triangular pores coexisting with 1D double-row molecular chains. The self-assembled ordered islands often grow from step edges onto the terraces, indicating that the steps are energetically favored adsorption sites acting as nucleation centers [16].

The individual molecules (see Figure 9a-b) in both motifs appear as six protrusions, which are arranged in two parallel groups of three protrusions. The outer four protrusions correspond to the peripheral phenyl substituents, while the two central protrusions correspond to the slightly upward bent pyrrole groups. This is evident from Figure 9d, where the STM image from Figure 9c is superimposed with a scaled molecular model; this appearance is attributed to a “saddle-shape” conformation [106, 107, 109, 146]. This results from a subtle balance between molecule-molecule and molecule-substrate interactions, and steric forces within the molecules. In contrast, for metal-free 2H-TCNPP on Cu(111), an “inverted” structure was found, characterized by direct N-Cu bonds and two nearly vertical pyrrole groups [120].

Figure 9e shows a high-resolution STM image of a 2D triangular porous honeycomb-type structure, with a primitive hexagonal unit cell with unit cell vectors of  $3.0 \pm 0.15$  nm and  $\gamma = 60 \pm 2^\circ$ , containing 3 molecules per unit cell. To gain further insight into the structure formation, the STM image from Figure 9e is overlaid with scaled molecular models of Cu-TCNPP in Figure 9f. This comparison shows that neighboring cyano groups face each other at the corners of the triangular pores. Here, three Cu-TCNPP molecules are rotated by  $60^\circ$  with respect to each other to form the regular triangular pores. Closer inspection reveals that the observed ordered network structure of Cu-TCNPP on Cu(111) is not due to mutual stabilization via attractive interaction, as reported for 2H-TCNPP on Ag(111) [120]. A direct CN-NC interaction is not expected due to electrostatic repulsion, and due to the large distance of peripheral cyano groups, T-type interaction,  $\pi$ - $\pi$  intermolecular stacking, hydrogen bonds, and dipolar coupling are ruled out [107, 119, 147]. Since the Cu(111) surface is known to offer adequate native adatoms, the 2D triangular porous honeycomb-type networks are stabilized via CN-Cu-NC interactions, in which the adatoms at the corners of the triangles fuse together with two Cu-TCNPP molecules [120].

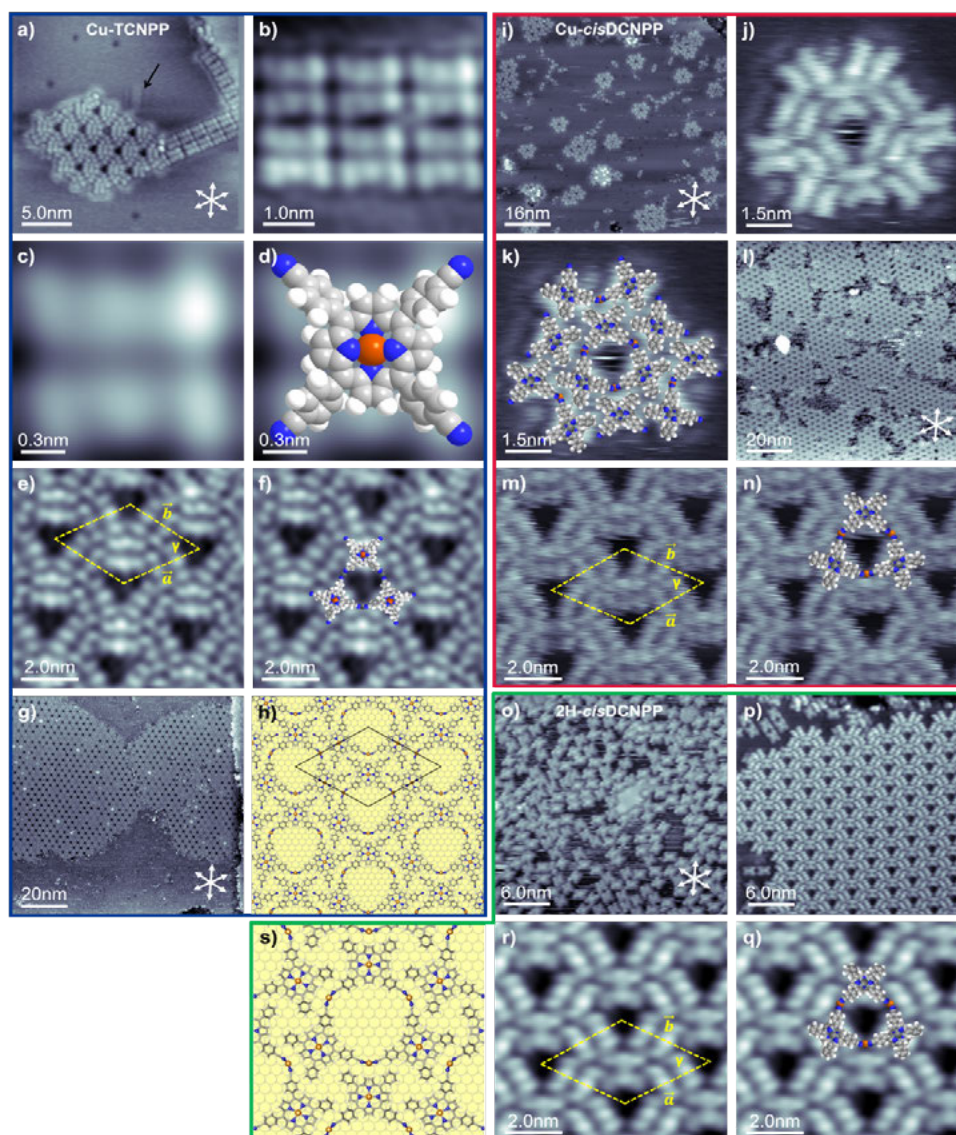


**Figure 9:** **a)** An average frame of 15 consecutively recorded STM images ( $30 \times 30 \text{ nm}^2$ ) of Cu-TCNPP, deposited and measured at RT, showing a 1D linear parallel structure and a 2D porous hexagonal honeycomb-type structure. **b)** Short 1D parallel molecular chains ( $5 \times 5 \text{ nm}^2$ ). **c)** High-resolution STM image ( $1.5 \times 1.5 \text{ nm}^2$ ) of a single Cu-TCNPP molecule with six protrusions, which are ascribed to the two iminic pyrrole groups (center) and the 4 phenyl (peripheral) groups. **d)** Single Cu-TCNPP molecule from (c) overlaid with a molecule model. **e)** STM image ( $10 \times 10 \text{ nm}^2$ ) of the highly ordered 2D porous honeycomb-type pattern with the lattice vectors of the unit cell indicated as dashed yellow lines. **f)** STM image of (e) overlaid with scaled models of Cu-TCNPP molecules. **g)** STM image ( $100 \times 100 \text{ nm}^2$ ) showing the full monomodal transformation of Cu-TCNPP after annealing at 400 K for 10 min. **h)** DFT-optimized structure of the porous honeycomb-type network showing a hexagonal ( $7\sqrt{3} \times 7\sqrt{3}$ ) $R30^\circ$  superstructure, in which the molecules are linked through Cu adatoms on Cu(111). **i)** STM image ( $80 \times 80 \text{ nm}^2$ ) showing Cu-cisDCNPP deposited and measured at RT. **j-k)** High-resolution STM image ( $7.5 \times 7.5 \text{ nm}^2$ ) showing a monoflake with molecular model superimposed. **l)** STM image ( $100 \times 100 \text{ nm}^2$ ) showing 2D porous network formation after annealing at 400 K for 1 h. **m-n)** Close-up STM image ( $10 \times 10 \text{ nm}^2$ ) with unit cell and tentative molecule model overlaid. **o)** STM image ( $30 \times 30 \text{ nm}^2$ ) showing 2H-cisDCNPP deposited and measured at RT. **p)** STM image showing Cu-cisDCNPP ( $30 \times 30 \text{ nm}^2$ ) converted from 2H-cisDCNPP by annealing at 400 K for 5 h. **q-r)** Close-up STM image ( $10 \times 10 \text{ nm}^2$ ) with unit cell and tentative molecule model overlaid. **s)** DFT-optimized structure of the porous honeycomb-type network with terminal CN groups connected by Cu atoms. The STM images were measured with  $U_{\text{bias}}$  between -1.22 and -1.0 V and  $I_{\text{set}}$  between 288 and 303 pA; for details see [P1]. Modified images and text from [P1] used with permission.

Figure 9g shows the STM image acquired at RT after heating the deposited Cu-TCNPP films to 400 K. The annealing results in a complete transformation to a hexagonal honeycomb-type structure with pronounced long-range order, without any 1D molecular double-row chains. In order to understand the driving forces that lead to the formation of the triangular porous hexagonal honeycomb-type structure of the adsorbed porphyrins, extensive DFT calculations were performed. Figure 9h shows a DFT-optimized structure model based on the STM image of Figure 9g. The calculated commensurate primitive hexagonal unit cell corresponds to a  $(7\sqrt{3} \times 7\sqrt{3}) R30^\circ$  superstructure with a lattice vector of 3.09 nm, which is in good agreement with the experimental values. In this structure, Cu-TCNPP molecules adsorb on the bridge sites, while the connecting Cu adatoms occupy threefold hollow sites. This information solely stems from the DFT calculations and not from STM (for details refer to [P1]). Furthermore, heating to 450 K leads to the formation of new species (randomly orientated individual molecules with four protrusions), which is tentatively assigned to the formation of intramolecular C-C bonds between the pyrrole and the phenyl groups following the dehydrogenation process [140, 141, 148] (not shown here, for details refer to [P1]).

Next, the number of cyano-functionalized substituents was changed from  $n = 4$  to  $n = 2$ -*cis* configuration. Figure 9i-k (red frame) depict STM images of Cu-*cis*DCNPP deposited and measured on Cu(111) at RT. It forms monoflakes with a triangular pore, along with bi- and multiflakes, all of which transform into the 2D porous hexagonal honeycomb-type structure at 400 K (see Figure 9l-n, red frame). Overall, the individual molecules within the flakes or honeycomb-type structure are characterized by two parallel elongated protrusions, which is identical to that proposed for Cu-TCNPP and indicates a “saddle-shape” conformation. Furthermore, its porous structure is identical to that of Cu-TCNPP and is stabilized by the local CN-Cu-NC bonding motif, as shown in DFT-optimized structure in Figure 9s (green frame).

Finally, the adsorption behavior of the metal-free 2H-*cis*DCNPP on Cu(111) at RT was investigated. 2H-*cis*DCNPP shows no order at RT (see Figure 9o, green frame), but is adsorbed as individual molecule, appearing as four bright lobes in the periphery and two dominating protrusions in the center (here it appears as one longish protrusion due to a different tip termination). The intramolecular conformation and adsorption behavior are very similar to that of 2H-TCNPP on Cu(111), where it is characterized by an “inverted” structure [120]. The deposited 2H-*cis*DCNPP films were then annealed at 400 K, resulting in an almost complete transformation into the same perfectly ordered 2D triangular porous hexagonal honeycomb-type structure as the other two porphyrins (see Figure 9p-r, green frame). The individual molecules within the long-range ordered structure appear as six protrusions, which

are arranged in two parallel rows of three protrusions. The intramolecular conformation is identical to that observed for Cu-TCNPP, indicating that 2H-*cis*DCNPP self-metalates with Cu atoms from the substrate to form Cu-*cis*DCNPP. Overall, the ordered 2D network has the identical triangular pore structure as described above for Cu-*cis*DCNPP and Cu-TCNPP, and is stabilized by CN-Cu-NC interactions.

To sum up, the ordered flakes and the porous hexagonal honeycomb-type structures all share the same structure-forming element: porous porphyrin triangles (distance of 3.1 nm) fused together via CN-Cu-NC interactions with Cu adatoms. The three porphyrin molecules are rotated 60° with respect to each other and aligned parallel to the substrate high-symmetry directions. Furthermore, the internal structure of the unit cell indicates that interactions between the other two porphyrin ligands — Cu-TCNPP with CN groups, and Cu-*cis*DCNPP and 2H-*cis*DCNPP without CN ligands — do not contribute significantly to the formation of the long-range ordered porous structure. This observation suggests that cyano-phenyl groups ( $n = 2$ ) in the “*cis*” position are the minimum requirement for the formation of a highly ordered 2D porous molecular pattern and that they are involved in directed attractive interactions. Complementing the STM, the DFT calculations provide detailed insights into the various energetic contributions leading to the observed long-range ordered hexagonal honeycomb-type structure with triangular pores, which is thermodynamically stable. For details refer to [P1].

## 4.2 Cyano-Functionalized Benzoporphyrin on Cu(111) [P2]

Following the investigation of the fundamental aspects of the adsorption behavior of three related cyano-functionalized tetraphenylporphyrin derivatives discussed above, this section summarizes the adsorption behavior and structure formation of a novel cyano-functionalized benzoporphyrin.

Figure 5 (green frame) in Section 2.6 depicts the chemical structure of 2H-5,10,15,20-tetrakis(4-cyanophenyl)-tetrabenzoporphyrin (2H-TCNPTBP), a tetrapyrrolic macrocycle functionalized with cyanophenyl substituents at four *meso*-positions, with each cyano end group pointing outward, and with benzene rings at four  $\beta$ -positions. To investigate the influence of linker groups (cyano- and isoindole (benzopyrrole) groups) on adsorption and self-assembly as a function of temperature, a sub-monolayer amount of 2H-TCNPTBP was deposited and measured at RT on Cu(111). 2H-TCNPTBP, with four cyano- and four isoindole groups, shows the coexistence of three prominent molecular arrangements, namely, a Kagome lattice structure, a quadratic pattern, and a hexagonal structure (see Figure 10).

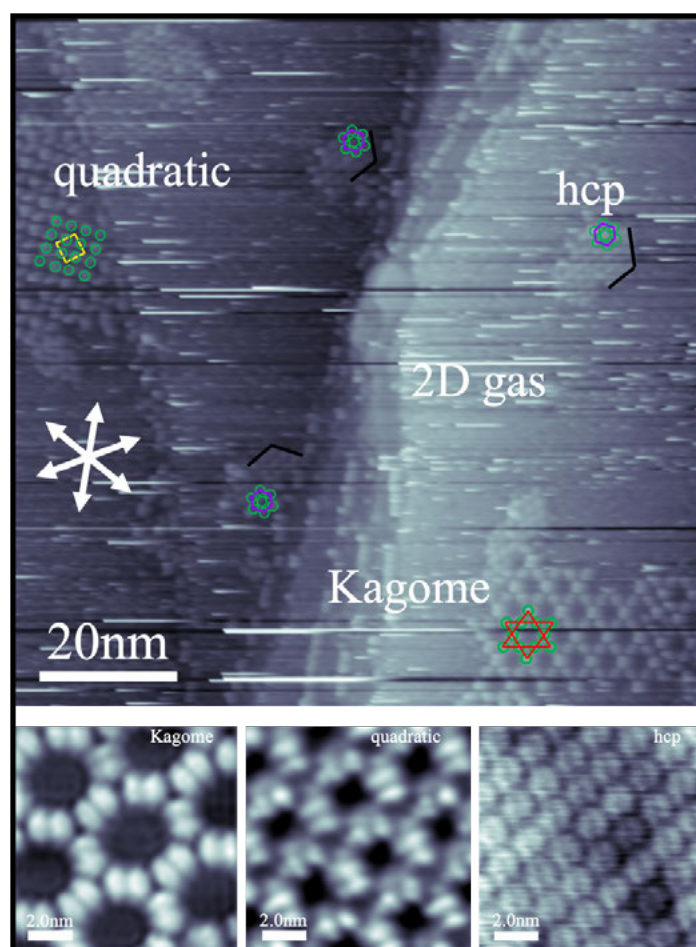


**Figure 10:** (Top) Overview STM image of 2H-TCNPTBP on Cu(111); ( $100 \times 100 \text{ nm}^2$ ,  $U_{\text{bias}} = 1.00 \text{ V}$ ,  $I_{\text{set}} = 298 \text{ pA}$ ) measured at RT, showing the coexistence of three ordered phases, the Kagome structure (red), the quadratic structure (yellow), and the hexagonal structure (violet), with the molecules indicated as green circles. The stripy, horizontal features are attributed to fast diffusing molecules, that is, a 2D gas phase, which coexists with the ordered 2D phases. (Bottom) The three observed structures on an enlarged scale. Original images and text from [P2] used with permission.

Figure 11 depicts the results for the Kagome (a-c, blue frame) and the quadratic structure (d-f, red frame). The individual molecules within the ordered phase of the Kagome and quadratic structures are characterized by two parallel rod-like bright protrusions with an elongated depression in-between and adopt a “saddle-shape” conformation [106, 107, 109, 146]. In the supramolecular Kagome arrangement, each molecule is connected to four neighbors, with three molecules forming an intersecting network of corner-sharing triangles. The structure is described with a primitive hexagonal unit cell ( $60 \pm 2^\circ$ ) containing three molecules. The primitive hexagonal unit cell corresponds to a  $(17 \times 17)$  superstructure with a lattice vector of  $4.40 \pm 0.30 \text{ nm}$ . In contrast, in the quadratic pattern, each molecule is connected to four neighboring molecules. The ordered structure can be described with a square unit cell of  $(88 \pm 3^\circ)$ , which contains two molecules and lattice vectors of  $3.30 \pm 0.20 \text{ nm}$ . Both porous structures have two different pore sizes, with the large pores of the Kagome structure having a

diameter of  $\sim 3$  nm and those of the quadratic structure of  $\sim 1.5$  nm; both have a molecular density of  $0.18$  molecules/nm<sup>2</sup>.

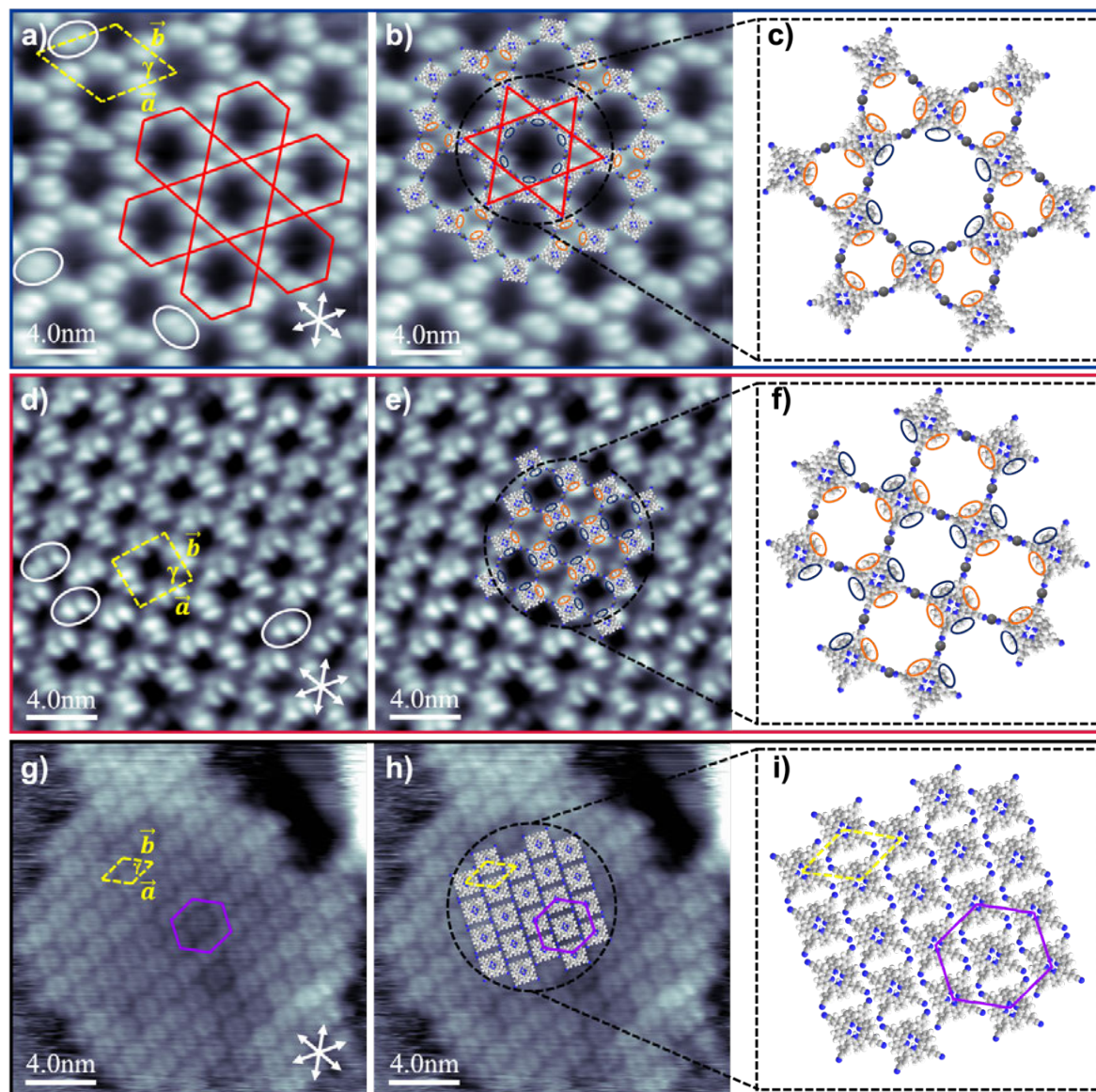


**Figure 11:** **a)** High-resolution STM image ( $20 \times 20$  nm<sup>2</sup>,  $U_{bias} = 1.01$  V,  $I_{set} = 298$  pA, measured at RT) showing the Kagome structure. The Kagome lattice is highlighted with red line frame, and the primitive unit cell with yellow broken line; individual misoriented molecules are marked with white ellipses. **b)** STM image of (a) overlaid with scaled models of 2H-TCNPTBP molecules. **c)** Proposed structural model of the Kagome structure, displaying an intersecting web of corner-sharing triangles. **d)** High-resolution STM image ( $20 \times 20$  nm<sup>2</sup>;  $U_{bias} = -1.01$  V,  $I_{set} = 290$  pA, measured at RT) showing the quadratic porous structure; the unit cell is indicated with broken yellow lines, and individual misoriented molecules are indicated with white ellipses. **e)** STM image of (d) overlaid with scaled models of 2H-TCNPTBP molecules. **f)** Proposed structural model of the quadratic structure. The orange and dark blue ellipses indicate the upward-bent and downward-bent isoindole groups in the saddle-shape conformation; gray spheres correspond to Cu adatoms, which interconnect neighboring molecules via CN-Cu-NC bonds, leading to the observed coordination networks. **g)** High-resolution STM image ( $20 \times 20$  nm<sup>2</sup>;  $U_{bias} = -1.00$  V,  $I_{set} = 294$  pA, measured at RT) showing a hexagonally close-packed phase. The structure is indicated with a violet hexagon, and the primitive unit cell is indicated with broken yellow lines. **h)** STM image of (g) overlaid with scaled models of 2H-TCNPTBP molecules. **i)** Proposed structural model of the H-bonded close-packed network. Modified images and text from [P2] used with permission.

To facilitate the identification of the supramolecular arrangements and the intermolecular networks, the STM images from Figure 11(a, d) are superimposed with scaled molecular models of 2H-TCNPTBP in Figure 11(b, e). The molecules in both structures are oriented such that the downward bent isoindole groups (dark blue ellipses) face the larger pores and the upward bent isoindole groups (orange ellipses) face the smaller pores. In the Kagome lattice, the large pore is formed by six downward bent isoindole groups at the hexagon's edges, with the sides formed by six CN-Cu-NC bonds, and the small pores are formed by the three upward bent isoindole groups at the trigon's edges, with the sides formed by three CN-Cu-NC bonds. In contrast, the large pore in quadratic structure is formed by four downward bent isoindole groups and four CN-Cu-NC bonds, while the smaller, less dark pores are formed by the four upward-bent isoindole groups and four CN-Cu-NC links. This arrangement type — cyano groups pointing head-on towards the cyano groups of neighboring molecules — indicates that both networks do not form via CN-NC coordination due to polarity, mutual interactions via attractive interactions [120], or T-type or  $\pi$ - $\pi$  intermolecular stacking observed for similar porphyrin derivative 2H-TPTBP on Ag(111), Cu(111), and Cu(110) [112]. In contrast, CN-Cu-NC interactions with Cu adatoms stabilize both porous structures, since the lone pair electrons provided by N atoms of the cyano groups have a high binding affinity towards transition metals [119, 120]. Notably, the Cu adatoms are not resolved in the STM images, most likely due to electronic effects [149, 150].

The other structure type observed on the surface is a hexagonally close-packed phase (see Figure 11g-i). This structure is already present at low coverages. At higher coverages, extended domains preferentially form (not shown here, for details refer to [P2]). Within the hexagonally close-packed phase, individual 2H-TCNPTBP molecules are again characterized by two parallel, rod-like, bright protrusions with an elongated depression in-between. These molecules adopt again a “saddle-shape” conformation. The structure is described with a primitive hexagonal unit cell ( $60 \pm 2^\circ$ ) containing one molecule. The primitive hexagonal unit cell corresponds to a  $(4\sqrt{3} \times 4\sqrt{3})R30^\circ$  superstructure with a lattice vector of  $1.65 \pm 0.15$  nm, and a molecular density of 0.42 molecules/nm<sup>2</sup>. From the structural model based on the STM, the cyanophenyl substituents of two molecules point towards the isoindole moieties of neighboring 2H-TCNPTBP molecule, while neighboring -CN groups have opposite orientations to each other. This configuration allows for H-bond formation [120, 151] between the electronegative N atoms of the terminal cyano-functionalized end groups and the sp<sup>2</sup>-hybridized carbon atom from a nearby molecule's isoindole moiety. Furthermore, attractive

dipole-dipole interactions of oppositely orientated cyano end groups contribute to stabilize this structure.

An important point to be addressed here is why Cu-coordinated structures with rather strong metal-organic coordination bonds coexist with an H-bonded structure with weaker attractive lateral interactions. This condition is possible if the metal-coordinated network takes up more space (i.e., has a lower density) than the H-bonded one [152, 153]. Cai et al. [152] reported that the loss of intermolecular interaction energy is overcompensated by the adsorption of additional molecules at high coverage. In general, the results support this interpretation when considering the molecular density in three phases: The Kagome and Quadratic phase exhibit a density of 0.18 molecules/nm<sup>2</sup>, while hexagonal phase shows a notably higher density of 0.42 molecules/nm<sup>2</sup> (ca. 2.3 times larger). These considerations lead to the conclusion that the coexistence results from the substantial increase in total adsorption energy due to the significantly higher molecule density observed in the close-packed network of the hexagonal phase.

Finally, the identified phases of 2H-TCNPTBP films on Cu(111) were heated to 450 K for 10 sec. Upon heating, the formation of an immobile species with a “clover-shape” appearance was observed, which is tentatively assigned to dehydrogenation and the formation of intramolecular C-C bonds between the isoindole and the phenyl groups [140, 141, 148].

To sum up, the three structures coexist due to their very similar energetics. The two Cu-coordinated porous structures (Kagome and quadratic) with the same molecular density are stabilized by the energy gain due to the network formation (CN-Cu-NC). In contrast, the hexagonal structure compensates its weaker intermolecular interactions (H-bond) by a factor of 2.3 higher molecular density. Likewise, kinetic stabilization cannot be ruled out. For details refer to [P2].

### **4.3 Mixture of Benzoporphyrins on Ag(111), Cu(111), and Cu(110) [P4]**

After discussing the adsorption behavior of the three related cyano-functionalized porphyrins and a novel cyano-functionalized benzoporphyrin in the previous Sections 4.1 and 4.2, respectively, this section addresses the self-assembly of exceedingly complex mixed benzoporphyrin derivatives, based on the results of [P4].

The literature on benzoporphyrin shows prospective applications in organic near-infrared light-emitting devices, in photodynamic therapy, in catalysis, in dye-sensitized solar cells, or as oxygen sensors, to name only a few [94, 154-156]. Despite their importance, only a few studies

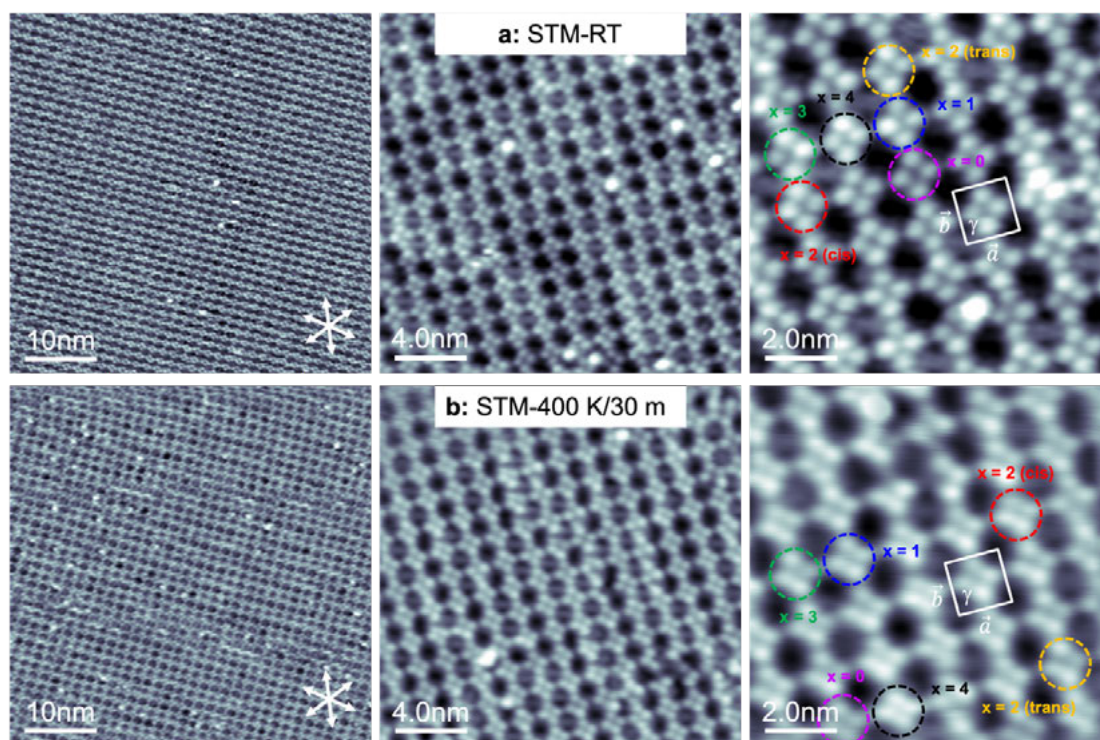
have been reported on their adsorption behavior on various metal surfaces, showing peculiar self-assembly [108, 112, 157-159], which could find potential uses in organic electronics or catalysis. However, despite these promising results, the study of benzoporphyrins is still in its infancy and lacks structural diversity. This deficit is mainly due to the difficulty of synthesizing functionalized isolated benzoporphyrin derivatives [160]. Since different molecules cannot be separated during the synthesis process [160, 161], the interactions of a mixture of six benzoporphyrin derivatives with bulky side groups on Ag(111), Cu(111), and Cu(110) were investigated using STM to identify and assign different molecules, along with the influence of linker groups on self-assembly as a function of temperature.

Figure 5 (red frame) in Section 2.6 depicts the chemical structure of a mixture of six 2H-tetrakis-(3, 5-di-*tert*-butylphenyl)(*x*)benzoporphyrins (2H-diTTBP(*x*)BPs, *x* = 0, 1, 2-*cis*, 2-*trans*, 3, and 4), a tetrapyrrolic macrocycle functionalized with (3, 5-di-*tert*-butyl)-phenyl substituents at all four *meso*-positions, with each *tert*-butyl end group pointing outwards, and with benzene rings at four  $\beta$ -positions.

To begin, a sub-monolayer amount of 2H-diTTBP(*x*)BPs was deposited and measured at RT on Ag(111), a relatively inert substrate that does not show strong interactions with metal-free porphyrins [107, 120]. 2H-diTTBP(*x*)BPs exhibit a very regular long-range ordered 2D porous phase (see Figure 12a). The structure is described by a square unit cell with lattice vectors  $\vec{a}$  ( $1.56 \pm 0.10$  nm) and  $\vec{b}$  ( $1.46 \pm 0.10$  nm), an angle of  $\gamma = 89 \pm 3^\circ$ , and a unit cell area of  $2.28$  nm<sup>2</sup>. The unit cell contains one molecule, yielding a density of  $0.44$  molecules/nm<sup>2</sup>. Following a thorough analysis of the high-resolution STM image in Figure 12a (right), all six molecules were identified and assigned (marked with colored dashed circles). The individual molecules within the ordered island of the porous square structure are identified by four quadratically arranged bright or dim protrusions corresponding to the isoindole groups, which adopt a “crown-shape” conformation [108]. This motif results from a subtle balance between molecule-substrate interactions and repulsive forces within the molecules. The intramolecular conformation is discussed further in Figure 13.

The adsorption behavior of porphyrin molecules is mostly determined by the subtle balance of molecule-molecule and molecule-substrate interactions. For 2H-TPP on Ag(111), supramolecular arrangements are formed as a result of T-type intermolecular interactions between the peripheral phenyl substituents of neighboring molecules [106, 107]. In contrast, on Cu(111), due to strong molecule-substrate interaction between the iminic nitrogen atoms of the porphyrin and the Cu atoms of the substrate, individual 2H-TPP molecules were

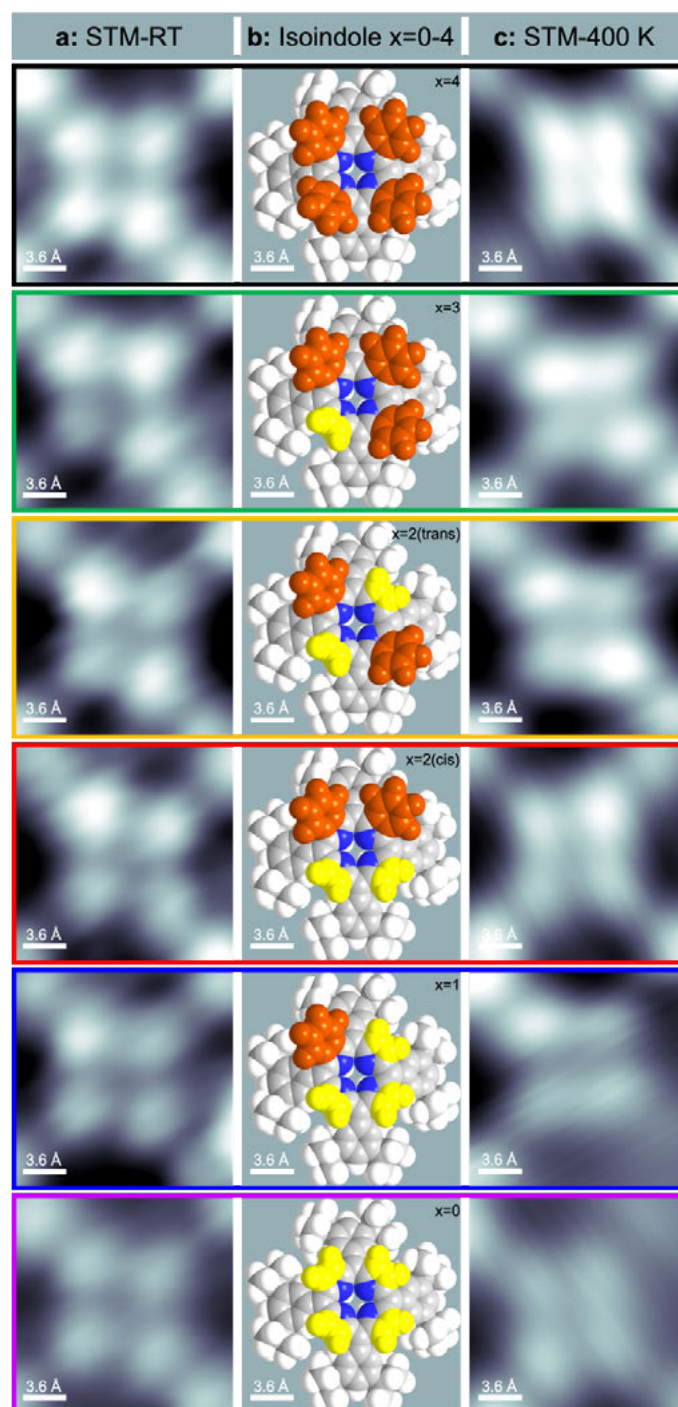
observed [115, 145]. Closer inspection reveals that the well-ordered porous square structure formation of 2H-diTTBP(x)BPs on Ag(111) is incompatible with the T-type or  $\pi$ - $\pi$  intermolecular stacking of a similar porphyrin derivative 2H-TPTBP on Ag(111), Cu(111), and Cu(110) [112]. The porous square phase observed in the mixture of 2H-diTTBP(x)BPs on Ag(111) surface indicates that the long-range order is stabilized by intermolecular interactions between neighboring molecules, mainly by van der Waals forces between the *tert*-butyl groups and phenyl groups of the adjacent molecules.



**Figure 12:** STM images of 2H-diTTBP(x)BPs on Ag(111), as overview (left,  $50 \times 50 \text{ nm}^2$ ), close-up (middle,  $20 \times 20 \text{ nm}^2$ ), and with high-resolution (right,  $10 \times 10 \text{ nm}^2$ ), measured at RT. **a)** Deposition at RT reveals a highly ordered long-range square phase. **b)** After annealing to 400 K for 30 min no changes are observed. In the high-resolution images, the six different molecules ( $x = 0, 1, 2\text{-cis}, 2\text{-trans}, 3,$  &  $4$ ) can be identified and are marked with dashed colored circles. The unit cells are shown as solid white lines, and the white arrows indicate the close-packed Ag(111) substrate directions. The STM images were measured with  $U_{\text{bias}}$  between 1.0 and 1.88 V and  $I_{\text{set}}$  between 89.3 and 201 pA; for details see Table S1 in the Supporting Information (SI) of [P4]. Original images and text from [P4] used with permission.

Figure 12b shows the STM image acquired at RT after heating to 400 K. Annealing yields no transformation, and the same regular long-range 2D porous phase was observed. The structure is described by an identical (within the experimental uncertainty) square unit cell with lattice vectors  $\vec{a}$  ( $1.56 \pm 0.10 \text{ nm}$ ) and  $\vec{b}$  ( $1.46 \pm 0.10 \text{ nm}$ ), an angle of  $\gamma = 92 \pm 3^\circ$ , and a unit cell area of  $2.28 \text{ nm}^2$ . The unit cell contains one molecule, yielding a density of  $0.44 \text{ molecules/nm}^2$  as for the film measured directly after RT deposition. Again, all six 2H-diTTBP(x)BPs (with  $x = 0, 1, 2\text{-cis}, 2\text{-trans}, 3,$  and  $4$ ) isoindole groups were identified and are marked with colored

dashed circles in the high-resolution STM image in Figure 12b (right). Overall, the long-range ordered porous square remains the same, indicating thermodynamic stability up to 400 K.



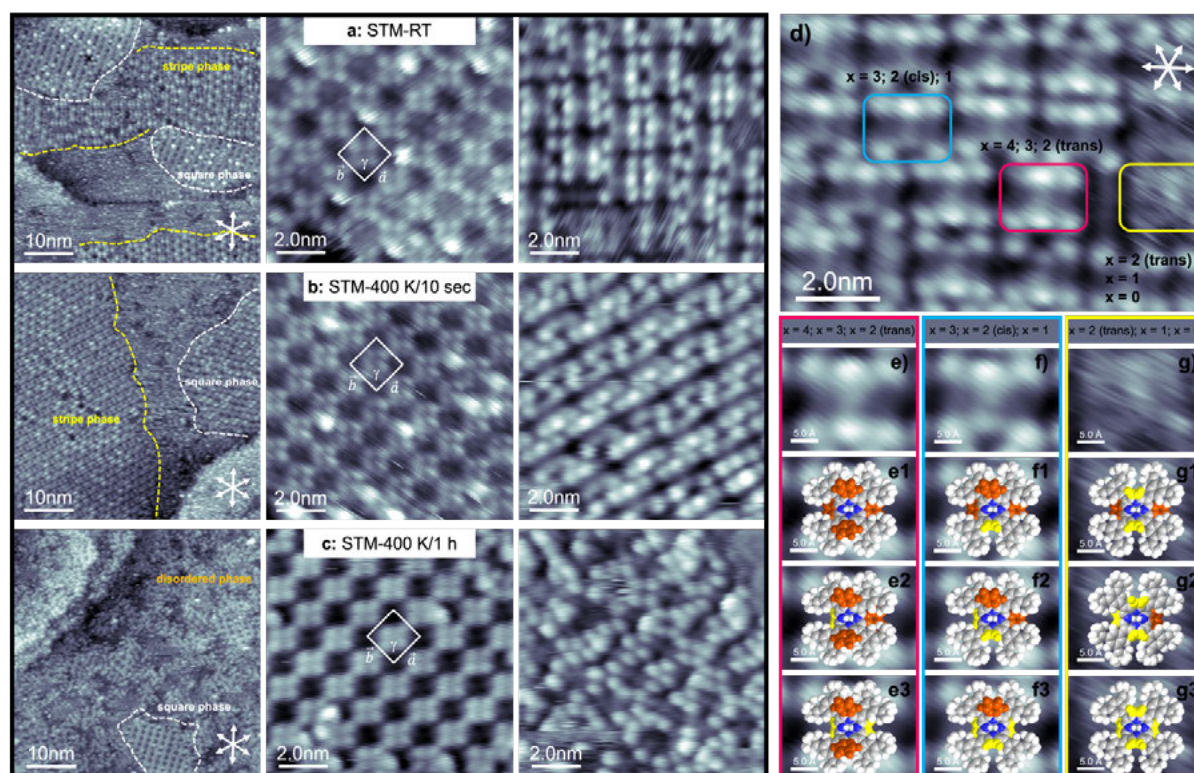
**Figure 13:** STM images ( $1.8 \times 1.8 \text{ nm}^2$ ) of  $2H\text{-diTTBP}(x)\text{BPs}$  on  $\text{Ag}(111)$  after **a)** adsorption at RT – cutout from Figure 12a-right, and **c)** after annealing to 400 K for 30 min – cutout from Figure 12b-right. Each molecule is characterized by four bright or dim protrusions. **b)** Scaled molecular models of the six individual molecules ( $x = 0, 1, 2\text{-cis}, 2\text{-trans}, 3, \& 4$ ). The proposed molecular model represents a “crown-shape” conformation: Upward bent isoindole groups are depicted in orange and correspond to bright protrusions in (a) and (c); upward bent pyrrole groups are depicted in yellow and correspond to dim protrusions. The six individual molecules are marked with differently colored frames, with the same color code as used in Figure 12. The STM images were measured with  $U_{\text{bias}} = 1.88 \text{ V}$  and  $I_{\text{set}} = 89.3$  or  $201 \text{ pA}$ ; for details see Table S1 in the SI of [P4]. Original images and text from [P4] used with permission.

Figure 13(a, c) shows the cutouts of the different molecules indicated in Figure 12a (RT) and Figure 12b (400 K) to gain insight into the intramolecular conformation. Each molecule is represented by four quadratically arranged, bright or dim protrusions separated by  $\sim 6$  Å. The “saddle-shape” conformation is a well-established conformation for many porphyrins [106, 107, 109, 146]. This intramolecular conformation, however, is inconsistent with the finding of four quadratically arranged protrusions for the molecules investigated here on Ag(111). The observed peculiar appearance is similar to that obtained by Lepper et al. [108] on Cu(111) for Ni(II)-5, 10, 15, 20-tetraphenyltetrabenzoporphyrin (Ni(II)-TPBP). The molecule’s quadratic appearance is attributed to four upward bent isoindole groups, which appear as four bright protrusions separated by  $\sim 6$  Å in STM. The proposed conformation is possible when an attractive substrate-molecule interaction pulls the macrocycle towards the substrate, and the tilt value of the isoindole groups increases due to steric repulsion of the *ortho*-substituents within the molecule.

Figure 13b depicts the proposed scaled molecular models for all six 2H-diTTBP(x)BPs molecules on Ag(111), with upward bent isoindole groups (orange) and upward bent pyrrole groups (yellow). The bright and dim protrusions correspond to the isoindole and pyrrole groups, respectively. The six individual 2H-diTTBP(x)BPs ( $x = 0, 1, 2$ -cis, 2-trans, 3, and 4) are marked with different colors (rectangular frame) and are displayed from bottom to top: A molecule with four dim lobes is assigned to  $x = 0$  (violet); one bright lobe and three dim lobes are assigned to  $x = 1$  (blue); two bright lobes and two dim lobes are assigned to  $x = 2$  (cis; red) or  $x = 2$  (trans; orange); three bright lobes and one dim lobe are assigned to  $x = 3$  (green); and finally, four bright lobes are assigned to  $x = 4$  (black). Hence, the suggested models align with Lepper et al.’s [108] interpretation. Moreover, the appearance of 2H-diTTBP(x)BPs and Ni(II)-TPBP suggests that the presence of *tert*-butyl groups or a metal ion has no effect on the conformation of the molecules within the ordered phase, similar to the findings reported for 2H-TPP and  $M^{2+}$ -TPPs [107, 145].

The adsorption behavior of 2H-diTTBP(x)BPs was then investigated on Cu(111), a substrate that is typically considered to be more reactive than Ag(111), particularly for N-containing metal-free porphyrins [107, 115]. A sub-monolayer amount of 2H-diTTBP(x)BPs was deposited and measured on Cu(111) at RT. The 2H-diTTBP(x)BPs molecules exhibit two notable molecular arrangements: a porous square phase and a stripe phase (see Figure 14a, black frame). The two phases have nearly identical surface areas, indicating similar adsorption energy. In addition, a disordered phase exists between the orderly islands. Figure 14a (top-middle) shows the structure that is described by a square unit cell with lattice vectors

$\vec{a}$  ( $1.48 \pm 0.10$  nm) and  $\vec{b}$  ( $1.60 \pm 0.12$  nm), an angle of  $\gamma = 93 \pm 4^\circ$ , and a unit cell area of  $2.37$  nm<sup>2</sup>. The unit cell contains one molecule, yielding a density of  $0.42$  molecules/nm<sup>2</sup>. Notably, within the experimental uncertainty, unit cell parameters are identical to those obtained above for 2H-diTTBP(x)BPs on Ag(111). The stripe phase in Figure 14a (top right) is another island type with a densely packed, locally ordered structure. However, it is not possible to provide a unit cell because there is no well-ordered long-range structure.



**Figure 14:** STM images of 2H-diTTBP(x)BPs on Cu(111) measured at RT (black frame): as overview (left,  $50 \times 50$  nm<sup>2</sup>) and with high-resolution (middle and right,  $10 \times 10$  nm<sup>2</sup>). **a)** Deposition at RT reveals a coexistence of ordered square and stripe phases, along with a disordered phase. **b)** After annealing at 400 K for 10 sec no changes are observed. **c)** After further annealing at 400 K for 1 h, a loss of the stripe phase is found leaving the square phase and a disordered phase on the surface. **d)** High-resolution (top,  $10 \times 7$  nm<sup>2</sup>) STM image of the stripe phase. **e-g)** Cutouts ( $2.5 \times 1.87$  nm<sup>2</sup>) overlaid with proposed scaled molecular models. The proposed molecular model represents a “saddle-shape” conformation with upward/downward bent isoindole groups depicted in orange and pyrrole groups in yellow. Three different appearances are observed with TWO bright protrusions (**e1-e3**: red frame;  $x = 4, 3,$  or  $2$ -trans), ONE bright protrusion (**f1-f3**: blue frame;  $x = 3, 2$ -cis, or  $1$ ), and ZERO bright protrusion (**g1-g3**: yellow frame;  $x = 2$ -trans,  $1,$  or  $0$ ). The unit cells are shown as solid white lines, and the white arrows indicate the close-packed Cu(111) substrate directions. The STM images were measured with  $U_{bias}$  between  $-1.59$  and  $+1.26$  V and  $I_{set}$  between  $95.7$  and  $299$  pA; for details see Table S1 in the SI of [P4]. Modified images and text from [P4] used with permission.

Individual 2H-diTTBP(x)BPs appear as four quadratically arranged bright or dim protrusions separated by  $\sim 6$  Å within the porous square phase. Due to lower resolution of STM image (probably caused by a different STM tip termination), only some of the 2H-diTTBP(x)BPs were identified, namely those with  $x = 0, 2$ -cis, and  $4$  (not shown, for details refer to [P4]). Moreover,

it was found that the overall intramolecular conformation is consistent with the detailed studies on Ag(111) mentioned above.

In contrast, in the stripe phase, individual 2H-diTTBP(x)BPs appear as six protrusions grouped in two parallel groups of three protrusions. The outer four protrusions (dim) are assigned to the peripheral phenyl substituents, while the two central protrusions (bright or dim) are assigned to the slightly upward bent isoindole (colored orange) or pyrrole (colored yellow) groups. This is evident from Figure 14d-g, where the cutouts of the STM image from Figure 14d are superimposed with scaled molecular models; this appearance is attributed to a “saddle-shape” conformation [106, 107, 109, 146]. The different 2H-diTTBP(x)BPs molecules were assigned based on their appearances observed in STM. In total, three different appearances were observed (see Figure 14e-g). Appearances with TWO bright central protrusions (red frame) are assigned to  $x = 4, 3,$  or 2-trans. Appearances with ONE bright central protrusion (blue frame) are assigned to  $x = 3, 2$ -cis or 1. Finally, appearances with ZERO bright central protrusion (yellow frame) are assigned to  $x = 2$ -trans, 1, or 0. For more information, refer to [P4].

Moreover, the stable long-range ordered porous square and stripe structures of 2H-diTTBP(x)BPs on Cu(111) are stabilized by intermolecular interactions between neighboring molecules, primarily through van der Waals forces between the *tert*-butyl groups, and possibly phenyl groups of the neighboring molecules [158]. Thus, the general intermolecular pattern is in line with previous observations on Ag(111).

In addition, flashing the identified phases of 2H-diTTBP(x)BPs on Cu(111) to 400 K (see Figure 14b, black frame) resulted in no changes. However, long heating results in the loss of the stripe phase, leaving the porous square phase intact and a disordered phase on the surface (see Figure 14c, black frame). The films of 2H-diTTBP(x)BPs on Cu(111) were annealed at 450 K. Upon heating, no ordered square or stripe phase was observed. Only a disordered phase was found (not shown here, for details refer to [P4]), which was tentatively ascribed to a dehydrogenation process within the porphyrin leading to the formation of intramolecular C-C bonds between the isoindole and the phenyl groups [140, 141, 148].

As a final step, the adsorption behavior of 2H-diTTBP(x)BPs was studied on Cu(110), a substrate that is considered to be more reactive than Ag(111) and Cu(111) due to its open structure [112]. A sub-monolayer amount of 2H-diTTBP(x)BPs was deposited and measured at RT on Cu(110). It exhibits no long-range ordered phases, but dispersed isolated molecules or short (two to three molecules) 1D chains along the  $\langle 1\bar{1}0 \rangle$  substrate directions. This observation is attributed to the interaction of the N-atoms of the downward bent isoindole or

pyrrole groups with the rough, trough-like Cu(110) surface. This interaction leads to certain preferential adsorption sites as the N-atoms get closer to the surface.

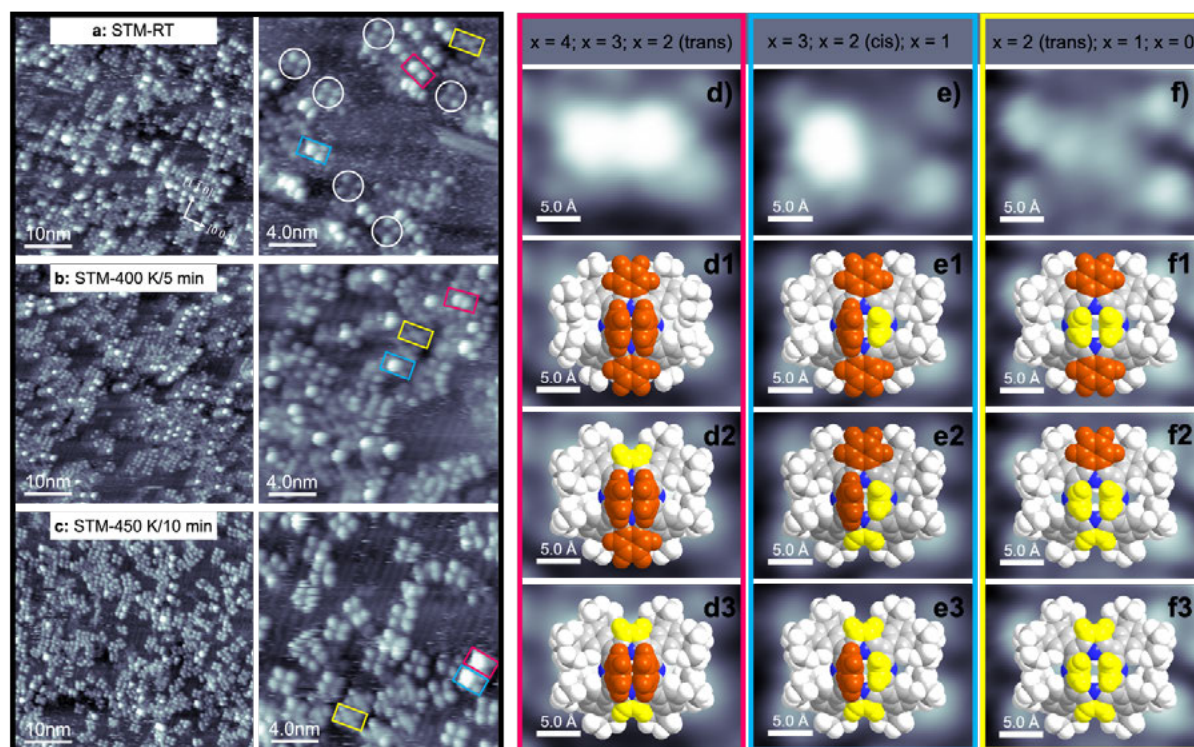


**Figure 15:** STM images of 2H-diTTBP(x)BPs on Cu(110) measured at RT (black frame): as an overview (left,  $50 \times 50 \text{ nm}^2$ ) and with close-up (right,  $20 \times 20 \text{ nm}^2$ ). **a)** Deposition at RT reveals the isolated molecules and the formation of short, isolated 1D chains. **b)** After annealing to 400 K for 5 min and **c)** 450 K for 10 min, the molecular appearance remains unchanged. The close-up STM images and the high-resolution images reveal individual isolated molecules with two conformations (measured at RT): a quadratic arrangement of four lobes (white circle or frame) and a rectangular arrangement with six lobes (colored frames). The latter is assigned to an “inverted” structure and has three different appearances (indicated by different colors). **d-f)** Cutouts ( $2.5 \times 1.86 \text{ nm}^2$ ; measured at RT) along with superimposed scaled molecular models of individual molecules with TWO bright protrusions (**d1-d3**: red frame;  $x = 4, 3, \text{ or } 2\text{-trans}$ ), ONE bright protrusion (**e1-e3**: blue frame;  $x = 3, 2\text{-cis}, \text{ or } 1$ ), and ZERO bright protrusion (**f1-f3**: yellow frame;  $x = 2\text{-trans}, 1, \text{ or } 0$ ). Isoindole groups are depicted in orange, and pyrrole groups are depicted in yellow. The white arrows indicate the close-packed Cu(110) substrate directions. The STM images were measured with  $U_{\text{bias}}$  between  $-1.28$  and  $+1.2 \text{ V}$  and  $I_{\text{set}}$  between  $195$  and  $197 \text{ pA}$ ; for details see Table S1 in the SI of [P4]. Modified images and text from [P4] used with permission.

Individual 2H-diTTBP(x)BPs on Cu(110) exhibit two conformations (see Figure 15a-c, black frame). The first shows four nearly quadratically arranged protrusions for the individual 2H-diTTBP(x)BPs molecules (marked with white circles), and differs from the “crown-shape” conformation on Ag(111) and Cu(111) discussed above. Here, the protrusions are separated by 10 to 12 Å, which is twice the distance of the “crown-shape” conformation. The structure is tentatively attributed to a different conformation, in which the isoindole and pyrrole groups are in the macrocycle plane and all phenyl groups are bent upward and rotated so that one of the bulky di-*tert*-butyl groups points upward. Furthermore, the appearance of the quadratically

arranged protrusions varies from molecule to molecule, making an unequivocal identification to the different 2H-diTTBP(x)BPs impossible. Hence, the interpretation must remain speculative. The second conformation (marked with different rectangles in Figure 15a-c) has a peculiar rectangular shape with four dim outer protrusions and two dim or bright central protrusions, indicative of an “inverted” conformation. This appearance is similar to that of 2H-TPP and 2H-TNP on Cu(111) [111, 162], but different from the appearance of the molecules in the stripe phase on Cu(111), as observed above. Overall, three distinct appearances of the two central protrusions were observed (see Figure 15d-f) and are tentatively linked with the number of isoindole groups. In Figure 15d-f, a bright central protrusion is attributed to a vertical isoindole group and a dim protrusion to a vertical pyrrole group (the horizontal isoindole or pyrrole groups cannot be identified). Thus, the appearances with TWO bright central protrusions (red frame) are assigned to  $x = 4, 3$ , or 2-trans. Appearances with ONE bright central protrusion (blue frame) are assigned to  $x = 3, 2$ -cis or 1. Finally, appearances with ZERO bright central protrusion (yellow frame) are assigned to  $x = 2$ -trans, 1, or 0.

In addition, the 2H-diTTBP(x)BPs on Cu(110) were heated to 400 and 450 K, respectively. It was found that the observed conformations and chains remain intact and are thermodynamically stable up to 450 K (not shown here, for details refer to [P4]).

To sum up, the three surfaces exhibited different adsorption behavior in terms of the long-range order and intramolecular conformation of the porphyrins. High-resolution STM images of all surfaces allowed for the identification of the different 2H-diTTBP(x)BPs. A “crown-shape” quadratic conformation on Ag(111) and Cu(111), an additional “saddle-shape” only on Cu(111), and an “inverted” structure and quadratic appearance on Cu(110) were deduced. The different conformations are attributed to the different degree of interactions between the iminic nitrogen atoms of the isoindole and pyrrole groups and the substrate atoms on the three surfaces. The ordered structures on Ag(111) and Cu(111) as well as 1D short chains on Cu(110) are stabilized by the outer periphery of the molecules (via van der Waals interactions between the *tert*-butyl and phenyl groups of neighboring molecules) rather than by the substrate or the number of isoindole groups. Thermal stability of the “crown-shape” conformation on Ag(111) and Cu(111), along with the intact isolated “inverted” molecules on Cu(110), imply that no reaction transpired. The loss of stripe phase on Cu(111) upon longer heating to 400 K implies a reaction, the details of which are unclear. Self-metalation with Cu atoms seems unlikely as metalated porphyrins tend to form islands. Furthermore, the presence of an intact “inverted” structure on Cu(110) indicates the absence of self-metalation. However, self-metalation cannot

be ruled out for molecules with four almost quadratically arranged protrusions. For more details, refer to [P4].

#### 4.4 Ionic liquid [C<sub>1</sub>C<sub>1</sub>Im][Tf<sub>2</sub>N] on Cu(111) [P3]

After investigating the fundamental molecular-level properties of complex porphyrin derivatives' adsorption behavior on various metal surfaces with potential implications in molecular devices or catalysis, the focus of this section shifts towards understanding the SCILL approach [47, 48]. In SCILL, the IL modifies the catalyst surface, and thus understanding the IL-catalyst interaction is of utmost importance. In order to identify the origin of distinct properties, a simple and commonly used IL (see Figure 7 in Section 2.7) consisting of symmetric 1,3-dimethylimidazolium [C<sub>1</sub>C<sub>1</sub>Im]<sup>+</sup> cations and [Tf<sub>2</sub>N]<sup>-</sup> anions was investigated as a prototype, using nc-AFM and STM in combination with DFT calculations plus complementary XPS measurements. The goal was to gain insight into the adsorption and reaction behavior, ion orientation, substrate interactions, intermolecular interactions, and structure formation on the reactive Cu(111) surface.

To begin, a sub-monolayer amount of [C<sub>1</sub>C<sub>1</sub>Im][Tf<sub>2</sub>N] was deposited on Cu(111) at 300 K and then transferred quickly (to avoid reactions that progress slowly over time) to the precooled AFM stage at 110 K. The sample was then heated in steps to 200, 250, 300, and 350 K at the AFM stage, and cooled back to 110 K for nc-AFM imaging. Figure 16a depicts the nc-AFM images after annealing to 200 K, which exhibit IL islands of different sizes at the steps and on the terraces. IL islands are found both in the ascending and descending side of the steps, suggesting that the steps are energetically favored and act as nucleation centers. The high-resolution nc-AFM image (see Figure 16a-right) reveals that the island consists of a close-packed phase with molecular rows arranged in a stripe pattern. The stripe structure is described by a rectangular unit cell with lattice vectors  $\vec{a}$  ( $1.90 \pm 0.08$  nm) and  $\vec{b}$  ( $0.90 \pm 0.05$  nm), an angle of  $\gamma = 90 \pm 3^\circ$ , and a unit cell area of  $1.71$  nm<sup>2</sup>. A commensurate  $\begin{bmatrix} 6 & 2 \\ -3 & 4 \end{bmatrix}$  superstructure was derived considering the measured angle of  $6^\circ$  between the unit cell vector  $\vec{a}$  and the high symmetry direction of the substrate. The unit cell contains two ion pairs, giving a density of  $1.17$  ions/nm<sup>2</sup>. This density was determined by comparing it with the low temperature checkerboard structures on Au(111) [55].

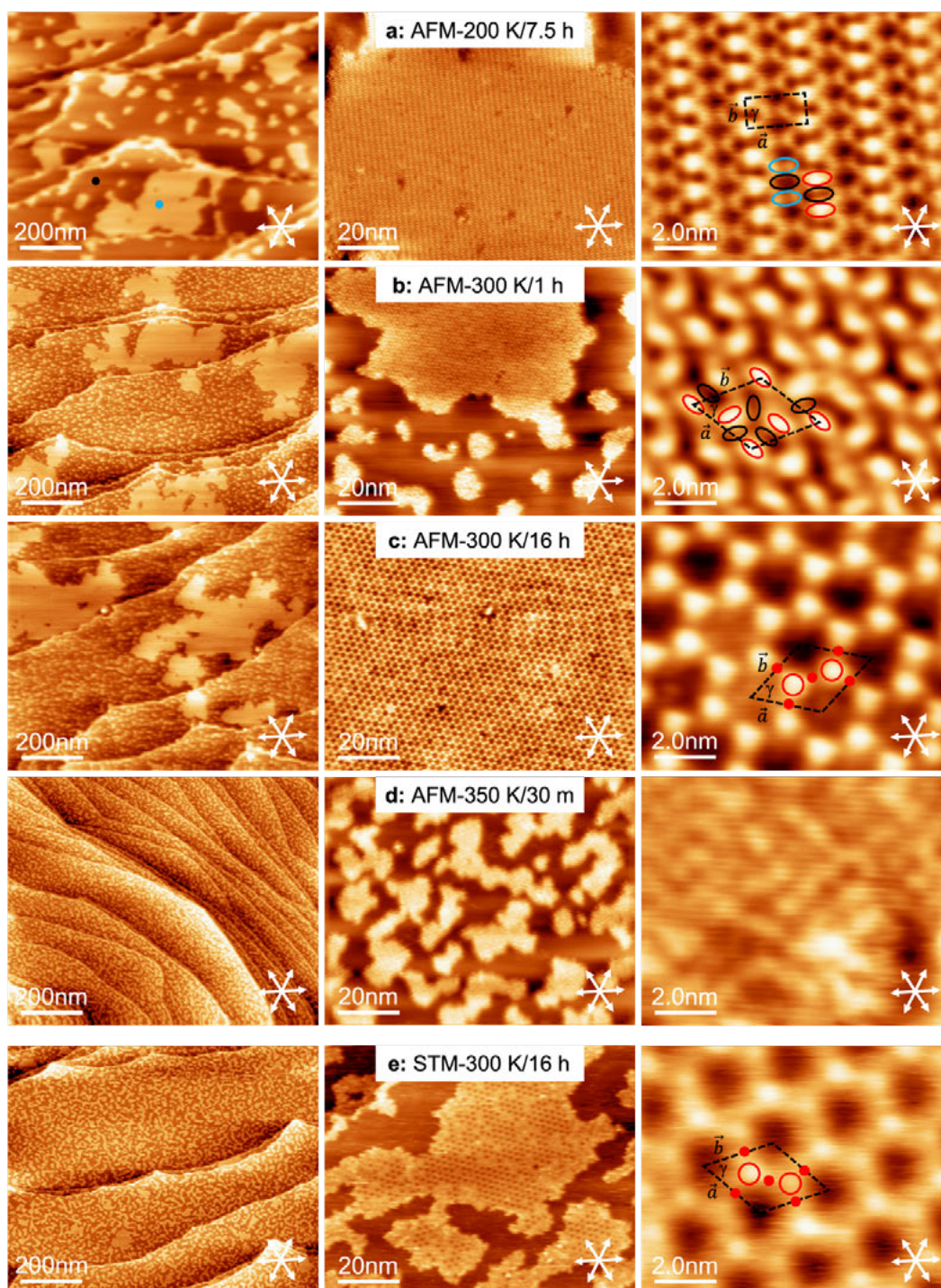


**Figure 16:** nc-AFM (a-d) and STM (e) images of 0.15 ML  $[C_1C_1Im][Tf_2N]$  on Cu(111): as overview (left,  $1000 \times 800 \text{ nm}^2$ ), close-up (middle,  $100 \times 80 \text{ nm}^2$ ), and with high-resolution (right,  $10 \times 8 \text{ nm}^2$ ). **a)** After annealing at 200 K for 7.5 h, ordered islands with a checkerboard-type structure and a nearly rectangular unit cell are observed; the right image is an average frame of nine consecutively recorded images. **b)** After annealing at 300 K for 1 h, disordered small islands coexist with large, ordered islands with hexagonal structure. **c)** After annealing at 300 K for  $\sim 16$  h, disordered small islands coexist with large IL islands with a highly ordered porous honeycomb structure. **d)** After annealing at 350 K for 30 min, only small, disordered islands are found. **e)** STM images following a different preparation route and annealing at 300 K for  $\sim 16$  h display the same honeycomb structure as seen in (c). The nc-AFM images were measured with  $\Delta f = -400$  or  $-500$  Hz, and the STM images with  $U_{\text{bias}} = 2 \text{ V}$  and  $I_{\text{set}} = 0.2$  or  $0.4 \text{ nA}$  (for details, see Table S4 in the SI of [P3]); the unit cells are shown as dashed black lines; covered and uncovered areas are denoted by blue and black dots, respectively. Original images and text from [P3] used with permission.

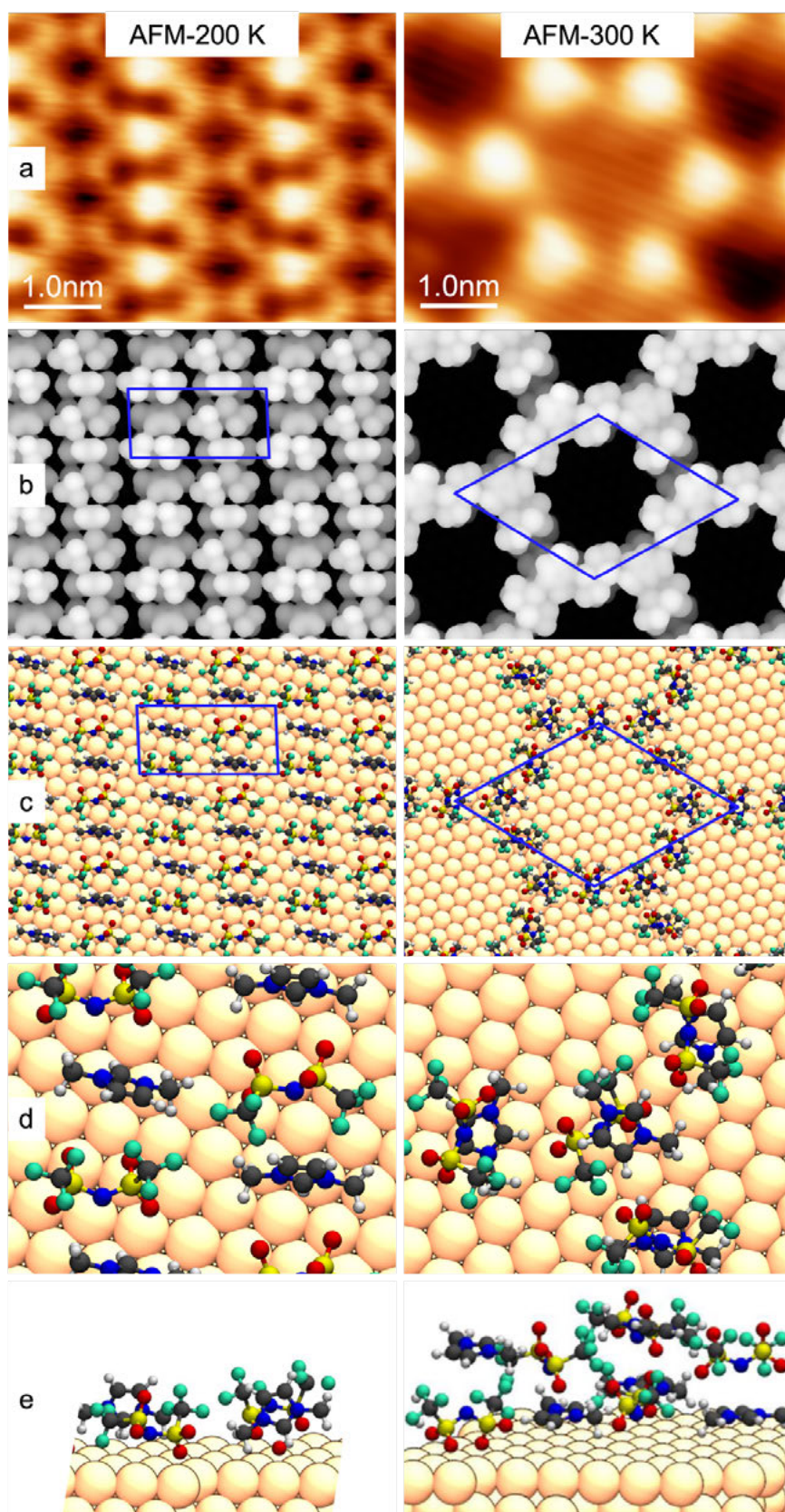
In Figure 16a (right), the very bright oval protrusions (red ellipses) and the two less bright protrusions (blue ellipses) are tentatively assigned to two differently oriented anions, and the dark areas in between (black ellipses) to the two cations. Thus, the anion to cation ratio is 1:1 with intact ion pairs and they are arrayed in a checkerboard-type [51] ionic tiling without decomposition, self-assembling into stripes. In addition, the chemical composition measured by the complementary XPS (not shown here, for details refer to [P3]) reveals that intact anions and cations are adsorbed next to each other at 200 K. Upon heating the deposited layer to 250 K, the observed stripe phase remained intact.

Figure 16b shows the nc-AFM images acquired at 110 K after heating to 300 K for 1 h. Annealing yields a transformation and reveals large islands coexisting with many disordered small islands. The structure observed on the large islands is defined by a hexagonal-type lattice ( $\gamma = 60 \pm 4^\circ$ ) with three bright longish protrusions (red ellipses) and three less bright protrusions (black ellipses). The unit cell vectors  $\vec{a}$  and  $\vec{b}$  have the same length of  $2.35 \pm 0.08$  nm and a unit cell area of  $4.78 \text{ nm}^2$ . When each protrusion is assumed to be an ion pair, the unit cell contains six ion pairs, resulting in a density of  $1.26$  ion pairs/ $\text{nm}^2$ . Figure 16c shows the nc-AFM images of the  $[\text{C}_1\text{C}_1\text{Im}][\text{Tf}_2\text{N}]$  film after extended heating to 300 K for 16 h. Large islands (ordered honeycomb structure) coexist with many small, disordered islands. The ordered structure found on large island is defined by unit cell vectors  $\vec{a}$  and  $\vec{b}$  of same length of  $2.35 \pm 0.08$  nm, an angle of  $\gamma = 60 \pm 4^\circ$ , and a unit cell area of  $4.78 \text{ nm}^2$ . A  $\begin{bmatrix} 8 & 2 \\ -2 & 10 \end{bmatrix}$  superstructure was derived from the measured angle of  $12^\circ$  between the unit cell vectors and the high symmetry direction of the substrate. The unit cell contains two bright protrusions (red circles) and three less bright protrusions (red dots). Again, each protrusion is assumed to be an ion pair, and the unit cell contains five ion pairs, resulting in a density of  $1.05$  ion pairs/ $\text{nm}^2$ . The unit cell size (lattice vector lengths of  $2.35$  nm) of the hexagonal structure is identical to that of the honeycomb structure. If one bright protrusion (or one ion pair) is removed from the hexagonal structure one obtains the honeycomb structure with a pore diameter of  $2$  nm. Thus, the hexagonal structure after heating the IL layer at  $300$  K can be considered as a transition structure from the stripe phase to the honeycomb phase. The complementary XPS results (not shown here, for details refer to [P3]) indicate that there is no IL desorption until  $300$  K. However, a large fraction of the IL gets converted into a new species, as shown by new and strongly shifted peaks that emerge in the XP spectra around  $275$  K and increase with time at  $300$  K. The unshifted peaks correspond to the ordered phases that remain intact, whereas the shifted peaks are assigned to their decomposition products that appear as disordered islands in

nc-AFM and STM. After heating to 350 K (see Figure 16d), only many small, disordered islands are seen by nc-AFM, which appear very similar to the small, disordered islands found at 300 K coexisting with the hexagonal and honeycomb structures. Also, heating the IL layers to 360 K in XPS shows the conversion of both anion and cation signals, indicating a complete decomposition of the IL on the surface (not shown here, for details refer to [P3]).

Notably, the honeycomb structure was also found following a different preparation route and measuring method. A sub-monolayer amount of  $[\text{C}_1\text{C}_1\text{Im}][\text{Tf}_2\text{N}]$  was deposited on Cu(111) at  $< 160$  K and measured using STM at 110 K. Up to 250 K, no ordered IL islands were found (not shown here, for details refer to [P3]). After heating to 300 K for 3-16 h, ordered IL islands (porous honeycomb structure) coexist with many small, disordered islands (see Figure 16e). The ordered honeycomb structure found on large islands is defined by unit cell vectors  $\vec{a}$  and  $\vec{b}$  of same length of  $2.36 \pm 0.08$  nm, an angle of  $\gamma = 60 \pm 4^\circ$ , and a unit cell area of  $4.82$  nm<sup>2</sup>. The unit cell contains two bright protrusions (red circles) and three less bright protrusions (red dots). Again, if each protrusion is assumed to be an ion pair, the unit cell contains five ion pairs, resulting in a density of  $1.04$  ion pairs/nm<sup>2</sup>. Overall, these parameters are identical to those observed using the other measuring technique (nc-AFM) and preparation route.

DFT calculations were performed to comprehend the structure of the ordered phases (stripe and honeycomb) and the bonding state of the IL adlayer based on the nc-AFM images. The experimentally determined lattice vectors of the stripe structure can be described by a  $\begin{bmatrix} 6 & 2 \\ -3 & 4 \end{bmatrix}$  commensurate superstructure. The lattice vectors  $\vec{a}$  (1.83 nm) and  $\vec{b}$  (0.92 nm) yield a unit cell area of  $1.68$  nm<sup>2</sup> with an angle of  $92.2^\circ$ , which matches extremely well with the experimental values determined from the nc-AFM images (within the margin of error). Figure 17b-e (left) shows the simulated nc-AFM images in form of charge density contour plots of the geometry-optimized stripe structure. It displays two nearly perpendicular cations, with the C<sub>2</sub> carbon atom of the imidazolium ring pointing towards the Cu surface, and two anions with different orientations. The distinct contrast of the anions observed by nc-AFM is most likely due to these two different orientations (i.e., 2-2 and 1-1 motif of the oxygen atoms). Overall, the anions and cations adsorb next to each other intact with an adsorption energy per ion pair of 3.5 eV, which can be decomposed into a contribution of  $\sim 1.6$  eV from the interaction with the substrate and  $\sim 2.0$  eV due to lateral interactions within the IL. For details, refer to [P3].



**Figure 17:** Surface structure of  $[C_1C_1Im][Tf_2N]$  on  $Cu(111)$  for the stripe phase (left) and the honeycomb phase (right). **a)** *nc*-AFM images (data from Figure 16). **b)** Charge density plots of the corresponding structures, as derived from DFT calculations. **c)** Geometry-optimized structures, as obtained from the DFT calculations. **d)** Close-up of the structures shown in (c). **e)** Side view of the structures shown in (c). Graphs (a) to (c) are shown on the same scale, as indicated by the scale bars in (a). Original images and text from [P3] used with permission.

In contrast, the honeycomb structure can be described by a  $\begin{bmatrix} 8 & 2 \\ -2 & 10 \end{bmatrix}$  superstructure based on the experimentally determined lattice vectors  $\vec{a}$  and  $\vec{b}$  ( $2.35 \pm 0.08$  nm). Based on the chemical composition measured by the complementary XPS (not shown here, for details refer to [P3]), the honeycomb structure is also attributed to intact IL ion pairs. Considering the specific properties of the honeycomb lattice, the bright (red circles) and dim (red dots) protrusions are assigned to oppositely oriented “sandwiches” consisting of stacked cations and anions that do not break charge neutrality. Figure 17b-e (right) depicts simulated nc-AFM images in form of charge density contour plots of geometry-optimized oppositely oriented honeycomb sandwiches.

From DFT calculations, the porous structure yields a lower adsorption energy per ion pair of 3.1 eV than that of the stripe structure (3.5 eV; due to its higher dispersion energy). The lower adsorption energy of the honeycomb structure is not expected from the experimental results, as heating is expected to trigger a change to a more stable structure. A likely reason for this unexpected behavior could be that the dissociated IL layer goes along with the formation of the honeycomb structure, and the associated energies would have to be included in the total energy balance, or that the geometry optimization did not find the global minimum with the highest binding energy in the computations (for details refer to [P3]).

To sum up, the adsorption and reaction of the IL  $[\text{C}_1\text{C}_1\text{Im}][\text{Tf}_2\text{N}]$  on the reactive Cu(111) surface were thoroughly investigated using a combination of experimental and theoretical methods, yielding a very complex thermal evolution with structural changes and decomposition effects at RT.

## 5 Conclusions

### English Version:

In this thesis, STM and nc-AFM disclose a tremendous richness of detail and a deep degree of comprehension on the molecular level. Both techniques yield real space information, which was applied to investigate the adsorption and reactivity of complex porphyrin derivatives and ionic liquids on different metal surfaces prepared under UHV conditions at or below RT.

The publication [P1] addresses the adsorption behavior of three related cyano-functionalized tetraphenylporphyrin derivatives, namely Cu-TCNPP, Cu-*cis*DCNPP, and 2H-*cis*DCNPP on Cu(111) by STM as a function of temperature combined with DFT calculations in order to identify the role of the cyano groups and the central Cu atom. Cu-TCNPP forms a hexagonal honeycomb-type structure at RT that coexists with 1D molecular chains and completely transforms to a long-range ordered hexagonal honeycomb-type structure at 400 K. Cu-*cis*DCNPP forms flakes at RT, including mono-, bi-, and multiflakes, and then transforms to a hexagonal honeycomb-type structure at 400 K. 2H-*cis*DCNPP shows no ordered structure at RT, but orders after self-metalation upon heating to 400 K. Thus, all three molecules form the same long-range triangular porous hexagonal honeycomb-type structure, in which molecules adopt “saddle-shape” conformation. The observed structures share the same structure-forming element, that is, porous porphyrin triangles (distance of 3.1 nm) fused together via CN-Cu-NC interactions with Cu adatoms. Three porphyrin molecules are rotated by 60° to each other, forming regular triangular pores with Cu adatoms located at the corners (not visible in STM). Complementing STM, DFT calculations offer more insight into various energetic contributions leading to the thermodynamically stable hexagonal honeycomb-type structure. In addition, the internal structure of the unit cell indicates that cyano-phenyl groups ( $n = 2$ ) in “*cis*” position are the minimum prerequisite to form a highly ordered 2D porous molecular pattern.

To expand the understanding of the influence of linker groups (cyano- and isoindole (benzopyrrole) groups), publication [P2] addresses the adsorption behavior and structure formation of the novel cyano-functionalized benzoporphyrin 2H-TCNPTBP on Cu(111) by STM as a function of temperature. 2H-TCNPTBP, with four cyano- and four isoindole groups, shows the coexistence of three types of network structures, namely, a Kagome lattice structure, a quadratic pattern, and a hexagonal structure at RT. All three structures have molecules in a “saddle-shape” conformation. The Kagome and quadratic structures are porous with different pore sizes (diameters: ~3 nm and ~1.5 nm respectively), are stabilized by CN-Cu-NC bonds

with Cu adatoms, and both have a molecular density of 0.18 molecules/nm<sup>2</sup>. The close-packed hexagonal structure has a molecular density of 0.42 molecules/nm<sup>2</sup> and is stabilized with much weaker intermolecular H-bonds and dipole-dipole interactions of oppositely oriented cyano end groups. While the two Cu-coordinated porous structures (Kagome and quadratic) with same molecular density are stabilized by the energy gain due to the network formation (CN-Cu-NC), the hexagonal structure compensates the weaker intermolecular interactions (H-bond) by a factor of 2.3 higher molecular density. Heating to 450 K yields an immobile species with a “clover-shape”, which is attributed to the dehydrogenation and the formation of intramolecular C-C bonds between the isoindole and the phenyl groups. This finding suggests that cyano functionalization of benzoporphyrins results in unusual 2D self-assembled lattice structures.

After gaining deeper insight into the role of linker groups, publication [P4] addresses the adsorption and self-assembly of exceedingly complex mixed benzoporphyrin derivatives 2H-diTTBP(x)BPs on Ag(111), Cu(111), and Cu(110) by STM as a function of temperature to provide further information on fundamental aspects. The mixture contains six different 2H-diTTBP(x)BPs with x = 0, 1, 2 (cis, trans), 3, and 4. On Ag(111), a long-range ordered 2D square phase was observed, which is stable up to 400 K. On Cu(111), an identical square phase coexists with a stripe phase, which disappears at 400 K. In contrast, on Cu(110) 2H-diTTBP(x)BPs adsorb as isolated molecules or dispersed short 1D chains (two to three molecules) along the  $\langle 1\bar{1}0 \rangle$  substrate directions, which remain intact up to 450 K. Notably, high-resolution STM images on all surfaces allow for the identification of different 2H-diTTBP(x)BPs. A “crown-shape” quadratic conformation on Ag(111) and Cu(111), an additional “saddle-shape” on Cu(111), and an “inverted” structure and quadratic appearance on Cu(110) were deduced. The different conformations are attributed to the different degree of interactions between the iminic nitrogen atoms of the isoindole and pyrrole groups and the substrate atoms on the three surfaces. Further, stabilization of the ordered 2D structures on Ag(111) and Cu(111) plus 1D short chains on Cu(110) is attributed to van der Waals interactions between the *tert*-butyl and phenyl groups of neighboring molecules. In addition, the thermal stability of the “crown-shape” conformation on Ag(111) and Cu(111) plus intact isolated “inverted” molecules on Cu(110), indicate that no reaction occurred. However, the loss of stripe phase on Cu(111) at 400 K implies a reaction, the nature of which is difficult to determine. A simple self-metalation with Cu atoms is unlikely, as metalated porphyrins exhibit island formation. Further, the presence of an intact “inverted” structure on Cu(110) indicates the absence of self-metalation. Moreover, self-metalation cannot be ruled out for molecules with four almost quadratically arranged protrusions. Overall, these findings show that the

long-range 2D order or 1D short chains are stabilized by the outer periphery of the molecules rather than the substrate or the number of isoindole groups.

Following the detailed characterization of the adsorption behavior of highly complex porphyrin derivatives on different metal surfaces, publication [P3] addresses the adsorption and reaction behavior of the ionic liquid  $[C_1C_1Im][Tf_2N]$  on Cu(111) by nc-AFM, STM, and complementary XPS in combination with DFT calculations. Understanding the IL-substrate interface is of utmost importance for further developing the SCILL approach.  $[C_1C_1Im][Tf_2N]$  on Cu(111) was deposited using two different preparation routes: either at RT followed by very fast cooling to 110 K, or directly at low temperature ( $< 160$  K). At 200 K, IL films self-assemble into highly ordered islands (stripe phase) with intact cations and anions arranged next to each other. DFT calculations reveal two identically oriented cations nearly perpendicular to the Cu surface and two anions with different orientations, in line with the distinct contrast of anions observed in nc-AFM at 200 K and an adsorption energy (from DFT) per ion pair of 3.5 eV. Extended heating to 300 K triggers the stripe phase to evolve first into a hexagonal phase, and then into a porous honeycomb structure that coexists with many small, disordered islands. The hexagonal structure is a transition structure from the stripe phase to the honeycomb phase. The honeycomb structure is proposed as an oppositely orientated stacked “sandwich structure” of intact anions and cations. DFT calculations support the proposed structure and show that it is stable on the surface with an adsorption energy of 3.1 eV. The chemical composition measured by complementary XPS reveals that intact anions and cations are adsorbed next to each other at 200 K, and that no IL desorption occurs until 300 K. A large fraction of the IL is transformed into a new dissociated species at around 275 K and increases with time at 300 K, as evidenced by XPS. The decomposition products appear as disordered islands in nc-AFM and STM. Upon heating to 350 K, only small, disordered islands are observed by nc-AFM, and XPS indicates a complete decomposition of the IL on the surface.

In summary, this thesis advances the molecular level understanding yielding novel detailed insights into the adsorption behavior of complex porphyrin derivatives and ionic liquids on different single crystal metal surfaces, with a focus on the specific roles of molecule-molecule and molecule-substrate interactions. The fundamental understanding obtained from the investigated systems in publication [P1-P4] might grant protocols as nanoscale templates for developing molecular devices or catalytic concepts.

**Deutsche Version:**

In dieser Arbeit enthüllen STM und nc-AFM einen enormen Detailreichtum und ein tiefes Verständnis auf molekularer Ebene. Beide Techniken liefern Informationen im Realraum, die zur Untersuchung der Adsorption und Reaktivität von komplexen Porphyrinderivaten und ionischen Flüssigkeiten auf verschiedenen Metalloberflächen verwendet wurden, die jeweils unter UHV-Bedingungen bei oder unter RT präpariert wurden.

Die Veröffentlichung [P1] befasst sich mit dem Adsorptionsverhalten von drei verwandten cyanofunktionalisierten Tetraphenylporphyrinderivaten, nämlich Cu-TCNPP, Cu-*cis*DCNPP und 2H-*cis*DCNPP, auf Cu(111) mittels STM als Funktion der Temperatur in Kombination mit DFT-Berechnungen, um die Rolle der Cyanogruppen und des zentralen Cu-Atoms zu identifizieren. Cu-TCNPP bildet bei RT eine hexagonale, wabenartige Struktur, die mit einer 1D-Molekülkette koexistiert; letztere wandelt sich bei 400 K vollständig in die hexagonale, wabenartige Struktur um. Cu-*cis*DCNPP bildet bei RT eine flockenartige Struktur, einschließlich Mono-, Bi- und Multiflocken, die sich bei 400 K in eine hexagonale, wabenartige Struktur umwandelt. 2H-*cis*DCNPP zeigt bei RT keine geordnete Struktur, sondern erst nach Selbstmetallisierung beim Erhitzen auf 400 K. Alle drei Moleküle formen dieselbe langreichweitig geordnete hexagonale Wabenstruktur, in der die Moleküle eine "sattelförmige" Konformation annehmen. Die beobachteten Strukturen haben dasselbe strukturbildende Element, nämlich poröse Porphyrindreiecke (Abstand: 3,1 nm), die über CN-Cu-NC-Wechselwirkungen mit Cu-Adatomen miteinander verbunden sind. Drei Porphyrinmoleküle sind dabei um 60° zueinander gedreht und bilden regelmäßige dreieckige Poren mit Cu-Adatomen an den Ecken; letztere sind im STM nicht sichtbar. Ergänzend zum STM bieten die DFT-Berechnungen weitere Einblicke in die verschiedenen energetischen Beiträge, die zu der thermodynamisch stabilen hexagonalen Wabenstruktur führen. Darüber hinaus deutet die interne Struktur der Einheitszelle an, dass Cyanophenylgruppen ( $n = 2$ ) in "*cis*"-Position die Mindestvoraussetzung für die Bildung eines hoch-geordneten porösen 2D-Molekülmusters sind.

Um das Verständnis des Einflusses von Linkergruppen (Cyano- und Isoindol (Benzopyrrol)-Gruppen) zu erweitern, befasst sich die Veröffentlichung [P2] mit dem Adsorptionsverhalten und der Strukturbildung des neuartigen cyanofunktionalisierten Benzoporphyrins 2H-TCNPTBP auf Cu(111) mittels STM als Funktion der Temperatur. 2H-TCNPTBP, mit vier Cyano- und vier Isoindolgruppen, zeigt bei RT die Koexistenz von drei Netzwerkstrukturen, nämlich einer Kagome-Gitterstruktur, einer quadratischen Struktur und

einer hexagonalen Struktur. In allen drei besitzen die Moleküle eine "sattelförmige" Konformation. Die Kagome- und die quadratische Struktur haben unterschiedliche Porengrößen (Durchmesser:  $\sim 3$  nm bzw.  $\sim 1,5$  nm), und beide haben eine Moleküldichte von  $0,18$  Moleküle/nm<sup>2</sup>. Sie werden durch den Energiegewinn aufgrund der Netzwerkbildung mit Cu-Adatomen (CN-Cu-NC) stabilisiert. Die dicht gepackte hexagonale Struktur mit einer Moleküldichte von  $0,42$  Moleküle/nm<sup>2</sup> wird durch intermolekulare H-Bindungen und Dipol-Dipol-Wechselwirkungen von entgegengesetzt orientierten Cyano-Endgruppen stabilisiert. Dabei kompensiert die um den Faktor 2,3 höhere Moleküldichte die schwächeren intermolekularen Wechselwirkungen. Beim Erhitzen auf 450 K entsteht eine immobile Spezies mit einer "Kleeblattform", die auf Dehydrogenierung und Bildung intramolekularer C-C-Bindungen zwischen den Isoindol- und den Phenylgruppen zurückgeführt wird. Diese Erkenntnisse deuten darauf hin, dass die Cyanofunktionalisierung von Benzoporphyrinen zu ungewöhnlichen selbstorganisierenden 2D-Gitterstrukturen führt.

Nach einem tieferen Einblick in die Rolle der Linker-Gruppen befasst sich die Veröffentlichung [P4] mit der Untersuchung der Adsorption und Selbstassemblierung von äußerst komplexen gemischten Benzoporphyrinderivaten 2H-diTTBP(x)BP auf Ag(111), Cu(111) und Cu(110) mittels STM als Funktion der Temperatur. Die Mischung enthält sechs verschiedene 2H-diTTBP(x)BP mit  $x = 0, 1, 2$  (cis, trans), 3 und 4. Auf Ag(111) wird eine langreichweitig geordnete quadratische 2D Phase beobachtet, die bis 400 K stabil ist. Auf Cu(111) koexistiert diese mit einer Streifenphase, die bei 400 K in die quadratische Phase umgewandelt wird. Im Gegensatz dazu adsorbieren 2H-diTTBP(x)BPs auf Cu(110) als isolierte Moleküle oder als verstreute kurze 1D-Ketten (zwei bis drei Moleküle) entlang der Substratrichtung  $\langle 1\bar{1}0 \rangle$ , die bis zu 450 K intakt bleiben. Auf allen Oberflächen ermöglichen hochauflösende STM-Bilder die Identifizierung verschiedener 2H-diTTBP(x)BP-Spezies: eine "kronenförmige" quadratische Konformation auf Ag(111) und Cu(111), eine zusätzliche "Sattelform" auf Cu(111), sowie eine "invertierte" Struktur und eine quadratische Struktur auf Cu(110). Die verschiedenen Konformationen werden auf unterschiedlich starke Wechselwirkungen zwischen den iminischen Stickstoffatomen der Isoindol- und Pyrrolgruppen und den Substratomen zurückgeführt. Die Stabilisierung der geordneten 2D-Strukturen auf Ag(111) und Cu(111) sowie der kurzen 1D-Ketten auf Cu(110) wird auf Van-der-Waals-Wechselwirkungen zwischen den *tert*-Butyl- und Phenylgruppen der benachbarten Moleküle zurückgeführt. Die thermische Stabilität der "kronenförmigen" Konformation auf Ag(111) und Cu(111) sowie die intakten isolierten "invertierten" Moleküle auf Cu(110) deuten darauf hin, dass keine Reaktion stattgefunden hat. Auf Cu(111) hingegen deutet der Verlust der Streifenphase bei 400 K auf

eine Reaktion hin, deren Natur aber schwer zu bestimmen ist. Eine einfache Selbstmetallisierung mit Cu-Atomen ist unwahrscheinlich, da metallisierte Porphyrine Inseln bilden. Außerdem weist das Auftreten einer intakten "invertierten" Struktur auf Cu(110) auf das Fehlen einer Selbstmetallisierung hin. Eine Selbstmetallisierung kann aber bei Molekülen mit vier fast quadratisch angeordneten Erhebungen nicht ausgeschlossen werden. Insgesamt zeigen diese Ergebnisse, dass die langreichweitige 2D-Ordnung oder die 1D-Kurzketten eher durch die äußere Peripherie der Moleküle als durch das Substrat oder die Anzahl der Isoindolgruppen stabilisiert werden.

Nach der detaillierten Charakterisierung des Adsorptionsverhaltens hochkomplexer Porphyrinderivate auf verschiedenen Metalloberflächen befasst sich Veröffentlichung [P3] mit dem Adsorptions- und Reaktionsverhalten der ionischen Flüssigkeit  $[C_1C_1Im][Tf_2N]$  auf Cu(111) mittels nc-AFM, STM und komplementären XPS Messungen, in Kombination mit DFT-Berechnungen. Die IL-Substrat-Grenzfläche ist von größter Bedeutung für SCILL-Systeme. Hierbei ist insbesondere die Rolle der IL für die Modifikation des Katalysators von Bedeutung.  $[C_1C_1Im][Tf_2N]$  wurde auf Cu(111) mit zwei verschiedenen Präparationsmethoden aufgebracht: entweder bei RT, gefolgt von einer sehr schnellen Abkühlung auf 110 K, oder direkt bei niedrigen Temperaturen ( $< 160$  K). Bei 200 K assemblieren sich die IL-Filme selbst zu hoch-geordneten Inseln (Streifenphase) mit intakten Kationen und Anionen, die nebeneinander angeordnet sind. DFT-Berechnungen zeigen zwei identisch fast senkrecht zur Cu-Oberfläche orientierte Kationen und zwei Anionen mit unterschiedlicher Orientierung, was mit dem deutlichen Kontrast der mittels nc-AFM bei 200 K beobachteten Anionen und einer Adsorptionsenergie (aus DFT) von 3,5 eV pro Ionenpaar übereinstimmt. Bei weiterem Erhitzen auf 300 K entwickelt sich die Streifenphase zunächst zu einer hexagonalen Phase und dann zu einer porösen Wabenstruktur, die mit vielen kleinen ungeordneten Inseln koexistiert. Die hexagonale Struktur ist eine Übergangsstruktur von der Streifenphase zur Wabenphase. Die Wabenstruktur wird als eine entgegengesetzt orientierte, gestapelte "Sandwich-Struktur" aus intakten Anionen und Kationen interpretiert. DFT-Berechnungen unterstützen die vorgeschlagene Struktur und zeigen, dass die Struktur auf der Oberfläche mit einer Adsorptionsenergie von 3,1 eV stabil ist. Darüber hinaus zeigen komplementäre XPS-Messungen, dass bei 200 K intakte Anionen und Kationen nebeneinander adsorbiert werden und dass bis 300 K keine IL-Desorption auftritt. Ein großer Teil der ionischen Flüssigkeit wird jedoch in neue Spezies umgewandelt, die bei etwa 275 K erscheinen und bei 300 K mit der Zeit zunehmen. Diese werden als Dissoziationsprodukte identifiziert und den

ungeordneten Inseln in ATM/STM zugeordnet. Beim Erhitzen auf 350 K deutet XPS auf die vollständige Zersetzung der IL auf der Oberfläche hin.

Zusammenfassend lässt sich sagen, dass diese Arbeit neue, detaillierte Einblicke in das Adsorptionsverhalten komplexer Porphyrinderivate und ionischer Flüssigkeiten auf verschiedenen Einkristall-Metalloberflächen liefert, wobei der Schwerpunkt auf der spezifischen Rolle von Molekül-Molekül- und Molekül-Substrat-Wechselwirkungen liegt. Das grundlegende Verständnis der in den Veröffentlichungen [P1-P4] untersuchten Systeme könnte als Vorlage zur Herstellung von porösen Templaten für die Entwicklung molekulare Geräte oder katalytischer Konzepte dienen.

## Acknowledgements

At this point, I want to express my gratitude to everyone without whom this thesis, but also this journey of my life, would not have been possible, and this is dedicated solely to them. I would like to thank:

- Prof. Dr. Hans-Peter Steinrück for giving me the opportunity to do my PhD at the Chair of Physical Chemistry II and for taking over my supervision. Thank you for giving me the freedom to develop and pursue my own ideas, for being very supportive, for helping me whenever I struggled, and for providing excellent scientific support and a distraction with motivational stories from your time whenever things went south in the lab. I learned a lot from you to become a better version of myself. Thank you for being a great and excellent scientific supervisor and for creating an environment where it was always a pleasure to come to work. Most of all, thank you for always being kindhearted.
- PD Dr. Hubertus Marbach for offering me with this PhD position. Though our time working together was short, thank you for your supervision and valuable scientific input, and for fostering a friendly group atmosphere.
- Prof. Dr. Rainer Fink for accepting and being on my PhD committee.
- Dr. Florian Maier, Dr. Andreas Bayer, Prof. Dr. Christian Papp, PD Dr. Ole Lytken, Dr. Andreas Späth, and Dr. Simon Jaekel for valuable feedback and discussions during chair seminars or IL meetings.
- All collaborators, for the fruitful scientific cooperation. Specially Prof. Dr. Norbert Jux for accepting and being on my PhD committee. Dr. Helen Hölzel and Dr. Michael Ruppel for the synthesis of several porphyrin derivatives. Prof. Dr. Andreas Görling and Dr. Lukas Fromm for carrying out the DFT calculations of ILs. Prof. Dr. Bernd Meyer and Martin Gurrath for carrying out the DFT calculations of porphyrins. Dr. Nicola Taccardi for the synthesis of ILs. Thank you all for always being open to discussion.
- Prof. Dr. Erdmann Spiecker (Institute of Micro- and Nanostructure Research, FAU) for accepting and being my co-mentor in the CLINT Integrated Research Training Group (CLINTiRTG).
- My former and present colleagues: Dr. Jan Brox, Dr. Ulrike Paap, Dr. Elif Bilgilişoy, Dr. Manuel Meusel, Dr. Christian Preischl, Dr. Michael Lepper, Dr. Rodrigo C. de Campos Ferreira, Afra Gezmis, Alexander Wolfram, Natalie Waleska Wellnhofer, Majid Shaker, and Stephen Massicot for the great working atmosphere. Thanks to all other PC II colleagues for a great time. I always enjoyed our activities like pleasant conversation, playing football in the summer and clicking pictures.
- Susana Kreß and Andrea Meixner-Wolf for helping me get through all the important bureaucratic work and for always smiling and welcoming.
- Hans-Peter Bäuml and Bernd Kreß for solving technical problems in the STM and AFM labs with your years of experience and magic. Many thanks to both of you for always asking me how I am doing, listening to me, and sharing some of your life experiences to help me move forward in difficult times.

## Acknowledgements

---

- Friedhold Wölfel and members of the mechanical workshop: Thomas Hofmann, Werner Hölfer, Viola Ziegler, Bernd Hofmann, and Hussein Alsaedi for your dedicated construction and/or repairing various equipment to provide excellent experimental working conditions. Thanks to Norman Anja Schmidt for the IT support. Andrea Buchner, Gertrud Weiß, and Martin Kolacyak for your support in purchasing materials for the research.
- Prof. Dr. M. Alexander Schneider (Chair of Solid State Physics, FAU) for giving me the start on my educational journey in Germany and for always being there since my very first day at FAU. Thank you very much.
- My dear ones and friends for their support and encouragement, even though we are separated by different time zones and distance. Thanks to my uncles, aunts, and cousins, Rita (didi and family), Madhu (didi and family), Padam (uncle/dai and family), Dik (dai), Mandip (bhai), Nirajan, Narayan, Amrita, Srikriti, Sachin Menon, Thomas Cournil, Sarah Smalley, and Kusum.
- My family for their endless love. Big thank you to my beloved parents (Saraswati and Tara Nath Adhikari). Special thank you to my sisters (Minita and Santa), brother (Raj Kumar), brothers-in-law (Harmen and Marek), sister-in-law (Srijana), and nephews–nieces (Milan, Aatmaj, Luna, Aashruti, and Linus Kiran). You are all my support, my strength, and my driving force. With all the weight I can put into these words: Thank you for everything! Many thanks to Laxmi and Ram Hari Duwadi for your understanding and love. My utmost respect to my girlfriend Samridhi Duwadi for understanding, supporting, and helping me navigate through the ups and downs with love and patience all these years from Nepal to Germany. Thank you for everything! ☺

## Bibliography

- [1] J.V. Barth, G. Costantini, K. Kern, Engineering atomic and molecular nanostructures at surfaces, *Nature*, 437 (2005) 671-679.
- [2] J.V. Barth, Molecular architectonic on metal surfaces, *Annu. Rev. Phys. Chem.*, 58 (2007) 375-407.
- [3] C. Joachim, J.K. Gimzewski, A. Aviram, Electronics using hybrid-molecular and mono-molecular devices, *Nature*, 408 (2000) 541-548.
- [4] G.M. Whitesides, Nanoscience, nanotechnology, and chemistry, *Small*, 1 (2005) 172-179.
- [5] K. Ariga, Molecular nanoarchitectonics: unification of nanotechnology and molecular/materials science, *Beilstein Journal of Nanotechnology*, 14 (2023) 434-453.
- [6] N.A. Kyeremateng, T. Brousse, D. Pech, Microsupercapacitors as miniaturized energy-storage components for on-chip electronics, *Nature nanotechnology*, 12 (2017) 7-15.
- [7] G.E. Moore, Cramming more components onto integrated circuits, *Proceedings of the IEEE*, 86 (1998) 82-85.
- [8] H. Marbach, Microscopic and Spectromicroscopic Insight and Fabrication of Nanoscaled Structures on Surfaces, in, FAU Erlangen-Nürnberg, 2010.
- [9] S. De Feyter, F.C. De Schryver, Two-dimensional supramolecular self-assembly probed by scanning tunneling microscopy, *Chemical Society Reviews*, 32 (2003) 139-150.
- [10] I. Fleming, Absolute configuration and the structure of chlorophyll, *Nature*, 216 (1967) 151-152.
- [11] C.E. Castro, Theory of heme protein reactivity, *Journal of Theoretical Biology*, 33 (1971) 475-490.
- [12] A.R. Battersby, Tetrapyrroles: the pigments of life, *Natural product reports*, 17 (2000) 507-526.
- [13] L.R. Milgrom, *The colours of life: an introduction to the chemistry of porphyrins and related compounds*, 1997.
- [14] W. Auwärter, D. Écija, F. Klappenberger, J.V. Barth, Porphyrins at interfaces, *Nature chemistry*, 7 (2015) 105-120.
- [15] H. Marbach, H.-P. Steinrück, Studying the dynamic behaviour of porphyrins as prototype functional molecules by scanning tunnelling microscopy close to room temperature, *Chemical Communications*, 50 (2014) 9034-9048.
- [16] H. Marbach, Surface-mediated in situ metalation of porphyrins at the solid-vacuum interface, *Accounts of chemical research*, 48 (2015) 2649-2658.
- [17] J.M. Gottfried, Surface chemistry of porphyrins and phthalocyanines, *Surface Science Reports*, 70 (2015) 259-379.
- [18] R. Guilard, K.M. Kadish, Some aspects of organometallic chemistry in metalloporphyrin chemistry: synthesis, chemical reactivity, and electrochemical behavior of porphyrins with metal-carbon bonds, *Chemical Reviews*, 88 (1988) 1121-1146.
- [19] B.M. Suijkerbuijk, R.J. Klein Gebbink, Merging porphyrins with organometallics: synthesis and applications, *Angewandte Chemie International Edition*, 47 (2008) 7396-7421.
- [20] S. Hiroto, Y. Miyake, H. Shinokubo, Synthesis and functionalization of porphyrins through organometallic methodologies, *Chemical reviews*, 117 (2017) 2910-3043.
- [21] I. Mochida, K. Suetsugu, H. Fujitsu, K. Takeshita, K. Tsuji, Y. Sagara, A. Ohyoshi, A kinetic study on reduction of nitric oxide over cobalt tetraphenylporphyrin supported on titanium dioxide, *Journal of Catalysis*, 77 (1982) 519-526.
- [22] R.L. Paddock, Y. Hiyama, J.M. McKay, S.T. Nguyen, Co (III) porphyrin/DMAP: an efficient catalyst system for the synthesis of cyclic carbonates from CO<sub>2</sub> and epoxides, *Tetrahedron Letters*, 45 (2004) 2023-2026.
- [23] K. Berg, P. Selbo, A. Weyergang, A. Dietze, L. Prasmickaite, A. Bonsted, B.Ø. Engesaeter, E. Angell-Petersen, T. Warloe, N. Frandsen, A. Høgset, Porphyrin-related photosensitizers for cancer imaging and therapeutic applications, *Journal of microscopy*, 218 (2005) 133-147.
- [24] W.M. Sharman, C.M. Allen, J.E. Van Lier, Photodynamic therapeutics: basic principles and clinical applications, *Drug discovery today*, 4 (1999) 507-517.
- [25] D. Filippini, A. Alimelli, C. Di Natale, R. Paolesse, A. D'Amico, I. Lundström, Chemical sensing with familiar devices, *Angewandte Chemie*, 118 (2006) 3884-3887.

- [26] N.A. Rakow, K.S. Suslick, A colorimetric sensor array for odour visualization, *Nature*, 406 (2000) 710-713.
- [27] P. Vilmercati, C.C. Cudia, R. Larciprete, C. Cepek, G. Zampieri, L. Sangaletti, S. Pagliara, A. Verdini, A. Cossaro, L. Floreano, A. Morgante, L. Petaccia, S. Lizzit, C. Battocchio, G. Polzonetti, A. Goldoni, Molecular orientations, electronic properties and charge transfer timescale in a Zn-porphyrin/C70 donor–acceptor complex for solar cells, *Surface science*, 600 (2006) 4018-4023.
- [28] W.M. Campbell, A.K. Burrell, D.L. Officer, K.W. Jolley, Porphyrins as light harvesters in the dye-sensitised TiO<sub>2</sub> solar cell, *Coordination Chemistry Reviews*, 248 (2004) 1363-1379.
- [29] T. Welton, Ionic liquids: a brief history, *Biophysical reviews*, 10 (2018) 691-706.
- [30] P. Wasserscheid, T. Welton, *Ionic liquids in synthesis*, Wiley Online Library, 2008.
- [31] T. Welton, Room-temperature ionic liquids. Solvents for synthesis and catalysis, *Chemical reviews*, 99 (1999) 2071-2084.
- [32] Y. Cao, T. Mu, Comprehensive investigation on the thermal stability of 66 ionic liquids by thermogravimetric analysis, *Industrial & engineering chemistry research*, 53 (2014) 8651-8664.
- [33] C. Maton, N. De Vos, C.V. Stevens, Ionic liquid thermal stabilities: decomposition mechanisms and analysis tools, *Chemical Society Reviews*, 42 (2013) 5963-5977.
- [34] H.-P. Steinrück, P. Wasserscheid, Ionic liquids in catalysis, *Catalysis Letters*, 145 (2015) 380-397.
- [35] T. Welton, Ionic liquids in catalysis, *Coordination chemistry reviews*, 248 (2004) 2459-2477.
- [36] M. Watanabe, M.L. Thomas, S. Zhang, K. Ueno, T. Yasuda, K. Dokko, Application of ionic liquids to energy storage and conversion materials and devices, *Chemical reviews*, 117 (2017) 7190-7239.
- [37] K.R. Seddon, A taste of the future, *Nature materials*, 2 (2003) 363-365.
- [38] N.V. Plechkova, K.R. Seddon, Applications of ionic liquids in the chemical industry, *Chemical Society Reviews*, 37 (2008) 123-150.
- [39] Y. Zhou, J. Qu, Ionic liquids as lubricant additives: a review, *ACS applied materials & interfaces*, 9 (2017) 3209-3222.
- [40] F. Bresme, A.A. Kornyshev, S. Perkin, M. Urbakh, Electrotunable friction with ionic liquid lubricants, *Nature Materials*, 21 (2022) 848-858.
- [41] D.S. Silvester, Recent advances in the use of ionic liquids for electrochemical sensing, *Analyst*, 136 (2011) 4871-4882.
- [42] D.S. Silvester, R. Jamil, S. Doblinger, Y. Zhang, R. Atkin, H. Li, Electrical double layer structure in ionic liquids and its importance for supercapacitor, battery, sensing, and lubrication applications, *The Journal of Physical Chemistry C*, 125 (2021) 13707-13720.
- [43] C. Pinilla, M.G. Del Pópolo, R.M. Lynden-Bell, J. Kohanoff, Structure and dynamics of a confined ionic liquid. Topics of relevance to dye-sensitized solar cells, *The Journal of Physical Chemistry B*, 109 (2005) 17922-17927.
- [44] G. Bousrez, O. Renier, B. Adranno, V. Smetana, A.-V. Mudring, Ionic liquid-based dye-sensitized solar cells—insights into electrolyte and redox mediator design, *ACS Sustainable Chemistry & Engineering*, 9 (2021) 8107-8114.
- [45] C.P. Mehnert, R.A. Cook, N.C. Dispenziere, M. Afeworki, Supported ionic liquid catalysis— A new concept for homogeneous hydroformylation catalysis, *Journal of the American Chemical Society*, 124 (2002) 12932-12933.
- [46] A. Riisager, R. Fehrmann, S. Flicker, R. van Hal, M. Haumann, P. Wasserscheid, Very stable and highly regioselective supported ionic-liquid-phase (SILP) catalysis: continuous-flow fixed-bed hydroformylation of propene, *Angewandte Chemie International Edition*, 44 (2005) 815-819.
- [47] S. Werner, N. Szesni, M. Kaiser, M. Haumann, P. Wasserscheid, A scalable preparation method for SILP and SCILL ionic liquid thin-film materials, *Chemical engineering & technology*, 35 (2012) 1962-1967.
- [48] U. Kernchen, B. Etzold, W. Korth, A. Jess, Solid catalyst with ionic liquid layer (SCILL)—A new concept to improve selectivity illustrated by hydrogenation of cyclooctadiene, *Chemical Engineering & Technology: Industrial Chemistry-Plant Equipment-Process Engineering-Biotechnology*, 30 (2007) 985-994.

- [49] K.R. Lovelock, Quantifying intermolecular interactions of ionic liquids using cohesive energy densities, *Royal Society open science*, 4 (2017) 171223.
- [50] H.-P. Steinrück, J. Libuda, P. Wasserscheid, T. Cremer, C. Kolbeck, M. Laurin, F. Maier, M. Sobota, P. Schulz, M. Stark, Surface science and model catalysis with ionic liquid-modified materials, *Advanced Materials*, 23 (2011) 2571-2587.
- [51] M. Lexow, F. Maier, H.-P. Steinrück, Ultrathin ionic liquid films on metal surfaces: adsorption, growth, stability and exchange phenomena, *Advances in Physics: X*, 5 (2020) 1761266.
- [52] H.-P. Steinrück, Recent developments in the study of ionic liquid interfaces using X-ray photoelectron spectroscopy and potential future directions, *Physical Chemistry Chemical Physics*, 14 (2012) 5010-5029.
- [53] F. Buchner, K. Forster-Tonigold, B. Uhl, D. Alwast, N. Wagner, H. Farkhondeh, A. Gross, R.J. Behm, Toward the microscopic identification of anions and cations at the ionic liquid| Ag (111) interface: a combined experimental and theoretical investigation, *ACS nano*, 7 (2013) 7773-7784.
- [54] B. Uhl, T. Cremer, M. Roos, F. Maier, H.-P. Steinrück, R.J. Behm, At the ionic liquid| metal interface: structure formation and temperature dependent behavior of an ionic liquid adlayer on Au (111), *Physical Chemistry Chemical Physics*, 15 (2013) 17295-17302.
- [55] M. Meusel, M. Lexow, A. Gezmis, S. Schötz, M. Wagner, A. Bayer, F. Maier, H.-P. Steinrück, Atomic force and scanning tunneling microscopy of ordered ionic liquid wetting layers from 110 K up to room temperature, *ACS nano*, 14 (2020) 9000-9010.
- [56] A. Wolfram, Q. Tariq, C.C. Fernández, M. Muth, M. Gurrath, D. Wechsler, M. Franke, F.J. Williams, H.-P. Steinrück, B. Meyer, O. Lytken, Adsorption energies of porphyrins on MgO (100): An experimental benchmark for dispersion-corrected density-functional theory, *Surface Science*, 717 (2022) 121979.
- [57] M. Ammon, M. Devarajulu, Y. Liu, M. Gurrath, D. Lungerich, N. Jux, B. Meyer, S. Maier, Adsorption and self-assembly of a mono-cyano Zn-tetraphenylporphyrin derivative on KBr (001) and MgO (001), *Surface Science*, 723 (2022) 122097.
- [58] J. Köbl, T. Wang, C. Wang, M. Drost, F. Tu, Q. Xu, H. Ju, D. Wechsler, M. Franke, H. Pan, H. Marbach, H.-P. Steinrück, J. Zhu, O. Lytken, Hungry Porphyrins: Protonation and Self-Metalation of Tetraphenylporphyrin on TiO<sub>2</sub> (110)-1×1, *ChemistrySelect*, 1 (2016) 6103-6105.
- [59] D. Wechsler, C.C. Fernández, Q. Tariq, N. Tsud, K.C. Prince, F.J. Williams, H.-P. Steinrück, O. Lytken, Interfacial Reactions of Tetraphenylporphyrin with Cobalt-Oxide Thin Films, *Chemistry—A European Journal*, 25 (2019) 13197-13201.
- [60] M. Ammon, A. Raabgrund, M.A. Schneider, Adsorption, self-assembly and self-metalation of tetra-cyanophenyl porphyrins on semiconducting CoO (100) films, *Surface Science*, 720 (2022) 122044.
- [61] F. Buchner, K. Forster-Tonigold, J. Kim, J. Bansmann, A. Groß, R.J. Behm, Interaction between Li, ultrathin adsorbed ionic liquid films, and CoO (111) thin films: a model study of the Solid| Electrolyte interphase formation, *Chemistry of Materials*, 31 (2019) 5537-5549.
- [62] C. Papp, H.-P. Steinrück, In situ high-resolution X-ray photoelectron spectroscopy—Fundamental insights in surface reactions, *Surface science reports*, 68 (2013) 446-487.
- [63] G. Binnig, H. Rohrer, C. Gerber, E. Weibel, Tunneling through a controllable vacuum gap, *Applied Physics Letters*, 40 (1982) 178-180.
- [64] G. Binnig, H. Rohrer, C. Gerber, E. Weibel, Surface studies by scanning tunneling microscopy, *Physical review letters*, 49 (1982) 57.
- [65] G. Binnig, C.F. Quate, C. Gerber, Atomic force microscope, *Physical review letters*, 56 (1986) 930.
- [66] F.J. Giessibl, Atomic resolution of the silicon (111)-(7×7) surface by atomic force microscopy, *Science*, 267 (1995) 68-71.
- [67] G. Meyer, N.M. Amer, Optical-beam-deflection atomic force microscopy: The NaCl (001) surface, *Applied Physics Letters*, 56 (1990) 2100-2101.
- [68] F.J. Giessibl, High-speed force sensor for force microscopy and profilometry utilizing a quartz tuning fork, *Applied physics letters*, 73 (1998) 3956-3958.
- [69] T.R. Albrecht, P. Grütter, D. Horne, D. Rugar, Frequency modulation detection using high-Q cantilevers for enhanced force microscope sensitivity, *Journal of applied physics*, 69 (1991) 668-673.

- [70] F.J. Giessibl, Forces and frequency shifts in atomic-resolution dynamic-force microscopy, *Physical Review B*, 56 (1997) 16010.
- [71] C.J. Chen, *Introduction to Scanning Tunneling Microscopy Third Edition*, Oxford University Press, USA, 2021.
- [72] B. Voigtländer, *Atomic force microscopy*, Springer, 2019.
- [73] E. Meyer, R. Bennewitz, H.J. Hug, Introduction to scanning tunneling microscopy, in: *Scanning Probe Microscopy: The Lab on a Tip*, Springer, 2021, pp. 13-45.
- [74] T. Fauster, L. Hammer, K. Heinz, M.A. Schneider, *Surface Physics: Fundamentals and Methods*, Walter de Gruyter GmbH & Co KG, 2020.
- [75] K. Bian, C. Gerber, A.J. Heinrich, D.J. Müller, S. Scheuring, Y. Jiang, Scanning probe microscopy, *Nature Reviews Methods Primers*, 1 (2021) 36.
- [76] G. Gamow, Zur quantentheorie des atomkernes, *Zeitschrift für Physik*, 51 (1928) 204-212.
- [77] K. Oura, V. Lifshits, A. Saranin, A. Zotov, M. Katayama, *Surface science: an introduction*, Springer Science & Business Media, 2013.
- [78] P.K. Hansma, J. Tersoff, Scanning tunneling microscopy, *Journal of Applied Physics*, 61 (1987) R1-R24.
- [79] S. Torbrügge, O. Schaff, J. Rychen, Application of the KolibriSensor® to combined atomic-resolution scanning tunneling microscopy and noncontact atomic-force microscopy imaging, *Journal of Vacuum Science & Technology B*, 28 (2010) C4E12-C14E20.
- [80] F.J. Giessibl, Advances in atomic force microscopy, *Reviews of modern physics*, 75 (2003) 949.
- [81] K. Besocke, An easily operable scanning tunneling microscope, *Surface Science*, 181 (1987) 145-153.
- [82] M. Lexow, B.S. Heller, F. Maier, H.-P. Steinrück, Anion exchange at the liquid/solid interface of ultrathin ionic liquid films on Ag (111), *ChemPhysChem*, 19 (2018) 2978-2984.
- [83] I. Horcas, R. Fernández, J. Gomez-Rodriguez, J. Colchero, J. Gómez-Herrero, A. Baro, WSXM: A software for scanning probe microscopy and a tool for nanotechnology, *Review of scientific instruments*, 78 (2007).
- [84] L.E. Webb, E.B. Fleischer, Crystal structure of porphine, *The Journal of Chemical Physics*, 43 (1965) 3100-3111.
- [85] B.M. Chen, A. Tulinsky, Redetermination of the Structure of Porphine, *Journal of the American Chemical Society*, 94 (1972) 4144-4151.
- [86] N.F. Phelan, M. Orchin, Cross conjugation, *Journal of Chemical Education*, 45 (1968) 633.
- [87] C. Storm, Y. Teklu, Nitrogen-hydrogen tautomerism in porphyrines and chlorines, *Journal of the American Chemical Society*, 94 (1972) 1745-1747.
- [88] H. Limbach, J. Hennig, R. Kendrick, C. Yannoni, Proton-transfer kinetics in solids: tautomerism in free base porphines by nitrogen-15 CPMAS NMR, *Journal of the American Chemical Society*, 106 (1984) 4059-4060.
- [89] J. Braun, M. Koecher, M. Schlabach, B. Wehrle, H.-H. Limbach, E. Vogel, NMR study of the tautomerism of porphyrin including the kinetic HH/HD/DD isotope effects in the liquid and the solid state, *Journal of the American Chemical Society*, 116 (1994) 6593-6604.
- [90] P. Liljeroth, J. Repp, G. Meyer, Current-induced hydrogen tautomerization and conductance switching of naphthalocyanine molecules, *Science*, 317 (2007) 1203-1206.
- [91] W. Auwärter, K. Seufert, F. Bischoff, D. Ecija, S. Vijayaraghavan, S. Joshi, F. Klappenberger, N. Samudrala, J.V. Barth, A surface-anchored molecular four-level conductance switch based on single proton transfer, *Nature nanotechnology*, 7 (2012) 41-46.
- [92] G. Bussetti, M. Campione, M. Riva, A. Picone, L. Raimondo, L. Ferraro, C. Hogan, M. Palummo, A. Brambilla, M. Finazzi, L. Duò, A. Sassella, F. Ciccacci, Stable Alignment of Tautomers at Room Temperature in Porphyrin 2D Layers, *Advanced Functional Materials*, 24 (2014) 958-963.
- [93] G. Moss, Nomenclature of tetrapyrroles (Recommendations 1986), *Pure and Applied Chemistry*, 59 (1987) 779-832.
- [94] C.M.B. Carvalho, T.J. Brocksom, K.T. de Oliveira, Tetrabenzoporphyrins: synthetic developments and applications, *Chemical Society Reviews*, 42 (2013) 3302-3317.
- [95] T.A. Jung, R. Schlittler, J. Gimzewski, Conformational identification of individual adsorbed molecules with the STM, *Nature*, 386 (1997) 696-698.

- [96] F. Moresco, G. Meyer, K.-H. Rieder, H. Tang, A. Gourdon, C. Joachim, Conformational changes of single molecules induced by scanning tunneling microscopy manipulation: A route to molecular switching, *Physical Review Letters*, 86 (2001) 672.
- [97] F. Moresco, G. Meyer, K.-H. Rieder, J. Ping, H. Tang, C. Joachim, TBPP molecules on copper surfaces: a low temperature scanning tunneling microscope investigation, *Surface science*, 499 (2002) 94-102.
- [98] F. Buchner, K. Comanici, N. Jux, H.-P. Steinrück, H. Marbach, Polymorphism of porphyrin molecules on Ag (111) and how to weave a rigid monolayer, *The Journal of Physical Chemistry C*, 111 (2007) 13531-13538.
- [99] S. Ditze, M. Stark, F. Buchner, A. Aichert, N. Jux, N. Luckas, A. Görling, W. Hieringer, J. Hornegger, H.-P. Steinrück, H. Marbach, On the energetics of conformational switching of molecules at and close to room temperature, *Journal of the American Chemical Society*, 136 (2014) 1609-1616.
- [100] K.-D. Flechtner, Photoelektronenspektroskopische Untersuchungen zur Adsorption und Reaktivität von Co(II)-, Zn(II)- und Fe(II)-Porphyrinen auf Ag(111), in, FAU Erlangen-Nürnberg, 2007.
- [101] Y.-L. Wang, B. Li, S. Sarman, F. Mocci, Z.-Y. Lu, J. Yuan, A. Laaksonen, M.D. Fayer, Microstructural and dynamical heterogeneities in ionic liquids, *Chemical reviews*, 120 (2020) 5798-5877.
- [102] R. Hayes, G.G. Warr, R. Atkin, Structure and nanostructure in ionic liquids, *Chemical reviews*, 115 (2015) 6357-6426.
- [103] K. Lovelock, C. Kolbeck, T. Cremer, N. Paape, P. Schulz, P. Wasserscheid, F. Maier, H.-P. Steinrück, Influence of different substituents on the surface composition of ionic liquids studied using ARXPS, *The Journal of Physical Chemistry B*, 113 (2009) 2854-2864.
- [104] G.M. Whitesides, J.P. Mathias, C.T. Seto, Molecular self-assembly and nanochemistry: a chemical strategy for the synthesis of nanostructures, *Science*, 254 (1991) 1312-1319.
- [105] M. Gottfried, H. Marbach, Surface-confined coordination chemistry with porphyrins and phthalocyanines: aspects of formation, electronic structure, and reactivity, *Zeitschrift für Physikalische Chemie*, 223 (2009) 53-74.
- [106] J. Brede, M. Linares, S. Kuck, J. Schwöbel, A. Scarfato, S.-H. Chang, G. Hoffmann, R. Wiesendanger, R. Lensen, P.H. Kouwer, J. Hoogboom, A.E. Rowan, M. Bröring, M. Funk, S. Stafström, F. Zerbetto, R. Lazzaroni, Dynamics of molecular self-ordering in tetraphenyl porphyrin monolayers on metallic substrates, *Nanotechnology*, 20 (2009) 275602.
- [107] F. Buchner, I. Kellner, W. Hieringer, A. Görling, H.-P. Steinrück, H. Marbach, Ordering aspects and intramolecular conformation of tetraphenylporphyrins on Ag (111), *Physical Chemistry Chemical Physics*, 12 (2010) 13082-13090.
- [108] M. Lepper, L. Zhang, M. Stark, S. Ditze, D. Lungerich, N. Jux, W. Hieringer, H.-P. Steinrück, H. Marbach, Role of specific intermolecular interactions for the arrangement of Ni (II)-5, 10, 15, 20-tetraphenyltetrabenzoporphyrin on Cu (111), *The Journal of Physical Chemistry C*, 119 (2015) 19897-19905.
- [109] S.P. Jarvis, S. Taylor, J.D. Baran, D. Thompson, A. Saywell, B. Mangham, N.R. Champness, J. Larsson, P. Moriarty, Physisorption controls the conformation and density of states of an adsorbed porphyrin, *The Journal of Physical Chemistry C*, 119 (2015) 27982-27994.
- [110] F. Albrecht, F. Bischoff, W. Auwärter, J.V. Barth, J. Repp, Direct identification and determination of conformational response in adsorbed individual nonplanar molecular species using noncontact atomic force microscopy, *Nano Letters*, 16 (2016) 7703-7709.
- [111] M. Lepper, J. Köbl, T. Schmitt, M. Gurrath, A. de Siervo, M.A. Schneider, H.-P. Steinrück, B. Meyer, H. Marbach, W. Hieringer, "Inverted" porphyrins: a distorted adsorption geometry of free-base porphyrins on Cu (111), *Chemical communications*, 53 (2017) 8207-8210.
- [112] L. Zhang, M. Lepper, M. Stark, T. Menzel, D. Lungerich, N. Jux, W. Hieringer, H.-P. Steinrück, H. Marbach, On the critical role of the substrate: the adsorption behaviour of tetrabenzoporphyrins on different metal surfaces, *Physical Chemistry Chemical Physics*, 19 (2017) 20281-20289.
- [113] F. Buchner, STM investigation of molecular architectures of porphyrinoids on a Ag (111) surface: supramolecular ordering, electronic properties and reactivity, Springer Science & Business Media, 2010.

- [114] W. Auwärter, A. Weber-Bargioni, A. Riemann, A. Schiffrin, O. Gröning, R. Fasel, J.V. Barth, Self-assembly and conformation of tetrapyrrolyl-porphyrin molecules on Ag (111), *The Journal of chemical physics*, 124 (2006).
- [115] F. Buchner, J. Xiao, E. Zillner, M. Chen, M. Röckert, S. Ditze, M. Stark, H.-P. Steinrück, J.M. Gottfried, H. Marbach, Diffusion, rotation, and surface chemical bond of individual 2 H-tetraphenylporphyrin molecules on Cu (111), *The Journal of Physical Chemistry C*, 115 (2011) 24172-24177.
- [116] L. Grill, M. Dyer, L. Lafferentz, M. Persson, M.V. Peters, S. Hecht, Nano-architectures by covalent assembly of molecular building blocks, *Nature nanotechnology*, 2 (2007) 687-691.
- [117] S. Haq, F. Hanke, M.S. Dyer, M. Persson, P. Iavicoli, D.B. Amabilino, R. Raval, Clean coupling of unfunctionalized porphyrins at surfaces to give highly oriented organometallic oligomers, *Journal of the American Chemical Society*, 133 (2011) 12031-12039.
- [118] S. Haq, F. Hanke, J. Sharp, M. Persson, D.B. Amabilino, R. Raval, Versatile bottom-up construction of diverse macromolecules on a surface observed by scanning tunneling microscopy, *ACS nano*, 8 (2014) 8856-8870.
- [119] B. Baker, M. Stöhr, Role of cyano groups in the self-assembly of organic molecules on metal surfaces, in: *Encyclopedia of Interfacial Chemistry: Surface Science and Electrochemistry*, Elsevier, 2018, pp. 153-165.
- [120] M. Lepper, T. Schmitt, M. Gurrath, M. Raschmann, L. Zhang, M. Stark, H. Hölzel, N. Jux, B. Meyer, M.A. Schneider, H.-P. Steinrück, H. Marbach, Adsorption behavior of a cyano-functionalized porphyrin on Cu (111) and Ag (111): from molecular wires to ordered supramolecular two-dimensional aggregates, *The Journal of Physical Chemistry C*, 121 (2017) 26361-26371.
- [121] K. Diller, A.C. Papageorgiou, F. Klappenberger, F. Allegretti, J.V. Barth, W. Auwärter, In vacuo interfacial tetrapyrrole metallation, *Chemical Society Reviews*, 45 (2016) 1629-1656.
- [122] W. Hieringer, K. Flechtner, A. Kretschmann, K. Seufert, W. Auwärter, J.V. Barth, A. Görling, H.-P. Steinrück, J.M. Gottfried, The surface trans effect: influence of axial ligands on the surface chemical bonds of adsorbed metalloporphyrins, *Journal of the American Chemical Society*, 133 (2011) 6206-6222.
- [123] N.A. Schmidt, R. Fink, W. Hieringer, Assignment of near-edge x-ray absorption fine structure spectra of metalloporphyrins by means of time-dependent density-functional calculations, *The Journal of chemical physics*, 133 (2010).
- [124] M. Chen, X. Feng, L. Zhang, H. Ju, Q. Xu, J. Zhu, J.M. Gottfried, K. Ibrahim, H. Qian, J. Wang, Direct synthesis of nickel (II) tetraphenylporphyrin and its interaction with a Au (111) surface: a comprehensive study, *The Journal of Physical Chemistry C*, 114 (2010) 9908-9916.
- [125] A. Baklanov, M. Garnica, A. Robert, M.-L. Bocquet, K. Seufert, J.T. Küchle, P.T. Ryan, F. Haag, R. Kakavandi, F. Allegretti, W. Auwärter, On-surface synthesis of nonmetal porphyrins, *Journal of the American Chemical Society*, 142 (2020) 1871-1881.
- [126] J.M. Gottfried, K. Flechtner, A. Kretschmann, T. Lukaszczuk, H.-P. Steinrück, Direct synthesis of a metalloporphyrin complex on a surface, *Journal of the American Chemical Society*, 128 (2006) 5644-5645.
- [127] K. Diller, F. Klappenberger, M. Marschall, K. Hermann, A. Nefedov, C. Wöll, J.V. Barth, Self-metalation of 2H-tetraphenylporphyrin on Cu (111): An x-ray spectroscopy study, *The Journal of chemical physics*, 136 (2012).
- [128] Y. Li, J. Xiao, T.E. Shubina, M. Chen, Z. Shi, M. Schmid, H.-P. Steinrück, J.M. Gottfried, N. Lin, Coordination and metalation bifunctionality of Cu with 5, 10, 15, 20-tetra (4-pyridyl) porphyrin: toward a mixed-valence two-dimensional coordination network, *Journal of the American Chemical Society*, 134 (2012) 6401-6408.
- [129] F. Buchner, K. Flechtner, Y. Bai, E. Zillner, I. Kellner, H.-P. Steinrück, H. Marbach, J.M. Gottfried, Coordination of iron atoms by tetraphenylporphyrin monolayers and multilayers on Ag (111) and formation of iron-tetraphenylporphyrin, *The Journal of Physical Chemistry C*, 112 (2008) 15458-15465.
- [130] D. Ecija, M. Trelka, C. Urban, P.d. Mendoza, E. Mateo-Martí, C. Rogero, J.A. Martín-Gago, A.M. Echavarren, R. Otero, J.M. Gallego, R. Miranda, Molecular conformation, organizational chirality, and iron metalation of meso-tetramesitylporphyrins on copper (100), *The Journal of Physical Chemistry C*, 112 (2008) 8988-8994.

- [131] T.E. Shubina, H. Marbach, K. Flechtner, A. Kretschmann, N. Jux, F. Buchner, H.-P. Steinrück, T. Clark, J.M. Gottfried, Principle and mechanism of direct porphyrin metalation: joint experimental and theoretical investigation, *Journal of the American Chemical Society*, 129 (2007) 9476-9483.
- [132] A. Kretschmann, M.-M. Walz, K. Flechtner, H.-P. Steinrück, J.M. Gottfried, Tetraphenylporphyrin picks up zinc atoms from a silver surface, *Chemical communications*, (2007) 568-570.
- [133] A. Weber-Bargioni, J. Reichert, A. Seitsonen, W. Auwärter, A. Schiffrin, J.V. Barth, Interaction of cerium atoms with surface-anchored porphyrin molecules, *The Journal of Physical Chemistry C*, 112 (2008) 3453-3455.
- [134] R. González-Moreno, C. Sánchez-Sánchez, M. Trelka, R. Otero, A. Cossaro, A. Verdini, L. Floreano, M. Ruiz-Bermejo, A. García-Lekue, J.Á. Martín-Gago, C. Rogero, Following the metalation process of protoporphyrin IX with metal substrate atoms at room temperature, *The Journal of Physical Chemistry C*, 115 (2011) 6849-6854.
- [135] C.M. Doyle, S.A. Krasnikov, N.N. Sergeeva, A.B. Preobrajenski, N.A. Vinogradov, Y.N. Sergeeva, M.O. Senge, A.A. Cafolla, Evidence for the formation of an intermediate complex in the direct metalation of tetra (4-bromophenyl)-porphyrin on the Cu (111) surface, *Chemical Communications*, 47 (2011) 12134-12136.
- [136] A. Goldoni, C.A. Pignedoli, G. Di Santo, C. Castellarin-Cudia, E. Magnano, F. Bondino, A. Verdini, D. Passerone, Room temperature metalation of 2H-TPP monolayer on iron and nickel surfaces by picking up substrate metal atoms, *ACS nano*, 6 (2012) 10800-10807.
- [137] S. Ditze, M. Stark, M. Drost, F. Buchner, H.-P. Steinrück, H. Marbach, Activation Energy for the Self-Metalation Reaction of 2H-Tetraphenylporphyrin on Cu (111), *Angewandte Chemie International Edition*, 51 (2012) 10898-10901.
- [138] J. Xiao, S. Ditze, M. Chen, F. Buchner, M. Stark, M. Drost, H.-P. Steinrück, J.M. Gottfried, H. Marbach, Temperature-dependent chemical and structural transformations from 2H-tetraphenylporphyrin to copper (II)-tetraphenylporphyrin on Cu (111), *The Journal of Physical Chemistry C*, 116 (2012) 12275-12282.
- [139] M. Lepper, J. Köbl, L. Zhang, M. Meusel, H. Hölzel, D. Lungerich, N. Jux, A. de Siervo, B. Meyer, H.-P. Steinrück, H. Marbach, Controlling the Self-Metalation Rate of Tetraphenylporphyrins on Cu (111) via Cyano Functionalization, *Angewandte Chemie International Edition*, 57 (2018) 10074-10079.
- [140] M. Röckert, M. Franke, Q. Tariq, S. Ditze, M. Stark, P. Uffinger, D. Wechsler, U. Singh, J. Xiao, H. Marbach, H.-P. Steinrück, O. Lytken, Coverage-and Temperature-Dependent Metalation and Dehydrogenation of Tetraphenylporphyrin on Cu (111), *Chemistry—A European Journal*, 20 (2014) 8948-8953.
- [141] M. Röckert, M. Franke, Q. Tariq, D. Lungerich, N. Jux, M. Stark, A. Kaftan, S. Ditze, H. Marbach, M. Laurin, J. Libuda, H.-P. Steinrück, O. Lytken, Insights in reaction mechanistics: isotopic exchange during the metalation of deuterated tetraphenyl-21, 23 D-porphyrin on Cu (111), *The Journal of Physical Chemistry C*, 118 (2014) 26729-26736.
- [142] A. Wiengarten, J.A. Lloyd, K. Seufert, J. Reichert, W. Auwärter, R. Han, D.A. Duncan, F. Allegretti, S. Fischer, S.C. Oh, Ö. Saglam, L. Jiang, S. Vijayaraghavan, D. Ććija, A.C. Papageorgiou, J.V. Barth, Surface-assisted cyclodehydrogenation; break the symmetry, enhance the selectivity, *Chemistry—A European Journal*, 21 (2015) 12285-12290.
- [143] L.M. Mateo, Q. Sun, S.X. Liu, J.J. Bergkamp, K. Eimre, C.A. Pignedoli, P. Ruffieux, S. Decurtins, G. Bottari, R. Fasel, T. Torres, On-surface synthesis and characterization of triply fused porphyrin-graphene nanoribbon hybrids, *Angewandte Chemie International Edition*, 59 (2020) 1334-1339.
- [144] Y. He, M. Garnica, F. Bischoff, J. Ducke, M.-L. Bocquet, M. Batzill, W. Auwärter, J.V. Barth, Fusing tetrapyrroles to graphene edges by surface-assisted covalent coupling, *Nature chemistry*, 9 (2017) 33-38.
- [145] F. Buchner, E. Zillner, M. Röckert, S. Gläbel, H.-P. Steinrück, H. Marbach, Substrate-Mediated Phase Separation of Two Porphyrin Derivatives on Cu (111), *Chemistry—A European Journal*, 17 (2011) 10226-10229.
- [146] W. Auwärter, F. Klappenberger, A. Weber-Bargioni, A. Schiffrin, T. Strunskus, C. Wöll, Y. Pennec, A. Riemann, J.V. Barth, Conformational adaptation and selective adatom capturing of

- tetrapyrrolyl-porphyrin molecules on a copper (111) surface, *Journal of the American Chemical Society*, 129 (2007) 11279-11285.
- [147] T. Yokoyama, S. Yokoyama, T. Kamikado, Y. Okuno, S. Mashiko, Selective assembly on a surface of supramolecular aggregates with controlled size and shape, *Nature*, 413 (2001) 619-621.
- [148] G. Di Santo, S. Blankenburg, C. Castellarin-Cudia, M. Fanetti, P. Borghetti, L. Sangaletti, L. Floreano, A. Verdini, E. Magnano, F. Bondino, C.A. Pignedoli, M.-T. Nguyen, R. Gaspari, D. Passerone, A. Goldoni, Supramolecular engineering through temperature-induced chemical modification of 2H-Tetraphenylporphyrin on Ag (111): flat Phenyl conformation and possible dehydrogenation Reactions, *Chemistry—A European Journal*, 17 (2011) 14354-14359.
- [149] L.A. Fendt, M. Stöhr, N. Wintjes, M. Enache, T.A. Jung, F. Diederich, Modification of supramolecular binding motifs induced by substrate registry: formation of self-assembled macrocycles and chain-like patterns, *Chemistry—A European Journal*, 15 (2009) 11139-11150.
- [150] Z. Shi, N. Lin, Porphyrin-based two-dimensional coordination Kagome lattice self-assembled on a Au (111) surface, *Journal of the American Chemical Society*, 131 (2009) 5376-5377.
- [151] J. Kuliga, L. Zhang, M. Lepper, D. Lungerich, H. Hölzel, N. Jux, H.-P. Steinrück, H. Marbach, Metalation and coordination reactions of 2 H-meso-trans-di (p-cyanophenyl) porphyrin on Ag (111) with coadsorbed cobalt atoms, *Physical Chemistry Chemical Physics*, 20 (2018) 25062-25068.
- [152] L. Cai, Q. Sun, M. Bao, H. Ma, C. Yuan, W. Xu, Competition between hydrogen bonds and coordination bonds steered by the surface molecular coverage, *ACS nano*, 11 (2017) 3727-3732.
- [153] Y. Wang, S. Fabris, T.W. White, F. Pagliuca, P. Moras, M. Papagno, D. Topwal, P. Sheverdyeva, C. Carbone, M. Lingenfelder, T. Classen, K. Kern, G. Costantini, Varying molecular interactions by coverage in supramolecular surface chemistry, *Chemical Communications*, 48 (2012) 534-536.
- [154] C. Borek, K. Hanson, P.I. Djurovich, M.E. Thompson, K. Aznavour, R. Bau, Y. Sun, S.R. Forrest, J. Brooks, L. Michalski, J. Brown, Highly efficient, near-infrared electrophosphorescence from a Pt–metalloporphyrin complex, *Angewandte Chemie International Edition*, 46 (2007) 1109-1112.
- [155] F. Ménard, V. Sol, C. Ringot, R. Granet, S. Alves, C. Le Morvan, Y. Queneau, N. Ono, P. Krausz, Synthesis of tetraglucosyl-and tetrapolyamine–tetrabenzoporphyrin conjugates for an application in PDT, *Bioorganic & medicinal chemistry*, 17 (2009) 7647-7657.
- [156] L. Hutter, B. Müller, K. Koren, S. Borisov, I. Klimant, Robust optical oxygen sensors based on polymer-bound NIR-emitting platinum (II)–benzoporphyrins, *Journal of Materials Chemistry C*, 2 (2014) 7589-7598.
- [157] J. Brox, R. Adhikari, M. Shaker, M. Ruppel, N. Jux, H. Marbach, S. Jaekel, H.-P. Steinrück, On the adsorption of different tetranaphthylporphyrins on Cu (111) and Ag (111), *Surface Science*, 720 (2022) 122047.
- [158] L. Zhang, M. Lepper, M. Stark, D. Lungerich, N. Jux, W. Hieringer, H.-P. Steinrück, H. Marbach, Self-assembly and coverage dependent thermally induced conformational changes of Ni (II)-meso-tetrakis (4-tert-butylphenyl) benzoporphyrin on Cu (111), *Physical Chemistry Chemical Physics*, 17 (2015) 13066-13073.
- [159] X.-Q. Yang, J.-J. Duan, J. Su, X. Peng, Z.-Y. Yi, R.-N. Li, J. Lu, S.-F. Wang, T. Chen, D. Wang, Aromatic ring fusion to benzoporphyrin via  $\gamma$ -ortho cyclodehydrogenation on a Ag (111) surface, *ACS nano*, 16 (2022) 13092-13100.
- [160] M. Ruppel, D. Lungerich, S. Sturm, R. Lippert, F. Hampel, N. Jux, A Comprehensive Study on Tetraaryltetrabenzoporphyrins, *Chemistry—A European Journal*, 26 (2020) 3287-3296.
- [161] M. Ruppel, L.-P. Gazetas, D. Lungerich, F. Hampel, N. Jux, Investigations of Low-Symmetrical Tetraaryltetrabenzoporphyrins Produced by Mixed Condensation Reactions, *The Journal of Organic Chemistry*, 85 (2020) 7781-7792.
- [162] J. Kuliga, S. Massicot, R. Adhikari, M. Ruppel, N. Jux, H.-P. Steinrück, H. Marbach, Conformation Controls Mobility: 2H-Tetranaphthylporphyrins on Cu (111), *ChemPhysChem*, 21 (2020) 423-427.

## Appendix

### A1 List of STM/nc-AFM Raw Data File IDs

Figures	Raw Data File IDs YYMMDD_###-###	Figures	Raw Data File IDs YYMMDD_###-###
Figure 9a-d	170710_10 to 24	Figure 14b(R)	190124_160
Figure 9e-f	170720_79	Figure 14c(L)	190110_35
Figure 9g	170712_74	Figure 14c(M)	190110_30
Figure 9i	170207_127	Figure 14c(R)	190109_59
Figure 9j-k	170207_69	Figure 14d-g	190121_38
Figure 9l	170303_6	Figure 15a(L)	190225_08
Figure 9m-n	170303_27	Figure 15a(R)	190222_84
Figure 9o	160425_19	Figure 15b(L)	190225_44
Figure 9p-r	160428_134 to 166	Figure 15b(R)	190225_46
Figure 10(T)	201118_65	Figure 15c(L)	190226_25
Figure 10(B-L)	201117_75	Figure 15c(R)	190226_26
Figure 10(B-M)	201118_107	Figure 15d-f	190222_70
Figure 10(B-R)	191023_97	Figure 16a(L)	20201125_43_1
Figure 11a-b	201118_156 to 160	Figure 16a(M)	20201126_35_1
Figure 11d-e	201118_107	Figure 16a(R)	20201126_27_3 to 27_11
Figure 11g-h	191023_97	Figure 16b(L)	20201130_83_1
Figure 12a(T-L)	190130_28	Figure 16b(M)	20201130_52_1
Figure 12a(T-M)	190131_39	Figure 16b(R)	20201130_73_1
Figure 12a(T-R)	190131_40	Figure 16c(L)	20201201_42_2
Figure 12b(B-L)	190201_20	Figure 16c(M)	20201201_47_1
Figure 12b(B-M)	190204_48 to 53	Figure 16c(R)	20201201_51_1 to 51_2
Figure 12b(B-R)	190204_58 to 77	Figure 16d(L)	20210826_44_4
Figure 13a	190131_40	Figure 16d(M)	20210828_88_1
Figure 13c	190204_58 to 77	Figure 16d(R)	20210826_95_1
Figure 14a(L)	190123_01	Figure 16e(L)	20200901_35_1
Figure 14a(M)	190122_07	Figure 16e(M)	20200901_36_3
Figure 14a(R)	190121_38	Figure 16e(R)	20200831_65_1
Figure 14b(L)	190124_206	Figure 17a(L)	20201126_27_3 to 27_11
Figure 14b(M)	190109_42	Figure 17a(R)	20201201_51_1 to 51_2

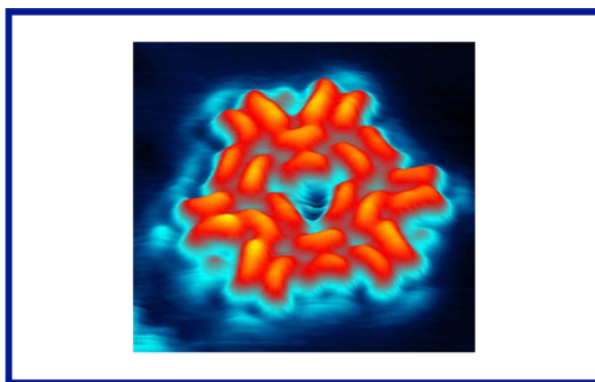
L = Left, M = Middle, R = Right, T = Top, B = Bottom, YY = Year, MM = Month, DD = Day, ###-### = Numbers

## A2 List of Publications

### Publication [P1]

**Formation of Highly Ordered Molecular Porous 2D Networks from Cyano-Functionalized Porphyrins on Cu(111),** R. Adhikari, G. Sigleithmaier, M. Gurrath, M. Meusel, J. Kuliga, M. Lepper, H. Hölzel, N. Jux, B. Meyer, H.-P. Steinrück, and H. Marbach, *Chem. Eur. J.* **2020**, *26*, 13408; [10.1002/chem.202001980](https://doi.org/10.1002/chem.202001980)

Copyright © 2020, The Authors. Published by Wiley-VCH GmbH. This is an open access article under the terms of the [Creative Commons Attribution-NonCommercial-NoDerivs](https://creativecommons.org/licenses/by-nc-nd/4.0/) License, which permits use and distribution in any medium, provided the original work is properly cited, the use is non-commercial and no modifications or adaptations are made.



⇒ Cover Feature: [10.1002/chem.202003357](https://doi.org/10.1002/chem.202003357)

# Chemistry A European Journal



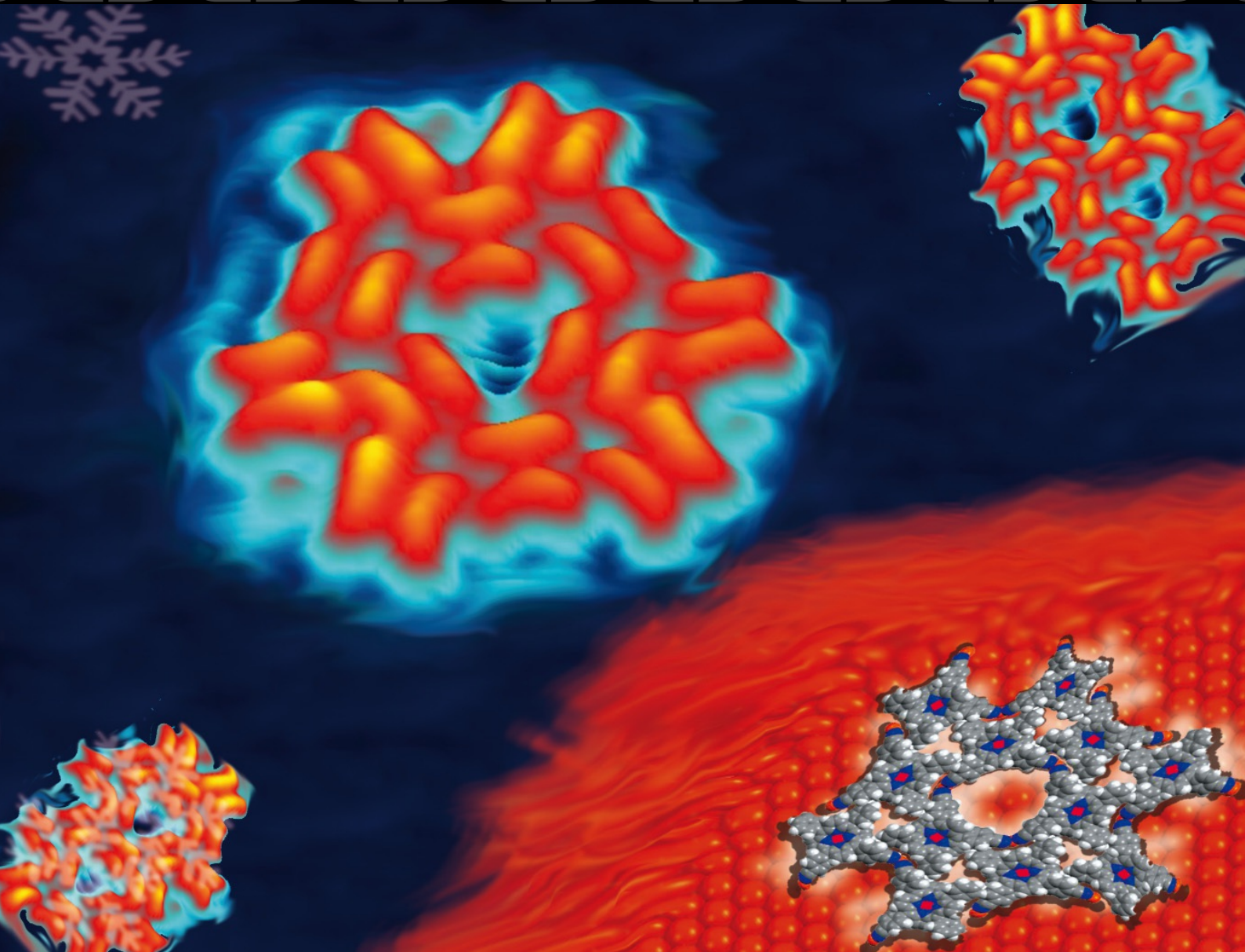
**Chemistry  
Europe**

European Chemical  
Societies Publishing

Cover Feature:

*B. Meyer, H.-P. Steinrück et al.*

Formation of Highly Ordered Molecular Porous 2D Networks from Cyano-Functionalized Porphyrins on Cu(111)



## ■ Porphyrins | Hot Paper |

# Formation of Highly Ordered Molecular Porous 2D Networks from Cyano-Functionalized Porphyrins on Cu(111)

Rajan Adhikari,<sup>[a]</sup> Gretel Siglreithmaier,<sup>[a]</sup> Martin Gurrath,<sup>[b]</sup> Manuel Meusel,<sup>[a]</sup> Jan Kuliga,<sup>[a]</sup> Michael Lepper,<sup>[a]</sup> Helen Hölzel,<sup>[c]</sup> Norbert Jux,<sup>[c]</sup> Bernd Meyer,<sup>\*,[b]</sup> Hans-Peter Steinrück,<sup>\*,[a]</sup> and Hubertus Marbach<sup>[a]</sup>

**Abstract:** We investigated the adsorption of three related cyano-functionalized tetraphenyl porphyrin derivatives on Cu(111) by scanning tunneling microscopy (STM) in ultra-high vacuum (UHV) with the goal to identify the role of the cyano group and the central Cu atom for the intermolecular and supramolecular arrangement. The porphyrin derivatives studied were Cu-TCNPP, Cu-*cis*DCNPP, and 2H-*cis*DCNPP, that is, Cu-5,10,15,20-tetrakis-(*p*-cyano)-phenylporphyrin, Cu-*meso-cis*-di(*p*-cyano)-phenylporphyrin and 2H-*meso-cis*-di(*p*-cyano)-phenylporphyrin, respectively. Starting from different structures obtained after deposition at room temperature, all three molecules form the same long-range ordered hexagonal honeycomb-type structure with triangular pores and

three molecules per unit cell. For the metal-free 2H-*cis*DCNPP, this occurs only after self-metalation upon heating. The structure-forming elements are pores with a distance of 3.1 nm, formed by triangles of porphyrins fused together by cyano-Cu-cyano interactions with Cu adatoms. This finding leads us to suggest that two cyano-phenyl groups in the “*cis*” position is the minimum prerequisite to form a highly ordered 2D porous molecular pattern. The experimental findings are supported by detailed density functional theory calculations to analyze the driving forces that lead to the formation of the porous hexagonal honeycomb-type structure.

## Introduction

It is still an ongoing challenge to organize matter on the molecular or even atomic scale. In this regard, the topic of self-assembled supramolecular networks of organic molecules on noble-metal surfaces developed as a vivid research field over the last two decades. Molecular self-assembly, based on molec-

ular recognition concepts in supramolecular chemistry,<sup>[1]</sup> aims at design, synthesis, and understanding of the assembly of a discrete number of molecular entities into larger ensembles. In the new supramolecular entities with larger shapes and sizes, the spatial organization of the functional building blocks is controlled by intermolecular forces such as hydrogen bonding,<sup>[2]</sup>  $\pi$ - $\pi$  stacking,<sup>[3]</sup> dipolar coupling,<sup>[4]</sup> metal coordination,<sup>[5]</sup> and dispersion forces, all of which are weaker than covalent bonding. Molecular self-assemblies and their properties on surfaces not only depend on the intermolecular interactions but also on the adsorbate-substrate interactions; therefore they can be tuned by modifications within the molecules<sup>[6]</sup> and by the choice of the underlying substrate.<sup>[7]</sup>

If it comes to the directed self-assembly toward functional molecular architectures, porphyrins<sup>[8]</sup> appear to be a particularly suitable class of molecules, since they are omnipresent in nature, for example in chlorophyll (Mg-center)<sup>[9]</sup> and heme (Fe-center).<sup>[10]</sup> Porphyrins consist of a tetrapyrrolic macrocycle with a central cavity, which can coordinate a variety of metal atoms.<sup>[9–11]</sup> Owing to these properties, porphyrins adsorbed at metal surfaces offer a rich playground for the detailed investigation and manipulation of desired systems. Recently, the attachment of one or more cyano-functionalized groups to porphyrins turned out to be particularly interesting, because the negatively charged N-atoms can interact through different bonding motifs with neighboring molecules. Notably, cyano groups cannot only contribute in hydrogen bonding and dipolar coupling, but also can coordinate to different metals.<sup>[4,12]</sup>

[a] R. Adhikari, G. Siglreithmaier, M. Meusel, J. Kuliga, Dr. M. Lepper, Prof. Dr. H.-P. Steinrück, Dr. H. Marbach  
 Lehrstuhl für Physikalische Chemie II  
 Friedrich-Alexander-Universität Erlangen-Nürnberg  
 Egerlandstr. 3, 91058 Erlangen (Germany)  
 E-mail: hans-peter.steinrueck@fau.de

[b] M. Gurrath, Prof. Dr. B. Meyer  
 Interdisciplinary Center for Molecular Materials (ICMM) and  
 Computer-Chemistry-Center (CCC)  
 Friedrich-Alexander-Universität Erlangen-Nürnberg  
 Nägelsbachstr. 25, 91052 Erlangen (Germany)  
 E-mail: bernd.meyer@fau.de

[c] H. Hölzel, Prof. Dr. N. Jux  
 Lehrstuhl für Organische Chemie II  
 Friedrich-Alexander-Universität Erlangen-Nürnberg  
 Nikolaus-Fiebiger-Str. 10, 91058 Erlangen (Germany)

Supporting information and the ORCID identification number(s) for the author(s) of this article can be found under:  
<https://doi.org/10.1002/chem.202001980>.

© 2020 The Authors. Published by Wiley-VCH GmbH. This is an open access article under the terms of Creative Commons Attribution NonCommercial-NoDerivs License, which permits use and distribution in any medium, provided the original work is properly cited, the use is non-commercial and no modifications or adaptations are made.

Furthermore, it was shown that the electron withdrawing effect of the peripheral cyano groups significantly influences the self-metalation of corresponding metal-free porphyrin derivatives on Cu(111).<sup>[12a]</sup>

In addition to the already reported individual molecules (0D)<sup>[12d]</sup> and molecular chains (1D)<sup>[12b]</sup> of cyano-functionalized porphyrins, we herein report the formation of peculiar porous networks (2D), which is again triggered by the functional cyano groups. Previously, 2D molecular porous networks were reported using different classes of organic molecules on single crystal metal surfaces.<sup>[13]</sup> These 2D molecular porous networks are especially interesting, since they have a high potential as “host template” for functional guest molecules, for example, to study the dynamics of guest binding within the pore or to localize them even at elevated temperatures for the manipulation by an STM tip. Moreover, the pores may also serve as nanoreactors.<sup>[14]</sup>

Generally, the self-assembly of ordered supramolecular networks depends on the nature and functionality of the corresponding molecular building blocks, the choice of the substrate and the applied conditions. For example, the porous networks formed by trimesic acid (TMA) and its larger relative 1,3,5-benzene-tribenzoic acid (BTB) have been studied on surfaces like HOPG<sup>[15]</sup> and Au(111).<sup>[16]</sup> Moreover, the porous networks stabilized by metal coordination captured increasing attention due to metal-ligand bonding, and thus its stability is stronger than usual hydrogen-bonded porous networks. More often, for the formation of metal-organic networks Fe, Co, Ni, or Cu atoms are introduced as linker metals for co-adsorbed organic molecules. Aside from directly introduced transition metal atoms, adatoms from the surface, onto which molecules are deposited, can be used for metal-organic coordination. Recently, examples for this type of interactions have been reported by Lepper et al. on Cu(111)<sup>[12b]</sup> and by Gottardi et al. on Au(111).<sup>[17]</sup>

Figure 1 depicts the chemical structures of Cu-TCNPP, Cu-*cis*DCNPP, and 2H-*cis*DCNPP, in which fourfold and twofold (*cis*)-cyano-phenyl groups are attached to the *meso*-position of the porphyrin core. In this contribution, we will show that the depicted metalated species tend to self-assemble into a peculiar well-ordered porous commensurate array, which is stable at RT. We will discuss the importance of the cyano-*cis* conformation as a prerequisite for the latter structure as well as the role of the metalated center.

The adsorption of the different molecules was studied by scanning tunneling microscopy (STM) and density functional

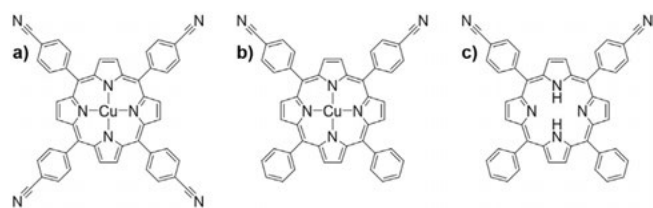


**Figure 1.** Chemical structure of different cyano-functionalized porphyrins: (a) Cu-TCNPP, (b) Cu-*cis*DCNPP, and (c) 2H-*cis*DCNPP.

theory (DFT) calculations. The DFT calculations are based on a modified dispersion correction scheme, which gave very accurate results for binding energies and structures of aromatic molecules on Cu and Ag surfaces in a recent benchmark study.<sup>[18,19]</sup> Details of the methods and the synthesis of the molecules are provided in the Supporting Information.

## Results and Discussion

### Cu-TCNPP on Cu(111):

Figure 2a depicts an STM image of Cu-TCNPP deposited on Cu(111) at RT, with an average coverage of 0.0084 ML (1 ML refers to one adsorbate molecule per surface atom). One can clearly distinguish two prominent molecular ordering patterns, namely a 2D hexagonal honeycomb-type motif and a 1D linear double-row motif. The self-assembled supramolecular ordered islands are often connected to step edges, which indicates that the steps are energetically favored adsorption sites, which act as nucleation centers.<sup>[11e]</sup> While no isolated Cu-TCNPP species could be imaged at RT, we observe clear indications for the existence of very mobile molecules on the surface, for example, attaching and detaching molecules and noisy streaks appearing in the fast scanning direction of the STM. The latter observation is attributed to fast Cu-TCNPP moving molecules, which can be interpreted as a two-dimensional (2D) gas phase.<sup>[11a]</sup> Similar observations have been reported for copper(II)-tetraphenylporphyrin (Cu-TPP) on Cu(111) at RT.<sup>[11a]</sup> In addition to the described behavior, we observe an individual molecule diffusing towards and away from the hexagonal honeycomb-type pattern in Figure 2a (indicated by an arrow; see also Figure S1 in the Supporting Information). This molecule moves along one of the high-symmetry crystallographic directions of the Cu(111) surface and is identified as 2H-TCNPP,<sup>[12b]</sup> which is a residue stemming from the synthesis of Cu-TCNPP. The 2H-TCNPP molecule appears as four bright lobes in the periphery and two dominating protrusions in the center. The diffusion of individual isolated metal-free porphyrins along high-symmetry crystallographic directions at RT is a common observation on Cu(111).<sup>[11b,e]</sup>

In the following, we will discuss the appearance of individual Cu-TCNPP molecules in the two motifs. The molecules in the 1D linear double-row motif are shown in Figure 2b and 2c on enlarged scales; they appear as six distinguishable, clearly recognizable protrusions, which are arranged in two parallel groups of three. By comparison with the chemical structure (c.f. Figure 1a) and STM reports concerning metallo-porphyrins in literature,<sup>[8–11]</sup> the outer four protrusions are assigned to the peripheral phenyl substituents, and the two central ones to the slightly bent up pyrrole groups; this is evident from Figure 2d, where the STM image from Figure 2c is overlaid with a scaled molecule model. The overall intramolecular conformation can be described as saddle-shape conformation with the pyrrole groups tilted out of the macrocyclic plane.<sup>[20]</sup> The elongated depression (dark line) between two parallel groups of three protrusions is referred to as molecular axis; it is aligned

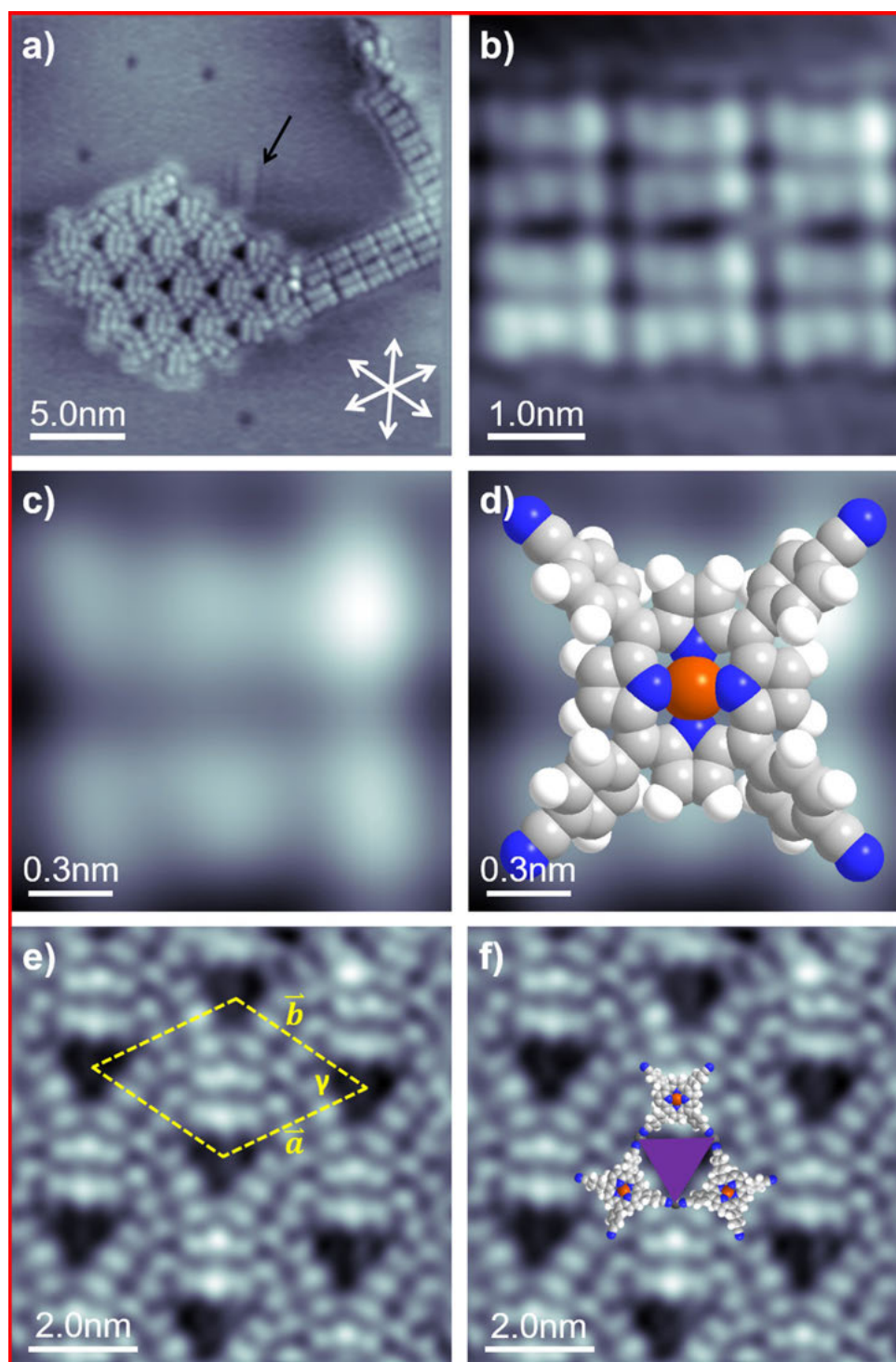


**Figure 2.** (a) Average frame of an STM movie (15 consecutively recorded images) of Cu-TCNPP, deposited and measured at RT, showing a 1D linear parallel motif and a 2D porous hexagonal honeycomb-type motif ( $30 \times 30 \text{ nm}^2$ ,  $U_{\text{bias}} = -1 \text{ V}$ ,  $I_{\text{set}} = 28.8 \text{ pA}$ ). (b) Short 1D parallel molecular chains ( $5 \times 5 \text{ nm}^2$ ,  $U_{\text{bias}} = -1 \text{ V}$ ,  $I_{\text{set}} = 28.8 \text{ pA}$ ). (c) High resolution STM image of a single Cu-TCNPP molecule with six protrusions, which are ascribed to the two iminic pyrrole groups (center) and the 4 phenyl (peripheral) groups ( $1.5 \times 1.5 \text{ nm}^2$ ,  $U_{\text{bias}} = -1 \text{ V}$ ,  $I_{\text{set}} = 28.8 \text{ pA}$ ). (d) Single Cu-TCNPP molecule overlaid with a molecule model ( $1.5 \times 1.5 \text{ nm}^2$ ,  $U_{\text{bias}} = -1 \text{ V}$ ,  $I_{\text{set}} = 28.8 \text{ pA}$ ). (e) STM image of the highly ordered 2D porous honeycomb-type pattern with the lattice vectors of the unit cell indicated as dashed yellow lines, respectively ( $10 \times 10 \text{ nm}^2$ ,  $U_{\text{bias}} = -1 \text{ V}$ ,  $I_{\text{set}} = 29 \text{ pA}$ ). (f) STM image of (e) overlaid with scaled models of Cu-TCNPP molecules.

to one of the high-symmetry crystallographic directions of the Cu(111) substrate.

Generally, the intramolecular conformation of TPPs on a surface is determined by a subtle balance between molecule-sur-

face and molecule-molecule interactions as well as steric forces within the molecule. The saddle-shape conformation is common for TPPs and slightly modified TPPs on a variety of surfaces. In contrast, metal-free 2H-TPP<sup>[21]</sup> and the correspond-

ing cyano-functionalized species 2H-(5-mono-(*p*-cyanophenyl)-(10,15,20-triphenyl)-porphyrin (2H-MCNPP), 2H-*cis*DCNPP, and 2H-TCNPP<sup>[12a,b]</sup> exhibit a very peculiar “inverted” structure on Cu(111), which is characterized by direct N–Cu bonds and two nearly upright pyrrole groups.<sup>[22]</sup>

Next, we analyze the supramolecular arrangement in the 2D hexagonal honeycomb-type motif in detail. Figure 2e shows a high resolution image clearly resolving the sub-molecular features and the highly ordered network with regular triangular pores. The structure can be described with a primitive hexagonal unit cell ( $\gamma = 60^\circ \pm 2^\circ$ ) containing 3 molecules and lattice vectors of  $3.0 \pm 0.15$  nm. In order to further elucidate the supramolecular structure and the intermolecular network, the STM image is overlaid with scaled models of Cu-TCNPP in Figure 2f. From this comparison, it is evident that neighboring cyano groups face each other at the corners of the triangular pores. Notably, the molecules enclosing the triangular pores are aligned along the three high-symmetry crystallographic directions of the Cu(111) surface.

The arrangement of the cyano groups at the corners of the triangular pores indicates that the observed supramolecular network of Cu-TCNPP on Cu(111) is not due to the mutual stabilization via attractive intermolecular interactions, which was proposed for the metal-free 2H-TCNPP on Ag(111).<sup>[12b]</sup> Considering the polarity of the cyano groups, a direct CN–NC interaction is not expected to be energetically favorable. Furthermore, we interpret that the commonly observed T-type and  $\pi$ – $\pi$  intermolecular stacking of porphyrin derivatives are not in line with the relatively large distance of peripheral cyano groups.<sup>[3,4,23]</sup> For the same reasons, we also rule out the known binding interaction for cyano groups, namely, via hydrogen bonds and dipolar coupling.<sup>[4,12d,e,18]</sup>

We rather propose that the terminating C–N groups are linked through native Cu adatoms. Indeed, the lone pair electrons provided by the N atoms of the functionalized cyano

end groups possess high binding affinity towards transition metals.<sup>[24]</sup> This mechanism has been reported frequently for N-terminated organic molecules for metal-organic network formation, since the Cu(111) surface is known to offer adequate native adatoms.<sup>[12d,25]</sup> We suggest that the native adatoms at the corners of the triangles fuse together two porphyrins by cyano-Cu-cyano interactions, and thereby stabilize the ordered 2D porous honeycomb-type networks (for details see DFT calculations below). Three Cu-TCNPP molecules are rotated by  $60^\circ$  with each other forming the regular triangular pores. The fact that the adatoms located at the corners of the triangular cavities are not visible in the STM images has been reported before for 3d-block transition metals within 2D porous networks on metal surfaces.<sup>[12b,d,24,26]</sup>

After analyzing the appearance of individual Cu-TCNPPs and their supramolecular arrangement, we performed annealing experiments to probe the stability of the different phases. Figure 3a shows the STM image acquired at RT after annealing at 400 K. Interestingly, we find a complete transformation to the monomodal appearance of the 2D hexagonal honeycomb-type pattern, with no 1D linear double-row motifs left.

The observation of the extended long-range ordered structure, which is perfectly aligned along the high symmetry directions of the substrate allows for further insights. The perfect alignment and the absence of any moiré pattern is a strong indication that the superstructure is commensurate with the underlying substrate. The driving force likely is that the linking Cu adatoms have a well-defined adsorption site on the Cu(111) surface. In Figure 3b, we depicted a structural model, which is based on the STM image in Figure 3a, and on the detailed DFT calculations presented below. Note that since we are not able to determine the exact positions of the Cu-TCNPP molecules on the Cu(111) lattice from our STM images, this information solely stems from the calculations. The primitive hexagonal unit cell corresponds to a  $(7\sqrt{3} \times 7\sqrt{3})R30^\circ$  superstructure,

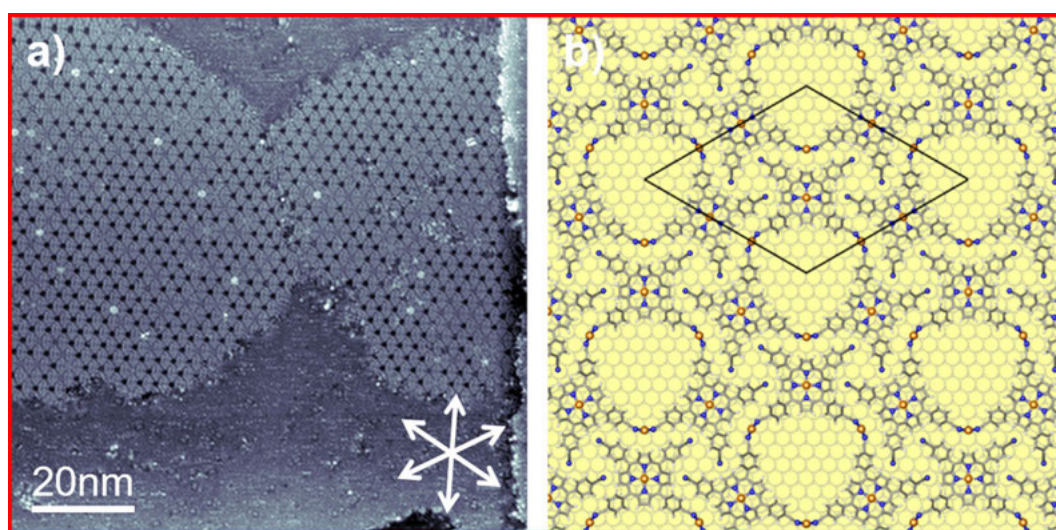


**Figure 3.** (a) A  $100 \times 100$  nm<sup>2</sup> STM image depicts the full monomodal transformation of Cu-TCNPP after annealing at 400 K ( $U_{\text{bias}} = -1$  V,  $I_{\text{set}} = 30$  pA); the high-symmetry crystallographic  $\langle 110 \rangle$  substrate directions are indicated as white double arrows. (b) DFT-optimized structure of the porous honeycomb-type network showing a hexagonal  $(7\sqrt{3} \times 7\sqrt{3})R30^\circ$  superstructure, in which the molecules are linked through Cu adatoms on Cu(111).

with a length of the lattice vector of 3.09 nm. In this structure, the porphyrins adsorb on bridge sites and the connecting Cu adatoms occupy threefold hollow sites (see below).

Further annealing to 450 K results in a loss of the long-range ordered structure, and the observation of randomly oriented individual molecules, which display four pronounced protrusions; see Figure S2 in the Supporting Information. We tentatively assign our observations to the formation of intramolecular C–C bonds between the phenyl groups and the porphyrin core, after dehydrogenation of the corresponding carbon atoms.<sup>[11a]</sup> Similar reactions have been proposed for 2H-TTP on Ag(111) after heating to above 525 K,<sup>[6b,27]</sup> for 2H-TTP on Cu(111)<sup>[28]</sup> and for 2H-TCNPP on Pd/Cu(111).<sup>[29]</sup> Moreover, from STM, we find that there is no long-range order any more, but most of the reacted molecules are still aligned along one of the high symmetry substrate directions. This likely is due to specific interactions of the cyano groups with the substrate Cu atoms.

#### Cu-*cis*DCNPP on Cu(111):

To gain deeper insight into the formation of 2D porous networks and in particular into the role of the cyano-functionalized phenyl groups, we varied the number of cyano-functionalized substitutions from four to two in *cis*-configuration. Figure 4a depicts an STM image of Cu-*cis*DCNPP deposited and measured at RT on Cu(111) with an average coverage of 0.0067 ML. We observe characteristic structures with one or more pores, which show a large similarity to the 2D hexagonal honeycomb-type motif observed for Cu-TCNPP (see above). We distinguish triangular “monoflakes” with one pore, “biflakes” with two pores and “multiflakes” with more than 2 pores. The molecularly resolved image of a monoflake in Figure 4b shows that the individual molecules within the flakes are characterized by two parallel elongated protrusions, which indicates a saddle-shape conformation,<sup>[21b]</sup> identical to that proposed for Cu-TCNPP. Notably, also a small number of monomers and dimers are visible, which are assigned to metal-free 2H-*cis*DCNPP molecules, which are most likely present in the Cu-*cis*DCNPP material as residues of the synthesis process.

In Figure 4c, the STM image of the monoflake shown in Figure 4b is superimposed with scaled models of Cu-*cis*DCNPP. Three molecules, rotated to each other by 60°, form the central triangular pore of the monoflake. From the tentative overlay, it becomes apparent that the neighboring cyano groups face each other at the corners of the triangular pore, which is the identical arrangement as for Cu-TCNPP (see above). Again, the three sides of the triangular pores reflect the three main high-symmetry crystallographic directions of Cu(111). Along the lines discussed for Cu-TCNPP, we propose that native Cu adatoms from the substrate stabilize the structure through local CN-Cu-NC motifs.

As a next step, we annealed the adsorbed layer to 400 K for 60 min. Figure 4d depicts the STM image acquired at RT after annealing. Interestingly, the triangular porous “monoflakes”, “biflakes” and “multiflakes” are not observed anymore, but instead have undergone a transformation towards a long-range-

ordered 2D porous hexagonal honeycomb-type pattern. Its structure is within the margins of error identical to the one observed for Cu-TCNPP. The comparison to Figure 3a shows smaller domains, with areas of uncovered substrate in between. This observation is likely due to the low mobility of the larger flakes, which serve as nucleation centers for the larger long-range-ordered domains. Interestingly, all pores in Figure 4d and 4e are empty, which is in contrast to Figure 3a, where some of the pores are filled by unidentified contaminations, which could originate from the synthesis process.

#### 2H-*cis*DCNPP on Cu(111):

To obtain further information on the formation of the observed long-range ordered porous networks and in particular to evaluate the role of the central Cu atom, we also studied the adsorption of the metal-free 2H-*cis*DCNPP on Cu(111) at RT with an average coverage of 0.0168 ML. Figure 5a depicts an STM image of 2H-*cis*DCNPP deposited and measured at RT on Cu(111). The molecules do not form any long-range ordered network, but are adsorbed as individual species. Each molecule appears as four bright lobes in the periphery, and two dominating protrusions in the center; the latter are hardly resolved and mostly appear as one longish protrusion. The molecular appearance and the general adsorption behavior is very similar to that of 2H-TCNPP on Cu(111),<sup>[12b]</sup> where the intramolecular conformation is described by the so-called “inverted” structure.<sup>[21b]</sup> In this structure, two opposite pyrrole rings are oriented perpendicular to the Cu surface, yielding the two bright central protrusions in the sub-molecularly resolved STM image, similar as seen in Figure 5a. The molecules are aligned along one of the high-symmetry crystallographic directions of the substrate, which is due to a strong attractive site-specific interaction between the iminic nitrogens of the macrocycle and the Cu atoms of the Cu(111) surface.<sup>[21]</sup> In a previous study of 2H-*cis*DCNPP on Cu(111) at much lower coverages, but otherwise similar conditions, the formation of dimers connected through native Cu adatoms was reported, along with self-metalation at 400 K.<sup>[12a]</sup> At the high coverage studied here, we do observe some dimers, but neither extended 1D chains nor 2D porous networks are evident.

As a next step, we annealed the adsorbed layer to 400 K for 300 min. After heating, we observe almost complete transformation of the individually adsorbed molecules into a perfectly ordered 2D hexagonal honeycomb-type porous structure, as depicted in Figure 5b. Obviously, the prolonged heating step leads to the formation of this thermodynamically more favorable long-range ordered structure. Notably, within the islands no single defect or adsorbed contaminations are observed. In the sub-molecularly resolved image in Figure 5c, the molecules appear as six clearly distinguishable protrusions, which are arranged in two parallel rows of three protrusions. This appearance is identical to that observed for Cu-TCNPP (see Figure 2), which is a strong indication that upon heating self-metalation of 2H-*cis*DCNPP with Cu atoms from the Cu(111) surface occurred, yielding Cu-*cis*DCNPP.<sup>[11a,e,30]</sup>

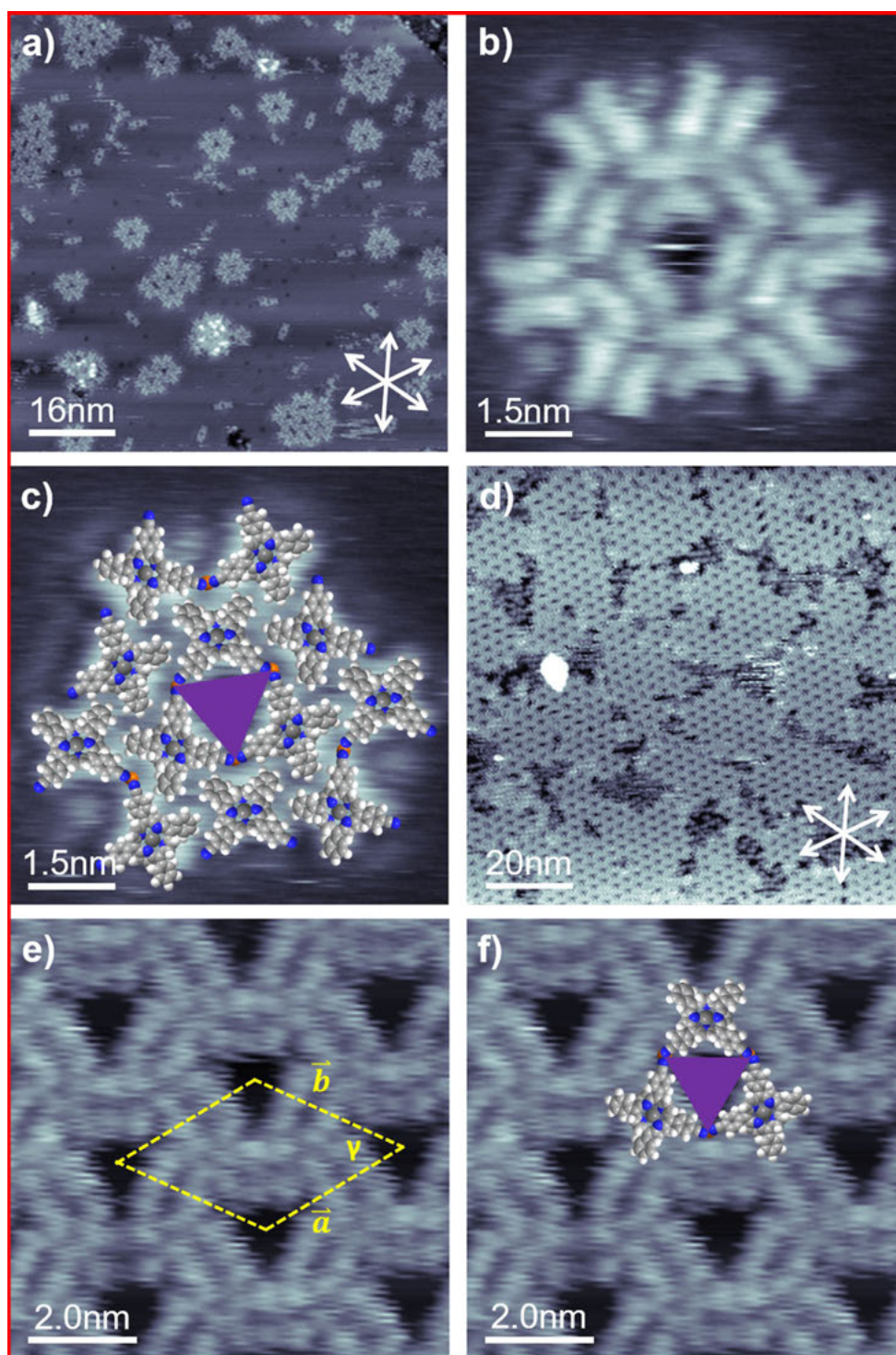


**Figure 4.** (a) A  $80 \times 80 \text{ nm}^2$  STM image showing Cu-*cis*DCNPP deposited and measured at RT ( $U_{\text{bias}} = -1.02 \text{ V}$ ,  $I_{\text{set}} = 28.8 \text{ pA}$ ). (b, c) High resolution STM image showing a monoflake with molecular model superimposed ( $7.5 \times 7.5 \text{ nm}^2$ ,  $U_{\text{bias}} = -1.02 \text{ V}$ ,  $I_{\text{set}} = 28.8 \text{ pA}$ ). (d) A  $100 \times 100 \text{ nm}^2$  STM image depicts 2D porous network formation after a 400 K annealing step ( $U_{\text{bias}} = -1.01 \text{ V}$ ,  $I_{\text{set}} = 29.5 \text{ pA}$ ). (e, f) Close-up STM image with unit cell and tentative molecule model overlaid ( $10 \times 10 \text{ nm}^2$ ,  $U_{\text{bias}} = -1.02 \text{ V}$ ,  $I_{\text{set}} = 28.8 \text{ pA}$ ).

The detailed analysis of the molecularly resolved STM images in Figure 5c reveals that the ordered 2D network has the identical structure with triangular pores as described above for Cu-*cis*DCNPP and Cu-TCNPP, within the margin of error. The STM image overlaid with scaled models of Cu-

*cis*DCNPP molecules in Figure 5d shows that neighboring cyano groups face each other at the corners of the triangular pore. Again, three molecules rotated by  $60^\circ$  to each other and oriented along the three main high-symmetry crystallographic directions of Cu(111) form the triangular pores. In analogy to

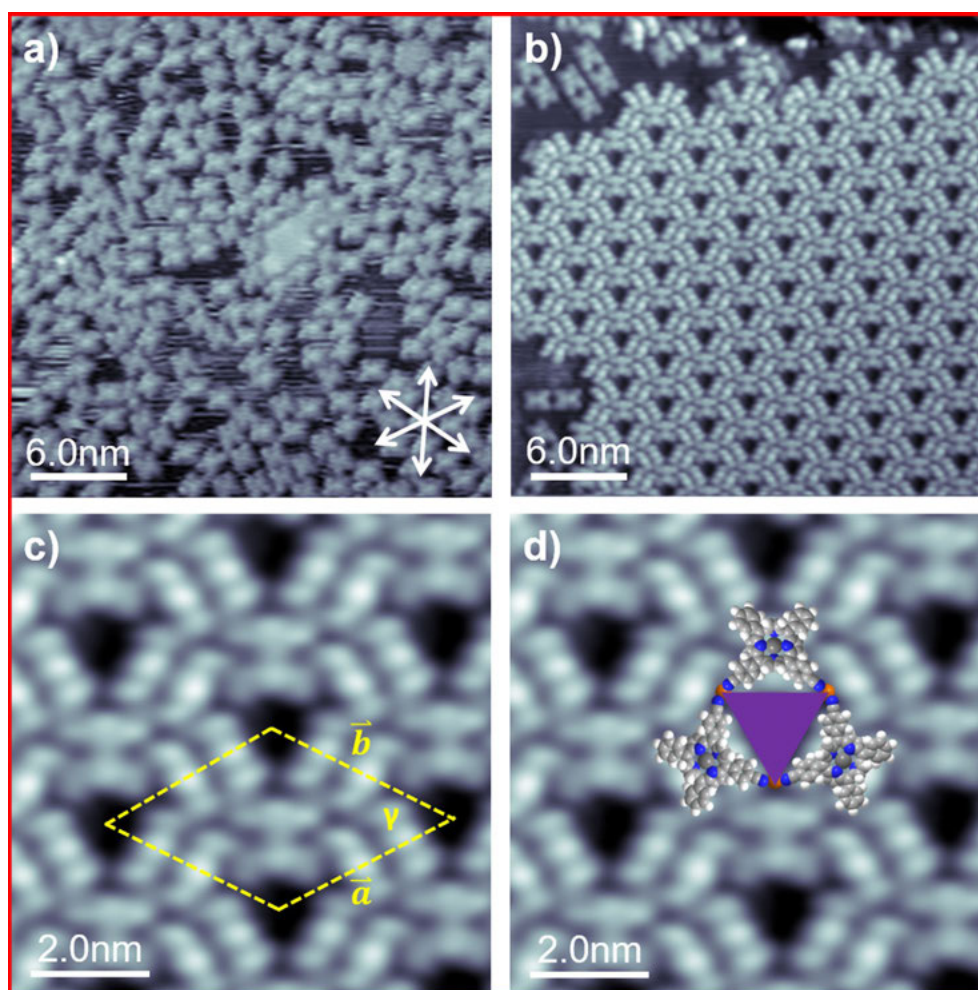


**Figure 5.** (a) A  $40 \times 40 \text{ nm}^2$  STM image showing 2H-*cis*DCNPP deposited and measured at RT ( $U_{\text{bias}} = -1 \text{ V}$ ,  $I_{\text{set}} = 30.3 \text{ pA}$ ). (b) Annealing at 400 K results in conversion of 2H-*cis*DCNPP into Cu-*cis*DCNPP ( $30 \times 30 \text{ nm}^2$ ,  $U_{\text{bias}} = -1.22 \text{ V}$ ,  $I_{\text{set}} = 29.4 \text{ pA}$ ). (c, d) Close-up STM image with unit cell and tentative molecule model overlaid ( $10 \times 10 \text{ nm}^2$ ,  $U_{\text{bias}} = -1.22 \text{ V}$ ,  $I_{\text{set}} = 29.4 \text{ pA}$ ).

the observations for Cu-*cis*DCNPP and Cu-TCNPP, we propose that the driving force for the formation of the observed porous pattern is a linking through native adatoms at the corners of the triangular pore, that is, the Cu-*cis*DCNPP molecules fuse together by CN-Cu-NC interactions as illustrated in Figure 5d.

Notably, 2H-TCNPP on Cu(111)<sup>[12b]</sup> did not show the transition to the porous structure upon annealing at elevated temperatures, which was observed here for 2H-*cis*DCNPP. This behavior is attributed to the significantly larger activation barrier for metalation for 2H-TCNPP.<sup>[12a]</sup>

### Theoretical calculations

To analyze the driving forces that lead to the formation of the porous hexagonal honeycomb-type structure of the adsorbed porphyrins, we performed extensive density functional theory (DFT) calculations. In a first series of calculations, we determined the preferred adsorption site of the CN-functionalized Cu porphyrins on the Cu(111) surface. The corrugation of the energy landscape, which is obtained when a Cu porphyrin is

translated over the surface, is rather weak (about 0.35 eV in the case of Cu-TPP, see Figure S5b in the Supporting Information), which leads to fast diffusion on Cu(111), as observed by STM. Nevertheless, there is one single site, which is clearly preferred by the porphyrins, independent of a CN functionalization. This site is determined by the interaction of the N atoms of the porphyrin core with Cu atoms of the substrate. The central porphyrin Cu atom is in a bridging position and the N atoms are roughly on-top of surface Cu atoms (see Figure 6). This position of the porphyrin core simultaneously guarantees that terminal CN groups point to on-top sites of the Cu(111) surface (see Figure 6b, c and Figure S6a, b). Only the on-top sites show an attractive interaction with the CN groups, the hollow and the bridge sites are repulsive.<sup>[12b]</sup> Furthermore, Figures S6c, d and S7b, c demonstrate that the terminal CN groups can easily incorporate Cu adatoms, which sit preferentially in fcc or hcp hollow sites.

All Cu porphyrins with and without CN functionalization maintain their gas-phase saddle-shape configuration upon adsorption on Cu(111). The downward-tilted pyrrole rings give rise to a dark line in the STM contrast. The calculations predict

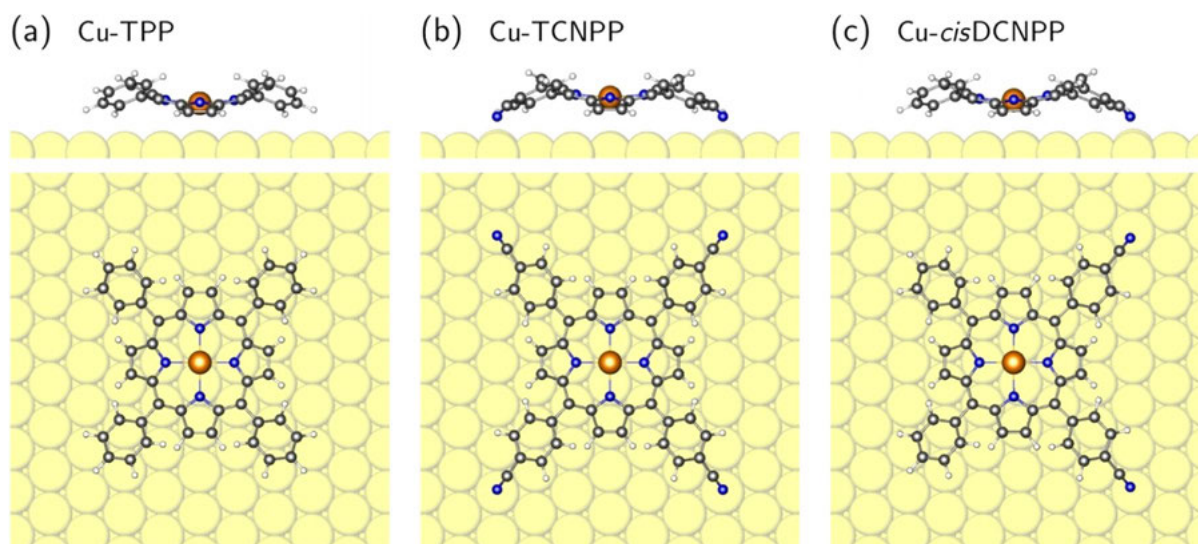


**Figure 6.** Side and top view of the relaxed structure of (a) Cu-TPP, (b) Cu-TCNPP and (c) Cu-*cis*DCNPP molecules on Cu(111) at their most favorable adsorption sites. In all cases, the saddle shape of the porphyrin is visible. The downward-tilted pyrrole rings (with slightly higher N atoms) are oriented along the densely-packed Cu rows. Cu, C, N and H atoms are shown in yellow, black, blue and white, respectively. The same color code is used in all figures.

that in the preferred orientation of the Cu porphyrins the dark line is aligned with the densely-packed Cu rows, which is in agreement with the experimental STM observation (see Figure 2c).

Next we performed a detailed analysis of the molecule-molecule interactions of the porphyrin molecules on the Cu(111) surface. Six configurations of Cu porphyrin molecules with and without CN functionalization as well as with and without Cu adatoms were considered, which will be discussed in the following step-by-step. Calculations were done with a  $(7\sqrt{3} \times 7\sqrt{3})R30^\circ$  surface unit cell containing three Cu porphyrin molecules. The experimentally observed honeycomb-type structure is characterized by two different types of molecular contacts: three molecules form a triangle with a large pore in the middle and CN groups facing each other at the corners. Subsequently, the triangles are densely packed and their outer rim connect in another triangular motif, in which the phenyl rings are roughly oriented in a T-shaped stacking (see Figure S8 in the Supporting Information). In the following we will refer to these two types of molecule-molecule interactions as the “pore” and the triangular “rim” contact.

The first important observation is that three porphyrin molecules can be arranged in a  $(7\sqrt{3} \times 7\sqrt{3})R30^\circ$  unit cell in such a way that (1) the pore and rim contacts proposed by the analysis of the STM images can be established, (2) the structure maintains a 3-fold symmetry and, most important, (3) all porphyrins adopt their preferred adsorption site, thereby gaining the largest possible adsorption energy.

We start by building this structure with the non-functionalized Cu-TPP porphyrins without CN groups (Figure 7a, c, structure 1; this structure is calculated as a hypothetical reference to evaluate the contributions of the different interactions). The centers of the pore and the triangular rim contact are hollow sites on the Cu(111) surface (see Figure 7a, c and Figure S8 in the Supporting Information). Without the terminal CN, the

pore is “open”, i.e., the phenyl rings are far enough apart that they do not interact. On the other hand, the rim contact is fully “closed” (see Figure 7a, c), i.e., the distance between the Cu-TPPs on Cu(111) (measured between the central Cu atoms) of 16.265 Å is close to the gas-phase value of 15.385 Å, which was obtained by a structure optimization of the Cu-TPP triangle without substrate (note that in the gas-phase calculation the phenyl rings are more upright-oriented with respect to the porphyrin plane than on the surface, which allows the molecules to come closer together).

By comparing the binding energy per molecule of this structure with the value for the single, well-separated molecule we can determine the strength of the molecule-molecule interaction  $E_{\text{int}}^{\text{rim}}$  for the rim contact. Since no “pore interaction” is present,  $E_{\text{int}}^{\text{rim}}$  is given by the difference  $\Delta E_b$  of the two binding energies. The rim interaction is attractive with about 0.11 eV per molecule (see Table 1). Since we do not observe that the Cu-TPP molecules are pulled out of their bridge position, the dispersion interaction across the rim is close to its optimum

**Table 1.** Calculated binding energy  $E_b^{\text{layer}}$  per molecule of Cu porphyrins on Cu(111) for the 6 porous honeycomb-type structures discussed in the text. All calculations were done with a  $(7\sqrt{3} \times 7\sqrt{3})R30^\circ$  unit cell containing three porphyrin molecules.  $E_b^{\text{single}}$  is the binding energy of a single, well-separated porphyrin molecule as given in Table S1. The difference  $\Delta E_b$  between the two binding energies describes the on-surface molecule-molecule interaction.

Porphyrin	$E_b^{\text{layer}}$ [eV]	$E_b^{\text{single}}$ [eV]	$\Delta E_b$ [eV]
1: Cu-TPP	3.50	3.39	+0.11
2: Cu- <i>cis</i> DCNPP	3.61	3.60	+0.01
3: Cu- <i>cis</i> DCNPP	3.68	3.60	+0.08
4: Cu-TCNPP	3.67	3.79	−0.12
5: Cu- <i>cis</i> DCNPP + Cu <sub>ad</sub>	4.06	3.44	+0.62
6: Cu-TCNPP + Cu <sub>ad</sub>	4.17	3.69	+0.48

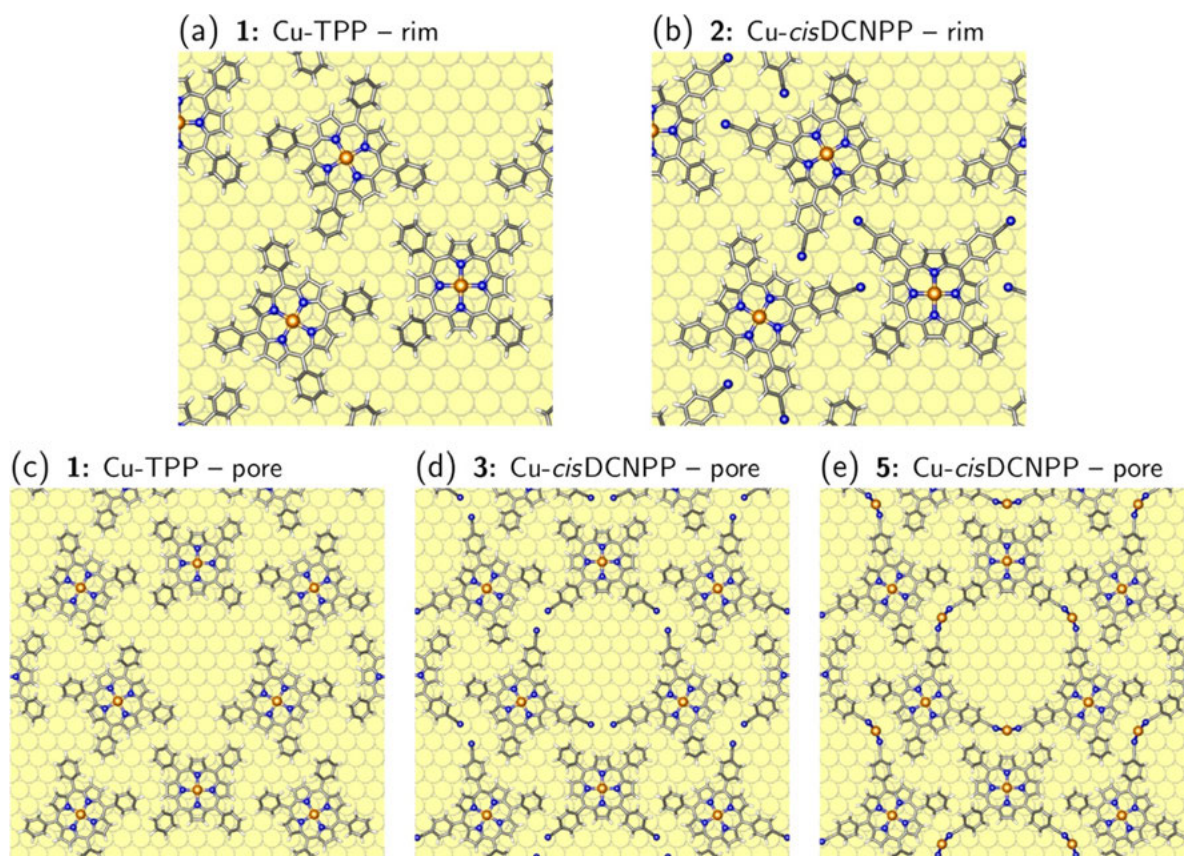


**Figure 7.** Atomic structure of the triangular contact at the rim, (a) without and (b) with terminal CN groups. (c) Open pore structure, (d) with terminal CN groups interacting with neighboring Cu atoms of the substrate, and (e) with terminal CN groups connected by Cu adatoms.

and cannot be increased further by bringing the Cu-TPP molecules closer together.

The next three structures 2–4 were obtained by adding CN groups to structure 1 (see Figure S9). Structure 2 consists of Cu-*cis*DCNPPs with CN groups in the rim area while still maintaining an “open” pore (see Figure 7b). The N atoms of the terminal CN groups coordinate to surface Cu atoms as in the case of well-separated adsorbates (see Figure 6b) and do not establish hydrogen bonds with the neighboring pyrrole rings. The lower-lying CN groups basically do not interact with the higher-lying pyrrole rings of the neighboring molecules. Consequently, the binding energy per molecule in the network structure is basically unchanged compared to the isolated adsorbate (i.e.  $\Delta E_b$  is almost zero, see Table 1). This shows that the same packing of “pore triangles” can be achieved with and without CN groups at the outer rim.

Structure 3 is also built of Cu-*cis*DCNPPs, but now the CN groups are pointing to the pore (see Figure 7d and Figure S9). These CN groups connect to neighboring Cu atoms on the Cu(111) surface. In previous studies, it was speculated that such an adsorption on neighboring sites could lead to an attractive interaction induced by a small lift of the Cu atoms out of the surface plane.<sup>[31]</sup> However, in our previous calculations<sup>[12b]</sup> we could not confirm the presence of an attractive interaction but found a small repulsion instead. Also here, the inspection of the binding energies points toward the absence of

a significant attractive interaction between neighboring CN-Cu sites. Structure 3 exhibits the same rim contact as structure 1 together with a pore contact consisting of terminal CN groups interacting with neighboring substrate Cu sites. The rim contact should give at least the same gain in binding energy  $\Delta E_b$  of 0.11 eV as observed in structure 1. However, for structure 3 we only observe a gain of 0.08 eV (see Table 1). The difference of 0.03 eV per Cu-*cis*DCNPP molecule stems from the pore interaction and is repulsive.

The absence of a significant attractive interaction of CN–Cu contacts involving neighboring Cu surface sites is furthermore demonstrated by repeating the calculations of the structural motif 3 with a larger ( $8\sqrt{3} \times 8\sqrt{3}$ )R30° unit cell, in which we can systematically open and close the pore and the rim contact (see Figure S10). No significant change in energy is observed when the CN–Cu sites are pulled apart by one Cu–Cu distance.

Also structure 4 (Figure S9d) of the porphyrins with four terminal CN groups (Cu-TCNPP) indicates a repulsive interaction for the pore contact. The binding energy per molecule is reduced with respect to the separated molecules. In the first place, the rim contact has become slightly repulsive since the porphyrins cannot be displaced anymore from their bridge sites (compare to structure 2 in Figure 7b and d), but obviously this is not compensated by a strong attractive pore interaction.

In summary, in the triangular pore motif, a strong repulsion between facing CN groups of neighboring porphyrin molecules is avoided by a bending-down of the CN groups and the formation of CN–Cu contacts with neighboring Cu surface atoms. However, this binding motif does not lead to a significant attractive interaction between the porphyrins. The experimentally observed dominant formation of the triangular pore structure and its thermal stability therefore cannot be explained by this binding motif.

On the other hand, Cu adatoms can mediate a strong attraction. If Cu adatoms are added to structure **3** (the result is structure **5**, see Figure 7e and Figure S11), the binding energy per molecule increases by 0.65 eV compared to separated molecules (see Table 1). Subtracting the contribution of the rim contact of 0.11 eV (see structure **1**), we find a strong attractive pore interaction of 0.54 eV per molecule. The origin of the attraction is that now two instead of only one CN group connect to a Cu adatom (or, in other words, less Cu adatoms for a given number of CN groups have to be created). The strong attractive pore interaction is also confirmed by adding Cu adatoms to structure **4** (giving structure **6**; see Figure 3b), where we find a value of 0.48 eV for the molecule-molecule interaction in the pore (assuming that the rim interaction is about zero, see structure **2**).

The overall larger binding energy for the network structures with Cu adatoms also implies that they are the thermodynamic ground state. This is in contrast to single molecules, where the DFT calculations predict a decomposition of adatom structures into molecules adsorbed on the terrace and a condensation of the Cu atoms at zero temperature (see Supporting Information).

## Conclusions

We investigated the adsorption of three related cyano-functionalized tetraphenyl porphyrin derivatives on Cu(111) by scanning tunneling microscopy (STM) in ultra-high vacuum (UHV) combined with detailed density functional theory (DFT) calculations. The goal was to identify the role of the cyano group and the central Cu atom for the intermolecular and supramolecular arrangement. The porphyrin derivatives studied were Cu-TCNPP, Cu-*cis*DCNPP, and 2H-*cis*DCNPP. Cu-TCNPP, with four cyano groups, forms a hexagonal honeycomb-type pattern with triangular pores, which coexists with 1D molecular double chains at room temperature (RT). Annealing to 400 K yields a complete transformation to a hexagonal honeycomb-type structure with pronounced long-range order. Cu-*cis*DCNPP, with two cyano groups in “*cis*” position, forms monoflakes with a triangular pore, along with bi- and multiflakes at RT, which all transform to the hexagonal honeycomb-type structure at 400 K. The metal-free 2H-*cis*DCNPP shows no order at RT, but self-metalates upon heating to 400 K and transforms into the same perfectly ordered hexagonal honeycomb-type structure as the other two porphyrins. The ordered flakes and the hexagonal honeycomb-type structures all contain the same structure-forming element, namely triangles of porphyrins fused together by cyano-Cu-cyano interactions with native

Cu adatoms. These three molecules are rotated to each other by 60° and are aligned parallel to the substrate high-symmetry directions; this alignment is enforced by the preferential adsorption arrangement of the porphyrins and it is stabilized by the linking Cu adatoms at threefold sites at the corners of the pores. These site-specific interactions with the Cu surface also make the long-range ordered structure commensurate. The DFT calculations provide detailed insights into the various energetic contributions that lead to the observed long-range ordered hexagonal honeycomb-type structure with triangular pores. Looking at the internal structure of the unit cell, one gets the impression that interactions of the other two porphyrin ligands (with CN groups for Cu-TCNPP, and without CN ligands for Cu-*cis*DCNPP and 2H-*cis*DCNPP) do not play a major role for the formation of the long-range order. This finding leads us to suggest that the twofold cyano-functionalized porphyrin with “*cis*” conformation is the minimum prerequisite to form a highly ordered 2D porous molecular pattern that might grant protocols as a nanoscaled template. To conclude, our findings suggest that the cyano groups as functional groups participate in directed attractive interactions, which will allow for the rational design and construction of a wide range of nano-scaled supramolecular architectures adsorbed to surfaces.

## Acknowledgements

The authors gratefully acknowledge funding by the German Research Foundation (DFG) through Research Unit FOR 1878 (funCOS) and the Collaborative Research Center SFB 953 (project number 182849149) at the Friedrich-Alexander-Universität Erlangen-Nürnberg. Open access funding enabled and organized by Projekt DEAL.

## Conflict of interest

The authors declare no conflict of interest.

**Keywords:** coordinated networks · cyano functionalization · density functional theory calculations · porphyrins · scanning tunneling microscopy

- [1] S. Anderson, H. L. Anderson, A. Bashall, M. McPartlin, J. K. Sanders, *Angew. Chem. Int. Ed.* **1995**, *34*, 1096–1099; *Angew. Chem.* **1995**, *107*, 1196–1200.
- [2] a) J. V. Barth, J. Weckesser, C. Cai, P. Günter, L. Bürgi, O. Jeandupeux, K. Kern, *Angew. Chem. Int. Ed.* **2000**, *39*, 1230–1234; *Angew. Chem.* **2000**, *112*, 1285–1288; b) A. Llanes-Pallas, M. Matena, T. Jung, M. Prato, M. Stöhr, D. Bonifazi, *Angew. Chem. Int. Ed.* **2008**, *47*, 7726–7730; *Angew. Chem.* **2008**, *120*, 7840–7844; c) J. A. Theobald, N. S. Oxtoby, M. A. Phillips, N. R. Champness, P. H. Beton, *Nature* **2003**, *424*, 1029.
- [3] S. Beniwal, S. Chen, D. Kunkel, J. Hooper, S. Simpson, E. Zurek, X. C. Zeng, A. Enders, *Chem. Commun.* **2014**, *50*, 8659–8662.
- [4] T. Yokoyama, S. Yokoyama, T. Kamikado, Y. Okuno, S. Mashiko, *Nature* **2001**, *413*, 619.
- [5] J. V. Barth, *Surf. Sci.* **2009**, *603*, 1533–1541.
- [6] a) W. Auwärter, K. Seufert, F. Bischoff, D. Eciija, S. Vijayaraghavan, S. Joshi, F. Klappenberger, N. Samudrala, J. V. Barth, *Nat. Nanotechnol.* **2012**, *7*, 41; b) A. Wiengarten, J. A. Lloyd, K. Seufert, J. Reichert, W.

- Auwärter, R. Han, D. A. Duncan, F. Allegretti, S. Fischer, S. C. Oh, *Chem. Eur. J.* **2015**, *21*, 12285–12290.
- [7] L. Zhang, M. Lepper, M. Stark, T. Menzel, D. Lungerich, N. Jux, W. Hieringer, H.-P. Steinrueck, H. Marbach, *Phys. Chem. Chem. Phys.* **2017**, *19*, 20281–20289.
- [8] W. Auwärter, D. Ćija, F. Klappenberger, J. V. Barth, *Nat. Chem.* **2015**, *7*, 105.
- [9] I. Fleming, *Nature* **1967**, *216*, 151.
- [10] C. E. Castro, *J. Theor. Biol.* **1971**, *33*, 475–490.
- [11] a) J. Xiao, S. Ditze, M. Chen, F. Buchner, M. Stark, M. Drost, H.-P. Steinrück, J. M. Gottfried, H. Marbach, *J. Phys. Chem. C* **2012**, *116*, 12275–12282; b) S. Ditze, M. Stark, M. Drost, F. Buchner, H. P. Steinrück, H. Marbach, *Angew. Chem. Int. Ed.* **2012**, *51*, 10898–10901; *Angew. Chem.* **2012**, *124*, 11056–11059; c) M. Stark, S. Ditze, M. Drost, F. Buchner, H.-P. Steinrück, H. Marbach, *Langmuir* **2013**, *29*, 4104–4110; d) M. Röckert, S. Ditze, M. Stark, J. Xiao, H.-P. Steinrück, H. Marbach, O. Lytken, *J. Phys. Chem. C* **2014**, *118*, 1661–1667; e) H. Marbach, *Acc. Chem Res.* **2015**, *48*, 2649–2658.
- [12] a) M. Lepper, J. Köbl, L. Zhang, M. Meusel, H. Hölzel, D. Lungerich, N. Jux, A. de Siervo, B. Meyer, H. P. Steinrück, *Angew. Chem. Int. Ed.* **2018**, *57*, 10074–10079; *Angew. Chem.* **2018**, *130*, 10230–10236; b) M. Lepper, T. Schmitt, M. Gurrath, M. Raschmann, L. Zhang, M. Stark, H. Hölzel, N. Jux, B. Meyer, M. A. Schneider, *J. Phys. Chem. C* **2017**, *121*, 26361–26371; c) J. Reichert, M. Marschall, K. Seufert, D. Ćija, W. Auwärter, E. Arras, S. Klyatskaya, M. Ruben, J. V. Barth, *J. Phys. Chem. C* **2013**, *117*, 12858–12863; d) L. A. Fendt, M. Stöhr, N. Wintjes, M. Enache, T. A. Jung, F. Diederich, *Chem. Eur. J.* **2009**, *15*, 11139–11150; e) M. Stöhr, S. Boz, M. Schär, M. T. Nguyen, C. A. Pignedoli, D. Passerone, W. B. Schweizer, C. Thilgen, T. A. Jung, F. Diederich, *Angew. Chem. Int. Ed.* **2011**, *50*, 9982–9986; *Angew. Chem.* **2011**, *123*, 10158–10162.
- [13] a) Q. Fan, C. Wang, L. Liu, Y. Han, J. Zhao, J. Zhu, J. Kuttner, G. Hilt, J. M. Gottfried, *J. Phys. Chem. C* **2014**, *118*, 13018–13025; b) C. Steiner, Z. Yang, B. D. Gliemann, U. Meinhardt, M. Gurrath, M. Ammon, B. Meyer, M. Kivala, S. Maier, *Chem. Commun.* **2018**, *54*, 11554–11557; c) Z. Tao, T. Wang, D. Wu, L. Feng, J. Huang, X. Wu, J. Zhu, *Chem. Commun.* **2018**, *54*, 7010–7013.
- [14] L. Piot, D. Bonifazi, P. Samori, *Adv. Funct. Mater.* **2007**, *17*, 3689–3693.
- [15] M. Lackinger, W. M. Heckl, *Langmuir* **2009**, *25*, 11307–11321.
- [16] V. Iancu, K.-F. Braun, K. Schouteden, C. Van Haesendonck, *Langmuir* **2013**, *29*, 11593–11599.
- [17] S. Gottardi, K. Müller, J. C. Moreno-López, H. Yildirim, U. Meinhardt, M. Kivala, A. Kara, M. Stöhr, *Adv. Mater. Interfaces* **2014**, *1*, 1300025.
- [18] B. P. Klein, J. M. Morbec, M. Franke, K. K. Greulich, M. Sachs, S. Parhizkar, F. C. Bocquet, M. Schmid, S. J. Hall, R. J. Maurer, B. Meyer, R. Tonner, C. Kumpf, P. Kratzer, J. M. Gottfried, *J. Phys. Chem. C* **2019**, *123*, 29219–29230.
- [19] S. R. Kachel, B. P. Klein, J. M. Morbec, M. Schöniger, M. Hutter, M. Schmid, P. Kratzer, B. Meyer, R. Tonner, J. M. Gottfried, *J. Phys. Chem. C* **2020**, *124*, 8257–8268.
- [20] a) A. Weber-Bargioni, W. Auwärter, F. Klappenberger, J. Reichert, S. Leffrancois, T. Strunskus, C. Wöll, A. Schiffrin, Y. Pennec, J. V. Barth, *ChemPhysChem* **2008**, *9*, 89–94; b) J. Brede, M. Linares, S. Kuck, J. Schwöbel, A. Scarfato, S.-H. Chang, G. Hoffmann, R. Wiesendanger, R. Lensen, P. H. Kouwer, *Nanotechnology* **2009**, *20*, 275602.
- [21] a) F. Albrecht, F. Bischoff, W. Auwärter, J. V. Barth, J. Repp, *Nano Lett.* **2016**, *16*, 7703–7709; b) M. Lepper, J. Köbl, T. Schmitt, M. Gurrath, A. de Siervo, M. A. Schneider, H.-P. Steinrück, B. Meyer, H. Marbach, W. Hieringer, *Chem. Commun.* **2017**, *53*, 8207–8210.
- [22] J. C. Moreno-López, D. J. Mowbray, A. Perez Paz, R. C. de Campos Ferreira, A. Ceccatto dos Santos, P. Ayala, A. de Siervo, *Chem. Mater.* **2019**, *31*, 3009–3017.
- [23] a) M. Lepper, L. Zhang, M. Stark, S. Ditze, D. Lungerich, N. Jux, W. Hieringer, H.-P. Steinrück, H. Marbach, *J. Phys. Chem. C* **2015**, *119*, 19897–19905; b) S. Grimme, *Angew. Chem. Int. Ed.* **2008**, *47*, 3430–3434; *Angew. Chem.* **2008**, *120*, 3478–3483.
- [24] N. Henningsen, R. Rurali, C. Limbach, R. Drost, J. Pascual, K. Franke, *J. Phys. Chem. Lett.* **2011**, *2*, 55–61.
- [25] D. Heim, D. Ćija, K. Seufert, W. Auwärter, C. Aurisicchio, C. Fabbro, D. Bonifazi, J. V. Barth, *J. Am. Chem. Soc.* **2010**, *132*, 6783–6790.
- [26] B. D. Baker Cortés, N. Schmidt, M. Enache, M. Stöhr, *J. Phys. Chem. C* **2019**, *123*, 19681–19687.
- [27] G. Di Santo, S. Blankenburg, C. Castellarin-Cudia, M. Fanetti, P. Borghetti, L. Sangaletti, L. Floreano, A. Verdini, E. Magnano, F. Bondino, *Chem. Eur. J.* **2011**, *17*, 14354–14359.
- [28] M. Röckert, M. Franke, Q. Tariq, S. Ditze, M. Stark, P. Uffinger, D. Wechsler, U. Singh, J. Xiao, H. Marbach, *Chem. Eur. J.* **2014**, *20*, 8948–8953.
- [29] A. Ceccatto dos Santos, R. C. de Campos Ferreira, J. C. Moreno-López, L. Barreto, M. Lepper, R. Landers, H.-P. Steinrück, H. Marbach, A. de Siervo, *Chem. Mater.* **2020**, *32*, 2114–2122.
- [30] M. Stark, S. Ditze, M. Lepper, L. Zhang, H. Schlott, F. Buchner, M. Röckert, M. Chen, O. Lytken, H.-P. Steinrück, *Chem. Commun.* **2014**, *50*, 10225–10228.
- [31] T.-C. Tseng, C. Urban, Y. Wang, R. Otero, S. L. Tait, M. Alcamí, D. Ćija, M. Trelka, J. M. Gallego, N. Lin, *Nat. Chem.* **2010**, *2*, 374–379.

Manuscript received: April 23, 2020

Accepted manuscript online: June 23, 2020

Version of record online: September 17, 2020

# Chemistry–A European Journal

Supporting Information

## Formation of Highly Ordered Molecular Porous 2D Networks from Cyano-Functionalized Porphyrins on Cu(111)

Rajan Adhikari,<sup>[a]</sup> Gretel Siglreithmaier,<sup>[a]</sup> Martin Gurrath,<sup>[b]</sup> Manuel Meusel,<sup>[a]</sup> Jan Kuliga,<sup>[a]</sup> Michael Lepper,<sup>[a]</sup> Helen Hölzel,<sup>[c]</sup> Norbert Jux,<sup>[c]</sup> Bernd Meyer,<sup>\*,[b]</sup> Hans-Peter Steinrück,<sup>\*,[a]</sup> and Hubertus Marbach<sup>[a]</sup>

## Experimental Section

**STM.** All experiments, sample preparations and STM measurements were performed in an ultrahigh vacuum (UHV) system with a base pressure in the low  $10^{-10}$  mbar regime. The preparation of the Cu(111) surface was done by sequential cycles of  $\text{Ar}^+$  ions bombardment (600 eV) followed by annealing at 850 K. STM was performed with an RHK UHV VT STM 300 operated at room temperature (RT) with RHK SPM 100 electronics. All STM images were obtained with a manually cut Pt/Ir tip in constant current mode. The bias voltage referred to the sample. The STM images were processed with the WSxM software.<sup>[1]</sup> For noise reduction, moderate filtering (background subtraction, Gaussian smoothing) was applied. The investigated porphyrin derivatives, Cu-TCNPP, Cu-*cis*DCNPP and 2H-*cis*DCNPP were deposited onto the substrate held at RT using a home-built Knudsen cell, with the crucible at 790, 675 and 645 K, respectively. The azimuthal orientation of the Cu(111) surface was determined through the diffusion direction of 2H-TPP along the  $\langle \bar{1}10 \rangle$  high-symmetry crystallographic axes at RT.<sup>[2]</sup>

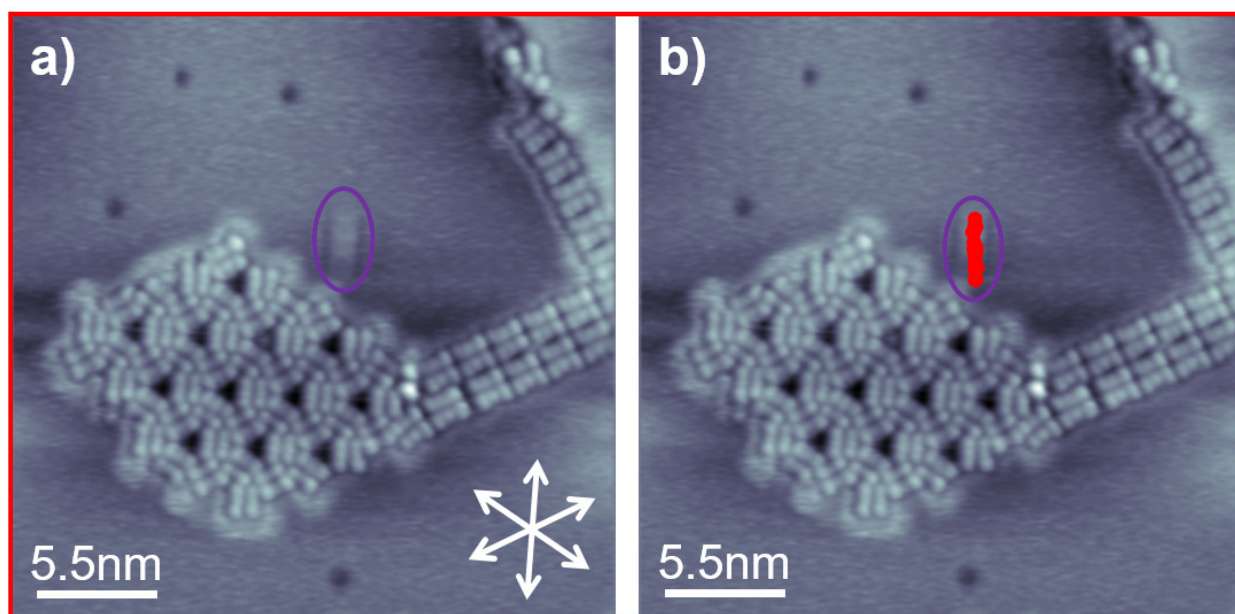


Figure S1: Average frame of an STM movie (15 consecutively recorded images) of Cu-TCNPP, deposited and measured at RT ( $27.5 \times 27.5 \text{ nm}^2$ ,  $U_{\text{bias}} = -1 \text{ V}$ ,  $I_{\text{set}} = 28.8 \text{ pA}$ ). A mobile metal-free 2H-TCNPP molecule diffusing along a high-symmetry crystallographic direction of the Cu(111) surface is marked in red and by a purple solid oval.

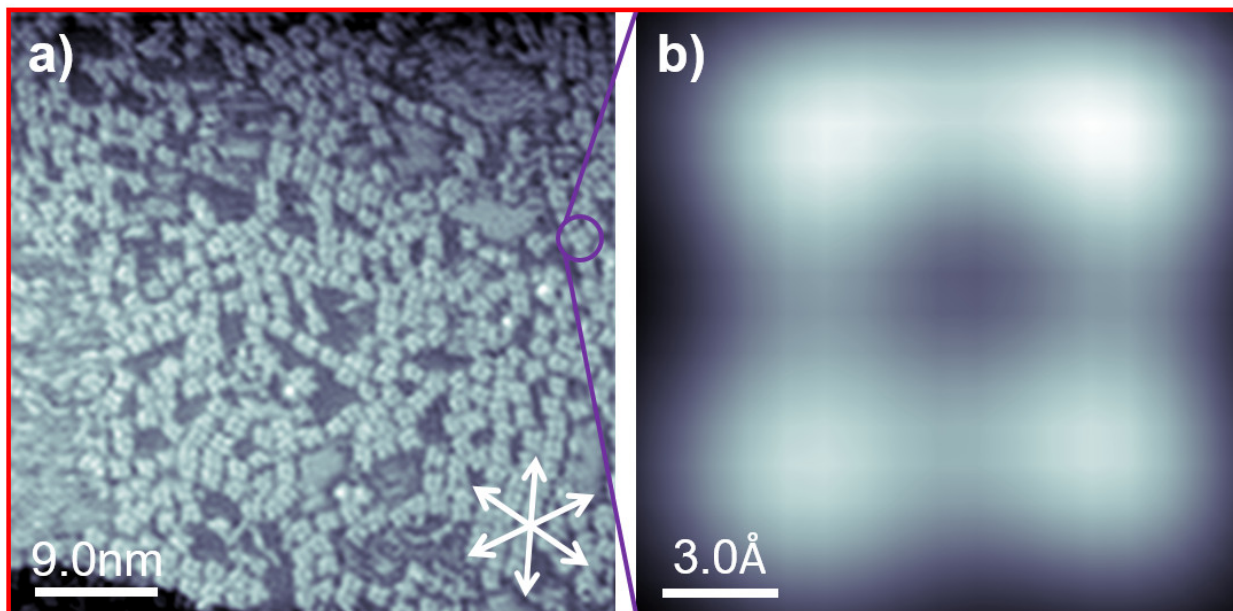
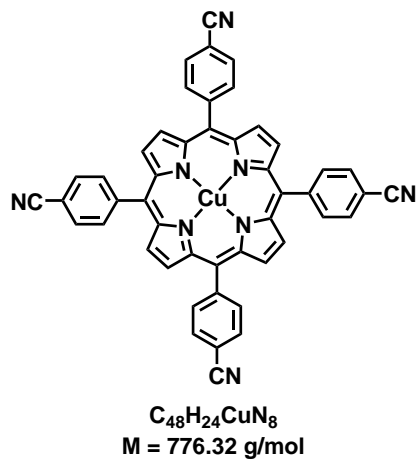


Figure S2: (a) The STM overview image ( $45 \times 45 \text{ nm}^2$ ), acquired at RT after annealing at 450 K, shows the loss of 2D long-range order and the appearance of randomly distributed individual molecules. (b) Magnified STM image of a single Cu-TCNPP molecule, which shows the change in appearance from six to four pronounced protrusions promoted by the annealing step ( $1.5 \times 1.5 \text{ nm}^2$ ,  $U_{\text{bias}} = -1 \text{ V}$ ,  $I_{\text{set}} = 30.3 \text{ pA}$ ).

**Synthesis.** All chemicals were purchased from Sigma-Aldrich<sup>®</sup>, Acros Organics<sup>®</sup>, Fluka<sup>®</sup>, Fisher Scientific<sup>®</sup> or Alfa Aesar<sup>®</sup> and used without further purification. Pyrrole, benzaldehyde and solvents for chromatography were distilled prior to usage. HPLC solvents were used for synthesis. Dichloromethane was distilled from  $\text{K}_2\text{CO}_3$ . High resolution mass spectrometry was performed on a Bruker maXis 4G UHR MS/MS or a Bruker micrOTOF II focus TOF MS spectrometer. Microwave-assisted reactions were carried out in a Biotage<sup>®</sup> initiator<sub>+</sub> monomode microwave reactor and its respective vials. Standard stirring rate was 600 rpm, fixed hold time (FHT) was on, and no external cooling was applied.

The free-base porphyrins were synthesized as reported earlier.<sup>[3,4]</sup> The metalation of the porphyrins was done by the following general procedure: The free-base porphyrin was dissolved in  $\text{CHCl}_3$  and stirred at room temperature. A saturated solution of  $\text{Cu}(\text{OAc})_2$  in  $\text{CH}_3\text{OH}$  was added. The mixture was stirred overnight at room temperature. The solvent was removed under reduced pressure. The crude product was purified by plug filtration ( $\text{SiO}_2$ , diameter: 3.5 cm, length: 7 cm,  $\text{CH}_2\text{Cl}_2$ ), yielding the metalated porphyrins as dark red solids. For further details (yields, etc.), please see the corresponding product data below.

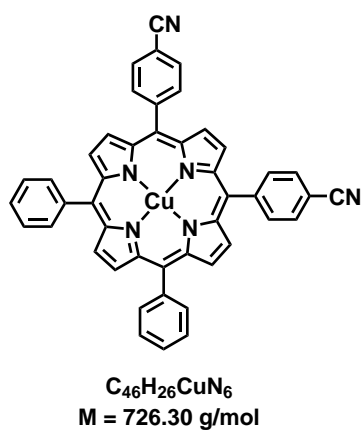


### Cu-TCNPP

The free-base porphyrin (0.040 g; 0.056 mmol) was dissolved in 10 mL CHCl<sub>3</sub>. 10 mL of the saturated solution Cu(OAc)<sub>2</sub> in CH<sub>3</sub>OH were used.

**Yield:** 80 % (0.035 g; 0.045 mmol)

**HRMS (APPI, ACN/CH<sub>2</sub>Cl<sub>2</sub>):** *m/z* calc. for C<sub>48</sub>H<sub>24</sub>CuN<sub>8</sub> [M<sup>+</sup>]: 775.1414; found: 775.1419



### Cu-cisDCNPP

The free-base porphyrin (0.010 g; 0.015 mmol) was dissolved in 3 mL CHCl<sub>3</sub>. 3 mL of the saturated solution Cu(OAc)<sub>2</sub> in CH<sub>3</sub>OH were used.

**Yield:** 100 % (0.011 g; 0.015 mmol)

**HRMS (APPI, ACN/CH<sub>2</sub>Cl<sub>2</sub>):** *m/z* calc. for C<sub>46</sub>H<sub>26</sub>CuN<sub>6</sub> [M<sup>+</sup>]: 725.1509; found: 725.1508

# Display Report

<b>Analysis Info</b>		Acquisition Date	6/11/2018 9:59:11 AM
Analysis Name	D:\Data\2018\Jux-2018\Hoelzel-HH-52-Cu-appi--.d		
Method	tune_low-APPI.m	Operator	MD
Sample Name	.ACN,CH2Cl2	Instrument	maXis
Comment			288882.20183
<b>Acquisition Parameter</b>			
Source Type	APPI	Ion Polarity	Positive
Focus	Not active	Set Capillary	700 V
Scan Begin	50 m/z	Set End Plate Offset	-500 V
Scan End	1550 m/z	Set Charging Voltage	0 V
		Set Corona	0 nA
		Set Nebulizer	2.5 Bar
		Set Dry Heater	220 °C
		Set Dry Gas	1.5 l/min
		Set Divert Valve	Waste
		Set APCI Heater	350 °C

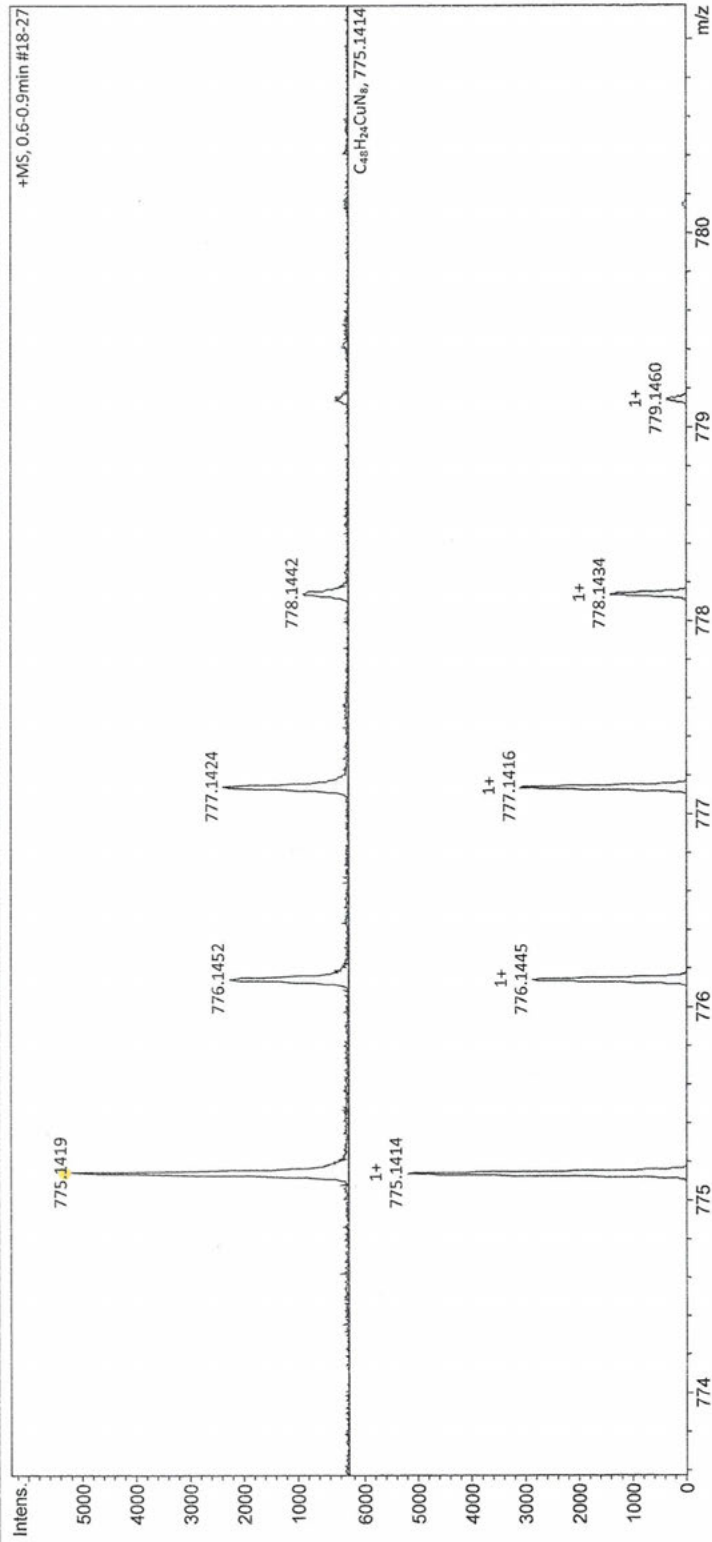


Figure S3: High-resolution mass spectra of Cu-TCNPP. Measured (top) and calculated (bottom) isotope pattern of the molecular ion peak.

# Display Report

<b>Analysis Info</b>		Acquisition Date	6/11/2018 9:47:46 AM
Analysis Name	D:\Data\2018\Jux-2018\Hoelzel-HH-10-Cu-appi--.d		
Method	tune_low-APPI.m	Operator	MD
Sample Name	ACN,CH2Cl2	Instrument	maXis
Comment			288882.20183
<b>Acquisition Parameter</b>			
Source Type	APPI	Set Nebulizer	2.5 Bar
Focus	Not active	Set Dry Heater	220 °C
Scan Begin	50 m/z	Set Dry Gas	1.5 l/min
Scan End	1550 m/z	Set Divert Valve	Waste
		Set APCI Heater	350 °C
		Ion Polarity	Positive
		Set Capillary	700 V
		Set End Plate Offset	-500 V
		Set Charging Voltage	0 V
		Set Corona	0 nA

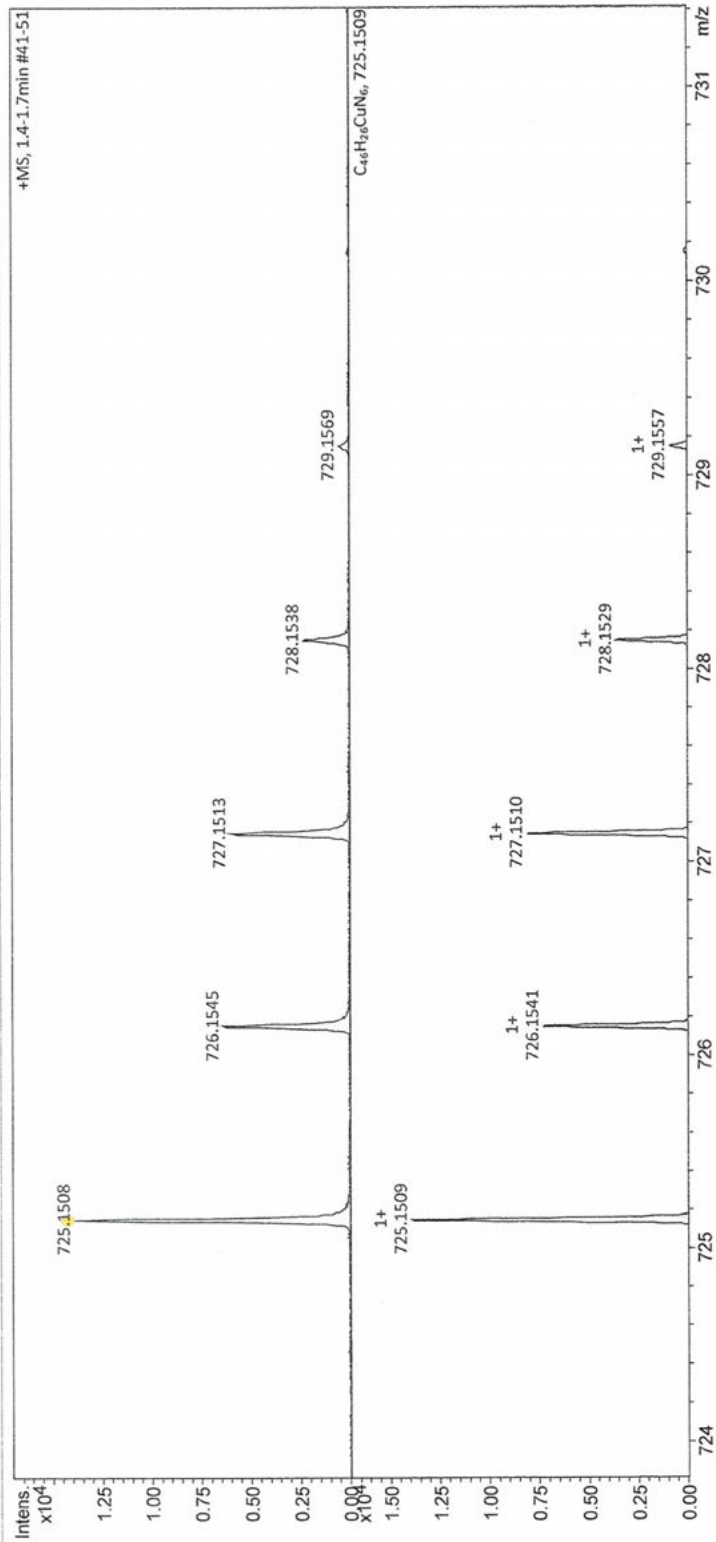


Figure S4: High-resolution mass spectra of Cu-*cis*DCNPP. Measured (top) and calculated (bottom) isotope pattern of the molecular ion peak.

# DFT Calculations

Spin-polarized DFT calculations were performed with the periodic plane-wave code `PWscf` of the Quantum Espresso software package.<sup>[5]</sup> The gradient-corrected PBE exchange-correlation functional of Perdew, Burke and Ernzerhof,<sup>[6]</sup> Vanderbilt ultrasoft pseudopotentials,<sup>[7]</sup> and a plane-wave basis set with a energy cutoff of 30 Ry were used. Dispersion corrections to PBE energies and forces were included by our  $D3^{\text{surf}}$  scheme.<sup>[8,9]</sup>  $D3^{\text{surf}}$  is an extension of the original D3 method proposed by Grimme et al.<sup>[10,11]</sup>, in which the parameter set of coordination-dependent  $C_6$  coefficients is extended by additional values for the substrate atoms at higher coordination numbers of the surface and bulk atoms.<sup>[8,9]</sup>

Cu(111) surfaces were represented by periodically repeated slabs with a thickness of three atomic layers. The calculations for single, non-interacting porphyrin molecules were done with a hexagonal ( $10 \times 10$ ) surface unit cell (300 Cu atoms).  $(7\sqrt{3} \times 7\sqrt{3})R30^\circ$  (441 Cu atoms) and  $(8\sqrt{3} \times 8\sqrt{3})R30^\circ$  (576 Cu atoms) unit cells containing three porphyrin molecules were used in the studies of porous hexagonal honeycomb-type adsorbate layers. The calculated PBE+ $D3^{\text{surf}}$  bulk lattice constant of Cu of 3.606 Å was chosen for the lateral extensions of the slabs. The atoms in the Cu bottom layer were kept fixed, and only the two upper layers together with the adsorbate were relaxed in the geometry optimizations using a force convergence threshold of 3 meV/Å. Well-converged structures and adsorption energies were obtained with a (2,2,1) Monkhorst-Pack  $k$ -point mesh together with a Gaussian smearing with a smearing width of 0.02 Ry.<sup>[3]</sup>

In the calculation of the energy profile (the potential energy surface for Cu-TPP displacement and diffusion), the lateral coordinates of the Cu atoms were kept fixed at their ideal positions and only the vertical coordinate was relaxed for the different porphyrin positions. At each point of the energy profile, the lateral coordinates of the central Cu atom of the porphyrin molecule were constrained to the respective value and all other coordinates (including the distance of the Cu atom from the surface) were relaxed.

## 1) Adsorption Site of CN-Functionalized Cu Porphyrins on Cu(111)

In the gas phase, Cu porphyrins adopt the saddle-shape conformation with  $D_{2d}$  symmetry: two opposite pyrrole rings are tilted up, the other two are tilted down. This alternating up and down tilt of the pyrrole rings is accompanied by an alternate left and right rotation of the outer phenyl units. The ruffled geometry with  $S_4$  symmetry, in which the pyrrole rings are not tilted but rotated alternately to the left and to the right, is slightly higher in energy.

To entangle the interaction of the porphyrin core with the Cu surface from the site-specific adsorption of terminal CN groups, we determined first the preferred adsorption site for Cu-

TPPs without cyano functionalization. Four different adsorption sites were probed, with the central Cu atom of the porphyrin sitting on-top of a surface Cu atom, above an fcc or hcp hollow site, and for a bridging position. Furthermore, two orientations were considered: either the two downward- or the two upward-tilted pyrrole rings were aligned along the main [110]-direction, i.e., the densely-packed Cu rows. Both orientations are related to each other by rotating the Cu-TPP by  $90^\circ$  or by flipping the Cu-TPP upside down. The global energy minimum is found for the bridge position and the orientation with the downward-tilted pyrrole rings along the Cu rows (see Figure S5a). This orientation is in agreement with the observed appearance of the Cu porphyrins in STM: the downward-tilted pyrrole rings give rise to a dark line along the Cu rows, whereas the upward-tilted pyrroles perpendicular to the Cu rows together with the four phenyl rings are seen as three bright protrusions above and below the dark line (see Figure 2c in the manuscript). As binding energy of single Cu-TPPs on Cu(111) we obtain a value of 3.39 eV. This is only slightly smaller than the binding energy of 3.58 eV for free-base 2H-TPPs on Cu(111) with inverted adsorption geometry<sup>[12]</sup> (calculated by the same PBE+D3<sup>surf</sup> approach). The binding site and the molecular orientation of Cu-TPP on Cu(111) are mainly determined by the position of the central N atoms. Figure S5a shows that all four nitrogens are above substrate Cu atoms, with a better match for the two N atoms of the upward-tilted pyrrole rings. Furthermore, these two N atoms are slightly below the central Cu atom of the porphyrin (thereby reducing the distance to the Cu atoms of the surface), whereas the two N atoms of the downward-tilted pyrroles are slightly above. A rotation of the Cu-TPP by  $90^\circ$  inverts the up-down pattern of the N atoms. This reduces the Cu-TPP binding energy by 0.15 eV, which demonstrates the importance of the N–Cu interactions. Of the other adsorption sites, the fcc and hcp hollow positions are unstable. The Cu-TPP molecules relax to the bridge position in the geometry optimization (see Figure S6b). The on-top site is metastable and represents the least favorable position for the Cu-TPP. Compared to the global energy minimum structure, the binding energy is reduced by 0.35 and 0.14 eV for the orientation with the downward-tilted pyrrole rings parallel and perpendicular to the Cu rows, respectively.

After having identified the preferred surface site for the Cu porphyrin core, we now add terminal CN groups. Previous DFT calculations have shown that HCN molecules bind with their N-side exclusively to on-top positions of the Cu(111) surface; when the D3 dispersion correction is not included in the DFT calculation, fcc, hcp and bridge sites are repulsive.<sup>[3]</sup> We start from the global optimum structure of the non-functionalized Cu-TPP molecule (see Figure S5a) and add four CN groups. As shown in Figure S6a, the CN groups nicely point toward the Cu atoms of the surface. In the subsequent geometry optimization the CN groups just bend down and establish their favored CN–Cu contact (see Figure S6b) with a N–Cu distance of 2.07 Å. Thus, having the porphyrin core at its most favorable adsorption site automatically guarantees that also added terminal CN groups can bind to the Cu surface in their preferred binding mode.

Figure S7a shows the relaxed structure when only two CN groups are added to the Cu-TPP. Here the porphyrin core is slightly pushed out of its preferred bridge site by about 0.4 Å. Obviously, the match between the position of the terminating CN groups and the surface Cu atoms is good, but not perfect. The energy landscape for shifting a Cu-TPP out of its

bridge site along the mirror symmetry plane (see Figure S5b) has a sinusoidal shape. The energy cost for a displacement of 0.4 Å is only about 0.03 eV. However, as a consequence of this small mismatch we have to expect that the Cu-TCNPP with four terminal CN groups, which has to stay in the bridge position, is slightly strained. Indeed, this is seen when we analyze the binding energies (see Table S1). The binding energy of the Cu-*cis*DCNPP molecule is 0.21 eV larger than for the non-functionalized Cu-TPP. We can attribute this gain of binding energy to the interaction of the CN groups with the surface. Taking into account that we have "lost" 0.03 eV in binding energy by displacing the porphyrin from the ideal bridge position, we can assign an interaction energy  $E_{\text{int}}^{\text{CN}}$  of about 0.12 eV to each CN–Cu contact. Based on this value for  $E_{\text{int}}^{\text{CN}}$  we would expect an increase in binding energy of 0.48 eV for the Cu-TCNPP with its four CN groups. However, from the DFT calculations we only obtain 0.40 eV. The small difference of about 0.08 eV is the strain energy, which is induced by the requirement that now all four CN groups connect to on-top Cu sites and the porphyrin core has to remain strictly in the bridge position.

Finally, we turn to the Cu adatoms. They occupy the fcc and hcp hollow sites on the Cu(111) surface. According to our DFT calculations their formation energy

$$E_{\text{f}}^{\text{Cu-ad}} = E_{\text{slab}}^{\text{Cu-ad}} - E_{\text{slab}}^{\text{Cu(111)}} - E_{\text{bulk}}^{\text{Cu}}$$

is about 0.82 eV for both sites.  $E_{\text{slab}}^{\text{Cu-ad}}$  and  $E_{\text{slab}}^{\text{Cu(111)}}$  are the total energies of a Cu(111) slab with and without a Cu adatom and  $E_{\text{bulk}}^{\text{Cu}}$  is the energy of a Cu bulk unit cell. Figure S6c shows an initial structure derived from the relaxed Cu-TPP molecule with *ad hoc* added CN groups and Cu adatoms. As in the case without adatoms, a very good geometrical match can be seen. In the geometry optimization the CNs readjust and establish a firm contact to the Cu adatoms with a N–Cu distance of 1.89 Å (see Figure S6d). Several other positions of the Cu adatoms were considered in the calculations, but they were all less favorable. Figures S7b+c show the relaxed structures for Cu-*cis*DCNPP and Cu-TCNPP when only two Cu adatoms are attached. In the case of Cu-*cis*DCNPP in Figure S7b, no displacement of the porphyrin core from the bridge site is visible, i.e., the geometrical match between the terminal CN groups and the adatoms is perfect and no strain is induced. On the other hand, for Cu-TCNPP in Figure S7c, the CN–Cu contact to Cu atoms of the terrace induces a small shift of the porphyrin toward the Cu adatoms.

For all structures with Cu adatoms the porphyrin binding energy was calculated according to

$$E_{\text{b}} = E_{\text{slab}}^{\text{Cu(111)}} + N_{\text{ad}}^{\text{Cu}} E_{\text{bulk}}^{\text{Cu}} + E_{\text{mol}}^{\text{porph}} - E_{\text{slab}}^{\text{porph/Cu-ad}} ,$$

which includes the energy that is required to form the Cu adatoms.<sup>[13]</sup>  $N_{\text{ad}}^{\text{Cu}}$  is the number of Cu adatoms in the structure and  $E_{\text{mol}}^{\text{porph}}$  is the gas-phase energy of the porphyrin. The calculated porphyrin binding energies with and without Cu adatoms are surprisingly similar (see Table S1). This means that the stronger interaction of the CN groups with the Cu adatoms almost exactly compensates the energy cost of creating the adatoms. However, the binding energies of the structures with adatoms are systematically smaller by a small margin. This means that the adatom structures with single molecules are thermodynamically unstable and should decompose into adsorbed molecules on the terrace and condensed Cu atoms at zero temperature unless hindered by kinetic effects.

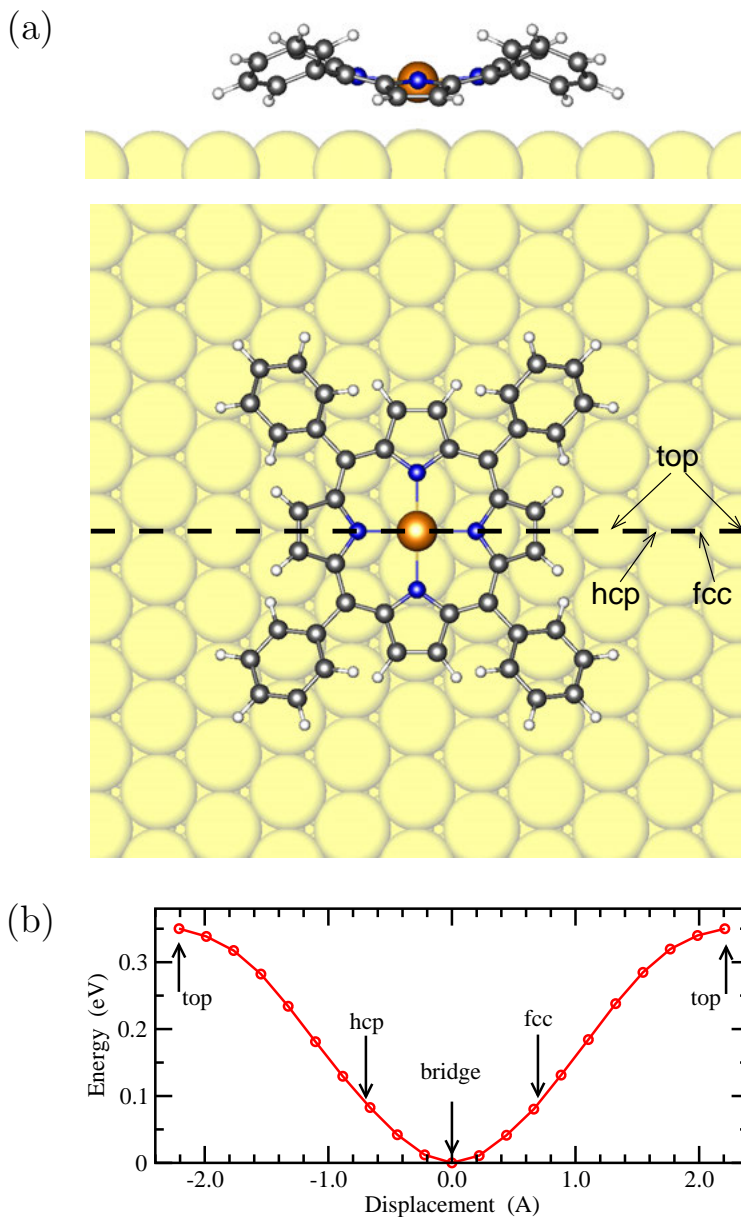
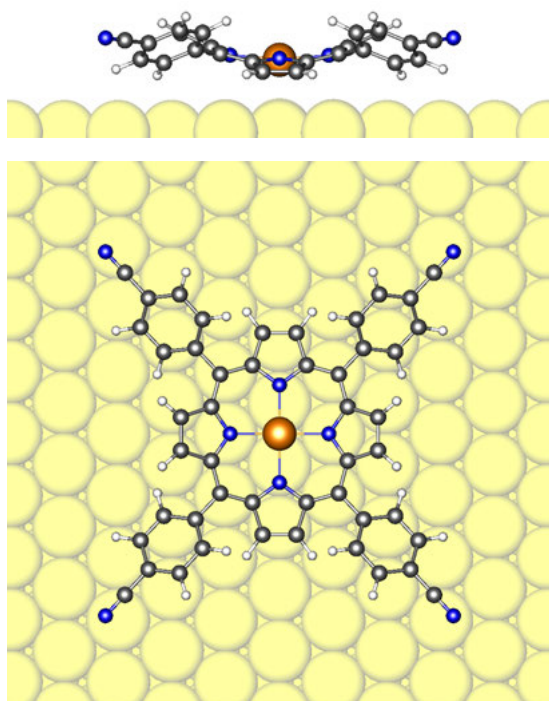
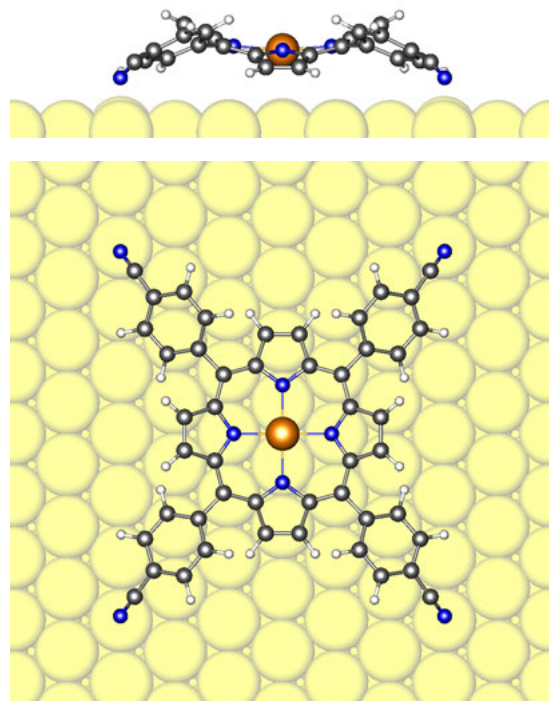


Figure S5: (a) Side and top view of the relaxed structure of a single Cu-TPP molecule on Cu(111) at its most favorable adsorption site. The saddle shape of the porphyrin is visible. The downward-tilted pyrrole rings (with slightly higher N atoms) are oriented along the densely-packed Cu rows. The black dashed line indicates the mirror symmetry plane. Cu, C, N and H atoms are shown in yellow, black, blue and white, respectively. The same color code is used in all figures. (b) Energy profile for the shift of Cu-TPP along the mirror symmetry line.

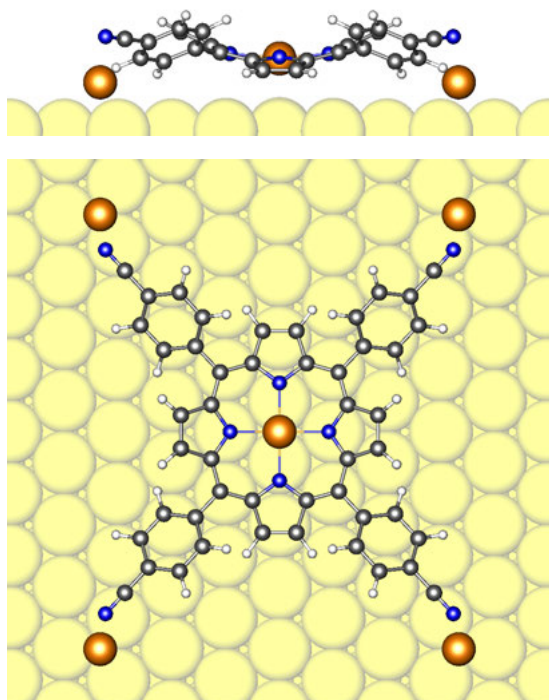
(a) Cu-TCNPP – initial



(b) Cu-TCNPP – final



(c) Cu-TCNPP – initial



(d) Cu-TCNPP – final

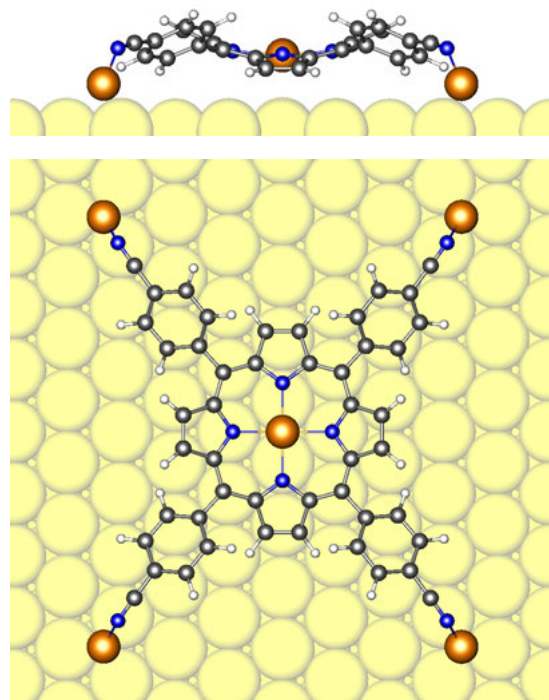
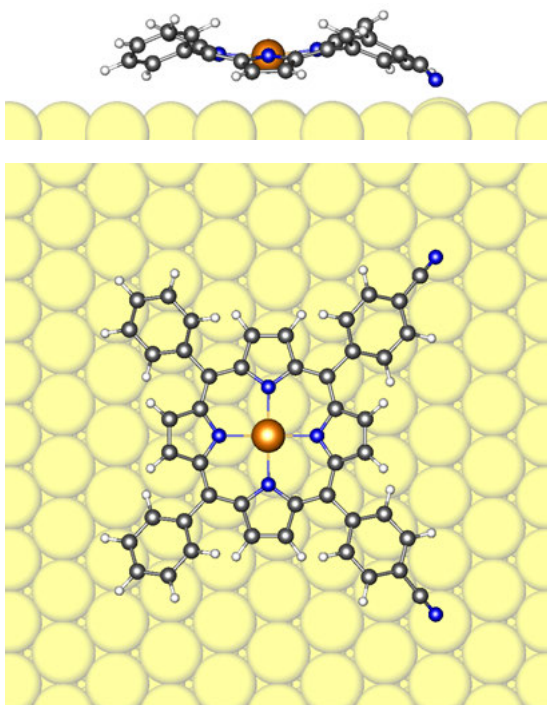
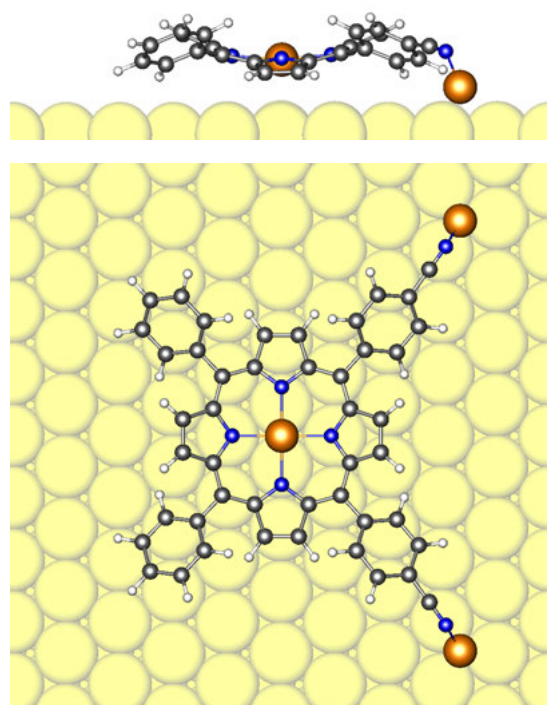


Figure S6: Side and top views of a single Cu-TCNPP molecule on Cu(111), (a,b) without and (c,d) with Cu adatoms. (a,c) show the relaxed structure of Cu-TPP from Figure S5a with *ad hoc* added CN groups. The porphyrin core is at its preferred adsorption site, simultaneously all CN groups point to a Cu on-top site or can easily connect to a Cu adatom. The final structures after geometry optimization are shown in (b,d).

(a) Cu-*cis*DCNPP



(b) Cu-*cis*DCNPP



(c) Cu-TCNPP

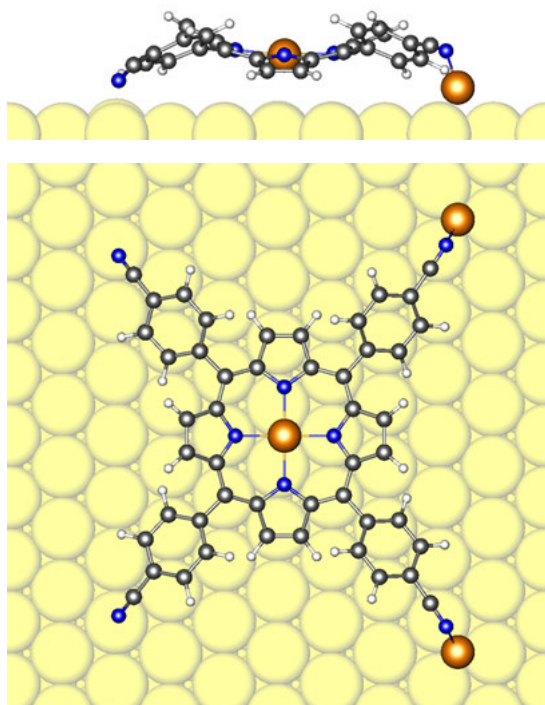


Figure S7: Side and top views of the relaxed structure of a single (a,b) Cu-*cis*DCNPP and (c) Cu-TCNPP molecule on Cu(111) without (a) and with two Cu adatoms (b,c). The mirror symmetry is preserved in all structures. If CN groups bind to the Cu substrate, the porphyrin core is slightly pushed out of its favored bridge position (a,c), whereas binding to Cu adatoms does not have this effect (b).

Table S1: Calculated binding energy  $E_b$  of single, well-separated Cu porphyrins on Cu(111).  $\Delta E_b$  is the change in binding energy with respect to non-functionalized Cu-TPP.  $E_{\text{int}}^{\text{CN}}$  is the interaction energy per terminal CN group with the Cu surface (first entry: with Cu atoms of the terrace, second entry: with Cu adatoms). Except where otherwise noted,  $E_{\text{int}}^{\text{CN}}$  is given by  $\Delta E_b$  divided by the number of CNs.  $\Delta d$  is the displacement of the porphyrin out of the bridge position.

Porphyrin	$E_b$ (eV)	$\Delta E_b$ (eV)	$E_{\text{int}}^{\text{CN}}$ (eV)	$\Delta d$ (Å)
Cu-TPP	3.39			—
Cu- <i>cis</i> DCNPP		+0.21	+0.12 <sup>[a]</sup> / —	0.42
Cu-TCNPP		+0.40	+0.10 <sup>[b]</sup> / —	—
Cu- <i>cis</i> DCNPP + 2 Cu <sub>ad</sub>		+0.05	— / +0.02	—
Cu-TCNPP + 2 Cu <sub>ad</sub>		+0.30	+0.12 <sup>[c]</sup> / +0.03	0.27
Cu-TCNPP + 4 Cu <sub>ad</sub>		+0.13	— / +0.03	—

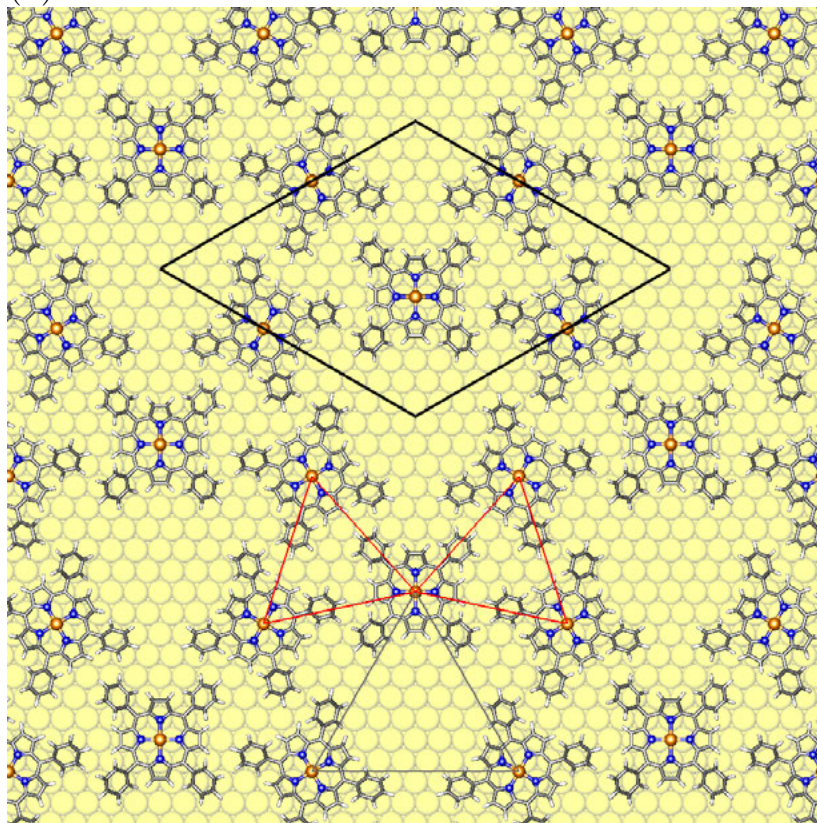
[a] An energy cost of 0.03 eV for the porphyrin displacement from the bridge site is included

[b] The strained state of the molecule is not taken into account

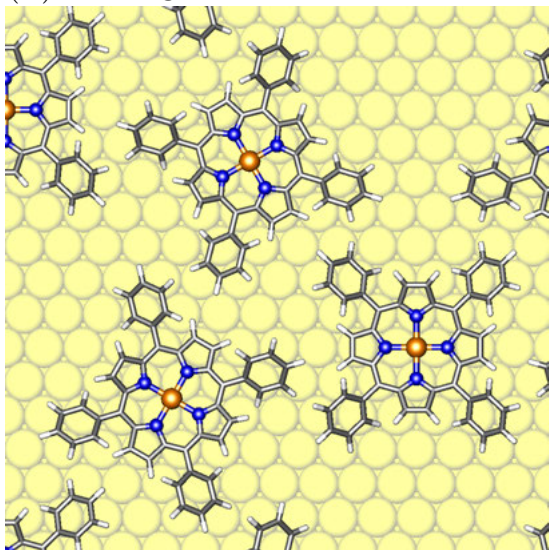
[c] The same value as for Cu-*cis*DCNPP is assumed; the remaining part is divided by 2

## 2) Details on Molecule–Molecule Interactions on Cu(111)

(a) Overview of Cu-TPP network



(b) Triangular contact at rim



(c) Central pore

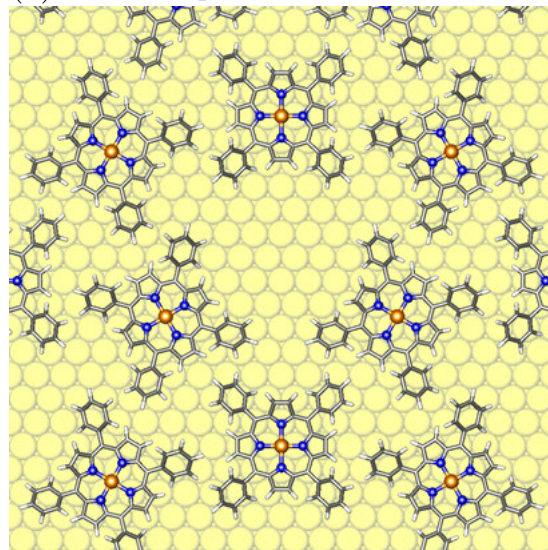
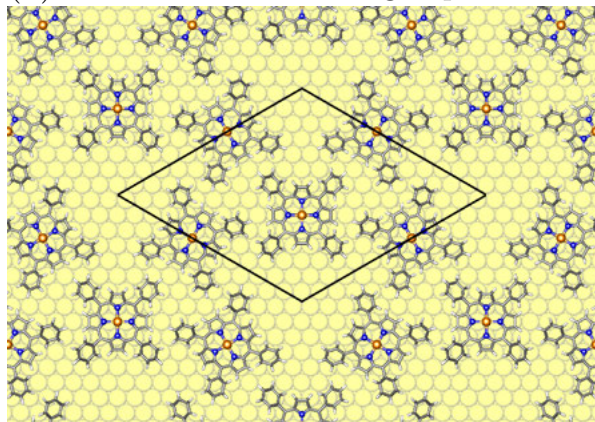
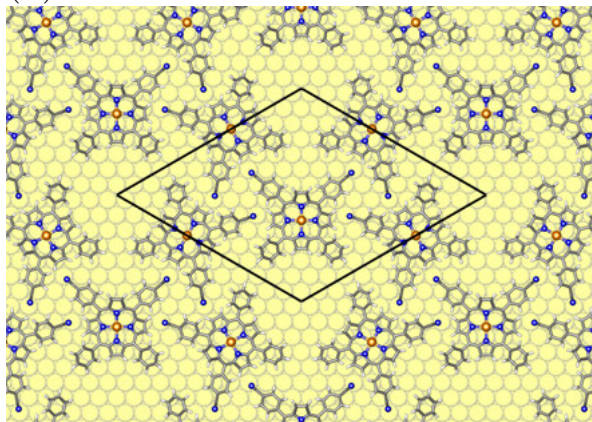


Figure S8: Relaxed structure of three Cu-TPPs in a  $(7\sqrt{3}\times 7\sqrt{3})R30^\circ$  unit cell of the Cu(111) surface (structure **1**). (a) shows an overview of the porous honeycomb-type pattern. The unit cell is indicated by black solid lines. (b) and (c) are enlarged cutouts focusing on the triangular contact at the rim (thin red lines) and the pore structure (thin gray lines), respectively. Both have a 3-fold symmetry axis in their center.

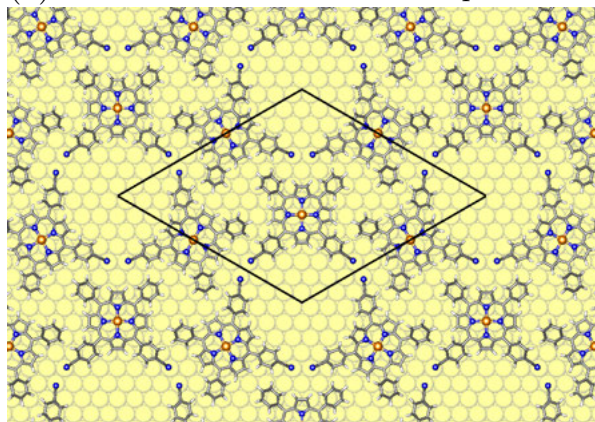
(a) Cu-TPP with no CN groups



(b) Cu-*cis*DCNPP with CN at rim



(c) Cu-*cis*DCNPP with CN at pore



(d) Cu-TCNPP with 4 CN groups

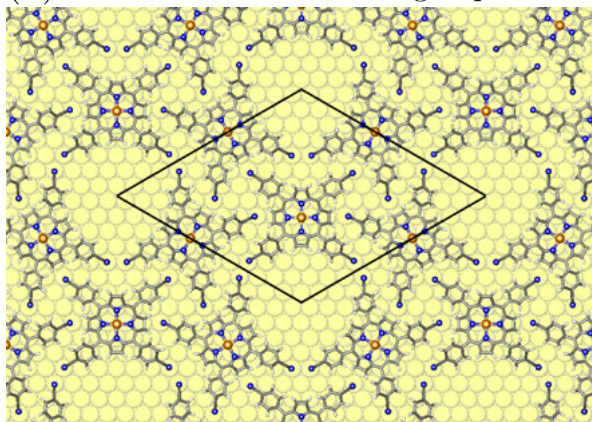


Figure S9: Stepwise addition of CN groups to the fictitious porous honeycomb-type structure of three Cu-TPP molecules in a  $(7\sqrt{3} \times 7\sqrt{3})R30^\circ$  unit cell of the Cu(111) surface. (a) without CN groups (structure **1**), (b) with CN groups at the rim (structure **2**), (c) with CN groups at the pore (structure **3**), and (d) with four CN groups (structure **4**). The unit cell is indicated by black solid lines.

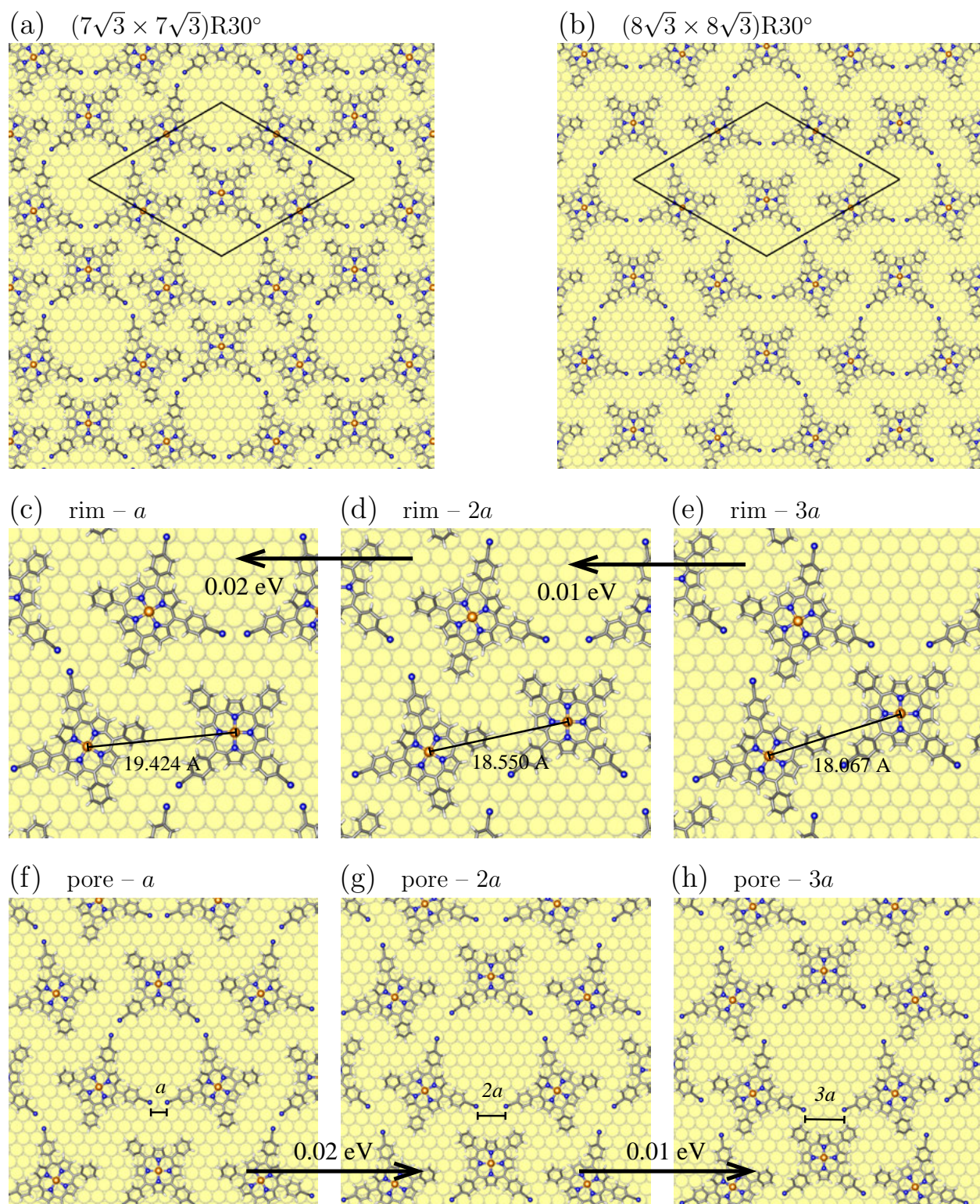


Figure S10: Pore structure motif with Cu-*cis*DCNPP molecules in (a) a  $(7\sqrt{3} \times 7\sqrt{3})R30^\circ$  (structure **3**) and (b) a  $(8\sqrt{3} \times 8\sqrt{3})R30^\circ$  unit cell. In the smaller cell, both pore and rim contact are fully established. In the larger cell, the pore can be opened by shifting the porphyrin molecules gradually outwards, thereby closing simultaneously the rim contact. A sequence of the shift, together with the change in the binding energy per molecule, is shown for an enlarged cutout (c-e) of the triangular rim contact and (f-h) of the pore structure. No significant molecule–molecule interactions are present.

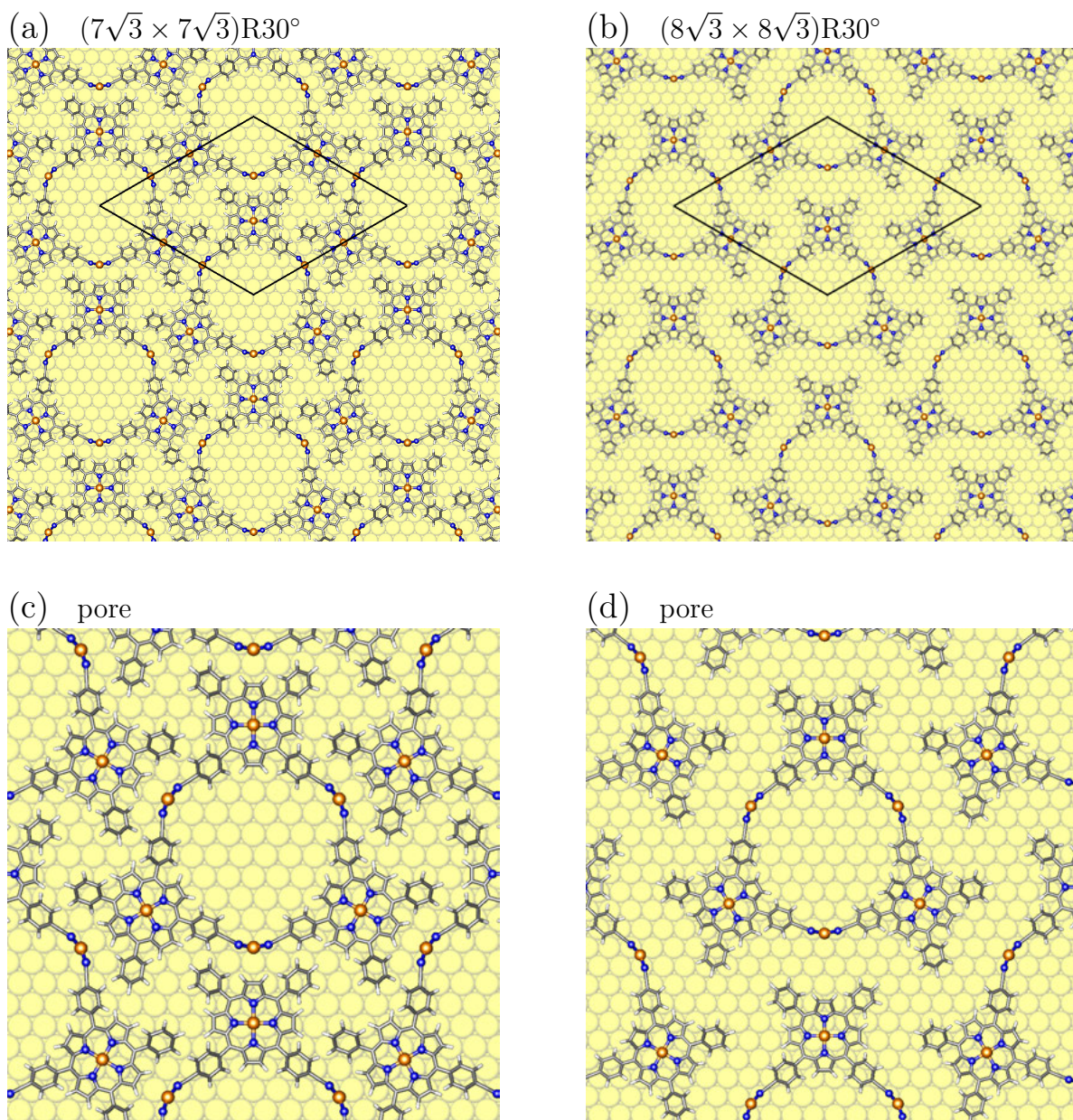


Figure S11: Pore structure motif with Cu-*cis*DCNPP molecules and Cu adatoms in (a) a  $(7\sqrt{3} \times 7\sqrt{3})R30^\circ$  (structure **5**) and (b) a  $(8\sqrt{3} \times 8\sqrt{3})R30^\circ$  unit cell with closed and open rim contact, respectively. (c,d) are enlarged cutouts of the pore region. In the smaller unit cell with closed rim contact, the binding energy per molecule is larger by 0.14 eV than for the larger cell with open rim. This is an independent, second estimate for the strength of the molecule–molecule interaction across the rim in the densely-packed configuration (see Table 1 in the manuscript).

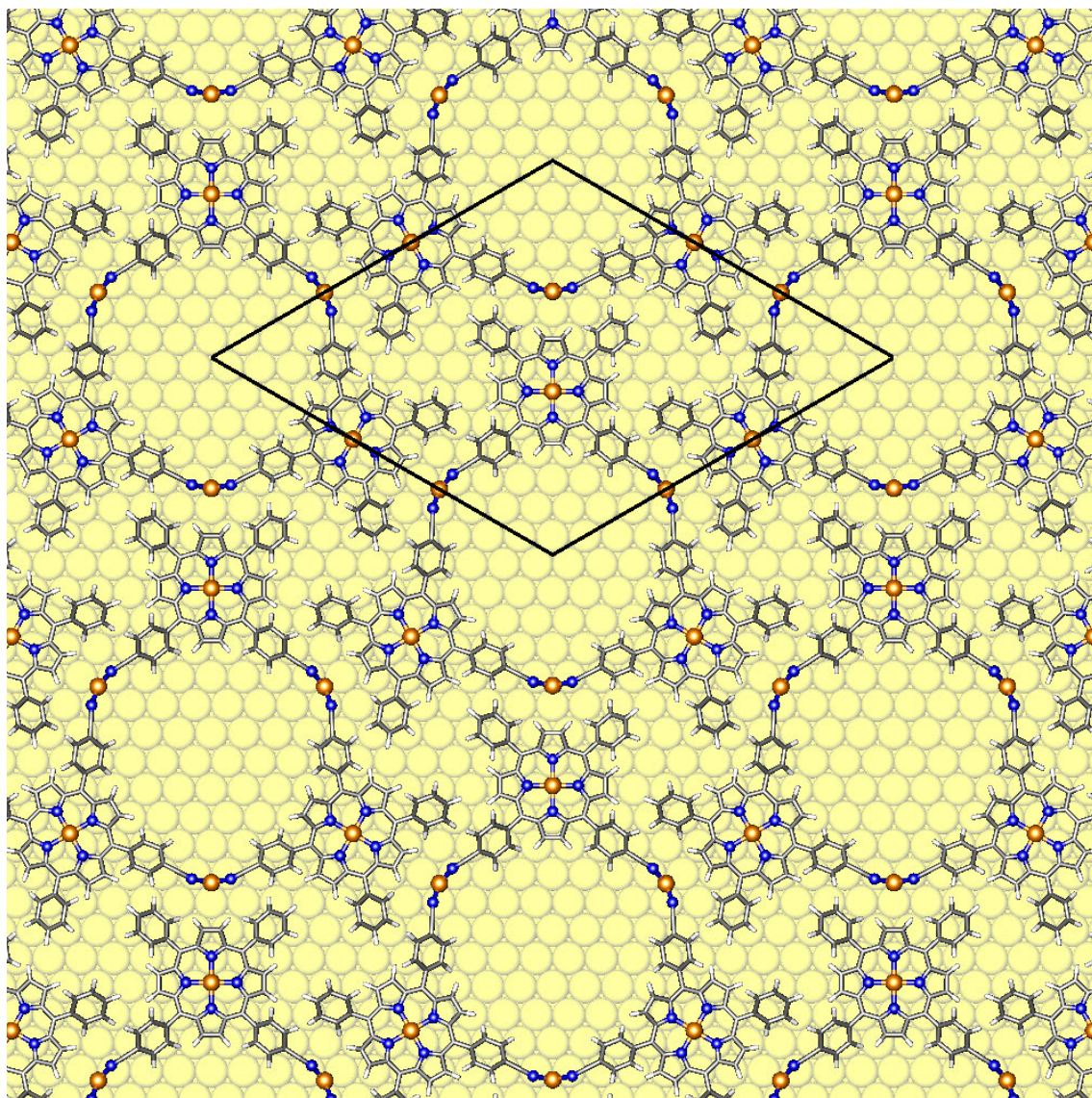


Figure S12: DFT-optimized structure of the porous honeycomb-type network of Cu-*cis*DCNPP porphyrins on Cu(111) (structure **5**). The  $(7\sqrt{3} \times 7\sqrt{3})R30^\circ$  unit cell with three porphyrin molecules is shown by black solid lines.

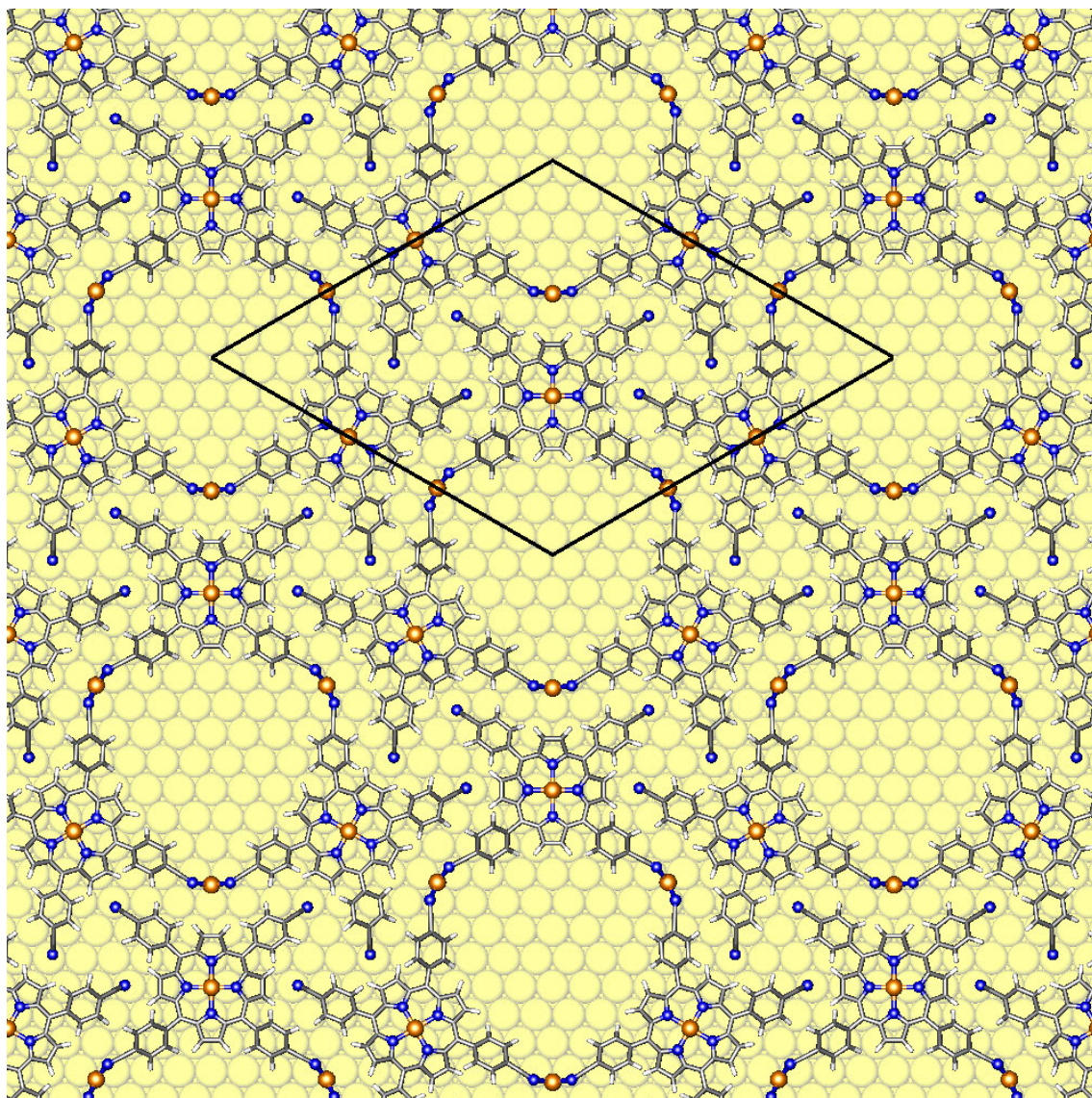


Figure S13: DFT-optimized structure of the porous honeycomb-type network of Cu-TCNPP porphyrins on Cu(111) (structure **6**). The  $(7\sqrt{3} \times 7\sqrt{3})R30^\circ$  unit cell with three porphyrin molecules is shown by black solid lines.

## References

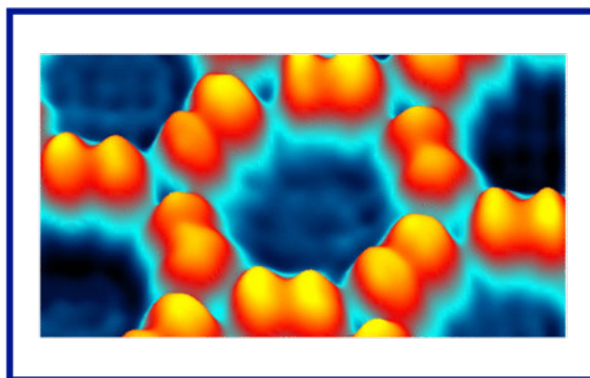
- [1] I. Horcas, R. Fernández, J.M. Gómez-Rodríguez, J. Colchero, J. Gómez-Herrero, A.M. Baro, WSXM: A software for scanning probe microscopy and a tool for nanotechnology, *Rev. Sci. Instrum.* **2007**, *78*, 013705.
- [2] F. Buchner, E. Zillner, M. Röckert, S. Gläsel, H.-P. Steinrück, H. Marbach, Substrate-Mediated Phase Separation of Two Porphyrin Derivatives on Cu (111), *Chem. Eur. J.* **2011**, *17*, 10226–10229.
- [3] M. Lepper, T. Schmitt, M. Gurrath, M. Raschmann, L. Zhang, M. Stark, H. Hölzel, N. Jux, B. Meyer, M.A. Schneider, H.-P. Steinrück, H. Marbach, Adsorption Behavior of a Cyano-Functionalized Porphyrin on Cu(111) and Ag(111): From Molecular Wires to Ordered Supramolecular Two-Dimensional Aggregates, *J. Phys. Chem. C* **2017**, *121*, 26361–26371.
- [4] M. Lepper, J. Köbl, L. Zhang, M. Meusel, H. Hölzel, D. Lungerich, N. Jux, A. de Siervo, B. Meyer, H.-P. Steinrück, H. Marbach, Controlling the Self-Metalation Rate of Tetraphenylporphyrins on Cu(111) via Cyano Functionalization, *Angew. Chem.* **2018**, *130*, 10230–10236; *Angew. Chem. Int. Ed.* **2018**, *57*, 10074–10079.
- [5] P. Giannozzi, S. Baroni, N. Bonini, M. Calandra, R. Car, C. Cavazzoni, D. Ceresoli, G.L. Chiarotti, M. Cococcioni, I. Dabo, A. Dal Corso, S. de Gironcoli, S. Fabris, G. Fratesi, R. Gebauer, U. Gerstmann, C. Gougoussis, A. Kokalj, M. Lazzeri, L. Martin-Samos, N. Marzari, F. Mauri, R. Mazzarello, S. Paolini, A. Pasquarello, L. Paulatto, C. Sbraccia, S. Scandolo, G. Sclauzero, A.P. Seitsonen, A. Smogunov, P. Umari, R.M. Wentzcovitch, QUANTUM ESPRESSO: A modular and open-source software project for quantum simulations of materials, *J. Phys.: Condens. Matter* **2009**, *21*, 395502.
- [6] J.P. Perdew, K. Burke, M. Ernzerhof, Generalized Gradient Approximation Made Simple, *Phys. Rev. Lett.* **1996**, *77*, 3865–3868; Erratum: *Phys. Rev. Lett.* **1997**, *78*, 1396.
- [7] D. Vanderbilt, Soft self-consistent pseudopotentials in a generalized eigenvalue formalism, *Phys. Rev. B* **1990**, *41*, 7892–7895.
- [8] B.P. Klein, J.M. Morbec, M. Franke, K.K. Greulich, M. Sachs, S. Parhizkar, F.C. Bocquet, M. Schmid, S.J. Hall, R.J. Maurer, B. Meyer, R. Tonner, Ch. Kumpf, P. Kratzer, J.M. Gottfried, The Molecule-Metal Bond of Alternant versus Nonalternant Aromatic Systems on Coinage Metal Surfaces: Naphthalene versus Azulene on Ag(111) and Cu(111), *J. Phys. Chem. C* **2019**, *123*, 29219–29230.
- [9] S.R. Kachel, B.P. Klein, J.M. Morbec, M. Schöniger, M. Hutter, M. Schmid, P. Kratzer, B. Meyer, R. Tonner, J.M. Gottfried, Chemisorption and Physisorption at the Metal/Organic Interface: Bond Energies of Naphthalene and Azulene on Coinage Metal Surfaces, *J. Phys. Chem. C*, **2020**, *124*, 8257–8268.

- [10] S. Grimme, J. Antony, S. Ehrlich, H. Krieg, A consistent and accurate ab initio parametrization of density functional dispersion correction (DFT-D) for the 94 elements H–Pu, *J. Chem. Phys.* **2010**, *132*, 154104.
- [11] S. Grimme, S. Ehrlich, L. Goerigk, Effect of the damping function in dispersion corrected density functional theory, *J. Comput. Chem.* **2011**, *32*, 1456–1465.
- [12] M. Lepper, J. Köbl, T. Schmitt, M. Gurrath, A. de Siervo, M.A. Schneider, H.-P. Steinrück, B. Meyer, H. Marbach, W. Hieringer, “Inverted” porphyrins: a distorted adsorption geometry of free-base porphyrins on Cu(111), *Chem. Commun.* **2017**, *53*, 8207–8210.
- [13] It is usually assumed that adatoms form by detachment from step edges. However, the energy required for removing a full row of atoms from a step edge (or a full layer of atoms from a surface) is exactly the bulk energy  $E_{\text{bulk}}^{\text{Cu}}$ .

**Publication [P2]**

**Self-Assembled 2D-Coordination Kagome, Quadratic, and Close-Packed Hexagonal Lattices Formed from a Cyano-Functionalized Benzoporphyrin on Cu(111),** R. Adhikari, J. Kuliga, M. Ruppel, N. Jux, H. Marbach, and H.-P. Steinrück, *J. Phys. Chem. C* **2021**, *125*, 13, 7204–7212; [10.1021/acs.jpcc.1c00746](https://doi.org/10.1021/acs.jpcc.1c00746)

Copyright © 2021, The Authors. Published by American Chemical Society. Reprinted with permission from The Journal of Physical Chemistry C. Further permissions related to this article should be directed to the American Chemical Society.



















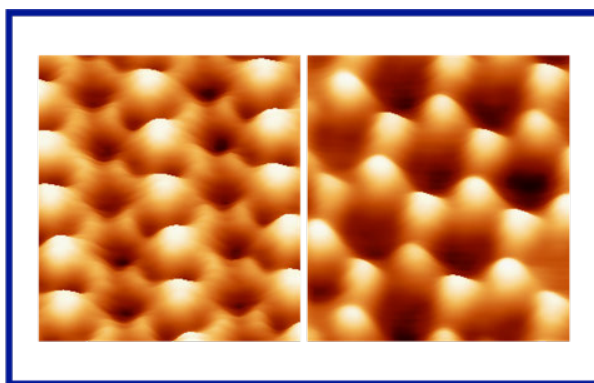


**Publication [P3]**

**Structure and Reactivity of the Ionic Liquid [C<sub>1</sub>C<sub>1</sub>Im][Tf<sub>2</sub>N] on Cu(111),** [R. Adhikari<sup>#</sup>](#), S. Massicot<sup>#</sup>, L. Fromm, T. Talwar, A. Gezmis, M. Meusel, A. Bayer, S. Jaekel, F. Maier, A. Görling, and H.-P. Steinrück, *Top. Catal.* **2023**, 1-18; [10.1007/s11244-023-01801-y](https://doi.org/10.1007/s11244-023-01801-y)

<sup>#</sup>shared first-authorship

Copyright © 2023, The Author(s). Published by Springer Nature. This is an open access article distributed under the terms of the [Creative Commons CC BY](#) license, which permits unrestricted use, distribution, and reproduction in any medium, provided the original work is properly cited.





# Structure and Reactivity of the Ionic Liquid [C<sub>1</sub>C<sub>1</sub>Im][Tf<sub>2</sub>N] on Cu(111)

Rajan Adhikari<sup>1</sup> · Stephen Massicot<sup>1</sup> · Lukas Fromm<sup>2</sup> · Timo Talwar<sup>1</sup> · Afra Gezmis<sup>1</sup> · Manuel Meusel<sup>1</sup> · Andreas Bayer<sup>1</sup> · Simon Jaekel<sup>1</sup> · Florian Maier<sup>1</sup> · Andreas Görling<sup>2</sup> · Hans-Peter Steinrück<sup>1</sup>

Accepted: 2 March 2023 / Published online: 11 April 2023  
© The Author(s) 2023

## Abstract

We studied the adsorption and reaction behavior of the ionic liquid (IL) 1,3-dimethylimidazolium bis[(trifluoromethyl) sulfonyl]imide ([C<sub>1</sub>C<sub>1</sub>Im][Tf<sub>2</sub>N]) on Cu(111) using non-contact atomic force microscopy (nc-AFM), scanning tunneling microscopy (STM), and angle-resolved X-ray photoelectron spectroscopy (ARXPS) in ultrahigh vacuum as a function of temperature, supported by density-functional theory (DFT) calculations. Our nc-AFM results for sub-monolayer IL films show that at 200 K, the IL self-assembles into highly ordered islands, with cations and anions arranged next to each other in a checkerboard-type phase. After extended annealing at 300 K, the structure transforms first to a hexagonal phase and then to a porous honeycomb phase. Simultaneously, many small, disordered islands are formed. Complementary ARXPS reveals no IL desorption until 300 K. However, a significant fraction of the IL is converted to a new species as deduced from new, strongly shifted peaks that develop in the XP spectra at around 275 K and grow with annealing time at 300 K. We correlate the remaining unshifted peaks to the ordered phases observed in nc-AFM and the shifted peaks to decomposition products, which appear as disordered islands in nc-AFM and STM. Upon further heating to 360 K, about 50% of the anions or their decomposition products desorb from the surface, while cation-related fragments mostly remain on the surface. From DFT, we obtain additional information on the structure of the ordered phases and the interaction of the IL with the substrate.

**Keywords** [C<sub>1</sub>C<sub>1</sub>Im][Tf<sub>2</sub>N] · Ionic liquids · Cu(111) · Non-contact-atomic force microscopy (nc-AFM) · Scanning tunneling microscopy (STM) · Angle-resolved X-ray photoelectron spectroscopy (ARXPS) · Density functional theory (DFT) calculations

## 1 Introduction

Ionic liquids (ILs) are composed of molecular ions and have attracted a lot of attention recently because of their unusual properties, such as a wide temperature range of liquid phase, electrochemical stability, very low vapor pressure at room temperature (RT), good ionic heat capacities, and potential as green solvents [1–5]. These properties render them good candidates for applications in a variety of fields

[2, 6]. Examples are thermal storage [7, 8], electrochemical applications [9], homogeneous catalysis [1, 2, 10, 11], dye sensitized solar cells [12], lubrication [13–15], fuel cell [16], nuclear energy utilization [17], biomedical sphere [18], and even telescope construction [19] to name only the few. Furthermore, by tailoring their properties with different functional groups one obtains task-specific reaction media [4, 20]. Their specific properties are governed by a complex combination of van der Waals, (unscreened) Coulomb, dipole, and hydrogen bonding interactions, which seldom occur together in other materials [21].

ILs are particularly interesting for catalytic applications. Two concepts have been developed and introduced, that is, the supported ionic liquid phase (SILP) approach [10, 22–24] and the solid catalyst with ionic liquid layer (SCILL) approach [24, 25]. In SILP, an IL film containing dissolved transition metal complexes is coated onto a porous support, whereas in SCILL a thin IL film is coated onto the active metal surface of a heterogeneous catalyst [24]. Both

Rajan Adhikari and Stephen Massicot shared first-authorship.

✉ Hans-Peter Steinrück  
hans-peter.steinrueck@fau.de

<sup>1</sup> Lehrstuhl für Physikalische Chemie II, Friedrich–Alexander–Universität Erlangen–Nürnberg, Egerlandstr. 3, 91058 Erlangen, Germany

<sup>2</sup> Lehrstuhl für Theoretische Chemie, Friedrich–Alexander–Universität Erlangen–Nürnberg, Egerlandstr. 3, 91058 Erlangen, Germany

SILP and SCILL systems are already in use commercially [26–28]. For example, Petronas employs a SILP system to capture mercury (Hg) from natural gas [29], while Clariant employs SCILL systems for the selective hydrogenation of unsaturated hydrocarbons [30].

In many applications, the interface of the IL with its environment, that is, IL–support [31, 32] and/or IL–vacuum(gas) interfaces, plays a crucial role [33]. The ultimate design, precise control, and understanding of the structural features of ILs at interfaces open the door to manifold applications in batteries, nanoscale tribology, electrical double-layer capacitors, and other fields. In energy storage devices such as lithium ion batteries, a thorough understanding of ionic behavior at the interface is required to understand the formation of the solid–electrolyte interphase. The noble metals gold, silver and copper are essential materials for such energy storage devices. Cu has been used as a current collector in lithium and sodium ion batteries (see ref [34] and references therein). Thus, understanding the nature of the interaction between an IL and the substrate promises a more controlled design and use of ILs for particular applications. This demand resulted in studies of IL–metal interfaces both in situ, under electrochemical conditions [31, 32], and ex situ, under ultraclean ultrahigh vacuum (UHV) conditions [35, 36]. Detailed information on the IL/substrate interface, obtained mostly by angle resolved X-ray photoelectron spectroscopy (ARXPS) and scanning tunneling microscopy (STM) on well-defined single crystal surfaces in UHV, can be found in a review article by Lexow et al. (see Ref. [36] and references therein), and in a number of earlier reviews, which also include data from ultraviolet photoelectron spectroscopy (UPS), inverse photoelectron spectroscopy (IPES), in addition to ARXPS (see Refs. [11, 35, 37–39] and references therein).

Most of the studies by ARXPS and/or STM have been done on inert single crystal surfaces such as Au(111) or Ag(111) [36, 40–42]. In nearly all cases, the formation of a wetting layer was observed, with both anions and cations adsorbed in a checkerboard-like structure in direct contact to the surface. This structure was initially derived from ARXPS, but was later on confirmed by molecularly resolved STM measurements at temperatures well below room temperature. The detailed structure and also stable imaging temperature thereby depended on the particular IL and the substrate. Quite recently, the experimental methods were complemented by non-contact atomic force microscopy (nc-AFM). Meusel et al. demonstrated for  $[C_1C_1Im][Tf_2N]$  on Au(111) that with variable temperature nc-AFM highly ordered structures can even be resolved at room temperature and above [43, 44]. At low temperature, they observed the coexistence of a stripe phase and a hexagonal phase—with

single molecule thickness—for the first layer on the surface. In this previous study, the individual anions in the wetting layer were identified from their larger height as compared to the flat-lying (and thus invisible) cations [43]. A stripe phase was also resolved for coverages in the multilayer range, where the growth proceeds through bilayer formation, demonstrating the layer-by-layer 2D growth of this IL on the very inert Au(111) surface [44]. Moreover, for certain substrate temperatures, upon deposition metastable 3D droplets were initially formed on top of the wetting layer, which converted into the 2D bilayer structure over time [45].

The aim of this study was to move on to the more reactive Cu(111) surface and investigate the adsorption, thermal evolution and possible reactions of  $[C_1C_1Im][Tf_2N]$  on this surface in order to determine potential differences to the Au(111) surface. This topic also appeared quite interesting to us, since in literature there are two studies for related systems, that is, by Biedron et al. for  $[C_8C_1Im][Tf_2N]$  on Cu(100) [46] and by Uhl et al. for  $[BMP][Tf_2N]$  on Cu(111) [47]. Interestingly, the results seemed to be in conflict with each other, but based on our study a reinterpretation of the data on Cu(111) leads to a consistent picture. We performed our study using in situ ARXPS (100–800 K) and variable temperature nc-AFM/STM (100–350 K). The scheme at the top of Table 1 shows the chemical and molecular structure of  $[C_1C_1Im][Tf_2N]$ . The nc-AFM/STM studies with sub-molecular resolution were performed for coverages around 0.15 monolayer (ML) of ion pairs, which corresponds to 30% of a full wetting layer (=0.30 WL) of  $[C_1C_1Im][Tf_2N]$  on Cu(111). To obtain complementary information, ARXPS measurements were performed for 0.3 and 0.5 ML. In addition, DFT calculations provide complementary insight into the structure and the bonding situation of the IL adlayer. To the best of our knowledge, this is the first time that individual ion pairs have been resolved and identified in an IL adlayer on Cu(111) using nc-AFM.

## 2 Experimental

The ionic liquid  $[C_1C_1Im][Tf_2N]$  was either bought from IoLiTec (used in the XPS measurements) or synthesized under ultra-clean conditions described in a previous publication [48] (used in the nc-AFM/STM measurements). It was thoroughly degassed under ultrahigh vacuum (UHV) prior to deposition to remove volatile impurities. In the literature, the cation  $[C_1C_1Im]^+$  is also known as  $[MMIm]^+$  [49], and the anion  $[Tf_2N]^-$  as  $[NTf_2]^-$  [50] or  $[TfSA]^-$  [51]. The scanning probe microscopy (SPM) and the ARXPS experiments were performed in two separate UHV systems. In both, the

**Table 1** Different structures and the corresponding unit cell parameters and unit cell areas, as obtained from nc-AFM and STM

Structure	Unit cell parameters	Matrix notation	Unit cell area [nm <sup>2</sup> ]	Ion pair density ( $\rho$ ) [ion pairs/nm <sup>2</sup> ]
Checkerboard-type (nc-AFM)	$ \vec{a} =1.90\pm 0.08$ nm $ \vec{b} =0.90\pm 0.05$ nm $\gamma=90\pm 3^\circ$	$\begin{bmatrix} 6 & 2 \\ -3 & 4 \end{bmatrix}$ $\gamma=92.2^\circ$	1.71	1.17
Hexagonal-type (nc-AFM)	$ \vec{a} = \vec{b} =2.35\pm 0.08$ nm $\gamma=60\pm 4^\circ$	$\begin{bmatrix} 8 & 2 \\ -2 & 10 \end{bmatrix}$ $\gamma=60^\circ$	4.78	1.26
Honeycomb-type (nc-AFM)	$ \vec{a} = \vec{b} =2.35\pm 0.08$ nm $\gamma=60\pm 4^\circ$ pore diameter ~ 2 nm	$\begin{bmatrix} 8 & 2 \\ -2 & 10 \end{bmatrix}$	4.78	1.05
Honeycomb-type (STM)	$ \vec{a} = \vec{b} =2.36\pm 0.08$ nm $\gamma=60\pm 4^\circ$ pore diameter ~ 2 nm	$\gamma=60^\circ$	4.82	1.04

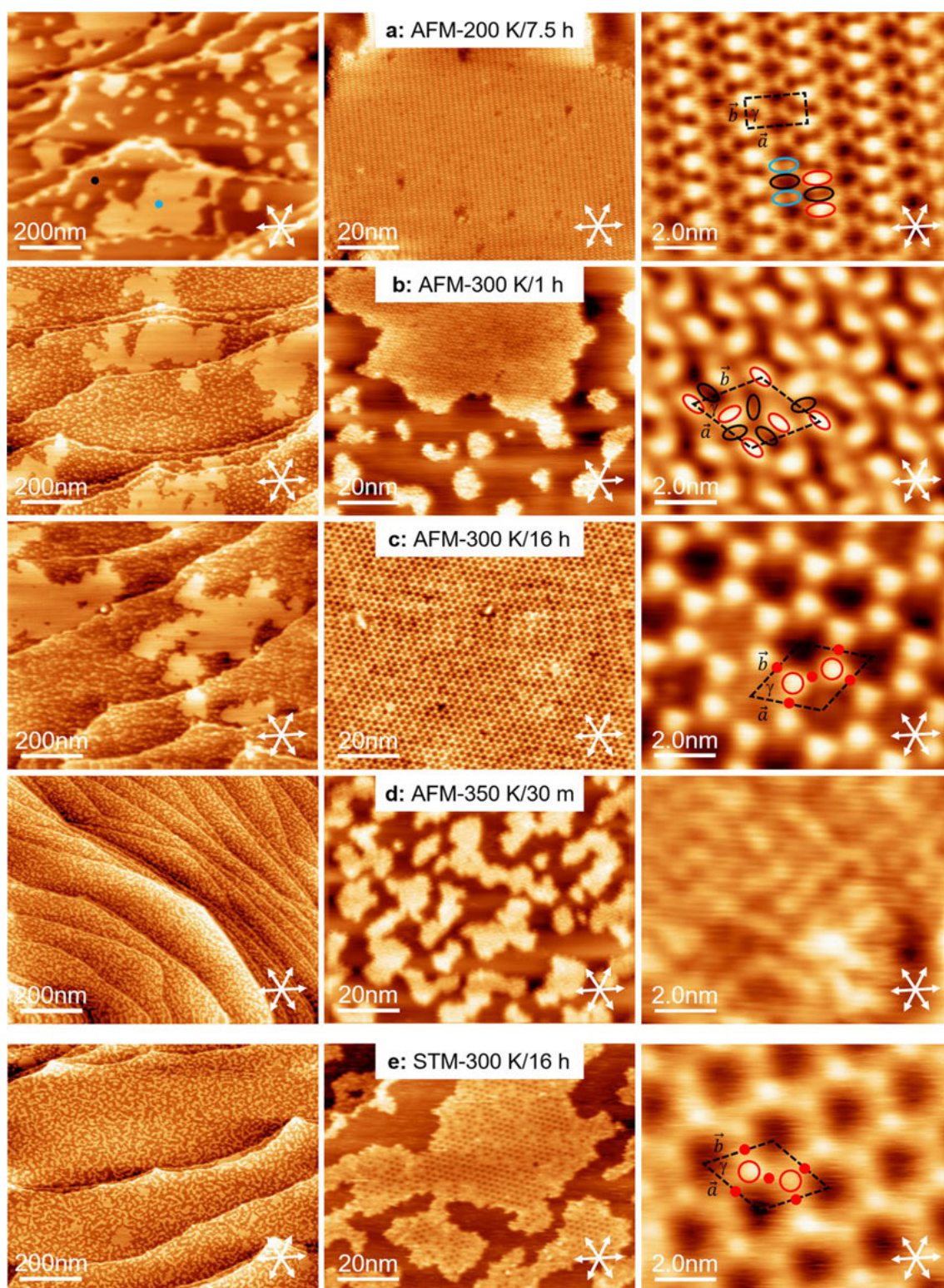
Also given are the unit cell area and the ion pair density,  $\rho$ ; for details see text. On top of the table the chemical and molecular structure of [C<sub>1</sub>C<sub>1</sub>Im][Tf<sub>2</sub>N] is depicted together with height of the cation (~0.3 nm) and anion (~0.5 nm); grey: C, white: H, blue: N, red: O, yellow: S, and green: F

clean Cu(111) surface was freshly prepared prior to each IL deposition using sequential cycles of Ar<sup>+</sup> ions bombardment (0.6 to 1 keV) at room temperature followed by a final annealing step at 800 to 900 K for approximately 10 min and consecutive cooling to the desired temperatures. The IL was deposited by physical vapor deposition (PVD) onto the substrate held at different temperatures as denoted using a home-built Knudsen cell [52] with the crucible temperature of 385–398 K. To ensure stable and reproducible evaporation rates, the IL adsorbate flux was monitored with a quartz crystal microbalance (QCM). IL coverages are denoted in ML, where 1 ML corresponds to a complete layer of vertically rented ion pairs. In case of a checkerboard structure with anions and cations adsorbed next to each other in direct contact to the surface, this coverage corresponds to 0.5 ML, which is also denoted as 1 WL (wetting layer).

The variable temperature nc-AFM and STM measurements were carried out in a two-chamber UHV system, using a Scienta Omicron VT-AFM-Q + -XA microscope, with a base pressure in the low 10<sup>-11</sup> mbar range [43]. Following IL deposition on the sample in the preparation chamber, it was then quickly transferred to the pre-cooled AFM/STM sample stage in the analysis chamber at 110 K for the measurements. All AFM images were obtained in non-contact mode with

silicon cantilevers, and the applied frequency shifts  $\Delta f$  in the employed experimental conditions ranged from – 300 to – 650 Hz vs the cantilever's resonance frequency, which is typically around ~ 270 to 300 kHz. The STM images were obtained with a manually cut Pt/Ir tip in constant current mode. The denoted bias voltages refer to voltages applied to the tip relative to the sample potential. The nc-AFM/STM images were processed using the WSxM software [53]. For noise reduction, moderate filtering (background subtraction, Gaussian smoothing) was applied.

The ARXPS measurements were performed in a two-chamber XPS system, which has previously been described in detail elsewhere [54]. The XP spectra were obtained using a non-monochromated Al K $\alpha$  X-ray source (SPECS XR 50, 1486.6 eV, 240 W) and a hemispherical electron analyzer (VG SCIENTA R3000). For all spectra, a pass energy of 100 eV was used, yielding an overall energy resolution of 0.9 eV [54]. The spectra were quantitatively evaluated using CasaXPS V2.3.16Dev6. For the Cu 2p<sub>3/2</sub> and the Auger-LMM substrate signals, Shirley backgrounds were subtracted and peaks were fitted with Lorentzian line shapes. For the IL-related S 2p, C 1s, N 1s, O 1s and F 1s regions, the positions and widths (fwhm) of the peaks were constrained (see Table S2 in the SI).



### 3 Theory

First-principles DFT calculations were performed with the VASP program package (Version 5.4.1) [55–57] using the PBE exchange–correlation functional [58]. The projector

augmented wave method (PAW) [59] was used to take into account the core electrons. An energy cutoff of 450 eV was chosen for the plane wave basis. To describe the long-ranged London dispersion interactions the DFT-D3 correction scheme [60] was applied, and a Methfessel-Paxton smearing

**Fig. 1** nc-AFM (a–d) and STM images (e) of 0.15 ML [C<sub>1</sub>C<sub>1</sub>Im][Tf<sub>2</sub>N] on Cu(111), as overview (left, 1000×800 nm<sup>2</sup>), close-up (middle, 100×80 nm<sup>2</sup>), and with high resolution (right, 10×8 nm<sup>2</sup>). **a** After annealing at 200 K for 7.5 h, ordered islands with a checkerboard-type structure and a nearly rectangular unit cell are observed; the right image is an average frame of nine consecutively recorded images. **b** After annealing at 300 K for 1 h, disordered small islands coexist with large ordered islands with hexagonal structure. **c** After annealing at 300 K for ~16 h, disordered small islands coexist with large IL islands with a highly ordered porous honeycomb structure. **d** After annealing at 350 K for 30 min, only small disordered islands are found. **e** STM images following a different preparation route and annealing at 300 K for ~16 h (see text) display the same honeycomb structure as seen in (c). The nc-AFM images were measured with  $\Delta f = -400$  or  $-500$  Hz, and the STM images with  $U_{bias} = 2$  V and  $I_{set}$  of 0.2 or 0.4 nA (for details, see Table S4 in the SI); the unit cells are shown as dashed black lines; covered and uncovered areas are denoted by blue and black dots, respectively. For more details see text

[61] with a broadening of 0.2 eV was included. A supercell approach with four layers of Cu atoms was used to model the systems, including a 20 Å layer of vacuum separating periodic images in  $z$ -direction. The experimental lattice parameter of 3.58 Å was used for the Cu bulk geometry. The two bottom layers were fixed, while the top two layers were relaxed during the optimizations. The geometry was optimized until all forces were smaller than 0.01 eV/Å. The model for the checkerboard structure with a  $\begin{bmatrix} 6 & 2 \\ -3 & 4 \end{bmatrix}$  supercell was calculated with a  $2 \times 4 \times 1$  and the larger hexagonal structures with the  $\begin{bmatrix} 8 & 2 \\ -2 & 10 \end{bmatrix}$  supercell with a  $2 \times 2 \times 1$  Gamma centered Monkhorst–Pack [62] k-point mesh. Adsorption energies  $E_{ads}$  were calculated as total energy differences between the clean surface unit cell  $E_{surf}$  plus the energy of the ions in gas phase  $E_{an} + E_{cat}$  minus the total energy of the combined system  $E_{sys}$  as  $E_{ads} = E_{an} + E_{cat} + E_{surf} - E_{sys}$ . Therefore, higher adsorption energies correspond to higher stability. The reference of the ionic liquid are the isolated ions in gas phase and not in the liquid phase. Isolated ions in gas phase represent the most simple and best defined reference. Furthermore, the comparison of different adsorption structures is not affected by the choice of the reference.

## 4 Results and Discussion

### 4.1 Atomic Force Microscopy and Scanning Tunneling Microscopy

In a first step, we investigated the adsorption and reaction behavior of 0.15 ML (=0.30 WL) of [C<sub>1</sub>C<sub>1</sub>Im][Tf<sub>2</sub>N] on Cu(111) using nc-AFM. The layers were deposited with the sample at 300 K. After deposition, the sample was immediately transferred to the precooled nc-AFM stage at 110 K

within 7 to 10 min, in order to avoid the progress of potential chemical reactions (as it will be shown later, changes at 300 K only occur very slowly over several hours). Thereafter, nc-AFM images were first measured at 110 K, and then the sample was stepwise-annealed for extended times to 200, 250, 300 and 350 K. After each annealing step, the sample was quickly cooled back to 110 K to freeze the present state for imaging.

Figure 1a shows the corresponding images after annealing to 200 K for 7 h 30 min. In the overview image (left), we observe extended IL islands of various sizes (left image, bright areas) at the steps and also on the terraces of the Cu(111) surface; IL-covered areas and large areas of uncovered Cu substrate are indicated by blue and black dots, respectively. Notably, directly after cooling to 110 K, very similar structures are observed, but with a smaller size of the ordered islands and reduced resolution (see SI, Figure S1). The IL islands are observed close to step edges from both the ascending and descending sides of the step edges, implying that the steps are energetically favored adsorption sites that serve as nucleation centers. The close-up in Fig. 1a (middle) shows one representative large island connected to a step edge. This island consists of a highly regular, close-packed phase with only few defects, giving rise to a stripe-like appearance. The high-resolution AFM image of one of the islands in Fig. 1a (right) reveals that the close-packed phase is characterized by molecular rows, that is, stripes with a nearly rectangular unit cell ( $\gamma = 90 \pm 3^\circ$ ), with lattice vectors  $\vec{a}$  ( $1.90 \pm 0.08$  nm) and  $\vec{b}$  ( $0.90 \pm 0.05$  nm), and a unit cell area 1.71 nm<sup>2</sup> (see Table 1). From the measured angle of  $6^\circ$  between the unit cell vector  $\vec{a}$  and the substrate high symmetry direction, we derive a commensurate  $\begin{bmatrix} 6 & 2 \\ -3 & 4 \end{bmatrix}$  superstructure, using standard matrix notation with a unit cell angle of  $92.2^\circ$ . We propose that the unit cell contains 2 ion pairs, yielding a density of 1.17 ion pairs/nm<sup>2</sup>. This analysis is based on the comparison to the low-temperature checkerboard-type structures on Au(111), with one ion pair per unit cell, and unit cell areas between 0.74 and 0.85 nm<sup>2</sup> [43]. We assign the very bright oval protrusion (red ellipses) and the two less bright protrusions (blue ellipses) to two differently oriented anions, and the dark areas in between (black ellipses) to the two cations; for more details, see DFT results below. From this consideration, we conclude that the anion to cation ratio is 1:1, that is, the ion pairs on the Cu(111) surface remain intact and are arranged in a checkerboard-type ionic surface tiling without dissociation, self-assembling into stripes. We will address the details of the structure together with the DFT calculations presented later on.

In a next step, we annealed the deposited layer at 250 K and then at 300 K. After annealing to 250 K for 45 min, we again find images with a stripe structure, albeit with a lower

resolution of the image (see SI, Figure S2), which likely is due to a different termination of the AFM tip.

After annealing to 300 K for 1 h, we observe a pronounced transformation of the film structure, which is evident from the corresponding nc-AFM images in Fig. 1b. In the overview image (left), large islands are found to coexist with many small islands distributed all over the surface (see also Figure S3 in the SI). The close-up image (middle) reveals long-range order for the large islands, and disorder for the small islands. In the high-resolution nc-AFM image of one of the large islands in Fig. 1b (right), we observe a hexagonal-type lattice with three bright longish protrusions (red ellipses) and three less bright protrusions (black ellipses) per unit cell (dashed black rhombus); the protrusions in the unit cell have different orientation. The unit cell lattice vectors  $\vec{a}$  and  $\vec{b}$  both have a length of  $2.35 \pm 0.08$  nm with  $\gamma = 60 \pm 4^\circ$ , resulting in a unit cell area of  $4.78$  nm<sup>2</sup>. Assuming that each protrusion now represents an ion pair (see thorough discussion below), we obtain six ion pairs per unit cell. The resulting density of  $1.26$  ion pairs/nm<sup>2</sup> is quite comparable to that of the stripe phase (see Table 1). The absence of long range order for the small islands is also evident from the high-resolution image shown in Figure S4 (left) in the SI.

After extended annealing to 300 K for 16 h, we see another pronounced change in the structural order of the adsorbed IL layer; see Fig. 1c. In the overview nc-AFM image (left) we again find large islands coexisting with a large number of small islands; the close-up image (middle) shows a highly ordered honeycomb structure of the large islands, while the small islands are again disordered (see also Figure S4 (middle) in the SI). From the high-resolution nc-AFM image of one of the large islands in Fig. 1c (right), we conclude that the unit cell (dashed black rhombus) contains two bright protrusions (red circles) and three less bright protrusions (red dots); we again assume that each protrusion corresponds to one ion pair. The lengths of the lattice vectors  $\vec{a}$  and  $\vec{b}$  are again  $2.35 \pm 0.08$  nm with  $\gamma = 60 \pm 4^\circ$ , resulting in a unit cell area of  $\sim 4.78$  nm<sup>2</sup>. Assuming five ion pairs per unit cell (see below), we obtain a density of  $1.05$  ion pairs/nm<sup>2</sup> (see Table 1). From the angle of  $12^\circ$  between the unit cell vectors and the substrate high symmetry directions we derive a  $\begin{bmatrix} 8 & 2 \\ -2 & 10 \end{bmatrix}$  superstructure using standard matrix notation, with an angle of  $60^\circ$ , for the porous honeycomb mesh. The pores of the honeycomb mesh have a diameter of roughly 2 nm. Interestingly, the size of the unit cell of the honeycomb structure is identical to that of the hexagonal structure (that is, lattice vector lengths of 2.35 nm), within the experimental uncertainty. Note that the honeycomb structure can be obtained from the overall hexagonal structure by removing one bright protrusion (that is, one ion pair), which results in the pore of the honeycomb structure. Thus,

the hexagonal structure can be seen as transition structure from the stripe phase to the honeycomb phase upon annealing the IL layer at 300 K.

Upon further heating to 350 K, the long-range ordered islands disappear, and only small, disordered islands are observed; see Fig. 1d, which is particularly evident from the high-resolution image (right). Interestingly, the appearance of these small islands is very similar to that of the above described small, disordered islands, which coexist with the hexagonal and honeycomb structures at 300 K (see comparison in Figure S4 in the SI).

Notably, we also obtain the honeycomb structure following a different preparation and measurement route. In contrast to the above-described preparation where the IL was deposited at room temperature and quickly cooled down to 110 K, we here deposited 0.15 ML (=0.30 WL) of [C<sub>1</sub>C<sub>1</sub>Im][Tf<sub>2</sub>N] onto Cu(111) held at low temperature ( $T < 160$  K), and measured at 110 K; here, the measurements were performed by STM and not by nc-AFM. While after adsorption at  $< 160$  K and also after annealing up to 250 K (for 15 min) no ordered IL islands could be found (see Figure S5 in SI), ordering is observed starting after extended annealing for 3–16 h at 300 K. The corresponding STM images after annealing for 16 h are shown in Fig. 1e. The overview image (left) shows the surface homogeneously covered with many small islands. When comparing these STM images with the previous nc-AFM overview images obtained after deposition at 300 K followed by immediate cooling to 110 K and then annealing to 300 K (Fig. 1c), we see much larger islands for the latter, which is attributed to Ostwald ripening during deposition at 300 K. After annealing the  $< 160$  K-deposited layer for 3–16 h at 300 K, we observe again two distinctly different structures coexisting on the surface: The close-up STM image in Fig. 1e (middle) shows a large IL island with a well-ordered inner part surrounded by a disordered rim; in addition, smaller disordered separate islands are seen. The well-ordered inner part of the large island displays the porous honeycomb structure with few defects and additional species in some pores, as deduced from their less-dark appearance. Figure 1e (right) shows the high-resolution STM image of the center of the island, with the primitive unit cell indicated by the dashed black rhombus. The porous honeycomb-type adlayer again has a primitive hexagonal unit cell. The lattice vectors  $\vec{a}$  and  $\vec{b}$  have an identical length of  $2.36 \pm 0.08$  nm with  $\gamma = 60 \pm 4^\circ$ , resulting in a pore diameter of  $\sim 2$  nm. The unit cell (area of  $4.82$  nm<sup>2</sup>) again contains two bright (red circles) and 3 less bright (red dots) protrusions, giving a density of  $1.04$  ion pairs/nm<sup>2</sup>; these parameters are identical to those observed using the other preparation route and nc-AFM as imaging technique. The comparison of the close-up images (middle) and high resolution images (right) for the two preparation routes in

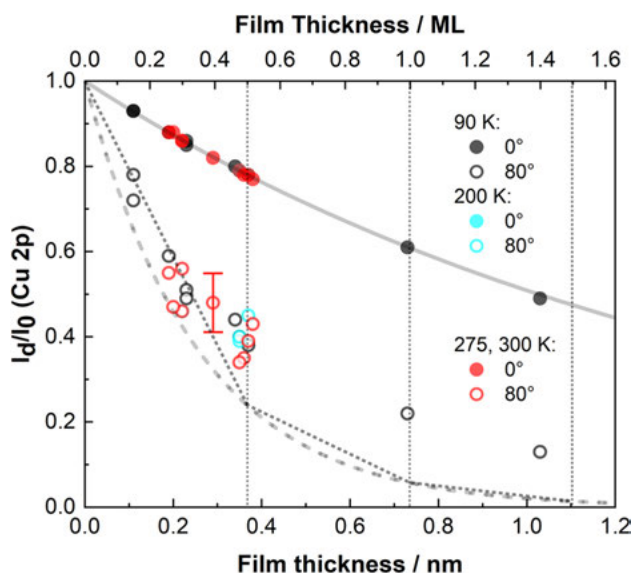


**Fig. 2** Dependence of the Cu 2p substrate signal (full symbols for 0° and open symbols for 80° emission) on IL film thickness for  $[C_1C_1Im][Tf_2N]$  on Cu(111) at 90, 200, 275 and 300 K. The film thickness of each layer was calculated from the attenuation of the Cu 2p signal at 0°. The solid and long-dashed lines show the exponential decay expected for a uniform increase in layer thickness for emission angles of 0° and 80°, respectively [36], based on the inelastic mean free path  $\lambda$  of 3.0 nm for the Cu 2p peak; the short-dashed lines for 80° are the prediction for perfect 2D layer-by-layer growth (section-wise filling of one layer of flat lying ion pairs after another, each with 0.5 ML coverage, see vertical lines). Up to 0.3 ML, very good agreement of the 80° data with the short-dashed lines is found, indicating the formation of a 2D layer; the fact that between 0.3 and 0.5 ML somewhat larger values are found indicate a small deviation from perfect 2D growth. For larger coverages, pronounced deviations from 2D growth are observed

Fig. 1 reveals a higher degree of order and less defects for the deposition at 300 K followed by fast cooling to 110 K.

## 4.2 X-ray Photoelectron Spectroscopy

### 4.2.1 Growth Behavior

Complementing the local scanning probe microscopy data, we also used XPS to follow the overall IL film growth. Figure 2 shows the attenuation of the normalized Cu  $2p_{3/2}$  signal  $I_d/I_0$  upon deposition of  $[C_1C_1Im][Tf_2N]$  at 90, 200, 275 or 300 K. After each deposition step, we measured the signals at both 0° and 80° emission angle. Under the assumption of perfect 2D growth, one can use the attenuation of the Cu 2p substrate signal at 0°,  $I_d/I_0$ , to calculate the mean film thickness  $d$  of the IL layer. From this thickness, we can then predict the attenuation at 80° for a two-dimensional IL layer at this thickness: the short-dashed grey lines represent ideal layer-by-layer 2D growth behavior in 80° for the WL (0.5 ML thickness) and another two layers on top

(the long-dashed grey line represents exponential decay and agrees with the short dashed lines for each completed layer, e.g. at 0.5 ML; for details of this approach, see refs [36, 63]. A coincidence of the measured 80° data with the predicted short-dashed lines reveals perfect 2D growth; 80° data falling above the lines indicate a deviation from layer-by-layer growth towards island growth (3D growth). Focusing first on low coverages/thicknesses up to 0.5 ML, the 80° data (open symbols) in Fig. 2 fall on or close to the short-dashed line until 0.3 ML, independent of temperature, indicating perfect 2D growth in this coverage regime. Interestingly, between 0.3 and 0.5 ML, all measured data systematically are slightly above the calculated 80° curve, which is attributed to moderate 3D growth. Such a behavior is rather unusual, since 2D growth of the first wetting layer up to 0.5 ML has been observed for a wide variety of ILs on different metal surfaces, independent of the growth mode at higher coverages. Examples are  $[C_1C_1Im][Tf_2N]$  on Au(111) [64] and Ag(111) [63],  $[C_8C_1Im][Tf_2N]$  on Ag(111) [63] and Au(111) [64] or  $[BMP][Tf_2N]$  on Au(111) [41]. The formation of the first flat wetting layer is commonly attributed to strong attractions of the ions towards the metal, e.g. by image dipoles. Above 0.5 ML, the 80° data Fig. 2 fall well above the dashed curve for ideal 2D-growth. This deviation is attributed to island formation in the multilayer regime. Note that such Stranski–Krastanov-type growth behavior is quite commonly observed for ILs with short chains, e.g. for  $[C_1C_1Im][Tf_2N]$  on Ag(111) [63] or  $[C_2C_1Im][TfO]$  on Au(111) [36, 65].

### 4.2.2 Adsorption and Thermal Evolution

In order to understand the ongoing surface chemistry of the IL in contact with the Cu(111) surface, we studied the IL layer in the low-coverage regime, during deposition and annealing by XPS. We performed measurements of all relevant IL core levels at selected temperatures, which are characteristic for the changes observed in nc-AFM, that is, 200, 275, 300 and 360 K. We investigated two coverages, namely 0.3 ML and 0.5 ML, which correspond to a partly (0.6 WL) and a more or less fully closed (1.0 WL) wetting layer, respectively; smaller coverages could not be studied reliably, due to poor signal intensities. Nevertheless, the measurements should allow for a comparison to the nc-AFM/STM measurements, which were performed for a 0.15 ML (=0.30 WL) coverage. XP spectra were measured for all core levels at 0° emission angle (and additionally at 80° for 200 K). The corresponding S 2p, C 1s, N 1s, O 1s and F 1s spectra are shown in Fig. 3 (0.5 ML) and Figure S6 (0.3 ML), along with their fits. Data at 0° and 80° are plotted in grey and blue, respectively. In addition, we also measured the corresponding 0° spectra of a multilayer film of 4.6 ML  $[C_1C_1Im][Tf_2N]$ , deposited at 90 K, as reference; these spectra are also included in Figs. 3 and S6 (bottom),

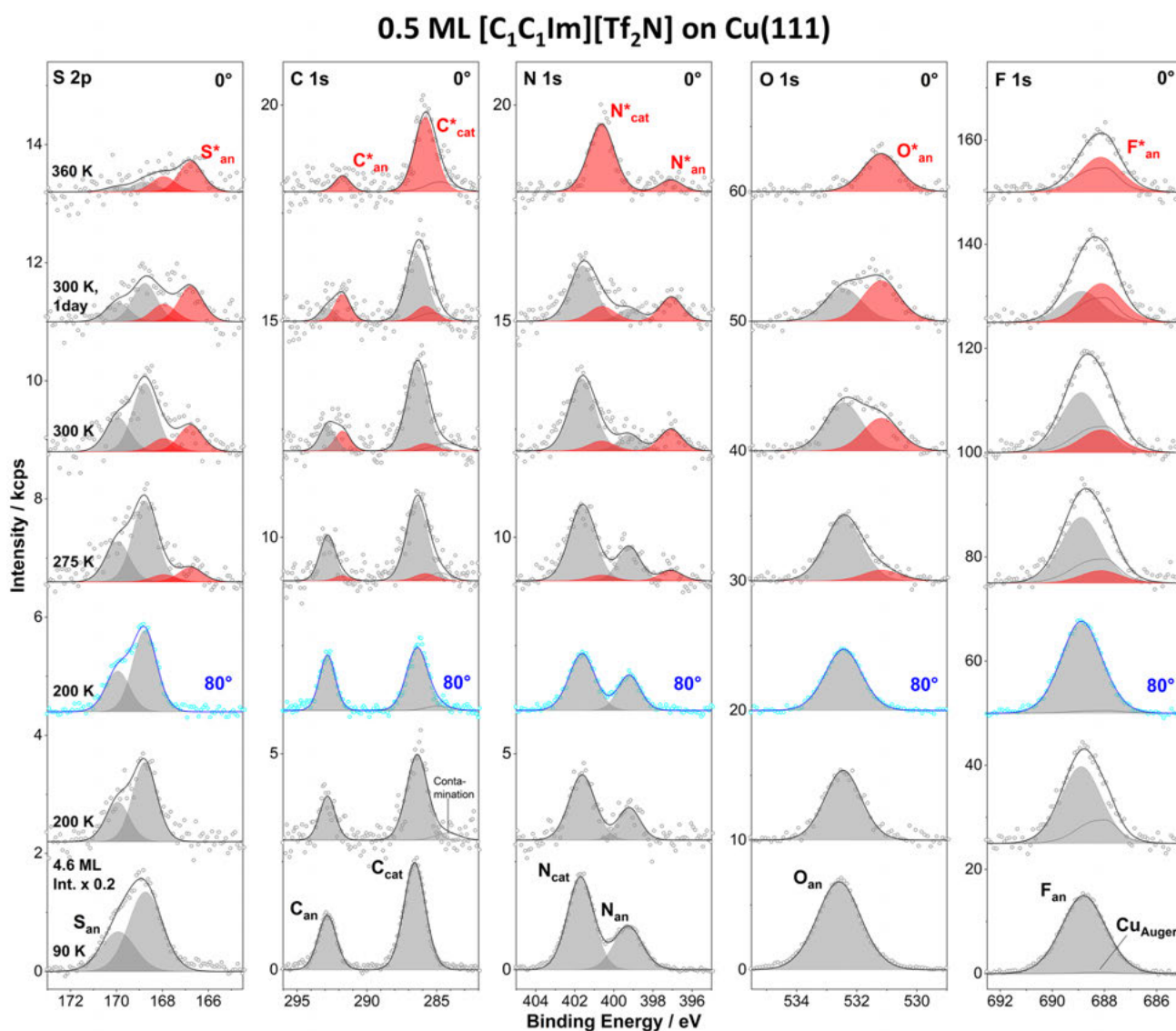


**Fig. 3** S 2p, C 1s, N 1s, O 1s and F 1s spectra of 0.5 ML [C<sub>1</sub>C<sub>1</sub>Im][Tf<sub>2</sub>N] on Cu(111) from 200 to 360 K, along with the spectra for 4.6 ML obtained at 90 K as reference for the bulk IL (bottom). For each denoted temperature, a new layer was freshly prepared and measured under normal (0°) and grazing emission (80°; shown only for 200 K in blue). For a better visualization, the 4.6 ML spectra are scaled

down by a factor of 0.2. Grey peaks indicate the signals of the intact IL, red peaks denote the peaks of the new species formed upon heating. In the C 1s spectra a small contamination of the surface was taken into account, as indicated exemplarily in the spectrum at 200 K; in the F 1s spectra, the overlapping Cu<sub>Auger</sub> signal was subtracted (for more details, see experimental section and SI)

downscaled by the factor 0.2 for better visualization. The quantitative analysis of the 0.5 ML spectra is provided in Table 2, and that of the 0.3 ML spectra in Table S1.

We start with discussing the 0° spectra of the 4.6 ML multilayer film at 90 K, as it represents the unperturbed intact IL. The cation displays two distinct peaks in the N 1s and C 1s region. The C<sub>cat</sub> peak at a binding energy of 286.6 eV is assigned to the three carbon atoms of the imidazolium ring and the two carbon atoms of the methyl groups attached to the nitrogen atoms. The N<sub>cat</sub> peak at 401.7 eV corresponds to the two nitrogen atoms in the imidazolium

ring. For the [Tf<sub>2</sub>N]<sup>-</sup> anion, the C<sub>an</sub> peak at 292.8 eV and the F<sub>an</sub> peak at 688.8 eV are assigned to the carbon and the fluorine atoms of the CF<sub>3</sub> group. The O<sub>an</sub> peak at 532.6 eV and the S<sub>an</sub> 2p<sub>1/2</sub> and 2p<sub>3/2</sub> duplet at 169.9 and 168.7 eV originate from the oxygen and sulphur of the sulfonyl-group, respectively, and the N<sub>an</sub> peak at 399.3 eV stems from the imidic nitrogen. The composition of the 4.6 ML film in Table 2 is in good agreement with the nominal composition within the experimental uncertainty (± 10%), confirming that the IL stays intact in the deposition process, in line with earlier studies [36].

**Table 2** Quantitative analysis of the composition of 0.5 ML  $[C_1C_1Im][Tf_2N]$  on Cu(111) at different temperatures, as derived from the XP spectra shown in Fig. 3 at 0° (and for 200 K also at 80°) emission angle

Temperature	$S_{an, sum}$	$C_{an, sum}$	$C_{cat, sum}$	$N_{cat, sum}$	$N_{an, sum}$	$O_{an, sum}$	$F_{an, sum}$	$\Sigma$
Nominal	<b>2</b>	<b>2</b>	<b>5</b>	<b>2</b>	<b>1</b>	<b>4</b>	<b>6</b>	<b>22</b>
360 K	0.9	0.7	4.1	1.9	0.3	2.0	3.5	13.3
300 K, 1 day	1.6	1.7	4.6	2.0	0.9	4.0	7.1	22.0
300 K	1.8	1.6	4.6	2.1	0.8	3.8	7.3	22.0
275 K	1.9	1.9	4.7	2.1	1.0	3.5	7.0	22.0
200 K, 80°	1.7	2.3	3.4	1.6	0.9	3.2	8.9	22.0
200 K	1.7	1.8	4.7	1.8	0.8	3.6	7.5	22.0
90 K	1.8	2.0	4.6	2.0	1.0	4.2	6.4	22.0

Bold value are nominal numbers, non-bold values are experimental data

Also given are the results for 4.6 ML deposited at 90 K and measured under 0° emission as reference for the bulk IL. For quantification, the shifted (marked with asterisk) and the unshifted signals of the IL were combined to provide the total atom number for each element

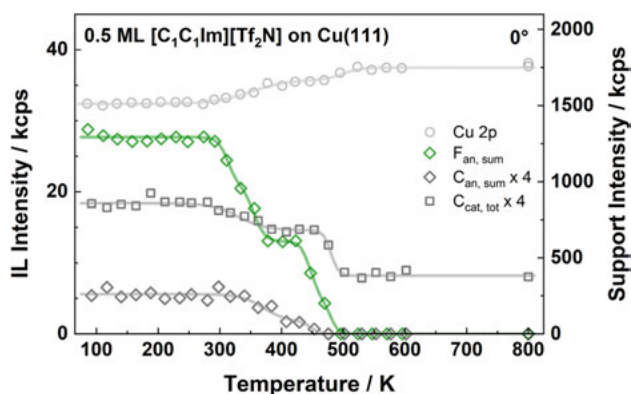


**Fig. 4** Thermal evolution of the Cu 2p (open light grey circles), F 1s (green diamonds) and C 1s (dark grey squares for  $C_{an}$ , and dark grey diamonds for  $C_{het,comb}$ ) intensities during heating a 0.5 ML  $[C_1C_1Im][Tf_2N]$  film on Cu(111). The IL was first deposited onto the sample at 88 K via PVD; thereafter, XP spectra were recorded while heating with a linear heating rate of 2 K/min up to 600 K; after flashing the sample eventually to 800 K for 5 min, a last data set was also recorded. The intensity scale for the Cu 2p signal is given on the right side and that of the F 1s and C 1s signals on the left. The symbols for the corresponding F and C species represent the sums of the corresponding unshifted and shifted (\*) intensities; note that in case of the  $C_{cation}$  region, only one broad peak could be used including the minor carbon contamination (see also Fig. 3 and for further details, see text)

The spectra for 0.5 and 0.3 ML  $[C_1C_1Im][Tf_2N]$  were recorded for all IL core levels at temperatures, at which we expected characteristic changes based on the thermal evolution observed in Fig. 1 and also Fig. 4 (see below); the full data set required ~90/130 min for all core levels of the 0.5/0.3 ML films. To minimize the influence of beam damage, always a new film was freshly prepared and measured at the indicated temperatures of 200, 275 and 300 K, except for the 360 and 500 K films, which were deposited at 300 and 200 K, respectively. Since the behavior is quite similar, the data for 0.5 and 0.3 ML will be discussed together. Thereby, the focus will be on the 0.5 ML films,

since the 0.3 ML films are more prone to beam damage, due to the longer measurement times required for the lower coverage.

For 200 K, we address the spectra at 0° (normal emission) and at 80° (grazing emission) in Fig. 3 (0.5 ML) and Figure S6 (0.3 ML), which allow for deriving information on the stoichiometry as well as the orientation of the IL on the surface. The 0° spectra are, apart from their lower intensities, very similar to those of the multilayer. The only difference is a small shift of some levels by up to 0.2 eV to lower binding energy, yielding the cation peaks  $C_{cat}$  at 286.4 eV and  $N_{cat}$  at 401.6 eV, and the anion peaks  $C_{an}$  at 292.8 eV,  $F_{an}$  at 688.9 eV,  $O_{an}$  at 532.4 eV,  $N_{an}$  at 399.2 eV, and the  $S_{an}$  duplet at 170.0/168.8 eV (for 0.5 ML); for an overview of the binding energies see Table S2 in the SI. These small shifts are attributed to more efficient screening due to the proximity of the metal surface (final state effect). For the analysis of the F 1s region, the  $Cu_{LMM}$  Auger peak at 688.0 eV, which overlaps with the  $F_{an}$  signal of the anion, has to be considered. This is done by using the Auger peak shape of the clean copper surface, downscaling it according to the IL-film related attenuation of the Cu 2p signal. By fitting the F 1s peak taking into account this downscaled Auger peak, we obtain the correct number of F atoms in Table 2 (note that at elevated temperatures, new species with shifted binding energies appear as discussed below; in Table 2, only the sum for each atom is given). The quantitative analysis of the 0° spectra in Table 2 (0.5 ML) and Table S1 (0.3 ML) yields atom numbers close to the nominal values within the experimental uncertainty ( $\pm 10\%$ ); the somewhat too large value of the F 1s signal is attributed to uncertainties in the described Auger peak correction procedure. The very good agreement of XPS quantification in 0° and IL stoichiometry again is a clear indication that the IL adsorbs intact at 200 K.

From the quantitative analysis of the 80° spectra at 200 K in Table 2 and Table S1, we gain insight into the orientation of  $[C_1C_1Im][Tf_2N]$  on the Cu(111) surface at this

temperature as already done earlier for this IL on Au(111) [64]: An intensity decrease at 80° as compared to 0° for certain IL signals of the two-dimensional WL indicates that the corresponding atoms are close to the metal surface and are attenuated by the atoms above, yielding lower than the nominal atom numbers. On the other hand, enhanced signals at 80° indicate that these atoms are near the vacuum, leading to larger than nominal atom numbers at 80°. At 200 K,  $F_{\text{an,sum}}$  exhibits a larger than nominal atom number and  $O_{\text{an,sum}}$  a lower than nominal atom number, indicating that the anion is adsorbed with the oxygen atoms towards the copper surface, while the  $\text{CF}_3$  groups preferentially point toward the vacuum, as it is often observed for ILs of this kind [36]. The cation signals  $C_{\text{cat,sum}}$  and  $N_{\text{cat,sum}}$  are systematically attenuated in 80° indicating that the imidazolium ring is closer to the surface than the  $\text{CF}_3$  groups of the anion. Overall, the adsorption behavior at 200 K thus shows clear similarities to that of comparable ILs on Ag(111) and Au(111) [36, 63, 64]. We therefore conclude also from the XPS data that  $[\text{C}_1\text{C}_1\text{Im}][\text{Tf}_2\text{N}]$  exhibits the checkerboard arrangement at 200 K as it is frequently observed for ILs, in which the anion and cation adsorb alternately next to each other on the surface [36].

We next address the spectra at higher temperatures. At 275 K, new peaks start to appear (marked in red, with an additional asterisk), at the expense of the original peaks (see Figs. 3 and S6), which decrease in intensity. The new peaks all exhibit pronounced shifts towards lower binding energies relative to the peaks of the intact IL at 200 K (see Table S2 in the SI). The anion-related peaks are shifted by  $-2.1$  eV for  $\text{N}_{\text{an}}^*$ ,  $-1.3$  eV for  $\text{O}_{\text{an}}^*$ ,  $-1.1$  eV for  $\text{C}_{\text{an}}^*$ ,  $-0.7$  eV for  $\text{F}_{\text{an}}^*$  and  $-2.0$  eV for  $\text{S}_{\text{an}}^*$ , and the cation-related peaks by  $-1.0$  eV for  $\text{N}_{\text{cat}}^*$  and  $-0.6$  eV for  $\text{C}_{\text{cat}}^*$ . As already mentioned above, in the quantitative analysis in Tables 2 and S1, only the sum of the shifted (\*) and the pristine signals of the IL is given (as indicated with subscript “sum”), in order to provide the total amount for each element.

Upon deposition at 300 K and measuring immediately afterwards, a further increase of the shifted signals and decrease of the unshifted signals is observed in Fig. 3 for 0.5 ML (and in Figure S7 on larger scale), and in Figure S6 for 0.3 ML. This “signal conversion” is even more pronounced when keeping the sample for one day at 300 K after deposition (without X-ray exposure to avoid any beam damage in the meantime), and measuring afterwards. Notably, despite the changes observed for the 275, 300 and 300 K (1 day) spectra, the overall IL composition in 0° (sum of shifted and unshifted signals) is still in good agreement with the nominal values for both investigated coverages (cf. Tables 2 and S1). Thus, no significant loss of individual atoms by desorption occurs up to 300 K (minor deviations might be due to the bad signal-to-noise ratio or indicate changes in ion orientation). The analysis of the XP spectra data for the 0.5 ML film measured immediately after deposition at 300 K in Fig. 3

shows that  $39 \pm 15\%$  of the original anion peaks at 200 K are converted to the new  $\text{N}_{\text{an}}^*$ ,  $\text{O}_{\text{an}}^*$ ,  $\text{C}_{\text{an}}^*$ ,  $\text{F}_{\text{an}}^*$  and  $\text{S}_{\text{an}}^*$  peaks. For the cation peaks, only a much smaller fraction of  $10 \pm 2\%$  is converted to  $\text{N}_{\text{cat}}^*$  and  $\text{C}_{\text{cat}}^*$ . After 1 day at 300 K, the total coverage slightly decreased, and the degree of conversion increases to  $58 \pm 10\%$  of the anions and  $20 \pm 2\%$  of the cations (with the total anion and cation signals still agreeing with the nominal composition; see Table 2). Note that for the 0.3 ML deposition series (see Figure S6), overall the same trend is observed as for the 0.5 ML discussed here, with the conversion to the (\*) species being, however, more pronounced. Most likely, the apparently more reactive situation in case of the 0.3 ML is related to increased beam damage effects since longer measurement times are required at the lower coverage regime to obtain reasonable signals. As will be discussed in detail in the next section, we propose that the unshifted anion and cation signals are due to intact ion pairs on the surface, forming the well-ordered striped phase at 200 K and the hexagonal and honeycomb phases at 300 K. On the other hand, the shifted signals are related to species within the disordered small islands, where cations and anions have partially reacted/decomposed at the copper surface into non-volatile fragments. The smaller fraction of shifted cation signals (as compared to the larger amount of shifted anion signals) is possibly related to the fact that some of the cation fragments still exhibit binding energy values close to the original peaks in contrast to the anion ones (see next section for more details).

At 360 K, the pristine IL signals have virtually disappeared, and only the shifted signals are left (Figs. 3 and S6). In particular, the total amount of  $C_{\text{an,sum}}$ ,  $O_{\text{an,sum}}$ ,  $F_{\text{an,sum}}$  and  $S_{\text{an,sum}}$ , that is, all elements involved in the anion, is reduced to  $\sim 50\%$  compared to the starting point (see Tables 2 and S1). The halving of the anion signals between 300 and 360 K is a strong indication for the desorption of anions or fragments of anions. Notably, this is in line with the in situ temperature-programmed XPS (TPXPS) experiment in Fig. 4 (see below), which also shows a drop of  $\sim 50\%$  starting from 300 K in the  $F_{\text{an}}$  signal (as representative for the whole anion). Simultaneously to the decrease of the total anion intensity, we observe the total conversion of the remaining cation signals  $C_{\text{cat}}$  and  $N_{\text{cat}}$  to the  $C_{\text{cat}}^*$  and  $N_{\text{cat}}^*$  species (at lower binding energies by  $-0.6$  and  $-1.0$  eV, respectively) along with a small intensity decrease, indicating that also the cation coverage is affected by the ongoing surface processes. Note that this situation at 360 K is likely to represent the one at 350 K in Fig. 1d, where only small disordered islands are observed in nc-AFM (for the initial coverage of 0.15 ML). At 500 K, all anion-derived signals have completely vanished (not shown), and only residual carbon and nitrogen species (with an approximate atomic ratio  $C_{\text{res}}: N_{\text{res}} = 5: 1$ ) remain at the copper surface. Moreover, an additional S 2p duplet

at 162.4/161.6 is observed at 500 K, which is attributed to atomic sulphur as a remaining decomposition product.

To follow the thermal evolution of the wetting layer more closely, we deposited 0.5 ML of  $[\text{C}_1\text{C}_1\text{Im}][\text{Tf}_2\text{N}]$  on Cu(111) at 88 K and subsequently heated to 600 K with a linear heating ramp of 2 K/min while performing temperature-programmed (TP)-XPS at normal emission. To minimize beam damage, we restricted our analysis to three core levels: Along with the Cu 2p substrate signal (to follow the overall film thickness), we measured only C 1 s and F 1 s spectra. After the ramp was finished, we recorded an additional data set after flashing to 800 K to look for further changes. Figure 4 depicts the quantitative analysis of the Cu 2p substrate signals, the total F 1 s signals  $F_{\text{an,sum}} (=F_{\text{an}} + F_{\text{an}}^*)$ , and the C 1 s signals of the anion carbon  $C_{\text{an,sum}} (=C_{\text{an}} + C_{\text{an}}^*)$  and cation carbon  $C_{\text{cat,tot}}$  (note that due to the reduced signal-to-noise ratio in this TPXPS series, a clear discrimination of  $C_{\text{cat}}$ ,  $C_{\text{cat}}^*$  and at higher temperatures residual carbon was impossible and we thus provide only the total amount using one broad peak for fitting this binding energy range); carbon intensities have been multiplied by factor four for better visualisation. All signals show characteristic intensity changes with temperature, which are in line with the data in Fig. 3. The  $F_{\text{an,sum}}$  signal stays constant from 100 to  $\sim 300$  K at  $\sim 28$  kcps. At higher temperatures, it decreases by about 50% to reach a plateau at  $\sim 13$  kcps at around 400 K, and finally drops zero at around 500 K. The  $C_{\text{an,sum}}$  signal shows the same change with temperature, which indicates the loss of  $\text{CF}_3$ -groups in course of the reaction/fragmentation discussed above. Note that the increase of the shifted  $F_{\text{an}}^*$  and  $C_{\text{an}}^*$  signals at the expense of the unshifted signals is also seen in the data of the TPXPS experiment (not shown), similar to the observations in Fig. 3. In contrast to the anion signals, the cation signal  $C_{\text{cat,tot}}$  shows much smaller changes in intensity. It initially remains constant until 300 K at  $\sim 18$  kcps, and thereafter only slightly decreases to  $\sim 15$  kcps at 370 K. After a plateau until 450 K, it finally drops to  $\sim 8$  kcps between  $\sim 460$  and 500 K, and then stays constant till 800 K; note that the remaining residual carbon C 1 s peak at 500 and 800 K is much broader compared to the original  $C_{\text{cat}}$  peak.

### 4.3 Comparison of nc-AFM/STM and XPS Results

When comparing the nc-AFM images in Fig. 1 and the XPS data in Figs. 3 and S6, we can derive information on the nature of the different surface species at the different temperatures. At 200 K, the adsorbed IL is found in long-range ordered islands, and the very small, disordered islands are absent in nc-AFM. In this temperature range, XPS only detects species with binding energies characteristic of the intact IL. XPS thus corroborates our interpretation of the microscopy data that at this temperature, namely that the deposited IL forms ordered islands consisting of intact ion

pairs regularly adsorbed next to each other in the checkerboard arrangement, giving rise to the stripe-like appearance as discussed above. At 300 K, we observe the transformation of the stripe-like island structure first to the hexagonal metastable transition phase and finally to the honeycomb structure. At the same time, we also observe an increasing number of small, disordered islands which coexist with the long-range ordered hexagonal and honeycomb phases. Starting at around 275 K, we also observe pronounced changes in XPS, that is, a partial transformation of the original IL peaks to new chemical shifted (\*) peaks. The observed chemical shifts range between 0.7 and 2.1 eV towards lower binding energies for the anion signals and 0.6–1.0 eV for the cation signals. They indicate a chemical reaction with partial decomposition of the IL on the Cu(111) surface. As the formation of the small disordered islands in nc-AFM is observed in the same temperature region as the formation of the new peaks in XPS, we conclude that the small disordered islands are mainly formed by the products of this ongoing reaction, while the remaining unshifted peaks originate from the intact IL ion pairs within the large and well-ordered islands. The small size of the disordered islands indicates that the decomposed species are to some extent mobile on the surface, which allow them to agglomerate into these islands. Notably up to 300 K, no desorption of reaction products occurs, since the sum of IL- and IL\*-signals does not change within the margin of uncertainty of the experiments. Upon heating to 350 K, in nc-AFM a complete conversion to small disordered islands occurs, which in XPS goes along with a complete disappearance of the unshifted peaks due to conversion to the shifted peaks. In addition,  $\sim 50\%$  of the anion signals and 10–20% of the cation signals are lost due to desorption of volatile species.

In the literature, two studies exist on related systems. Biedron et al. performed a detailed comparative XPS, UPS and STM study of  $[\text{C}_8\text{C}_1\text{Im}][\text{Tf}_2\text{N}]$  deposited onto Cu(100) and Au(111) at and above room temperature [46]. They observed that on Au(111), the XPS binding energies of all IL peaks of the layer in direct contact with the surface show only a small uniform shift relative to multilayer spectra. In contrast on Cu(100), they observed that for the first layer, the anion-related signals are shifted to lower binding energy by  $-2.0$  eV for  $\text{N}_{\text{an}}^*$ ,  $-1.5$  eV for  $\text{O}_{\text{an}}^*$ ,  $-0.8$  eV for  $\text{C}_{\text{an}}^*$ ,  $-0.6$  eV for  $\text{F}_{\text{an}}^*$  and  $-1.8$  eV for  $\text{S}_{\text{an}}^*$ , as deduced from their spectra (cf. Figure 6 of [46]; the positions of the cation peaks were difficult to discern); these values agree to within max. 0.3 eV with the values observed for the shifted peaks in this study. At the same time, the stoichiometry corresponded to that of an intact IL. Biedron et al. attributed these shifts to a much stronger interaction of the intact IL with the Cu(100) surface, which they also used to explain the more stable imaging conditions at the monolayer coverages on Cu(100) as compared to Au(111).

The second study was performed by Uhl et al. who deposited 1-butyl-1-methylpyrrolidinium bis(trifluoromethylsulfonyl)imide ([BMP][Tf<sub>2</sub>N]) on Cu(111) at 80 K in the sub-monolayer range, also using STM and XPS for characterization [47]. While up to 200 K no changes were observed, annealing to 300–350 K yielded pronounced shifts of the anion peaks towards lower binding energy by  $-1.1$  eV for C\*<sub>an</sub>,  $-0.5$  eV for F\*<sub>an</sub> and  $-2.3$  eV for S\*<sub>an</sub>, a decrease of oxygen by 60%, and in addition the formation of atomic sulphur, indicating major structural changes of the IL layer and partial decomposition of the anion at this temperature. The binding energies of the shifted anion signals are similar to those found in this study (deviations between 0.1 and 0.3 eV) and also for [C<sub>8</sub>C<sub>1</sub>Im][Tf<sub>2</sub>N] on Cu(100) by Biedron et al. Interestingly, Uhl et al. report essentially unaffected [BMP]<sup>+</sup>-related signals at 300 K, which agrees with the dominance of the unshifted [C<sub>1</sub>C<sub>1</sub>Im]<sup>+</sup> XPS signals of our study at 300 K as shown in Fig. 3: slightly depending on annealing time and initial coverage, only 10–20% of the pristine cation signals are converted at this temperature, in contrast to the much stronger conversion of anion signals.

Based on our results, we are now able to derive a comprehensive understanding of the two studies by Biedron et al. and Uhl et al. and resolve apparent discrepancies [46, 47]. We propose that for all three investigated systems, that is, [C<sub>8</sub>C<sub>1</sub>Im][Tf<sub>2</sub>N] on Cu(100), [BMP][Tf<sub>2</sub>N] on Cu(111), and [C<sub>1</sub>C<sub>1</sub>Im][Tf<sub>2</sub>N] on Cu(111) overall the same adsorption and reaction behavior is observed, with some differences in the reaction temperatures: For adsorption at low temperatures (< 200 K), the corresponding IL adsorbs intact and with signatures typically observed for non-reactive surfaces like Au or Ag, in terms of XPS binding energies and formation of a checkerboard structure. Upon heating to or adsorption at room temperature, a very similar behavior is observed in XPS for the three systems studied that is, the [Tf<sub>2</sub>N]<sup>−</sup> signals exhibit pronounced shifts toward lower binding energies, indicating that for all systems a similar conversion of mainly the anion peaks occurs. In this first step, the cation signals are not (or only moderately) affected. Based on our findings and in contrast to what was proposed by Biedron et al., we assign the observed shifts of the anion peaks not to an enhanced interaction of the pristine IL with the Cu surface, but to a temperature-induced reaction, which progresses with time at 300 K. Above room temperature, in a second step most of the cation signals also show a pronounced shift, while the shifted anion signals remain at the same binding energy, but decrease by 50%. This behavior indicates decomposition of the ILs and/or partial desorption of the ILs or reaction products. After this step, no long-range order can be detected in nc-AFM or STM.

At this point, we have to address the chemical nature of the reaction products formed above 275 K in our sub-ML

studies of [C<sub>1</sub>C<sub>1</sub>Im][Tf<sub>2</sub>N] films on Cu(111). We attribute the simultaneous formation of the new peaks observed in XPS and of the disordered islands in nc-AFM to a reaction/decomposition of the IL on the surface yielding new surface species. These might be related to one (or to a combination) of the following three explanations:

Explanation (1), which is most favoured by us, is the partial decomposition of the IL above 275 K to small and non-volatile fragments such as NH<sub>x</sub>, SO<sub>x</sub>, fluorocarbon species (CF<sub>3</sub>), carbene-like and/or other species, which remain in the small disordered islands on the surface at 300 K. The fact that the degree of conversion of the unshifted to the shifted peaks in XPS is different for the anion and cations (~40% and 10%, respectively, e.g. for 0.5 ML) could indicate that for the cation several decomposition products with different XPS binding energies are formed, one of which is similar to that of the unshifted peaks of the intact IL. After annealing to 360 K, a part of the anion-related fragments (likely charge neutral) has desorbed, as concluded from the ~50% loss of anion signals.

Another decomposition path could be given by explanation (2), where the [C<sub>1</sub>C<sub>1</sub>Im]<sup>+</sup>-cations of the IL are deprotonated in C2-position and Cu-carbenes are formed, binding to the Cu(111) surface or to copper adatoms. The protons would be transferred to copper and could react with the anions to form neutral H[Tf<sub>2</sub>N], which subsequently desorbs above 350 K. For example, the formation of an organometallic copper dicarbene was observed in STM, XPS and DFT calculations by Jiang et al. [66]: The authors reacted 1,3-Dimethyl-1H-imidazol-3-ium-2-carboxylate with Cu(111), which forms [C<sub>1</sub>C<sub>1</sub>Im\*]Cu[C<sub>1</sub>C<sub>1</sub>Im\*] dimers at the surface after CO<sub>2</sub> elimination ([C<sub>1</sub>C<sub>1</sub>Im\*] is denoted here as the carbene after deprotonation of [C<sub>1</sub>C<sub>1</sub>Im]<sup>+</sup> at position 2). An explanation along these lines can, however, be ruled out, since we observe similar changes in the XP spectra with temperature for the related IL [C<sub>1</sub>C<sub>1</sub>C<sub>1</sub>Im][Tf<sub>2</sub>N] (Figure S8 and Table S3 in the SI), where the most acidic proton of [C<sub>1</sub>C<sub>1</sub>Im]<sup>+</sup> in position 2 is replaced by a methyl group, and thus deprotonation should not occur (or should occur only at considerably higher temperatures). Furthermore, carbene formation also appears to be very unlikely since for [BMP][Tf<sub>2</sub>N] on Cu(111) overall a very similar thermal evolution to that of [C<sub>1</sub>C<sub>1</sub>Im][Tf<sub>2</sub>N] on Cu(111) is found (see discussion above).

Finally, we cannot completely rule out a third explanation (3), namely that upon heating to 275 K and above, parts of the intact IL reorganize without decomposition, e.g. by interaction with Cu adatoms, forming a specific Cu-IL complex. The complexation would have to affect the electronic structure of the still intact IL such that the corresponding IL signals exhibit the observed strong decreases in binding energy. The formed Cu-IL complex could also be an initial step towards carbene formation, initiating also the

decomposition of the IL and the desorption of H[Tf<sub>2</sub>N] at 360 K. We consider this last option, however, as rather unlikely.

#### 4.4 Ordered Structures and DFT Calculations

As final step we aim for a more detailed understanding of the ordered structures based on the nc-AFM images in Fig. 1 through corresponding DFT calculations.

##### 4.4.1 Stripe Structure at 200 K

The stripe structure Fig. 1a (right) and Fig. 5a (left) has a rectangular unit cell ( $\gamma = 90 \pm 3^\circ$ ) with vectors  $\vec{a}$  ( $1.90 \pm 0.08$  nm) and  $\vec{b}$  ( $0.90 \pm 0.05$  nm), yielding a unit cell area of  $\sim 1.71$  nm<sup>2</sup> (see Table 1). This structure is similar to the stripy structure observed for the same IL on Au(111), with a unit cell area of  $\sim 0.74$  nm<sup>2</sup>, and one ion pair per unit cell [43]. If we assume a comparable ion pair density in the wetting layer on both surfaces, this is a strong indication that the unit cell on Cu(111) in Fig. 1 and Fig. 5a (left) contains 2 ion pairs, which yields an ion pair density of 1.17 ion pairs/nm<sup>2</sup>. In Fig. 1 (see above), we tentatively assigned the very bright oval protrusion (red ellipses) and the two less bright protrusions (blue ellipses) to two differently oriented anions, and the dark areas in between (black ellipses) to the two cations.

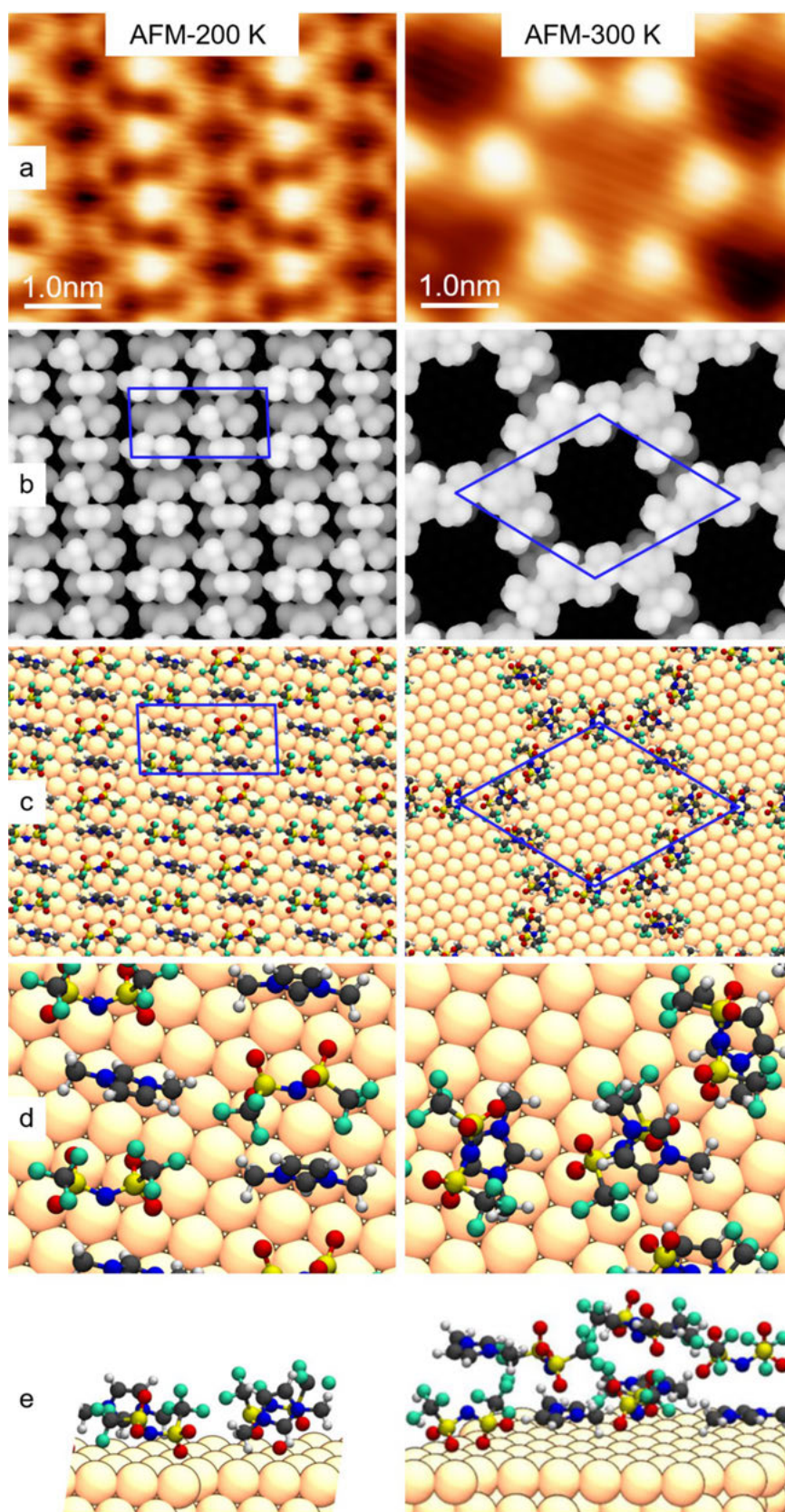
As a next step, we discuss the results from DFT. Because we have a highly ordered structure, we calculated a commensurate structure with a  $\begin{bmatrix} 6 & 2 \\ -3 & 4 \end{bmatrix}$  superstructure. The lattice vectors  $\vec{a}$  (1.83 nm) and  $\vec{b}$  (0.92 nm) with an angle  $\gamma$  of  $92.2^\circ$  yield a unit cell area of  $\sim 1.68$  nm<sup>2</sup>, which (within the margin of error) very well agrees with the experimental values determined from the nc-AFM images. The resulting structure after geometry optimization is shown in Fig. 5c, d and e (left). It reveals two similarly oriented cations with their plane nearly perpendicular to the surface, and the C2 carbon atom of the imidazolium ring pointing downwards, that is, towards the surface. Interestingly, the two anions have different orientations: one is adsorbed nearly vertically with all four oxygen atoms of the sulfonyl groups pointing downwards in 2–2 orientation adsorption motif, and the six F atoms of the two CF<sub>3</sub> groups pointing away from the surface towards vacuum; the other is adsorbed side-on with only one oxygen atom of each sulfonyl group attached to the surface, that is, in 1–1 orientation adsorption motif, and 3 F atoms pointing towards vacuum. These two different orientations are likely responsible for the different contrast of the anions observed by nc-AFM. The DFT structure is also in line with the overall orientation derived from XPS (see above). The resulting adsorption energy  $E_{ads}$ , which is the energy difference between the

isolated ion pair in the gas phase and adsorbed in the proposed layer, yields a value of 3.5 eV per ion pair, indicating a very stable structure. One should note here that small modifications to the unit cell yield quite similar results. In an attempt to simulate the nc-AFM images using a simplified approach, we calculated charge density contour plots; the corresponding image is shown in Fig. 5b (left). The agreement with the experimental data is surprisingly good, considering the fact that the contrast strongly depends on the status of the nc-AFM tip and the simplicity of the calculation. One interesting aspect are the different contributions to the calculated total adsorption energy; the detailed analysis shows that the vertical interaction of the ions with the copper surface via their image charges amounts to  $\sim 1.6$  eV, while the lateral Coulomb interaction within the checkerboard wetting layer amounts to  $\sim 2.0$  eV (see Tables S6 and S7 for details on the different contributions to the adsorption energies; the geometries of the different calculated geometries are provided in a separate zip-file).

##### 4.4.2 Honeycomb Structure at 300 K

We next address the honeycomb structure. The lattice vectors  $\vec{a}$  and  $\vec{b}$  have an identical length of  $2.35 \pm 0.08$  nm, yielding an unit cell area of 4.78 nm<sup>2</sup>. It can be described by a  $\begin{bmatrix} 8 & 2 \\ -2 & 10 \end{bmatrix}$  superstructure. Based on the significant fraction of unshifted XPS peaks of anions and cations, we attribute the honeycomb structure to intact IL ion pairs. When addressing the number of ion pairs per unit cell, we have to consider the specific properties of the honeycomb lattice. The unit cell of the honeycomb structure in Fig. 1c (right) and Fig. 5a (right) has 2 bright protrusions (indicated as circles) and 3 dimmer ones (dots). If we assume that the bright protrusions are either anion or cation (and not anions and cations that coincidentally exhibit the same brightness), this immediately implies that the bright protrusions cannot be anions and the dimmer ones cations (or vice versa), as this would violate charge neutrality. One solution is that the bright and dim protrusions are oppositely oriented “sandwiches” composed of stacked cations and anions. Based on our assignment of the well-ordered honeycomb-structure to intact IL ion pairs with unshifted XPS peaks (see previous sections), we propose that the XPS binding energies are not affected by the opposite orientation of the sandwiches; we thus observe only one narrow peak for each element. This structure contains 5 ion pairs per unit cell, which yields an ion pair density of 1.05 ion pairs/nm<sup>2</sup>, which is slightly smaller than that of the stripe structure. The fact that some of the pores of the honeycomb structure are empty and some have a dim background is attributed to leftovers of the transformation process.

**Fig. 5** Surface structure of  $[C_1C_1Im][Tf_2N]$  on Cu(111) for the stripe phase (left) and the honeycomb phase (right). **a** nc-AFM images (data from Fig. 1). **b** Charge density plots of the corresponding structures, as derived from DFT calculations. **c** Geometry-optimized structures, as obtained from the DFT calculations. **d** Close-up of the structures shown in (c). **e** Side view of the structures shown in (c). Graphs (a) to (e) are shown on the same scale, as indicated by the scale bars in (a)



For the honeycomb structure with oppositely oriented sandwiches we also performed DFT calculations. The corresponding structure is shown in Fig. 5c, d and e (right) and the corresponding calculated charge density contour plots in Fig. 5b (right). The structure yields an adsorption energy  $E_{ads}$  per ion pair of 3.1 eV, which demonstrates the stability of this porous arrangement. Notably, this adsorption energy value is smaller than the value of 3.5 eV calculated for the nearly rectangular checkerboard-type structure (see above). The reason for the higher adsorption energy of the checkerboard structure is its larger dispersion energy compared to the honeycomb structure; see SI, Table S6. The lower dispersion energy of the honeycomb structure is not surprising because it consists of IL pairs in a sandwich geometry. The top IL molecules of each pair have a larger distance from the metal substrate leading to a smaller dispersion interaction with the substrate. In the checkerboard structure, on the other hand, all IL molecules are in direct contact with the metal substrate structure. One should note that the lower adsorption energy of the honeycomb structure is not expected from the experimental findings, as from a simple consideration one would assume a higher adsorption energy, since upon annealing a transformation towards a more stable structure should occur. Possible reasons are that in the experiment the decomposition of a fraction of the IL layer (yielding the disordered islands) goes along with the formation of the honeycomb structure, and the related energies would have to be included in the total energy balance. An alternative explanation would be that in the calculations, the geometry optimization did not find the global minimum with maximum binding energy. One possible, though unlikely, alternative could be that we actually do not have the structure proposed above, but that a metastable intermediate complex including Cu substrate or adatoms is formed. In particular nitrogen atoms, which are present in the anion and the cation, are known to play an important role in the formation of Cu coordinated frameworks on surfaces [67, 68–70]. The latter considerations are, however, pure speculation.

## 5 Summary and Conclusions

We investigated the initial formation and thermal stability of sub-monolayer ionic liquid films on Cu(111) as a function of temperature with non-contact atomic force and scanning tunneling microscopy, angle-resolved X-ray photoelectron spectroscopy, and density-functional theory calculations. The IL  $[C_1C_1Im][Tf_2N]$  was deposited either at room temperature followed by very fast cooling to 110 K, or directly at low temperatures. Both procedures lead to the adsorption of intact IL on the surface. The thermal evolution of the adsorbate structure and chemical composition was then

investigated by stepwise annealing. The nc-AFM and the STM studies were performed for a coverage of 0.15 ML, which corresponds to ~30% of the surface being covered with a wetting layer of anions and cations adsorbed next to each other in direct contact with the Cu(111) surface. Due to the low signals, the corresponding XPS studies were performed for coverages of 0.5 and 0.3 ML, which correspond to 100% and 60% of the full wetting layer, respectively.

Annealing to 200 K leads to the formation of large islands. Each island consists of one or more domains of a highly ordered phase characterized by molecular rows, that is, stripes with a nearly rectangular unit cell ( $\gamma = 90 \pm 3^\circ$ ), with lattice vectors of  $\vec{a}$  ( $1.90 \pm 0.08$  nm) and  $\vec{b}$  ( $0.90 \pm 0.05$  nm), and a unit cell area of  $1.71$  nm<sup>2</sup>. The checkerboard-type adlayer can be described by a  $\begin{bmatrix} 6 & 2 \\ -3 & 4 \end{bmatrix}$  superstructure; the protrusions visible in nc-AFM are assigned to two types of differently oriented anions and the dark spots in-between to the cations. The chemical composition measured by XPS confirms that at 200 K intact anions and cations are indeed adsorbed next to each other. Based on the nc-AFM and XPS results and the DFT calculations, we propose that the unit cell contains 2 ion pairs, yielding a density of  $1.17$  ion pairs/nm<sup>2</sup>. From DFT, we derived an adsorption energy per ion pair of 3.5 eV, which can be decomposed into a contribution of ~1.6 eV from the interaction with the substrate and ~2.0 eV due to lateral interactions within the IL (see SI, Table S7).

Upon heating to 300 K and annealing at this temperature for hours, we observe a sequence of structural changes in the nc-AFM images which are accompanied by pronounced changes in the XP spectra. In nc-AFM, we observe for the large islands first the transformation of the stripe structure to an overall hexagonal structure and finally to a well-ordered honeycomb-type structure with a pore size of ~2 nm, which goes along with the additional appearance of numerous small disordered islands. Simultaneously, a partial conversion of the initial IL peaks towards peaks shifted to lower binding energies is observed in XPS, which is most pronounced for the anions. From the simultaneous appearance of the small disordered islands and the pronounced changes in XPS, we propose that a chemical reaction yielding partial IL decomposition occurs around 300 K, with the reaction products forming the disordered islands. The large islands with the hexagonal and the honeycomb structure still consist of intact ion pairs. Upon further heating to 350 K, only small disordered islands are observed by nc-AFM, and in XPS, the conversion of all anion and cation signals indicates a complete decomposition of the IL on the surface. Notably at this temperature, nearly 50% of the anion-derived reaction products but only 10–20% of the cationic ones left the surface as deduced from the related signal decreases in XPS.

Interestingly, the well-ordered hexagonal and honeycomb structures of the large islands at 300 K have the identical unit cells with lattice vector lengths  $2.35 \pm 0.08$  nm and a unit cell area of  $\sim 4.78$  nm<sup>2</sup>; they can be described by a  $\begin{bmatrix} 8 & 2 \\ -2 & 10 \end{bmatrix}$  superstructure with an angle of 60°. For the overall hexagonal structure, we assume six ion pairs per unit cell, which yields a density of 1.26 ion pairs/nm<sup>2</sup>, and for the honeycomb structure five ion pairs per unit cell, which yields a density of 1.05 ion pairs/nm<sup>2</sup>. Notably, the honeycomb structure can be obtained from the overall hexagonal structure by removing one ion pair, which results in the pore of the honeycomb structure. Thus, the hexagonal structure can be seen as metastable transition structure from the stripe phase to the honeycomb phase upon annealing the IL layer at 300 K. From the unit cell area and the number of ion pairs per unit cell, we conclude that in the two structures the IL is not adsorbed in the commonly observed checkerboard arrangement with anions and cation next to each other. We rather propose that they adopt a stacked “sandwich structure” of anions and cations, with the sandwiches adsorbed on the surface alternatingly with opposite orientations. Our DFT calculations indeed show that such a structure is quite stable on the surface with an adsorption energy of 3.1 eV.

To conclude, by a combination of experimental and theoretical methods, we were able to obtain detailed insights into the adsorption and reaction of the IL [C<sub>1</sub>C<sub>1</sub>Im][Tf<sub>2</sub>N] on the Cu(111) surface. In contrast to the adsorption of the same IL on Au(111), a very complex thermal evolution with structural changes and decomposition effects was observed even at room temperature due to the more reactive copper atoms. Moreover, our results allowed for solving apparently conflicting results of two previous studies of related ILs on copper surfaces. We are confident that such model thin film studies under well-defined conditions to gain a molecular understanding into IL-metal interactions at interfaces eventually will allow for a more controlled design and use of ILs for particular applications in many areas.

**Supplementary Information** The online version contains supplementary material available at <https://doi.org/10.1007/s11244-023-01801-y>.

**Acknowledgements** Funded by the Deutsche Forschungsgemeinschaft (DFG, German Research Foundation)—Project-ID 431791331 – SFB 1452 (Catalysis at Liquids Interfaces, CLINT).

**Funding** Open Access funding enabled and organized by Projekt DEAL. Funding was provided by Deutsche Forschungsgemeinschaft (Project-ID 431791331).

## Declarations

**Conflict of interest** The authors declare no competing interest.

**Open Access** This article is licensed under a Creative Commons Attribution 4.0 International License, which permits use, sharing,

adaptation, distribution and reproduction in any medium or format, as long as you give appropriate credit to the original author(s) and the source, provide a link to the Creative Commons licence, and indicate if changes were made. The images or other third party material in this article are included in the article's Creative Commons licence, unless indicated otherwise in a credit line to the material. If material is not included in the article's Creative Commons licence and your intended use is not permitted by statutory regulation or exceeds the permitted use, you will need to obtain permission directly from the copyright holder. To view a copy of this licence, visit <http://creativecommons.org/licenses/by/4.0/>.

## References

1. Welton T (1999) Room-temperature ionic liquids. Solvents for synthesis and catalysis. *Chem Rev* 99(8):2071–2084
2. Wasserscheid P, Keim W (2000) Ionic liquids—new “solutions” for transition metal catalysis. *Angew Chem Int Ed* 39(21):3772–3789
3. Wasserscheid P, Welton T (2008) Ionic liquids in synthesis, vol 1. Wiley, New York
4. Plechkova NV, Seddon KR (2008) Applications of ionic liquids in the chemical industry. *Chem Soc Rev* 37(1):123–150
5. Welton T (2018) Ionic liquids: a brief history. *Biophys Rev* 10(3):691–706
6. Binnemans K (2005) Ionic liquid crystals. *Chem Rev* 105(11):4148–4204
7. Crosthwaite JM, Muldoon MJ, Dixon JK, Anderson JL, Brennecke JF (2005) Phase transition and decomposition temperatures, heat capacities and viscosities of pyridinium ionic liquids. *J Chem Thermodyn* 37(6):559–568
8. Piper SL, Kar M, MacFarlane DR, Matuszek K, Pringle JM (2022) Ionic liquids for renewable thermal energy storage—a perspective. *Green Chem* 24(1):102–117
9. Endres F, El Abedin SZ (2006) Air and water stable ionic liquids in physical chemistry. *Phys Chem Chem Phys* 8(18):2101–2116
10. Riisager A, Fehrmann R, Flicker S, van Hal R, Haumann M, Wasserscheid P (2005) Very stable and highly regioselective supported ionic-liquid-phase (SILP) catalysis: continuous-flow fixed-bed hydroformylation of propene. *Angew Chem Int Ed* 44(5):815–819
11. Steinrück H-P, Wasserscheid P (2015) Ionic liquids in catalysis. *Catal Lett* 145(1):380–397
12. Pinilla C, Del Pópolo MG, Lynden-Bell RM, Kohanoff J (2005) Structure and dynamics of a confined ionic liquid. Topics of relevance to dye-sensitized solar cells. *J Phys Chem B* 109(38):17922–17927
13. Zhou F, Liang Y, Liu W (2009) Ionic liquid lubricants: designed chemistry for engineering applications. *Chem Soc Rev* 38(9):2590–2599
14. Cooper PK, Staddon J, Zhang S, Aman ZM, Atkin R, Li H (2019) Nano- and macroscale study of the lubrication of titania using pure and diluted ionic liquids. *Front Chem* 7:287
15. Bresme F, Kornyshev AA, Perkin S, Urbakh M (2022) Electrotunable friction with ionic liquid lubricants. *Nat Mater* 21(8):848–858
16. Avid A, Ochoa JL, Huang Y, Liu Y, Atanassov P, Zenyuk IV (2022) Revealing the role of ionic liquids in promoting fuel cell catalysts reactivity and durability. *Nat Commun* 13(1):1–13
17. Li R, Zhao Y, Chen Y, Liu Z, Han B, Li Z, Wang J (2018) Imidazolite ionic liquids for high-capacity capture and reliable storage of iodine. *Commun Chem* 1(1):1–8

18. Tanner EE (2022) Ionic liquids charge ahead. *Nat Chem* 14(7):842–842
19. Borra EF, Seddiki O, Angel R, Eisenstein D, Hickson P, Seddon KR, Worden SP (2007) Deposition of metal films on an ionic liquid as a basis for a lunar telescope. *nature* 447 (7147):979–981
20. Seddon KR (2003) A taste of the future. *Nat Mater* 2(6):363–365
21. Crowhurst L, Lancaster NL, Pérez Arlandis JM, Welton T (2004) Manipulating solute nucleophilicity with room temperature ionic liquids. *J Am Chem Soc* 126(37):11549–11555
22. Mehnert CP, Cook RA, Dispenziere NC, Afeworki M (2002) Supported ionic liquid catalysis—a new concept for homogeneous hydroformylation catalysis. *J Am Chem Soc* 124(44):12932–12933
23. Riisager A, Fehrmanna R, Haumann M, Wasserscheid P (2006) Supported ionic liquids: versatile reaction and separation media. *Top Catal* 40(1):91–102
24. Werner S, Szesni N, Kaiser M, Haumann M, Wasserscheid P (2012) A scalable preparation method for SILP and SCILL ionic liquid thin-film materials. *Chem Eng Technol* 35(11):1962–1967
25. Zhang GR, Etzold BJ (2021) Emerging applications of solid catalysts with ionic liquid layer concept in electrocatalysis. *Adv Func Mater* 31(28):2010977
26. Kalb RS (2020) Toward industrialization of ionic liquids. In: *Commercial applications of ionic liquids*. Springer, New York, pp 261–282
27. Marinkovic JM, Riisager A, Franke R, Wasserscheid P, Haumann M (2018) Fifteen years of supported ionic liquid phase-catalyzed hydroformylation: material and process developments. *Ind Eng Chem Res* 58(7):2409–2420
28. Naicker L, Schörner M, Kremitzl D, Friedrich HB, Haumann M, Wasserscheid P (2022) Influencing the product distribution in citral hydrogenation using ionic liquid modified Cu catalysts. *ChemCatChem* 14(19):e202200388
29. Abai M, Atkins MP, Hassan A, Holbrey JD, Kuah Y, Nockemann P, Oliferenko AA, Plechkova NV, Rafeen S, Rahman AA (2015) An ionic liquid process for mercury removal from natural gas. *Dalton Trans* 44(18):8617–8624
30. Szesni N, Hagemeyer A, Grossmann F, Fischer R, Urbancic M, Lugmair C, Sun M, Hou HC, Lowe DM (2013) Catalyst composition for selective hydrogenation with improved characteristics. Google Patents
31. Endres F, Hoeffft O, Borisenko N, Gasparotto LH, Prowald A, Al-Salman R, Carstens T, Atkin R, Bund A, El Abedin SZ (2010) Do solvation layers of ionic liquids influence electrochemical reactions? *Phys Chem Chem Phys* 12(8):1724–1732
32. Endres F, Borisenko N, El Abedin SZ, Hayes R, Atkin R (2012) The interface ionic liquid (s)/electrode (s): in situ STM and AFM measurements. *Faraday Discuss* 154:221–233
33. Santos CS, Baldelli S (2010) Gas–liquid interface of room-temperature ionic liquids. *Chem Soc Rev* 39(6):2136–2145
34. Lahiri A, Borisenko N, Olschewski M, Pulletikurthi G, Endres F (2018) Anomalous electroless deposition of less noble metals on Cu in ionic liquids and its application towards battery electrodes. *Faraday Discuss* 206:339–351
35. Steinrück HP, Libuda J, Wasserscheid P, Cremer T, Kolbeck C, Laurin M, Maier F, Sobota M, Schulz P, Stark M (2011) Surface science and model catalysis with ionic liquid-modified materials. *Adv Mater* 23(22–23):2571–2587
36. Lexow M, Maier F, Steinrück H-P (2020) Ultrathin ionic liquid films on metal surfaces: adsorption, growth, stability and exchange phenomena. *Adv Phys X* 5(1):1761266
37. Lovelock KR, Villar-Garcia IJ, Maier F, Steinrück H-P, Licence P (2010) Photoelectron spectroscopy of ionic liquid-based interfaces. *Chem Rev* 110(9):5158–5190
38. Steinrück H-P (2010) Surface science goes liquid! *Surf Sci* 604(5–6):481–484
39. Steinrück H-P (2012) Recent developments in the study of ionic liquid interfaces using X-ray photoelectron spectroscopy and potential future directions. *Phys Chem Chem Phys* 14(15):5010–5029
40. Buchner F, Forster-Tonigold K, Uhl B, Alwast D, Wagner N, Farkhondeh H, GrossBehm RJr A (2013) Toward the microscopic identification of anions and cations at the ionic liquid|Ag (111) interface: a combined experimental and theoretical investigation. *ACS Nano* 7(9):7773–7784
41. Uhl B, Cremer T, Roos M, Maier F, Steinrück H-P, Behm RJ (2013) At the ionic liquid|metal interface: structure formation and temperature dependent behavior of an ionic liquid adlayer on Au (111). *Phys Chem Chem Phys* 15(40):17295–17302
42. Uhl B, Huang H, Alwast D, Buchner F, Behm RJ (2015) Interaction of ionic liquids with noble metal surfaces: structure formation and stability of [OMIM][TFSA] and [EMIM][TFSA] on Au (111) and Ag (111). *Phys Chem Chem Phys* 17(37):23816–23832
43. Meusel M, Lexow M, Gezmis A, Schötz S, Wagner M, Bayer A, Maier F, Steinrück H-P (2020) Atomic force and scanning tunneling microscopy of ordered ionic liquid wetting layers from 110 K up to room temperature. *ACS Nano* 14(7):9000–9010
44. Meusel M, Lexow M, Gezmis A, Bayer A, Maier F, Steinrück H-P (2020) Growth of multilayers of ionic liquids on Au (111) investigated by atomic force microscopy in ultrahigh vacuum. *Langmuir* 36(45):13670–13681
45. Meusel M, Gezmis A, Jaekel S, Lexow M, Bayer A, Maier F, Steinrück H-P (2021) Time- and temperature-dependent growth behavior of ionic liquids on Au (111) studied by atomic force microscopy in ultrahigh vacuum. *J Phys Chem C* 125(37):20439–20449
46. Biedron AB, Garfunkel EL, Castner EW Jr, Rangan S (2017) Ionic liquid ultrathin films at the surface of Cu (100) and Au (111). *J Chem Phys* 146(5):054704
47. Uhl B, Buchner F, Gabler S, Bozorgchenani M, Behm RJ (2014) Adsorption and reaction of sub-monolayer films of an ionic liquid on Cu (111). *Chem Commun* 50(62):8601–8604
48. Lovelock K, Kolbeck C, Cremer T, Paape N, Schulz P, Wasserscheid P, Maier F, Steinrück H-P (2009) Influence of different substituents on the surface composition of ionic liquids studied using ARXPS. *J Phys Chem B* 113(9):2854–2864
49. Miller SF, Friedrich HB, Holzapfel CW (2012) The effects of SCILL catalyst modification on the competitive hydrogenation of 1-octyne and 1, 7-octadiene versus 1-octene. *ChemCatChem* 4(9):1337–1344
50. Heinze M, Zill J, Matysik J, Einicke W, Gläser R, Stark A (2014) Solid–ionic liquid interfaces: pore filling revisited. *Phys Chem Chem Phys* 16(44):24359–24372
51. Hoffmann V, Pulletikurthi G, Carstens T, Lahiri A, Borodin A, Schammer M, Horstmann B, Latz A, Endres F (2018) Influence of a silver salt on the nanostructure of a Au (111)/ionic liquid interface: an atomic force microscopy study and theoretical concepts. *Phys Chem Chem Phys* 20(7):4760–4771
52. Lexow M, Heller BS, Maier F, Steinrück HP (2018) Anion exchange at the liquid/solid interface of ultrathin ionic liquid films on Ag (111). *ChemPhysChem* 19(22):2978–2984
53. Horcas I, Fernández R, Gomez-Rodriguez J, Colchero J, Gómez-Herrero J, Baro A (2007) WSXM: a software for scanning probe microscopy and a tool for nanotechnology. *Rev Sci Instrum* 78(1):013705
54. Maier F, Gottfried JM, Rossa J, Gerhard D, Schulz PS, Schwiager W, Wasserscheid P, Steinrück HP (2006) Surface enrichment and depletion effects of ions dissolved in an ionic liquid: an X-ray photoelectron spectroscopy study. *Angew Chem Int Ed* 45(46):7778–7780

55. Kresse G, Hafner J (1993) Ab initio molecular dynamics for liquid metals. *Phys Rev B* 47(1):558
56. Kresse G, Furthmüller J (1996) Efficient iterative schemes for ab initio total-energy calculations using a plane-wave basis set. *Phys Rev B* 54(16):11169
57. Kresse G, Furthmüller J (1996) Efficiency of ab-initio total energy calculations for metals and semiconductors using a plane-wave basis set. *Comput Mater Sci* 6(1):15–50
58. Perdew JP, Burke K, Ernzerhof M (1996) Generalized gradient approximation made simple. *Phys Rev Lett* 77(18):3865
59. Kresse G, Joubert D (1999) From ultrasoft pseudopotentials to the projector augmented-wave method. *Phys Rev B* 59(3):1758
60. Grimme S, Antony J, Ehrlich S, Krieg H (2010) A consistent and accurate ab initio parametrization of density functional dispersion correction (DFT-D) for the 94 elements H-Pu. *J Chem Phys* 132(15):154104
61. Methfessel M, Paxton A (1989) High-precision sampling for Brillouin-zone integration in metals. *Phys Rev B* 40(6):3616
62. Monkhorst HJ, Pack JD (1976) Special points for Brillouin-zone integrations. *Phys Rev B* 13(12):5188
63. Lexow M, Talwar T, Heller BS, May B, Bhui RG, Maier F, Steinrück H-P (2018) Time-dependent changes in the growth of ultrathin ionic liquid films on Ag (111). *Phys Chem Chem Phys* 20(18):12929–12938
64. Cremer T, Stark M, Deyko A, Steinrück H-P, Maier F (2011) Liquid/solid interface of ultrathin ionic liquid films: [C1C1Im][Tf2N] and [C8C1Im][Tf2N] on Au (111). *Langmuir* 27(7):3662–3671
65. Rietzler F, May B, Steinrück H-P, Maier F (2016) Switching adsorption and growth behavior of ultrathin [C2C1Im][OTf] films on Au (111) by Pd deposition. *Phys Chem Chem Phys* 18(36):25143–25150
66. Jiang L, Zhang B, Médard G, Seitsonen AP, Haag F, Allegretti F, Reichert J, Kuster B, Barth JV, Papageorgiou AC (2017) N-Heterocyclic carbenes on close-packed coinage metal surfaces: bis-carbene metal adatom bonding scheme of monolayer films on Au. *Ag and Cu Chem Sci* 8(12):8301–8308
67. Klappenberger F, Weber-Bargioni A, Auwärter W, Marschall M, Schiffrin A, Barth J (2008) Temperature dependence of conformation, chemical state, and metal-directed assembly of tetrapyrrolyl-porphyrin on Cu (111). *J Chem Phys* 129(21):214702
68. Fendt LA, Stöhr M, Wintjes N, Enache M, Jung TA, Diederich F (2009) Modification of supramolecular binding motifs induced by substrate registry: formation of self-assembled macrocycles and chain-like patterns. *Chemistry* 15(42):11139–11150
69. Lepper M, Schmitt T, Gurrath M, Raschmann M, Zhang L, Stark M, Hölzel H, Jux N, Meyer B, Schneider MA (2017) Adsorption behavior of a cyano-functionalized porphyrin on Cu (111) and Ag (111): from molecular wires to ordered supramolecular two-dimensional aggregates. *J Phys Chem C* 121(47):26361–26371
70. Adhikari R, Siglreithmaier G, Gurrath M, Meusel M, Kuliga J, Lepper M, Hölzel H, Jux N, Meyer B, Steinrück HP (2020) Formation of highly ordered molecular porous 2D networks from cyano-functionalized porphyrins on Cu (111). *Chemistry* 26(59):13408–13418

**Publisher's Note** Springer Nature remains neutral with regard to jurisdictional claims in published maps and institutional affiliations.

## Supporting Information to

### Structure and Reactivity of the Ionic Liquid [C<sub>1</sub>C<sub>1</sub>Im][Tf<sub>2</sub>N] on Cu(111)

Rajan Adhikari<sup>1,#</sup>, ORCID: 0000-0002-3089-8179, Stephen Massicot<sup>1,#</sup>, ORCID: 0000-0002-2530-8015, Lukas Fromm<sup>2</sup>,  
Timo Talwar<sup>1</sup>, Afra Gezmis<sup>1</sup>, Manuel Meusel<sup>1</sup>, Andreas Bayer<sup>1</sup>, ORCID: 0000-0002-7353-3532,  
Simon Jaekel<sup>1</sup>, ORCID: 0000-0002-8160-4628, Florian Maier<sup>1</sup>, ORCID: 0000-0001-9725-8961,  
Andreas Görling<sup>2</sup>, ORCID: 0000-0002-1831-3318, and Hans-Peter Steinrück<sup>1,\*</sup>, ORCID: 0000-0003-1347-8962

<sup>1</sup>Lehrstuhl für Physikalische Chemie II, Friedrich–Alexander–Universität Erlangen–Nürnberg,  
Egerlandstr. 3, 91058 Erlangen, Germany

<sup>2</sup>Lehrstuhl für Theoretische Chemie, Friedrich–Alexander–Universität Erlangen–Nürnberg,  
Egerlandstr. 3, 91058 Erlangen, Germany

\*Corresponding author: [hans-peter.steinrueck@fau.de](mailto:hans-peter.steinrueck@fau.de)

# Shared first-authorship

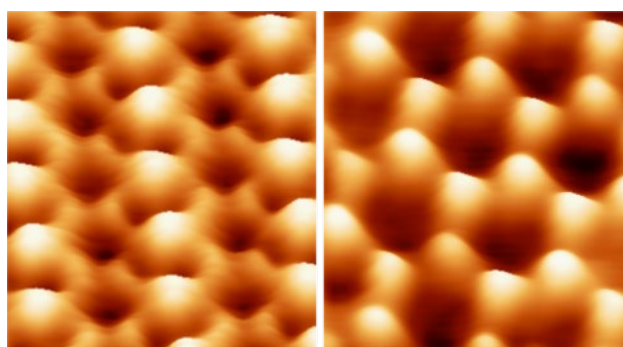
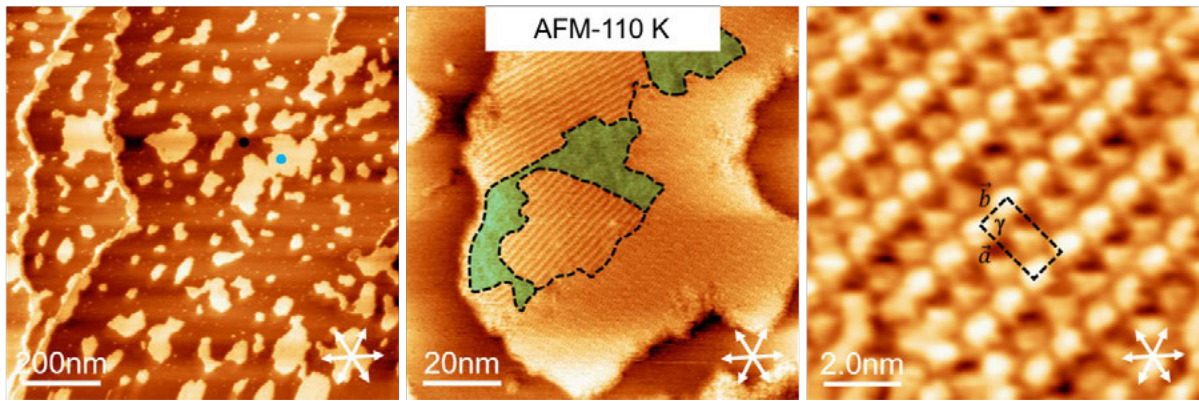
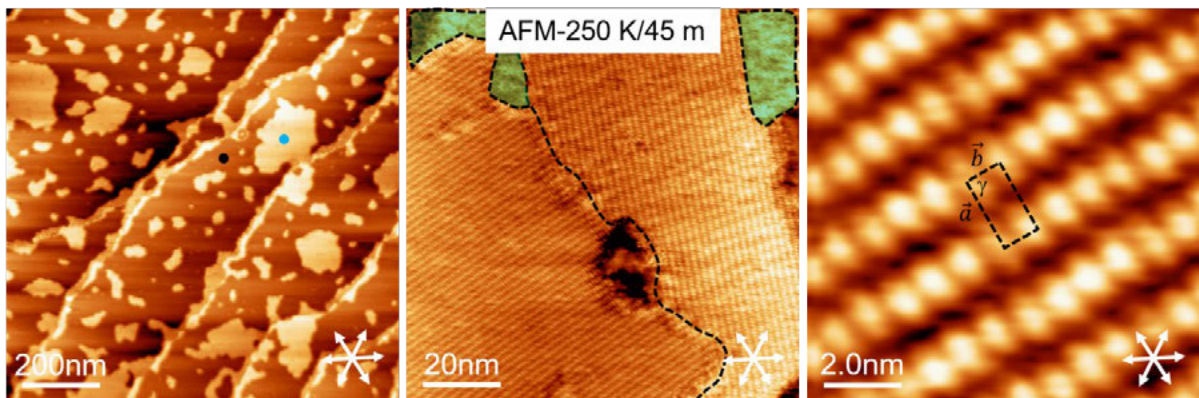


Figure: TOC



**Figure S1.** nc-AFM images of  $[\text{C}_1\text{C}_1\text{Im}][\text{Tf}_2\text{N}]$  on Cu(111), deposited at 300 K, quickly cooled down and measured at 110 K. (left) Overview image ( $1000 \times 1000 \text{ nm}^2$ ) showing IL islands of various shapes and sizes. The blue and black dots indicate IL-covered and IL-free area, respectively. (Middle) Close-up image ( $100 \times 100 \text{ nm}^2$ ) of an ordered phase of differently oriented domains coexisting with a disordered phase incorporated in-between; boundaries are marked with dashed black lines. (Right) High-resolution image ( $10 \times 10 \text{ nm}^2$ ) of the ordered phase, which is characterized by molecular rows, that is, stripes with almost a rectangular unit cell ( $\gamma = 90 \pm 3^\circ$ ), with lattice vectors  $\vec{a}$  ( $1.90 \pm 0.08 \text{ nm}$ ) and  $\vec{b}$  ( $0.90 \pm 0.05 \text{ nm}$ ). For details of the phase and the structure, see text. All images were measured with  $\Delta f = -400 \text{ Hz}$ .



**Figure S2.** nc-AFM images, measured at 110 K after annealing an adsorbed IL adlayer of  $[\text{C}_1\text{C}_1\text{Im}][\text{Tf}_2\text{N}]$  on Cu(111) at 250 K for 45 min. (left) Overview image ( $1000 \times 1000 \text{ nm}^2$ ,  $\Delta f = -400 \text{ Hz}$ ) shows IL islands of various shapes and sizes. The blue and black dots indicate IL-covered and IL-free area. (Middle) Close-up image ( $100 \times 100 \text{ nm}^2$ ,  $\Delta f = -600 \text{ Hz}$ ) depicting an ordered phase of two differently oriented domains with disordered species incorporated in-between; boundaries are marked with broken black lines. (Right) High-resolution image ( $10 \times 10 \text{ nm}^2$ ,  $\Delta f = -400 \text{ Hz}$ ) of the ordered phase, which is characterized by molecular rows, that is, stripes with a nearly rectangular unit cell ( $\gamma = 90 \pm 3^\circ$ ) with lattice vectors  $\vec{a}$  ( $1.90 \pm 0.08 \text{ nm}$ ) and  $\vec{b}$  ( $0.90 \pm 0.05 \text{ nm}$ ), highlighted with broken black lines. For details of the phase and the structure, see manuscript.

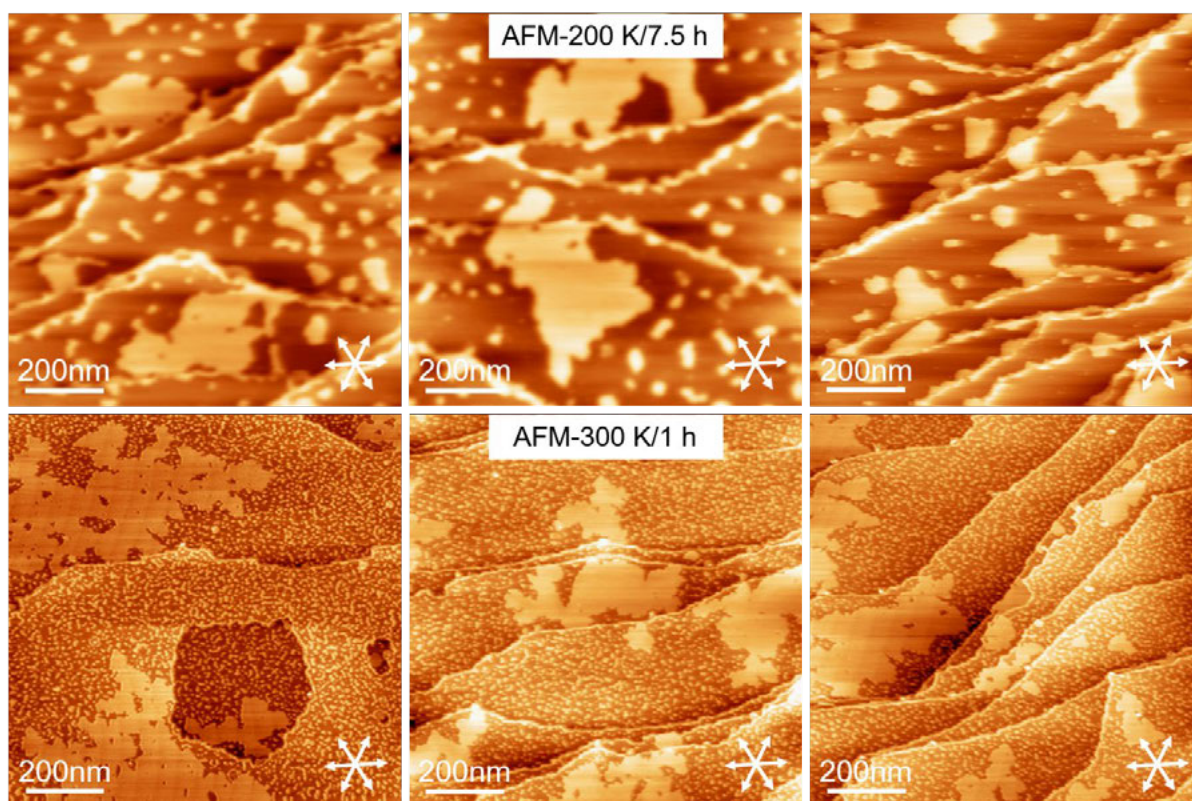


**Figure S3.** Comparison of a series of nc-AFM overview images ( $1000 \times 1000 \text{ nm}^2$ ,  $\Delta f = -400 \text{ Hz}$ ) of  $[\text{C}_1\text{C}_1\text{Im}][\text{Tf}_2\text{N}]$  on Cu(111) annealed at 200 K (top) and 300 K (bottom), measured at 110 K. The images clearly show the transformation upon heating, from only large and medium sized islands at 200 K to the coexistence of large and many very small islands at 300 K. High resolution images (Figure 1 in the manuscript) reveal that the large islands are ordered (stripe phase at 200 K, honeycomb phase at 300 K), while the very small islands are disordered (see Figure S4). For details, see manuscript.

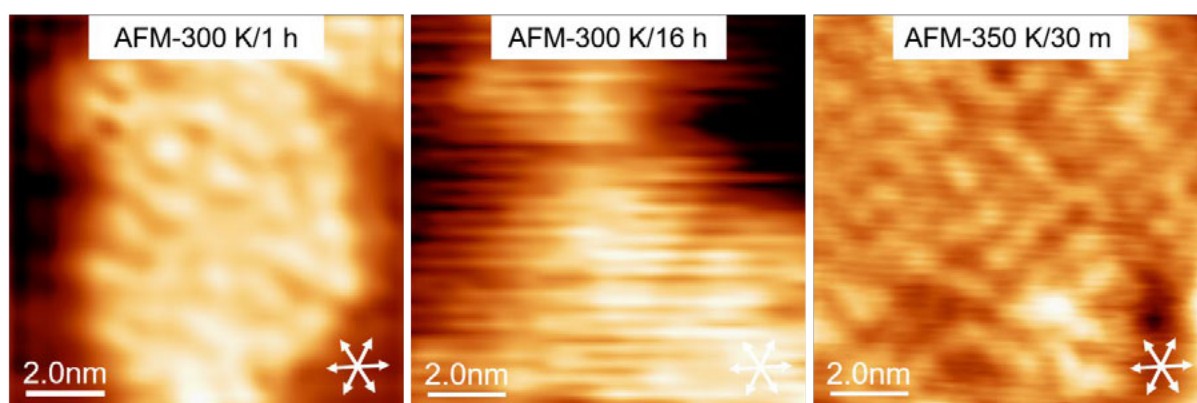


**Figure S4.** High-resolution nc-AFM images ( $10 \times 10 \text{ nm}^2$ ,  $\Delta f = -500 \text{ Hz}$ ) of the small islands with disordered internal structure observed after annealing an adsorbed IL adlayer of  $[\text{C}_1\text{C}_1\text{Im}][\text{Tf}_2\text{N}]$  on Cu(111). (Left) At 300 K for 1 h; these islands coexist with large hexagonal-type islands, see Figure 1b. (Middle) At 300 K for 16 h; these islands coexist with large honeycomb-type islands, see Figure 1c. (Right) At 350 K for 30 min; at this temperature, only small disordered islands exist on the surface, see Figure 1d. For details, see manuscript.

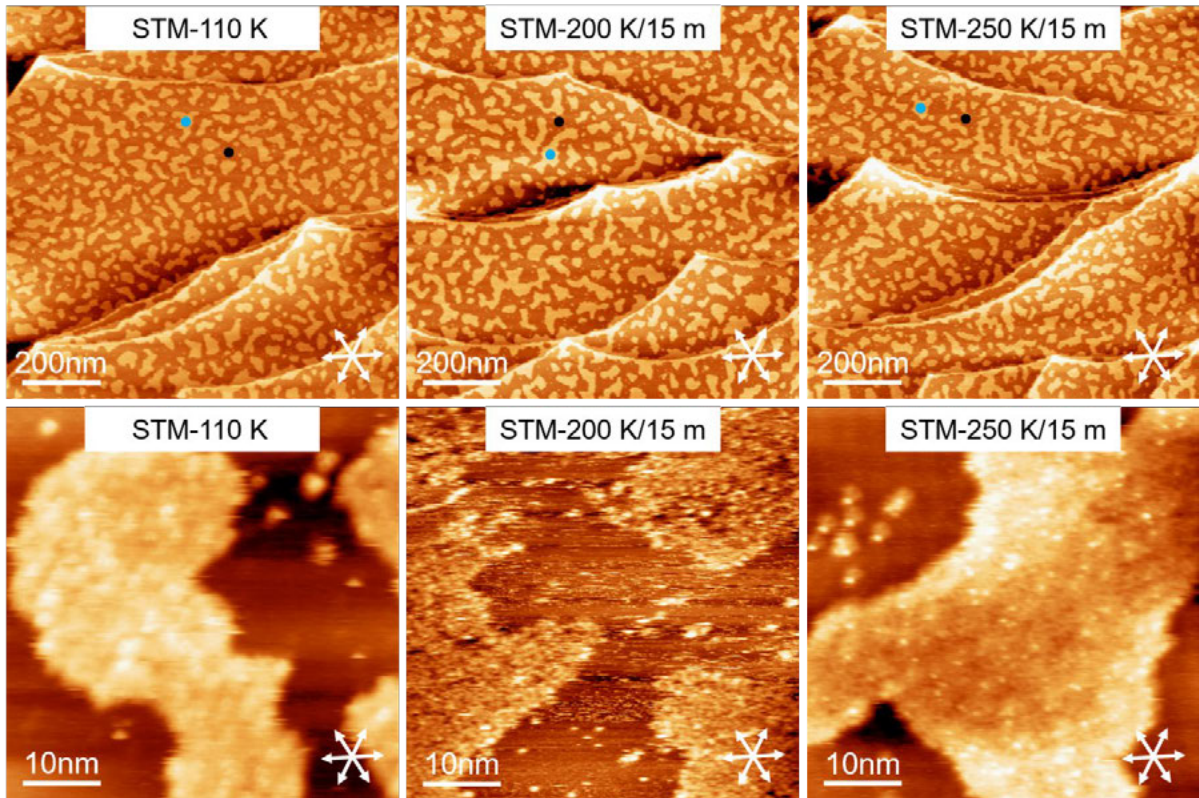


**Figure S5.** STM images of  $[C_1C_1Im][Tf_2N]$  on Cu(111), deposited at  $<160$  K and measured at 110 K (left); the overview image (top,  $1000 \times 1000 \text{ nm}^2$ ,  $U_{bias} = 2 \text{ V}$ ,  $I_{set} = 0.5 \text{ nA}$ ) and the close-up image (bottom,  $50 \times 50 \text{ nm}^2$ ,  $U_{bias} = 2 \text{ V}$ ,  $I_{set} = 1.0 \text{ nA}$ ) show IL islands of various shapes and sizes without long-range order. (Middle) acquired at 110 K after annealing the IL adlayer at 200 K for 15 min; the overview image (top,  $1000 \times 1000 \text{ nm}^2$ ,  $U_{bias} = 2 \text{ V}$ ,  $I_{set} = 0.5 \text{ nA}$ ) also shows IL islands of various shapes and sizes; the close-up image (bottom,  $50 \times 50 \text{ nm}^2$ ,  $U_{bias} = 2 \text{ V}$ ,  $I_{set} = 0.6 \text{ nA}$ ) reveals again the absence of an ordered phase. (Right) STM image acquired at 110 K after annealing the IL adlayer at 250 K for 15 min; the overview image (top,  $1000 \times 1000 \text{ nm}^2$ ,  $U_{bias} = 2 \text{ V}$ ,  $I_{set} = 0.2 \text{ nA}$ ) also shows IL islands of various shapes and sizes, and the close-up image (bottom,  $50 \times 50 \text{ nm}^2$ ,  $U_{bias} = 2 \text{ V}$ ,  $I_{set} = 0.6 \text{ nA}$ ) shows again only a disordered phase. In the overview images, the blue and black dots indicate IL-covered and IL-free areas. For details, see manuscript.

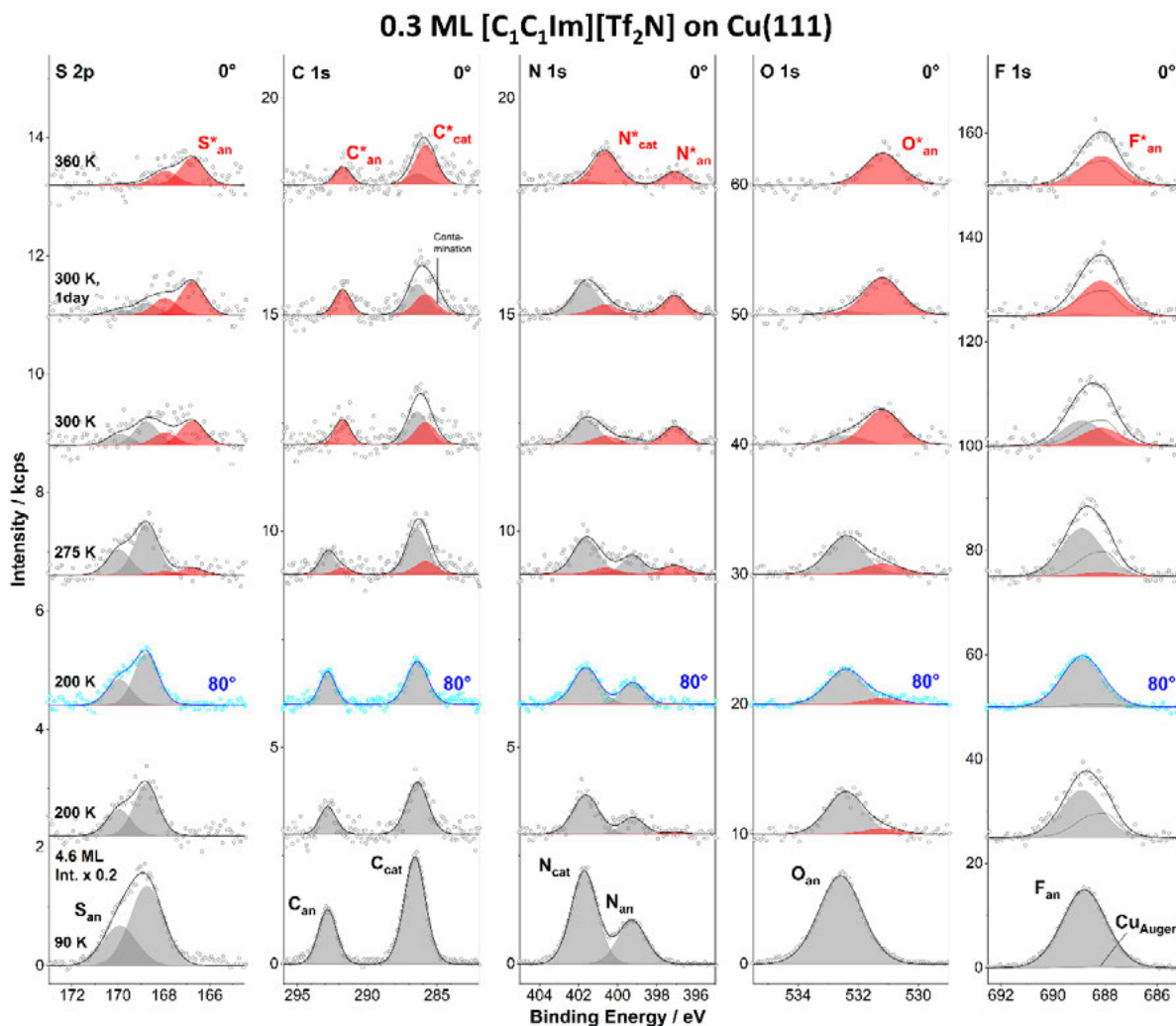


**Figure S6.** S 2p, C 1s, N 1s, O 1s and F 1s spectra of 0.3 ML [C<sub>1</sub>C<sub>1</sub>Im][Tf<sub>2</sub>N] on Cu(111) from 200 to 360 K, along with the spectra for 4.6 ML obtained at 90 K as reference for the bulk IL (bottom). For each denoted temperature, a new layer were freshly prepared and measured under normal (0°) and grazing emission (80°; shown only for 200 K in blue). For a better visualization, the 4.6 ML spectra are scaled down by a factor of 0.2. Grey peaks indicate the signals of the intact IL, red peaks denote the peaks of the new species formed upon heating. In the C 1s spectra a small contamination of the surface was taken into account, as indicated exemplarily in the spectrum at 200 K; in the F 1s spectra, the overlapping Cu<sub>Auger</sub> signal was subtracted (for more details, see experimental section and SI).

**Table S1.** Quantitative analysis of the composition of **0.3 ML** [C<sub>1</sub>C<sub>1</sub>Im][Tf<sub>2</sub>N] on Cu(111) at different temperatures, as derived from the XP spectra shown in Figure S6 at 0° (and for 200 K also at 80°) emission angle. Also given are the results for 4.6 ML deposited at 90 K and measured under 0° emission as reference for the bulk IL. For quantification, the shifted (marked with asterisk) and the unshifted signals of the IL were combined to provide the total atom number for each element.

Temperature	S <sub>an, sum</sub>	C <sub>an, sum</sub>	C <sub>cat, sum</sub>	N <sub>cat, sum</sub>	N <sub>an, sum</sub>	O <sub>an, sum</sub>	F <sub>an, sum</sub>	Σ
<b>nominal</b>	<b>2</b>	<b>2</b>	<b>5</b>	<b>2</b>	<b>1</b>	<b>4</b>	<b>6</b>	<b>22</b>
<b>360 K</b>	1.0	0.9	4.4	1.7	0.5	2.6	4.6	15.7
<b>300 K, 1 day</b>	1.7	1.9	5.1	2.1	1.0	3.7	6.5	21.4
<b>300 K</b>	1.7	1.9	5.1	1.6	1.0	3.7	7.1	22.0
<b>275 K</b>	1.8	1.7	4.7	1.7	1.0	3.6	7.4	22.0
<b>200 K, 80°</b>	<b>1.9</b>	<b>2.2</b>	<b>3.9</b>	<b>1.7</b>	<b>0.9</b>	<b>3.4</b>	<b>7.9</b>	<b>22.0</b>
<b>200 K</b>	1.8	1.9	4.6	1.8	1.3	3.9	7.3	22.0
<b>90 K</b>	1.8	2.0	4.6	2.0	1.0	4.2	6.4	22.0

### Subtraction of Auger-LMM and contamination signals

On the (freshly cleaned) Cu(111) surface an Auger-LMM signal and additional small surface contaminations in the C 1s or O 1s region may occur. After film deposition these signals are damped and have to be subtracted for the quantitative analysis of the IL signals. The expected damping factor,  $I_d/I_0$ , is calculated via the substrate Cu 2p<sub>3/2</sub> damping by taking into account the different mean free pathes  $\lambda_{Cu2p}$  and  $\lambda_{Aug/Cont}$  for Cu 2p<sub>3/2</sub> photoelectrons and Auger electrons/contamination photoelectrons, respectively:

$$\frac{I_{d, Auger/cont.}}{I_{0, Auger/cont.}} = \left( \frac{I_{d, Cu 2p}}{I_{0, Cu 2p}} \right)^{\frac{\lambda_{Cu 2p}}{\lambda_{Auger/cont.}}}$$

**Table S2.** Binding energies and fit parameter fwhm used for fitting the different XPS peaks

Signal	S <sub>an</sub>	S <sub>an</sub> *	C <sub>an</sub>	C <sub>an</sub> *	C <sub>cat</sub>	C <sub>cat</sub> *	N <sub>cat</sub>	N <sub>cat</sub> *	N <sub>an</sub>	N <sub>an</sub> *	O <sub>an</sub>	O <sub>an</sub> *	F <sub>an</sub>	F <sub>an</sub> *
Binding Energy / eV	168.77	166.77	292.83	291.75	286.40	285.82	401.63	400.64	399.21	397.08	532.44	531.19	688.89	688.15
fwhm / eV	1.23		1.32		1.79		1.56		1.38		1.43		1.45	

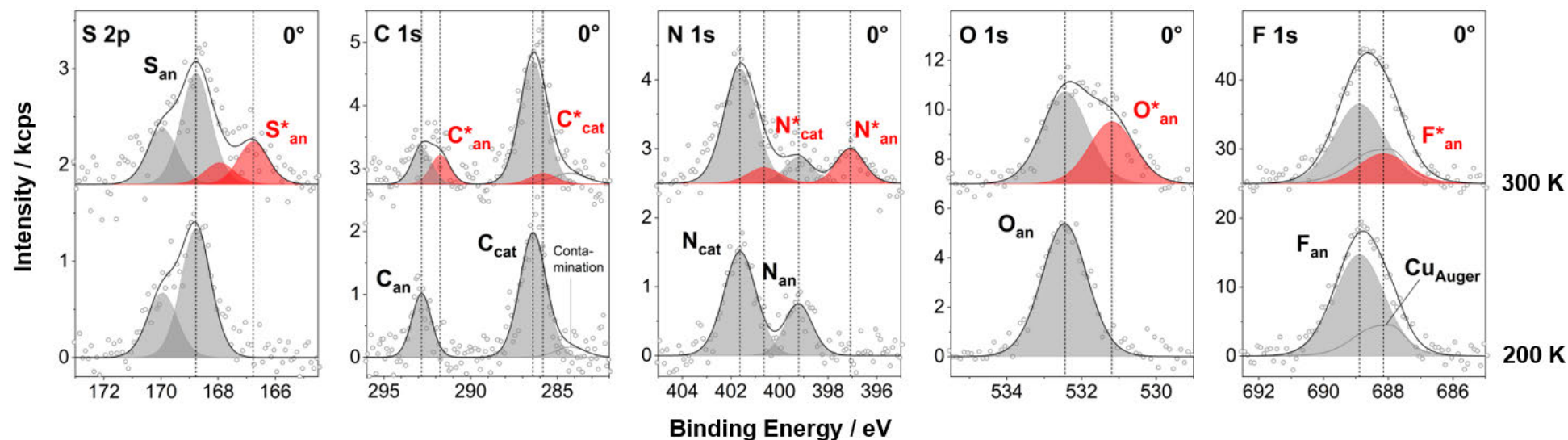


**Figure S7.** S 2p, C 1s, N 1s, O 1s and F 1s spectra of 0.5 ML [C<sub>1</sub>C<sub>1</sub>Im][Tf<sub>2</sub>N] on Cu(111) at 200 and 300 K; data from Figure 3, but at an enlarged scale. Grey peaks indicate the signals of the intact IL, red peaks denote the peaks of the new species formed upon heating. Vertical lines indicate the peak positions – see Table S2. In the C 1s spectra a small contamination of the surface was taken into account; in the F 1s spectra, the overlapping Cu<sub>Auger</sub> signal was subtracted.

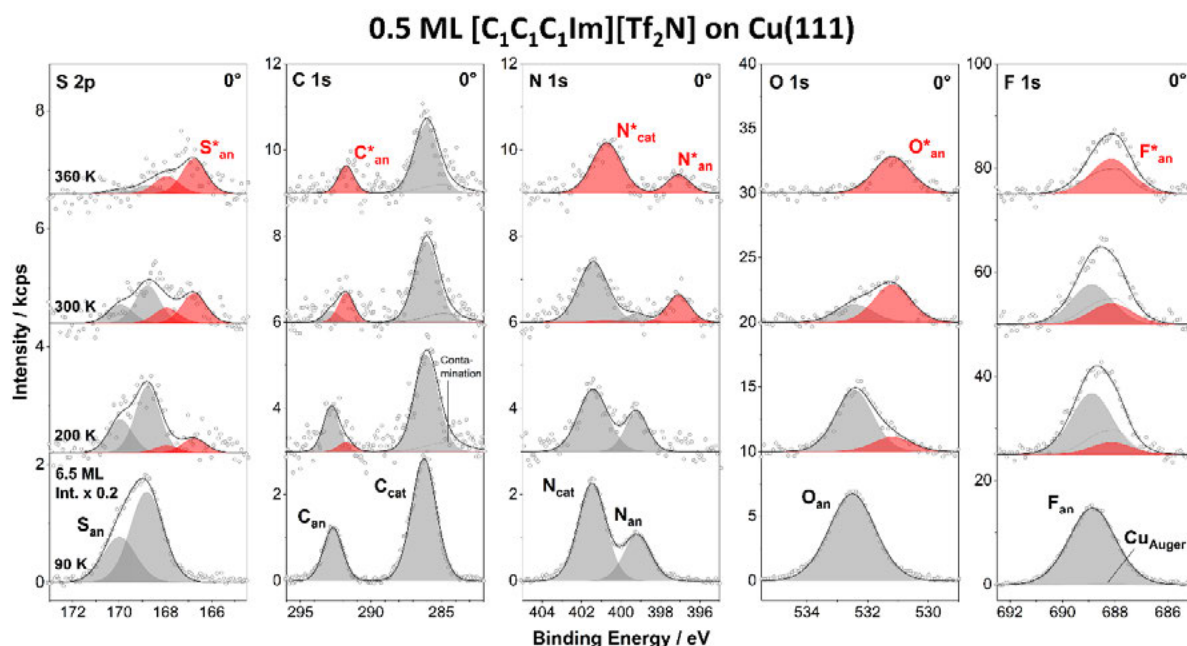


**Figure S8.** S 2p, C 1s, N 1s, O 1s and F 1s spectra of 0.5 ML [C<sub>1</sub>C<sub>1</sub>C<sub>1</sub>Im][Tf<sub>2</sub>N] on Cu(111) from 200 to 360 K, along with the spectra for 6.5 ML obtained at 90 K as reference for the bulk IL (bottom). The spectra have been measured for freshly prepared layers (for sample preparation see text) at the denoted temperatures under normal emission (0°). For better visualization, the 6.5 ML spectra are scaled down by a factor of 0.2. Grey peaks indicate the signals of the intact IL, red peaks denote the peaks of new species formed upon heating. In the C 1s spectra a small contamination of the surface was taken into account, as indicated exemplarily in the spectrum at 200 K. In the F 1s spectra, Cu<sub>Auger</sub> peak was subtracted (for details see experimental section)

**Table S3.** Quantitative analysis of the composition of **0.5 ML** [C<sub>1</sub>C<sub>1</sub>C<sub>1</sub>Im][Tf<sub>2</sub>N] on Cu(111) at different temperatures, as derived from the XP spectra shown in Figure S7 at 0° emission angle. Also given are the data for 6.5 ML obtained at 90 K under 0° emission as reference for the bulk IL. For quantification, the shifted (marked with asterisk) and the unshifted signals of the IL were combined to provide the total atom number for each element.

Temperature	S <sub>an, sum</sub>	C <sub>an, sum</sub>	C <sub>cat, sum</sub>	N <sub>cat, sum</sub>	N <sub>an, sum</sub>	O <sub>an, sum</sub>	F <sub>an, sum</sub>	Σ
nominal	2	2	6	2	1	4	6	23
360 K	0.9	1.1	4.0	1.6	0.4	1.8	3.3	13.2
300 K	1.7	1.9	5.8	2.3	1.0	3.4	6.9	23.0
200 K	1.7	2.1	5.7	1.9	0.9	3.8	6.9	23.0
90 K	1.9	1.9	5.7	2.1	1.0	4.1	6.2	23.0

**Table S4.** List of nc-AFM and STM images in Figure 1, and Figures S1 - S5, along with their operating conditions and File IDs.

Figures	Methods	nc-AFM set frequency $\Delta f$ [Hz]	STM $U_{bias}$ [V], $I_{set}$ [nA]	File IDs [YYMMDD_##_##]
1a (L)	nc-AFM	-400 Hz		20201125_43_1
1a (M)	nc-AFM	-400 Hz		20201126_35_1
1a (R) / 5a (L)	nc-AFM	-400 Hz		20201126_27_3 to 27_11
1b (L)	nc-AFM	-400 Hz		20201130_83_1
1b (M)	nc-AFM	-500 Hz		20201130_52_1
1b (R)	nc-AFM	-400 Hz		20201130_73_1
1c (L)	nc-AFM	-500 Hz		20201201_42_2
1c (M)	nc-AFM	-500 Hz		20201201_47_1
1c (R) / 5a (R)	nc-AFM	-500 Hz		20201201_51_1 to 51_2
1d (L)	nc-AFM	-400 Hz		20210826_44_4
1d (M)	nc-AFM	-400 Hz		20210826_88_1
1d (R)	nc-AFM	-400 Hz		20210826_95_1
1e (L)	STM		2 V, 0.4 nA	20200901_35_1
1e (M)	STM		2 V, 0.4 nA	20200901_36_3
1e (R)	STM		2 V, 0.2 nA	20200831_65_1
S1 (L)	nc-AFM	-400 Hz		20201124_41_1
S1 (M)	nc-AFM	-400 Hz		20201124_95_1
S1 (R)	nc-AFM	-400 Hz		20201124_105_1
S2 (L)	nc-AFM	-400 Hz		20201126_59_2
S2 (M)	nc-AFM	-600 Hz		20201127_30_1
S2 (R)	nc-AFM	-400 Hz		20201126_190_1
S3 (L-T)	nc-AFM	-400 Hz		20201125_43_1
S3 (M-T)	nc-AFM	-400 Hz		20201126_6_1
S3 (R-T)	nc-AFM	-400 Hz		20201125_143_2
S3 (L-B)	nc-AFM	-400 Hz		20201127_75_1
S3 (M-B)	nc-AFM	-400 Hz		20201130_83_1
S3 (R-B)	nc-AFM	-400 Hz		20201201_73_1
S4 (L)	nc-AFM	-500 Hz		20201130_48_1
S4 (M)	nc-AFM	-500 Hz		20201201_38_1
S4 (R)	nc-AFM	-400 Hz		20210826_95_1
S5 (L-T)	STM		2 V, 0.5 nA	20200826_11_21
S5 (M-T)	STM		2 V, 0.5 nA	20200827_66_1
S5 (R-T)	STM		2 V, 0.2 nA	20200829_2_5
S5 (L-B)	STM		2 V, 1.0 nA	20200826_24_3
S5 (M-B)	STM		2 V, 0.6 nA	20200827_39_1
S5 (R-B)	STM		2 V, 0.6 nA	20200829_17_2

L = Left, M = Middle, R = Right, T = Top, and B = Bottom

**Table S5.** List of the preparation conditions and File IDs for the XP spectra in Figure 2, 3, 4, S6, S7 and S8.

Figure	Temperature	ID
2	275, 300 K	210512-05 & -08 210623-04 & -06 210804-03 & -04 210804-05 & -06 210908-05 & -07 210910-05 & -06 210930-05 & -07 211111-03 & -04 211118-05 & -06 211123-03 & -04 211215-01 & -02
	200 K	210831-04 & -06 210902-05 & -06 211025-05 & -06 211104-03 & -04
	90 K	210629-03 & -04 210707-04 & -05 210707-06 & -07 210707-08 & -09 210709-03 & -04 210709-05 & -06 210714-03 & -05 210714-06 & -07 210723-04 & -05 210723-06 & -07
3	360 K	210914-05
	300 K, 1 day	210923-01
	300 K	210907-04
	275 K	210928-07
	200 K, 80°	210902-06
	200 K	211112-03
	90 K	210705-05
4	84 K ↓ 800 K	210709-07 ↓ 210709-18
S6	360 K	211029-04
	300 K, 1 day	211130-01
	300 K	211110-04
	275 K	211117-03
	200 K, 80°	211104-04
	200 K	211029-03
	90 K	210705-05
S7	300 K	210907-04
	200 K	211112-03
S8	360 K	221004-04
	300 K	220923-04
	200 K	220918-04
	90 K	220921-05

**Table S6:** DFT results for the most stable structures; energies given in eV

	<b>total energy</b>	<b>total disp energy</b>	<b>adsorption energy</b>	<b>adsorption energy “without disp”</b>	<b>disp adsorption energy</b>	<b>geometry</b>
ion pair	-178.99	-0.67	-	-	-	IL_ref
anion	-87.62	-0.25	-	-	-	Anion_ref
cation	-90.08	-0.14	-	-	-	Cation_ref
surf 62	-462.58	-42.79	-	-	-	Surf62_ref
surf 82	-1295.13	-120.31	-	-	-	Surf82_ref
struct1 62	-825.01	-48.05	-3.51	-1.28	-2.24	struct62_1
struct2 62	-824.92	-48.03	-3.47	-1.24	-2.22	struct62_2
struct3 62	-824.88	-48.04	-3.45	-1.22	-2.23	struct62_3
struct4 62	-824.80	-48.11	-3.41	-1.14	-2.27	struct62_4
struct1 82	-2198.97	-130.71	-3.07	-1.38	-1.69	struct82_1
struct2 82	-2198.23	-130.30	-2.92	-1.31	-1.61	struct82_2

The entry ‘struct1 62’ in Table S6 refers to the stripe structure discussed in the main text. The entries ‘struct2 62’, ‘struct3 62’ and ‘struct4 62’ refer to other geometries representing local minima. The entry ‘struct1 82’ refers to the honeycomb structure in the main text. The entry ‘struct2 82’ refers to another geometry representing a local minimum.

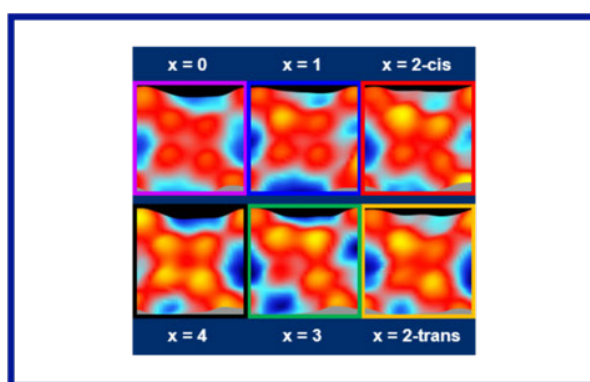
**Table S7:** Decomposition of DFT energies in horizontal interactions present already in a freestanding IL layer and vertical interactions with the substrate emerging after placing the IL layer on the substrate; energies in eV. For a description of the considered stripe and honeycomb structure see text right after Table S6.

	<b>total energy freestanding IL</b>	<b>total disp energy freestanding IL</b>	<b>horizontal interaction</b>	<b>vertical interaction</b>	<b>disp horizontal interaction</b>	<b>disp vertical interaction</b>
struct1 62 (2 ion pairs)	-359.31	-1.77	-1.96	-1.56	-0.49	-1.74
struct1 82 (5 ion pairs)	-898.36	-4.63	-1.97	-1.10	-0.53	-1.15
struct2 82 (5 ion pairs)	-898.64	-4.53	-2.03	-0.89	-0.51	-1.09

### Publication [P4]

**Structure and Conformation of Individual Molecules upon Adsorption of a Mixture of Benzoporphyrins on Ag(111), Cu(111), and Cu(110) Surfaces,** R. Adhikari, J. Brox, S. Massicot, M. Ruppel, N. Jux, H. Marbach, and H.-P. Steinrück, *ChemPhysChem*, **2023**, e202300355; [10.1002/cphc.202300355](https://doi.org/10.1002/cphc.202300355)

Copyright © 2023, The Authors. ChemPhysChem published by Wiley-VCH GmbH. This is an open access article under the terms of the [Creative Commons Attribution-NonCommercial-NoDerivs](https://creativecommons.org/licenses/by-nc-nd/4.0/) License, which permits use and distribution in any medium, provided the original work is properly cited, the use is non-commercial and no modifications or adaptations are made.



⇒ Cover Profile: [10.1002/cphc.202300539](https://doi.org/10.1002/cphc.202300539)

⇒ Front Cover: [10.1002/cphc.202300540](https://doi.org/10.1002/cphc.202300540)

# Structure and Conformation of Individual Molecules upon Adsorption of a Mixture of Benzoporphyrins on Ag(111), Cu(111), and Cu(110) Surfaces



Rajan Adhikari



Dr. Jan Brox



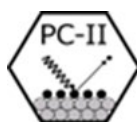
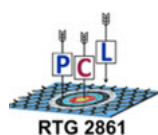
Stephen Massicot



Dr. Michael Ruppel



Prof. Dr. Norbert Jux

Dr. Hubertus  
MarbachProf. Dr. Hans-Peter  
Steinrück

The front cover artwork is provided by the groups of Prof. Dr. Hans-Peter Steinrück and Prof. Dr. Norbert Jux at the Friedrich-Alexander-Universität (FAU) Erlangen-Nürnberg. The image shows a mixture of six 2H-tetrakis-(3, 5-di-tert-butyl-phenyl)(x)benzoporphyrins (2H-diTTBP(x)BPs,  $x = 0, 1, 2$ -cis, 2-trans, 3, or 4) molecules forming a porous square structure on Ag(111) as observed in scanning tunneling microscopy (STM) at room temperature. Read the full text of the Research Article at 10.1002/cphc.202300355.

## What is the most significant result of this study?

The investigated system contained a mixture of six different 2H-diTTBP(x)BPs with  $x = 0, 1, 2$ -cis, 2-trans, 3, and 4, as obtained from synthesis. For the three surfaces, Ag(111), Cu(111) and Cu(110), we found different adsorption and reaction behaviour concerning intramolecular conformations and ordering of the porphyrins. In principle, on all surfaces, our high-resolution STM images allow for identifying the different 2H-diTTBP(x)BPs.

## What prompted you to investigate this topic/problem?

Benzoporphyrins have a variety of potential practical applications in organic near infrared light-emitting devices, in organic photovoltaics, or as oxygen sensors. Despite these promising properties, there have been very few fundamental studies of their adsorption and reaction behavior on single crystal surfaces. The topic is still in its early stage of investigation, which is particularly true given the difficulty of synthesizing isolated functionalized benzoporphyrin derivatives.

## Is your current research mainly fundamental or rather applied?

We always target at a fundamental understanding at the molecular or even atomic level. We image complex molecules using scanning tunneling microscopy and aim at evaluating

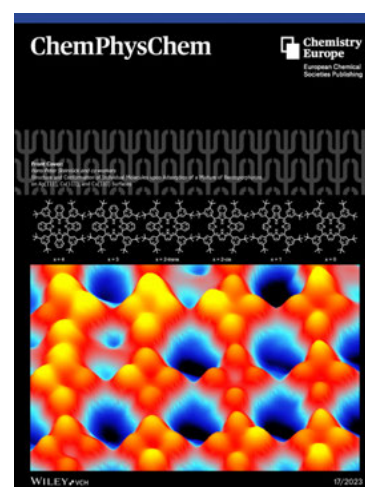
how they interact with and on surfaces, with the goal of obtaining new materials or new substances. As a result, the current study will serve as an excellent basis for more application-driven research, such as in molecular scale electronic devices or catalysis.

## Who designed the cover?

Rajan Adhikari conceptualized the cover design and did the 3D topography and rendering.

## Acknowledgements

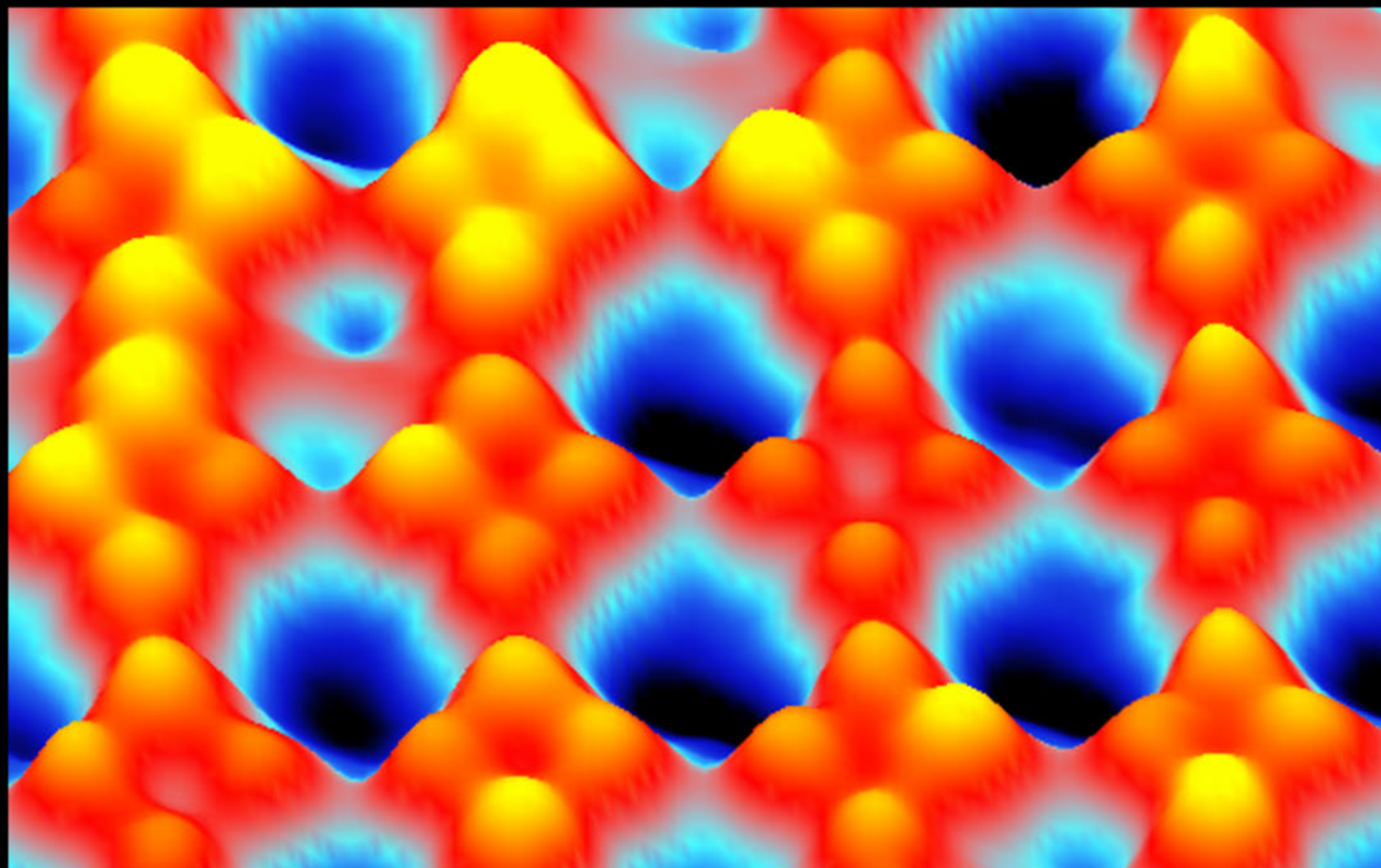
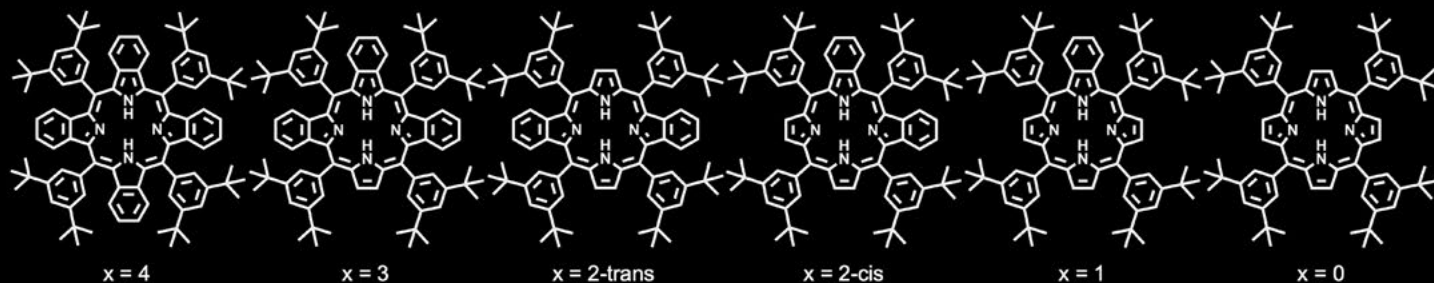
The authors gratefully acknowledge funding by the German Research Foundation (DFG) through RTG 2861 (project number 491865171) at the Friedrich-Alexander-Universität Erlangen-Nürnberg and the TU Dresden, and SFB 953 (project number 182849149) at the Friedrich-Alexander-Universität Erlangen-Nürnberg.

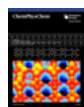


**Front Cover:**

*Hans-Peter Steinrück and co-workers*

Structure and Conformation of Individual Molecules upon Adsorption of a Mixture of Benzoporphyrins on Ag(111), Cu(111), and Cu(110) Surfaces





# Structure and Conformation of Individual Molecules upon Adsorption of a Mixture of Benzoporphyrins on Ag(111), Cu(111), and Cu(110) Surfaces

Rajan Adhikari,<sup>[a]</sup> Jan Brox,<sup>[a]</sup> Stephen Massicot,<sup>[a]</sup> Michael Ruppel,<sup>[b]</sup> Norbert Jux,<sup>[b]</sup> Hubertus Marbach,<sup>[a]</sup> and Hans-Peter Steinrück\*<sup>[a]</sup>

We investigated the adsorption behavior of a mixture of six 2H-tetrakis-(3, 5-di-*tert*-butylphenyl)(x)benzoporphyrins (2H-diTTBP(x)BPs,  $x=0, 1, 2$ -cis, 2-trans, 3, and 4) on Ag(111), Cu(111) and Cu(110) at room temperature by scanning tunneling microscopy (STM) under ultra-high vacuum conditions. On Ag(111), we observe an ordered two-dimensional square phase, which is stable up to 400 K. On Cu(111), the same square phase coexists with a stripe phase, which disappears at 400 K. In contrast, on Cu(110), 2H-diTTBP(x)BPs adsorb as immobile isolated molecules or dispersed short chains along the  $[1\bar{1}0]$  substrate direction, which remain intact up to 450 K. The stabilization of the 2D supramolecular structures on

Ag(111) and Cu(111), and of the 1D short chains on Cu(110) is attributed to van der Waals interactions between the *tert*-butyl and phenyl groups of neighboring molecules. From high-resolution STM, we can assign all six 2H-diTTBP(x)BPs within the ordered structures. Moreover, we deduce a crown shape quadratic conformation on Ag(111) and Cu(111), an additional saddle-shape on Cu(111), and an inverted structure and a quadratic appearance on Cu(110). The different conformations are attributed to the different degree of interaction of the iminic nitrogen atoms of the isoindole and pyrrole groups with the substrate atoms.

## Introduction

The organization of matter at the molecular or even atomic level is still a difficult task. The goal is to develop molecular scale devices, that is, devices that contain a single molecule or molecular assembly embedded as a key component,<sup>[1]</sup> which not only meet the increasing technical demands of the miniaturization of conventional Si-based electronic devices but also offers an ideal window of exploring the inherent properties of materials at the molecular level. In order to realize, e.g., molecular scale electronic devices from organic building blocks, one has to control and characterize the adsorption and arrangement of molecular nanostructures on suitable substrates with high precision. To enable the fabrication of nanometer-size structures, significant efforts have been made to develop the

fundamental understanding of the adsorption and properties of functional organic molecules on various substrates.<sup>[2]</sup> Investigation of the different self-assembled structures of the molecules on surfaces is of fundamental importance, because the physical and chemical properties of the various molecular assemblies depend on their structures and conformations.<sup>[3]</sup> Additionally, in a molecular device, the conformation of the molecule at the interface is key.<sup>[1a,4]</sup> The molecule should not lose its functionality, or else, the device may not function. Many studies have been performed using scanning tunneling microscopy (STM), which opens up the possibility to directly investigate and/or identify the conformation of individual molecules, such as porphyrins,<sup>[2d,5]</sup> in their adsorbed states on single crystal coinage metal surfaces.

Among the class of nitrogen-containing macrocycles, porphyrins are omnipresent in nature<sup>[6]</sup> and are most exploited representatives, in part because of their significance to biology.<sup>[7]</sup> They are an essential building block of living systems, e.g., for oxygen transport in mammals and photosynthesis. Their unique electronic and magnetic characteristics have led to manifold applications in a variety of electronic devices.<sup>[8]</sup> The ideal conformation of a porphyrin has D<sub>4</sub> symmetry, but due to the inherent flexibility of the porphyrin macrocycle, the conformation of a porphyrin can be customized by the interactions with substrates,<sup>[2b,c]</sup> substitution with particular functional end groups,<sup>[3c,9]</sup> molecular coverage,<sup>[10]</sup> heat treatments,<sup>[2b,11]</sup> presence (metalation) or absence of metal center,<sup>[3a,9a,12]</sup> which also further alters porphyrin's adsorption behavior as well as its physical and chemical nature.

Porphyrins and phthalocyanines adsorbed on metal surfaces have so far received extensive attention within the category of

[a] R. Adhikari, Dr. J. Brox, S. Massicot, Dr. H. Marbach, Prof. Dr. H.-P. Steinrück  
Lehrstuhl für Physikalische Chemie II  
Friedrich-Alexander-Universität Erlangen-Nürnberg  
Egerlandstr. 3, 91058 Erlangen, Germany  
E-mail: hans-peter.steinrueck@fau.de  
Homepage: <https://chemie.nat.fau.de/ak-steinrueck/>

[b] Dr. M. Ruppel, Prof. Dr. N. Jux  
Lehrstuhl für Organische Chemie II  
Friedrich-Alexander-Universität Erlangen-Nürnberg  
Nikolaus-Fiebiger-Str. 10, 91058 Erlangen, Germany

Supporting information for this article is available on the WWW under <https://doi.org/10.1002/cphc.202300355>

© 2023 The Authors. ChemPhysChem published by Wiley-VCH GmbH. This is an open access article under the terms of the Creative Commons Attribution Non-Commercial NoDerivs License, which permits use and distribution in any medium, provided the original work is properly cited, the use is non-commercial and no modifications or adaptations are made.

nitrogen-containing macrocycles.<sup>[13]</sup> Tetraannulated derivatives, in particular tetrabenzoporphyrins,<sup>[14]</sup> represent an intriguing class of  $\pi$ -extended tetrapyrroles, due to their intermediate position between regular porphyrins and phthalocyanines. Benzoporphyrins have a variety of potential practical applications, such as organic near-infrared devices,<sup>[15]</sup> oxygen sensors,<sup>[16]</sup> photodynamic therapy,<sup>[17]</sup> organic thin-film transistors,<sup>[18]</sup> and dye-sensitized solar cells.<sup>[14,19]</sup> Despite this relevance, only very few investigations of their adsorption behavior on different metal surfaces have been reported to date.<sup>[20]</sup> For 2H-5,10,15,20-tetrakis-(2-naphthyl)-benzoporphyrin (2H-TNBP) on Cu(111), individual molecules were observed, whereas islands with square arrangements were observed on Ag(111);<sup>[20a]</sup> for 2H-5,10,15,20-tetrakis(4-cyanophenyl)-tetrabenzoporphyrin (2H-TCNPTBP), Kagome, quadratic lattice, and hexagonal networks coexist on Cu(111);<sup>[20b]</sup> for 2H-5,10,15,20-tetraphenyltetrabenzoporphyrin (2H-TPTBP), 2D islands with the molecules arranged in a herringbone structure are found on Cu(111) and Ag(111), whereas on Cu(110) 1D molecular chains were observed;<sup>[20c]</sup> for Ni(II)-5, 10, 15, 20-tetraphenyltetrabenzoporphyrin (Ni-TPBP), oblique, herringbone, and cross structures coexist on Cu(111);<sup>[20d]</sup> and finally for Ni(II)-meso-tetrakis(4-*tert*-butylphenyl)-benzoporphyrin (Ni-TTBPP), islands with square arrangement were observed on Cu(111).<sup>[20e]</sup> Such arrangements

could find potential applications in organic electronics or catalysis.

Regardless of these promising properties, research on tetrabenzoporphyrins is still only at the beginning, in particular concerning their structural diversity and the resulting properties on different surfaces. This is particularly true, since the synthesis of functionalized isolated benzoporphyrin derivatives is very challenging. Ruppel et al.<sup>[21]</sup> reported a synthetic protocol with a library of 30 functionalized A4-symmetric tetraaryl-tetrabenzoporphyrins (TATBPs) utilizing a readily established 2H-isoindole synthon. It provides quick access to a library of different molecules; however, the separation of statistical mixtures is frequently difficult and challenging.<sup>[21–22]</sup> For the synthesis of here studied molecules, 2H-tetrakis-(3, 5-di-*tert*-butylphenyl)(*x*)benzoporphyrins (2H-diTTBP(*x*)BPs), a mixed condensation of pyrrole and the 2H-isoindole synthon with 3,5-di-*tert*-butylbenzaldehyde were used, yielding a mixture of six different porphyrin species; thereby “*x*” indicates the number of isoindole groups (also denoted as benzopyrrole groups) in the different porphyrins. Figure 1 shows the chemical structures of the six 2H-diTTBP(*x*)BPs. The synthesis and characterization of the mixture of the 2H-diTTBP(*x*)BP molecules was done in an analogous way as has been described by Ruppel et al.<sup>[21]</sup> elsewhere.

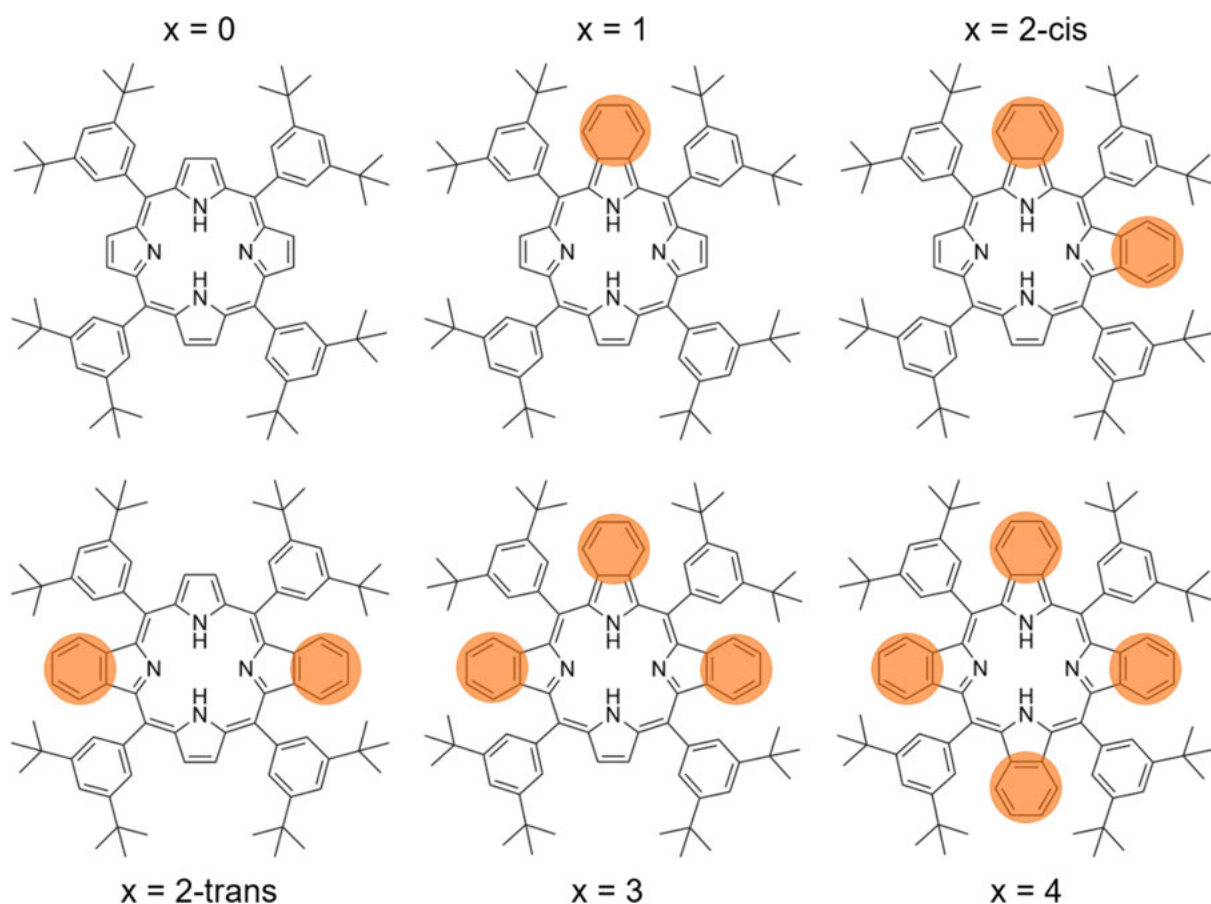


Figure 1. Chemical structure of the different 2H-diTTBP(*x*)BPs.

Herein, we present a detailed investigation of the self-assembly of 2H-diTTBP(x)BPs on Ag(111), Cu(111) and Cu(110) as a function of temperature to provide further information on fundamental aspects. While the different molecules cannot be separated in the synthesis process, we were able to identify and/or assign all six porphyrin species within the long-range ordered structures on Ag(111) and Cu(111) based on our submolecular resolution STM images. These long-range ordered structures are stabilized by van der Waals forces between the adjacent *tert*-butyl groups of neighboring molecules. On /bk; Cu(110), however, we evidence for the first time, to the best of our knowledge, a peculiar "inverted" adsorption geometry<sup>[23]</sup> for any benzoporphyrin derivative.

## Results and Discussion

### 2H-diTTBP(x)BPs on Ag(111)

In a first step, we investigated the adsorption behavior of 2H-diTTBP(x)BPs on Ag(111), a substrate which is considered as rather inert and does not tend to exhibit strong interactions

with metal-free porphyrins, as deduced from STM.<sup>[12,25]</sup> Sub-monolayer coverage porphyrin films (total surface coverage of ~50%) were deposited onto the sample at RT, and the measurements were carried out also at RT. In addition, the sample was annealed to 400 K, and the subsequent STM measurements were again performed at RT.

Figure 2a shows the images measured after the deposition at RT. The overview image (left) and close-up image (middle), displays a very regular, monomodal 2D island, with nearly perfect long-range order and only very few defects. The high-resolution STM image in Figure 2a (right) shows that the phase is characterized by a square unit cell ( $\gamma = 89 \pm 3^\circ$ ), with unit cell lattice vectors  $\vec{a} = 1.56 \pm 0.10$  nm and  $\vec{b} = 1.46 \pm 0.10$  nm, and a unit cell area of  $2.28$  nm<sup>2</sup>. We propose that the unit cell contains one molecule, yielding a density of  $0.44$  molecules/nm<sup>2</sup>. As mentioned above, the deposited 2H-diTTBP(x)BPs mixture contains six different molecules, containing 0, 1, 2 (cis and trans), 3, or 4 isoindole groups (see Figure 1). From the detailed inspection of the high-resolution STM image in Figure 2 (right), we are indeed able to identify and assign all six molecules, which are marked with differently colored dashed circles. Each individual molecule can be identified by four characteristic

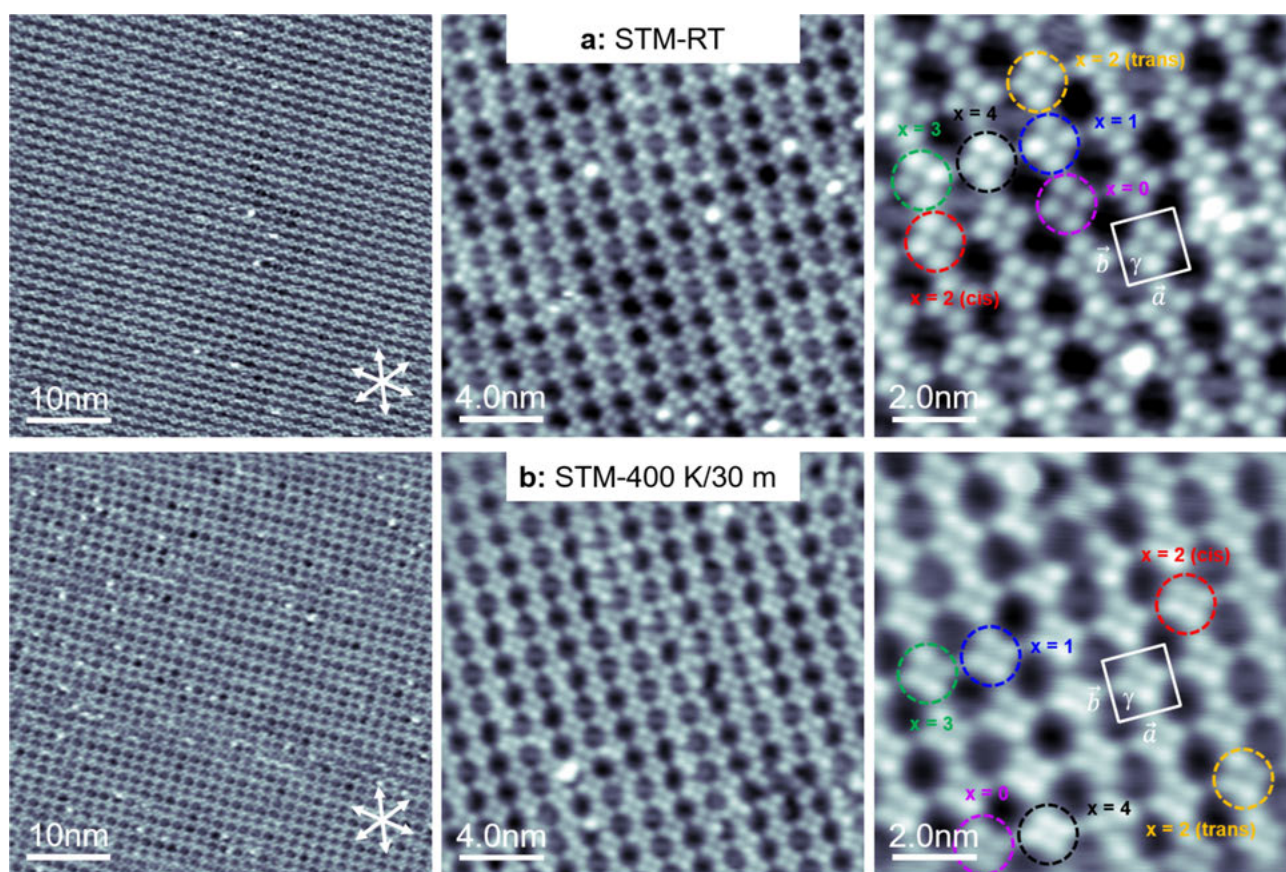


**Figure 2.** STM images of 2H-diTTBP(x)BPs on Ag(111), as overview (left,  $50 \times 50$  nm<sup>2</sup>), close-up (middle,  $20 \times 20$  nm<sup>2</sup>), and with high resolution (right,  $10 \times 10$  nm<sup>2</sup>), measured at RT. a) Deposition at RT reveals a highly ordered long-range square phase. b) After annealing to 400 K for 30 min no changes are observed; the middle and right image in (b) are an average frame of 6 and 20 consecutive images, respectively. In the high-resolution images, the six different molecules ( $x=0, 1, 2$ -cis,  $2$ -trans,  $3$ , &  $4$ ) can be identified and are marked with dashed colored circles. The unit cells are shown as solid white lines, and the white arrows indicate the close-packed Ag(111) substrate directions. For more details, see text. The STM images were measured with  $U_{bias}$  between 1.0 and 1.88 V and  $I_{set}$  between 89.3 and 201 pA; for details see Table S1 in the Supporting Information.

lobes, that is, bright or dim protrusions that correspond to the isoindole groups. This appearance is attributed to a “crown-shape” conformation,<sup>[20d]</sup> which results from a subtle balance between molecule-substrate interactions and repulsive forces within the molecules. We will address the details of the intramolecular conformation later on in Figure 3.

Typically, the subtle balance between molecule-molecule and molecule-substrate interactions determines the adsorption behavior of porphyrins and other large organic molecules. On Ag(111), supramolecular arrangements of 2H-tetraphenylporphyrin (2H-TPP) are formed as a result of T-shaped intermolecular interactions between the peripheral phenyl substituents of neighboring molecules.<sup>[25a,26]</sup> In contrast, due to strong molecule-substrate interaction between the iminic nitrogen atoms of the porphyrin and the Cu atoms of the substrate, individual 2H-TPP molecules were observed on Cu(111) at RT.<sup>[27]</sup> For 2H-diTTBP(x)BPs on Ag(111), we do not expect site-specific molecule-substrate interactions, which would yield such immobilized isolated molecules. Furthermore, the observed long-range supramolecular arrangement is also not compatible with the commonly observed T-shaped and  $\pi$ - $\pi$  intermolecular stacking of a similar porphyrin derivative, that is, 2H-TPTBP on Ag(111), Cu(111) and Cu(110).<sup>[20c]</sup> Thus, we propose that the formation and lateral stabilization of the long-range ordered supramolecular arrangement observed in Figure 2a are driven by intermolecular interactions between neighboring molecules, which are mainly mediated via van der Waals forces between the *tert*-butyl groups and possibly phenyl groups of neighboring molecules.

To probe the stability of the phase, we annealed the deposited porphyrin films to 400 K for 30 min. Figure 2b shows the corresponding images after this annealing step, measured at RT. We again observe a very regular, monomodal 2D island, with nearly perfect long-range order and only very few defects. The high-resolution STM image in Figure 2b (right) shows an (within the experimental uncertainty) identical square lattice ( $\gamma = 92 \pm 3^\circ$ ), with lattice vectors  $\vec{a} = 1.56 \pm 0.10$  nm and  $\vec{b} = 1.46 \pm 0.10$  nm, and a unit cell area of 2.28 nm<sup>2</sup>. Assuming one molecule per unit cell, we obtain an identical density of 0.44 molecules/nm<sup>2</sup> as for the layer measured directly after deposition at RT. Again, we were able to identify all six 2H-diTTBP(x)BPs (with  $x=0, 1, 2$ -cis, 2-trans, 3, and 4 isoindole groups), which are marked with colored dashed circles in the high-resolution STM image in Figure 2b (for details see Figure 3 below). Overall, the STM images in Figure 2b show that the long-range ordered monomodal 2D phase remains unchanged and is thus thermodynamically stable at 400 K.

To obtain further insight, we analyze the appearance of the individual 2H-diTTBP(x)BP molecules in more detail. Figure 3a and 3c show enlarged cutouts of the different molecules indicated in Figure 2a (RT) and Figure 2b (400 K), respectively. Each appears as four quadratically arranged, clearly identifiable bright or dim protrusions, which are separated by  $\sim 6$  Å. Generally, a subtle balance between molecule-molecule and molecule-substrate interactions as well as steric forces within the molecule determine the intramolecular conformation of TPPs on a surface. For many porphyrins and slightly modified

TPPs, the “saddle-shape” conformation is the well-established conformation.<sup>[20,25a,26,27b,28]</sup> However, this intramolecular conformation is not compatible with the observation of four quadratically arranged protrusions observed for the molecules on Ag(111) studied here. Thus, we need to consider a different intramolecular conformation. Interestingly, the observed peculiar appearance is very similar to that observed by Lepper et al. for Ni(II)-5, 10, 15, 20-tetraphenyltetrabenzoporphyrin (Ni-TPBP) on Cu(111).<sup>[20d]</sup> They assign the quadratic appearance of the molecule to four upward bent isoindole groups, which appear as four bright protrusions in STM, separated by  $\sim 6$  Å. The suggested structure is conceivable when an attractive substrate-molecule interaction pulls the macrocycle towards the substrate, increasing the tilting value of isoindole groups due to steric repulsion of the ortho-substituents within the molecule.

The proposed scaled molecular models for each of the 2H-diTTBP(x)BPs molecules on Ag(111) are depicted in Figure 3b, with the upward bent isoindole groups colored in orange, and the upward bent pyrrole groups in yellow. Due to their larger size, the isoindole groups are assigned to the bright protrusion and the pyrrole groups to the dim protrusions. The six individual 2H-diTTBP(x)BPs ( $x=0, 1, 2$ -cis, 2-trans, 3, and 4) are labeled with different colors (rectangular frame) and are displayed from bottom to top: A molecule with four dim lobes is assigned to  $x=0$  (violet); one bright lobe and three dim lobes are assigned to  $x=1$  (blue); two bright lobes and two dim lobes are assigned to  $x=2$  (cis; red) or  $x=2$  (trans; orange); three bright lobes and one dim lobe are assigned to  $x=3$  (green); and finally, four bright lobes are assigned to  $x=4$  (black).

Overall, our proposed models are in line with the interpretation of Lepper et al.,<sup>[20d]</sup> and the *tert*-butyl groups are nearly parallel to the surface in this geometry. In accordance with the suggested molecular geometry, the attractive interaction is due to van der Waals forces between the extended  $\pi$ -systems of the *tert*-butyl groups and the macrocycle of the molecule and the Ag substrate. The similarity of the appearances of 2H-diTTBP(x)BPs molecules on Ag(111) and Ni(II)-TPBP indicates that the overall conformation of the molecules within the ordered layer is not significantly influenced by presence of the *tert*-butyl groups or by the presence of a metal ion instead of two hydrogen atoms, similar to the observations for 2H-TPP and  $M^{2+}$ -TPPs.<sup>[25a,27a]</sup>

## 2H-diTTBP(x)BPs on Cu(111)

To gain deeper insight into the adsorption behavior of 2H-diTTBP(x)BPs, we also investigated their properties on Cu(111). Considering the well-established differences in the adsorption behavior of 2H-TPP on Cu(111) and Ag(111),<sup>[25a,27b]</sup> we expect a substantially different adsorption behavior or conformation also for 2H-diTTBP(x)BPs on the two surfaces. This is because Cu(111) is generally considered as a more reactive surface than Ag(111), in particular concerning N-containing molecules. Sub-monolayer coverage porphyrin films (total surface coverage of  $\sim 50\%$ ) were deposited onto a sample at RT, and measurements were carried out also at RT, before the sample was annealed to 400

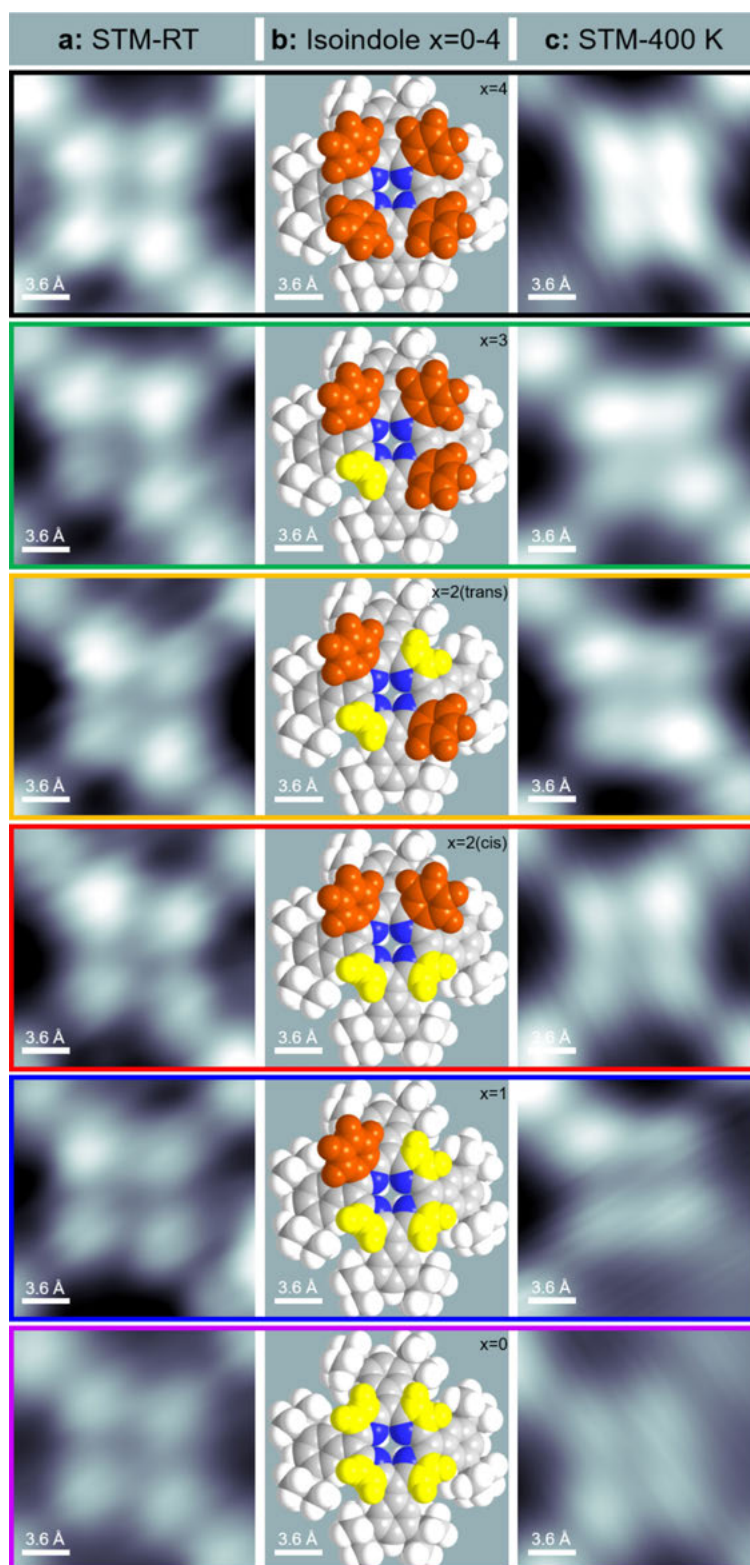


**Figure 3.** STM images ( $1.8 \times 1.8 \text{ nm}^2$ ) of 2H-diTBP( $x$ )BPs on Ag(111) after a) adsorption at RT - cutout from Figure 2a-right, and c) after annealing to 400 K for 30 min - cutout from Figure 2b-right. Each molecule is characterized by four bright or dim protrusions. b) Scaled molecular models of the six individual molecules ( $x = 0, 1, 2\text{-cis}, 2\text{-trans}, 3, \& 4$ ). The proposed molecular model represents a “crown-shape” conformation: Upward bent isoindole groups are depicted in orange and correspond to bright protrusions in (a) and (c); upward bent pyrrole groups are depicted in yellow and correspond to dim protrusions. The six individual molecules are marked with differently colored frames, with the same color code as used in Figure 2; for more details, see text. The STM images were measured with  $U_{\text{bias}} = 1.88 \text{ V}$  and  $I_{\text{set}} = 89.3$  or  $201 \text{ pA}$ ; for details see Table S1.

or 450 K to investigate the role of temperature. After each annealing step, STM was performed at RT.

Figure 4a shows the STM images after the deposition at RT (for a more extensive data set see Figure S1 in the SI). In the overview image (left), one can clearly distinguish two different self-assembled molecular ordering patterns, namely a square phase and a stripe phase, marked with white and yellow dashed lines, respectively. These structures coexist on the surface, establishing a polymorphism of the adsorbate system. The

ordered islands often grow from step edges onto the terraces, which leads us to suggest that the steps are energetically favored adsorption sites, which also act as nucleation centers for island growth.<sup>[2c]</sup> The two phases cover about similar surface areas, which suggests a comparable adsorption energy. Between the ordered islands, a disordered phase exists, and noisy streaks are visible in the fast-scanning direction of the STM, indicating the existence of mobile molecules on the surface. This streaky appearance is ascribed to molecules moving too

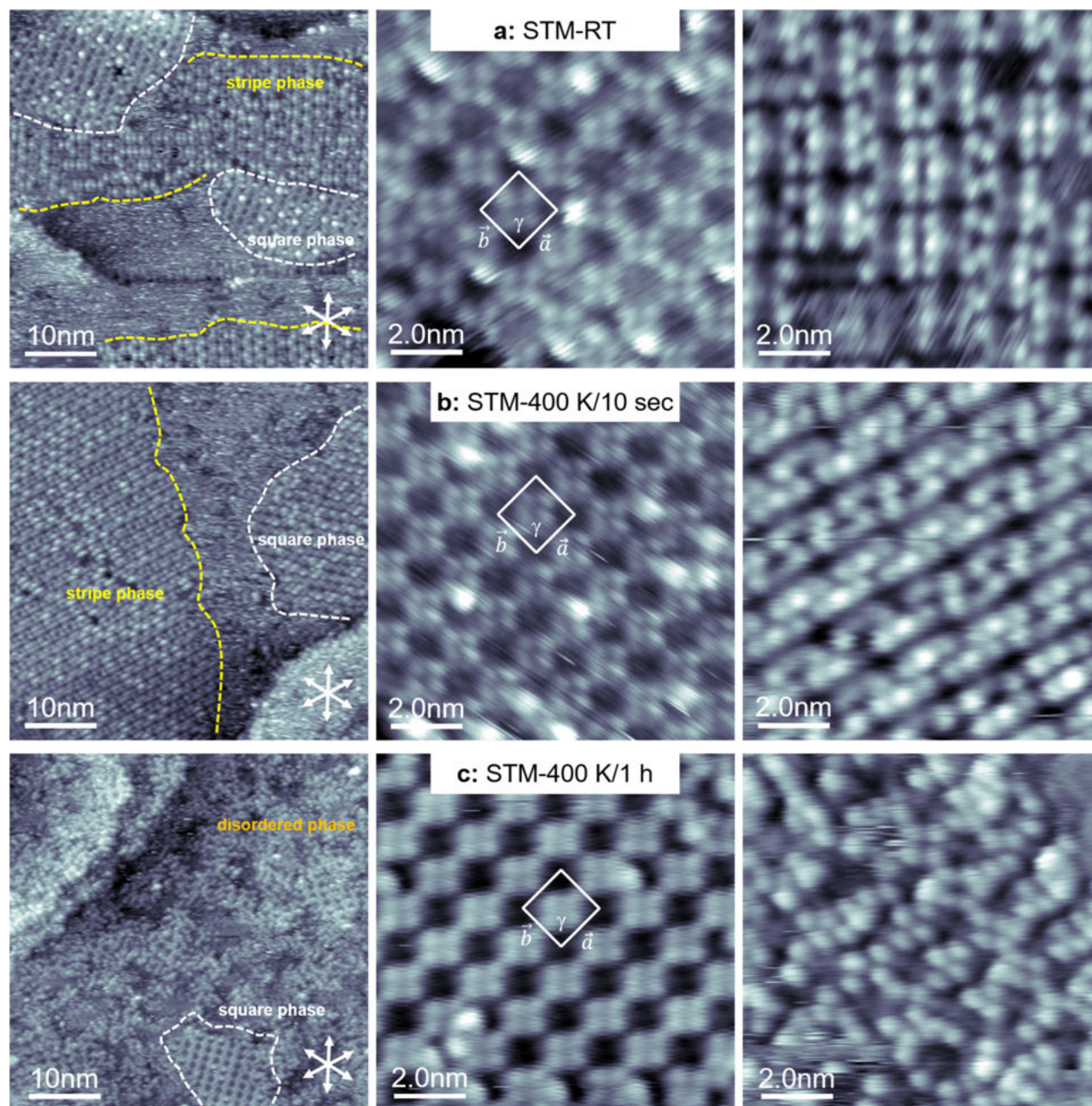


**Figure 4.** STM images of 2H-diTTBP(x)BPs on Cu(111), as overview (left,  $50 \times 50 \text{ nm}^2$ ) and with high resolution (middle, right,  $10 \times 10 \text{ nm}^2$ ), measured at RT. a) Deposition at RT reveals a coexistence of ordered square and stripe phases, along with a disordered phase. b) After annealing at 400 K for 10 sec no changes are observed. c) After further annealing at 400 K for 1 h, a loss of the stripe phase is found leaving the square phase and a disordered phase on the surface. The unit cells are shown as solid white lines, and the white arrows indicate the close-packed Cu(111) substrate directions. For more details, see text. The STM images were measured with  $U_{\text{bias}}$  between  $-1.59$  and  $+1.26 \text{ V}$  and  $I_{\text{set}}$  between  $95.7$  and  $299 \text{ pA}$ ; for details see Table S1.

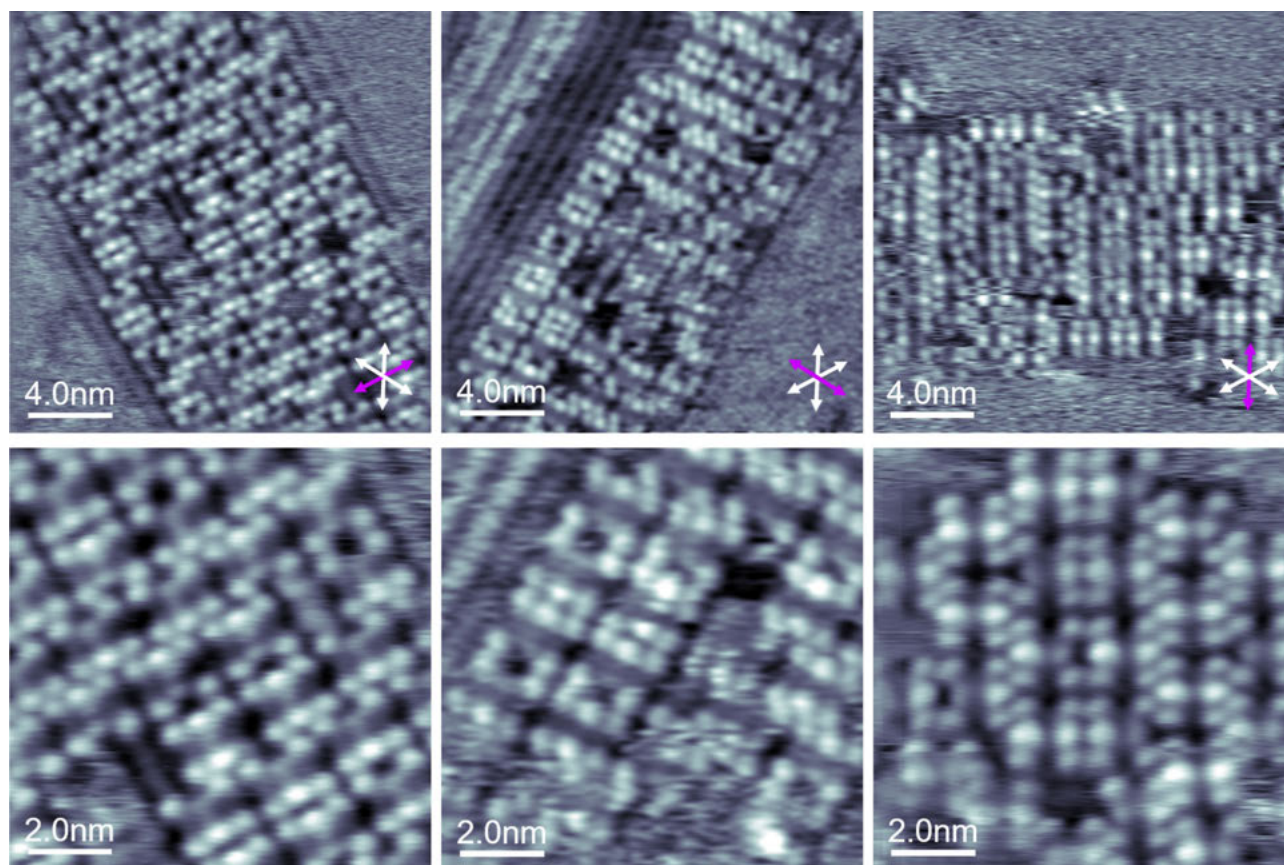
fast to be imaged by STM, which is in line with a two-dimensional (2D) gas phase.<sup>[25a,27a,29]</sup>

Figure 4a (middle) shows high resolution images of the phase with the square lattice ( $\gamma = 93 \pm 4^\circ$ ), with unit cell lattice vectors  $\vec{a} = 1.48 \pm 0.10$  nm and  $\vec{b} = 1.60 \pm 0.12$  nm. These values yield a unit cell area of  $2.37$  nm<sup>2</sup>, and – with one molecule per unit cell – a density of  $0.42$  molecules/nm<sup>2</sup>. Notably these parameters are, within the experimental uncertainty, identical to those observed above for 2H-diTTBP(x)BPs on Ag(111). The second island type, the stripe phase in Figure 4a (right), also displays a densely packed, locally ordered structure. However, due to the absence of a well-defined long-range order, it is not possible to provide a unit cell. The phase consists of molecular rows, which are perfectly aligned along the high symmetry directions of the substrate. This is particularly evident from Figure 5, where three different domains, rotated by each other by  $120^\circ$ , are depicted. The perfect alignment and the absence of any moiré pattern is a strong indication that the stripe phase is commensurate with the underlying substrate. The driving force likely is that the molecules have a well-defined adsorption site on the Cu(111) surface.

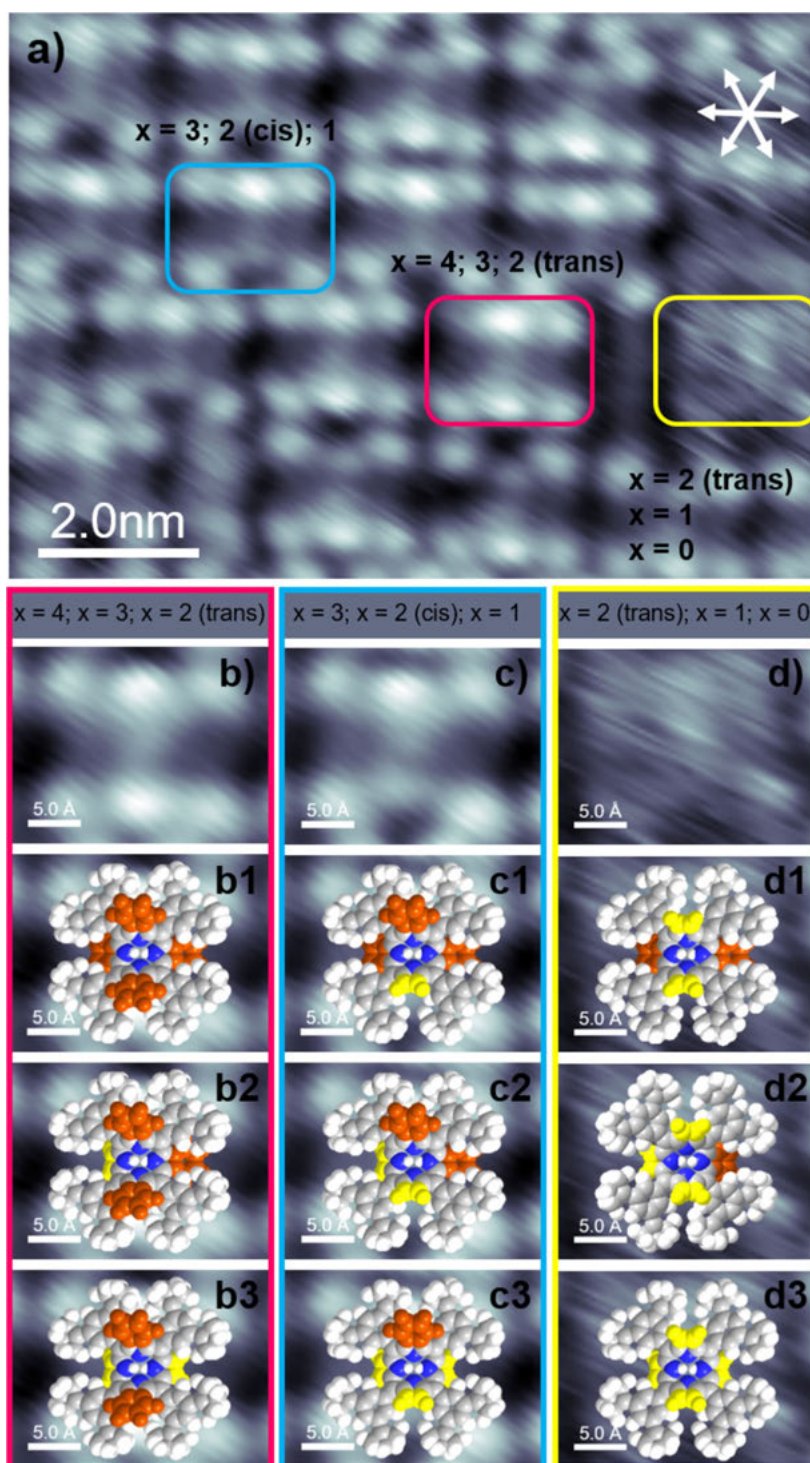
To gain additional insight, we discuss the appearance of individual 2H-diTTBP(x)BPs molecules within the square and the stripe phase in Figure 4 and Figure S1. In the high-resolution

image of the square phase obtained after heating to 400 K in Figure S2 (left), we were able to identify some of the 2H-diTTBP(x)BPs, that is, those with  $x=0$ , 2-cis, and 4. These individual molecules are denoted again by colored dashed circles, with the same color code used as for Ag(111) in Figure 3. Due to the lower resolution of the STM image (likely caused by a different STM tip termination), we were unable to identify and assign all of the six different porphyrin species. In the enlarged cutouts in Figure S2 (right; top row), the molecules appear as four, clearly identifiable bright or dim protrusions separated by  $\sim 6$  Å. The proposed scaled molecular models are overlaid and depicted in Figure S2 (right; bottom row), using the same color code for the rectangular frame. The overall intramolecular conformation is in line with the findings on Ag(111) that were discussed in detail above.

We next discuss the appearance of individual 2H-diTTBP(x)BPs within the stripe phase depicted in Figure 6 (top). Note that in contrast to the situation for the square phase on Ag(111) in Figure 3 and on Cu(111) in Figure S2, where the molecules all had a quadratic appearance with 4 protrusions, we here observe a rectangular appearance with 6 protrusions for stripe phase. Nevertheless, we are again able to assign the different appearances to different 2H-diTTBP(x)BPs molecules, if we now assume an intramolecular structure with a saddle-



**Figure 5.** STM images of the stripe phase of 2H-diTTBP(x)BPs on Cu(111) measured at RT, as overview (top,  $20 \times 20$  nm<sup>2</sup>) and with high resolution (bottom,  $10 \times 10$  nm<sup>2</sup>). The white arrows indicate the close-packed Cu(111) substrate directions. The stripe phase was found aligned along all high symmetry axes (marked with purple arrow). For more details, see text. The STM images were measured with  $U_{\text{bias}} = -1.0$  V and  $I_{\text{set}}$  between 293 and 298 pA; for details see Table S1.



**Figure 6.** a) STM image of the stripe phase of 2H-diTTBP(x)BPs on Cu(111) measured at RT with high resolution (top,  $10 \times 7 \text{ nm}^2$ ; for details see also Figure 4a,b and Figure 5). b–d) Cutouts ( $2.5 \times 1.87 \text{ nm}^2$ ) overlaid with proposed scaled molecular models. Each molecule displays six protrusions: the outer four are assigned to the peripheral phenyl substituents, and the two central ones to the slightly bent up isoindole or pyrrole groups. The elongated depression (dark line) between two parallel groups of three protrusions is referred to as molecular axis. The proposed molecular model represents a “saddle-shape” conformation with upward/downward bent isoindole groups depicted in orange and pyrrole groups in yellow. Three different appearances are observed with TWO bright protrusions (b1–b3: red frame;  $x = 4, 3, \text{ or } 2$ -trans), ONE bright protrusion (c1–c3: blue frame;  $x = 3, 2$ -cis, or 1), and ZERO bright protrusions (d1–d3: yellow frame;  $x = 2$ -trans, 1, or 0). For more details, see text. The STM image were measured with  $U_{\text{bias}} = -1.0 \text{ V}$ ,  $I_{\text{set}} = 296 \text{ pA}$ ; for details see Table S1.

shape. Thereby, two of the isoindole or pyrrole groups are bent upward and two are bent downward. In Figure 6 (top) we

observe 3 different appearances which are indicated by differently colored rounded-edge rectangles, which all display 6

protrusions. The elongated depression (dark line) between two parallel groups of three protrusions is referred to as molecular axis; it is aligned, that is, parallel to one of the high-symmetry crystallographic directions of the Cu(111) substrate.

The outer four protrusions, that is, those at the edges of the rectangle always appear dim. By comparison with the chemical structure in Figure 1 and STM reports concerning different porphyrins in literature (see ref.<sup>[20a,b,25a,27b]</sup> and references therein), we assign them to the peripheral phenyl substituents. The two central protrusions appear either as bright or as dim, and are assigned to the slightly upward bent isoindole or pyrrole of the saddle-shaped molecule; this is evident from Figure 6 (bottom columns, b–d), where enlarged cutouts of the STM image from Figure 6a are overlaid with a scaled molecule models. Thereby, upward bent isoindole groups are colored orange, while upward bent pyrrole groups are colored yellow.

Altogether, we can identify 3 different appearances in Figure 6. TWO bright central protrusions (red frame) are assigned to  $x=4$  (b1), with two upward and two downward bent isoindole groups, or to  $x=3$  (b2), with two upward bent isoindole groups and downward bent isoindole and pyrrole groups, or to  $x=2$ -trans (b3), with two upward bent isoindole groups and two downward bent pyrrole groups. Appearances with ONE bright central protrusion (blue frame) are assigned to  $x=3$  (c1), with upward bent isoindole and pyrrole groups and two downward bent isoindole groups, or to  $x=2$ -cis (c2), with upward bent isoindole and pyrrole groups, and downward bent isoindole and pyrrole groups, or to  $x=1$  (c3), with upward bent isoindole and pyrrole groups and two downward bent pyrrole groups. Appearances with ZERO bright central protrusions (yellow frame) are assigned to  $x=2$ -trans (d1), with two upward bent pyrrole groups and two downward bent isoindole groups, or to  $x=1$  (d2), with two upward bent pyrrole groups and downward bent isoindole and pyrrole groups, or to  $x=0$  (d3), with two upward bent and two downward bent pyrrole groups.

After discussing the intramolecular conformations, we address the intermolecular interactions. For TPPs, the supramolecular arrangement is stabilized by T-shaped interactions between the phenyl rings of the neighboring porphyrins. Thereby, each phenyl group points directly to the center of a phenyl group of a neighboring molecule. Since in 2H-diTTBP(x)BPs two *tert*-butyl groups are attached to the 3- and 5-position of the phenyl groups, neither T-shaped interactions nor  $\pi$ - $\pi$  intermolecular stacking can occur. We instead propose that the formation and lateral stabilization of the observed supramolecular arrangements are mainly mediated via van der Waals forces between the *tert*-butyl groups and possibly phenyl groups of neighboring molecules.<sup>[20e,30]</sup> Furthermore, the overall intermolecular theme is consistent with the findings on the Ag(111) surface discussed above. The observation of the same square phase of the mixture of 2H-diTTBP(x)BPs on both surfaces indicates that the long-range order of this phase is predominantly stabilized by the outer periphery of the molecules and not by the substrate or the number of isoindole groups.

To probe the stability of the phases, we annealed the deposited porphyrin films to 400 K for 10 sec and for 1 h.

Figure 4b–c show the corresponding images after this annealing step, measured at RT. We initially observed no change in the phases. Long heating, on the other hand, results in the loss of the stripe phase, leaving the square phase and a disordered phase on the surface. Finally, we annealed the adsorbed layers on Cu(111) to 450 K for 20 min. Figure S3 shows the STM images acquired at RT after the annealing process. Remarkably, no ordered square lattice or stripe phase is observed anymore. We observed only a disordered phase. We tentatively assign our observations to a dehydrogenation process within the porphyrin yielding the formation of new intramolecular C–C bonds between the isoindole and the phenyl groups (see refs.<sup>[20b,29,31]</sup> and references therein).

### 2H-diTTBP(x)BPs on Cu(110)

As a final step, we investigated the adsorption and reaction behavior of 2H-diTTBP(x)BPs on Cu(110). This surface is characterized by close-packed Cu rows along the  $[1\bar{1}0]$  direction, which yield a unidirectional corrugation. Its open structure is expected to make the surface more reactive than Ag(111) or Cu(111), and it has been therefore also selected as a template substrate.<sup>[20c,32]</sup> Sub-monolayer coverage porphyrin films (total surface coverage of  $\sim 40\%$ ) were deposited onto the sample at RT, and measurements were carried out also at RT. Additional measurements were performed after annealing the sample to 400 or 450 K, and subsequent cooling down to RT.

Figure 7a shows the corresponding STM images after deposition at RT. In the overview image (left) and close-up image (right), we observe no long-range ordered phases, but dispersed individual molecules or short linear chains, composed of two to three molecules, at the step edges and on terraces. The chains are aligned along the  $[1\bar{1}0]$  direction of the substrate. We attribute our observations to the interaction of the nitrogen atoms of the downward bent isoindole or pyrrole groups, which get closer to the surface on the comparably rough, trough-like Cu(110) surface, leading to specifically favored adsorption sites. The observation of only individual molecules or small ensembles indicates that these specific adsorption sites impose a lateral distance of the molecules, which does not fit to the ordered phases observed on Cu(111), which are stabilized via the lateral van der Waals forces between neighboring molecules.<sup>[20c,d,33]</sup> For too large ensembles, the energetic costs for occupying non-optimum adsorption sites cannot be overcompensated by the energy gain due to attractive lateral interactions.

The molecules on Cu(110) are found in two conformations in Figure 7. The first displays four nearly quadratically arranged protrusions (indicated by white circles). The second is a peculiar rectangular shape with six protrusions (indicated by rectangles), with four dim protrusions at the edges and two dim or bright protrusions in the center of the molecule. This appearance is clearly different from the appearance of the molecules in the stripe phase on Cu(111). It is, however, similar to the appearance of 2H-tetraphenylporphyrins (2H-TTP) and 2H-tetranaphthylporphyrins (2H-TNP) on Cu(111),<sup>[23,34]</sup> which both

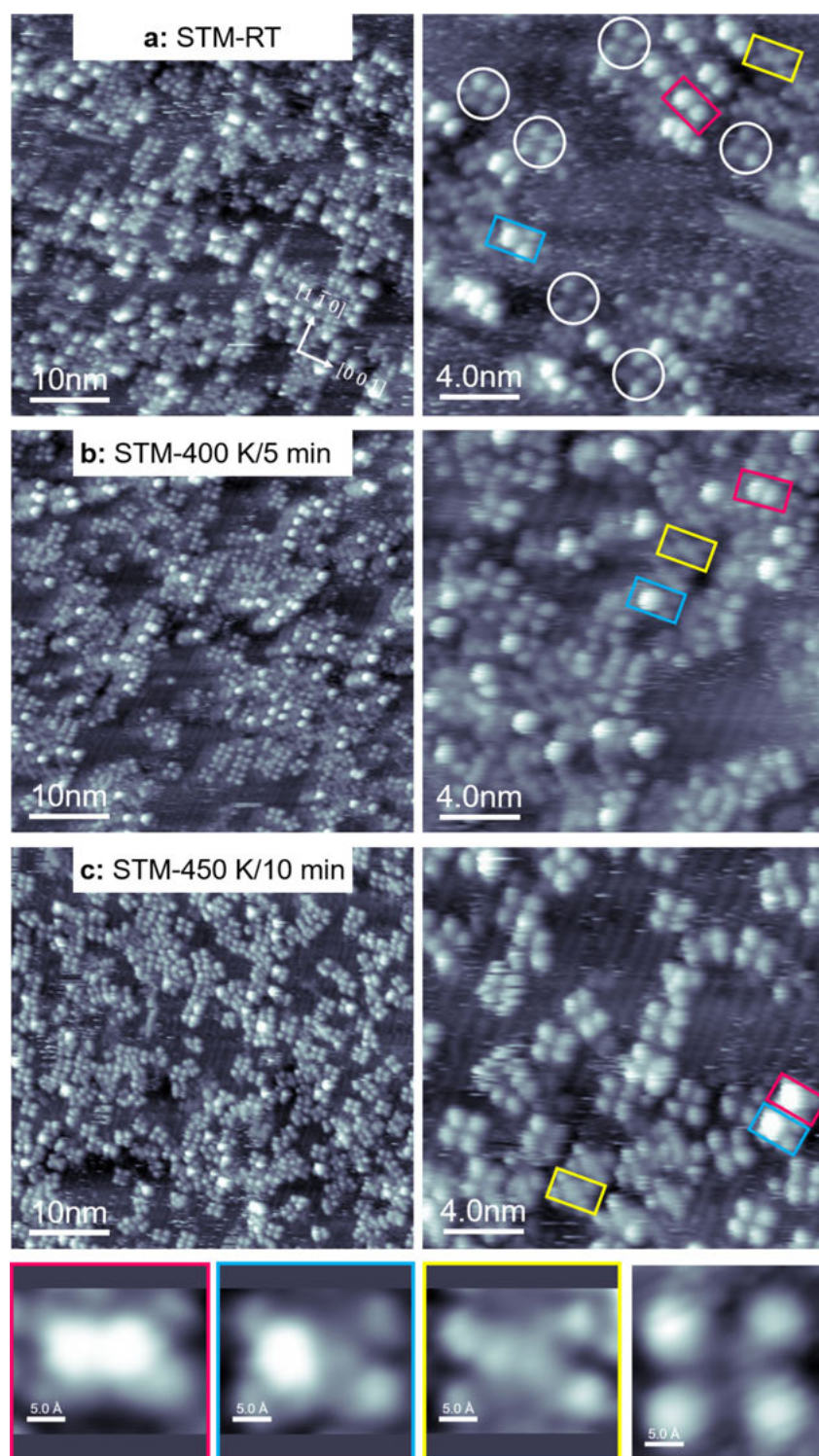


**Figure 7.** STM images of 2H-dTTBP(x)BPs on Cu(110), as an overview (left,  $50 \times 50 \text{ nm}^2$ ), with close-up (right,  $20 \times 20 \text{ nm}^2$ ), and with high resolution (bottom left three,  $2.5 \times 1.86 \text{ nm}^2$ ; bottom-right,  $2.5 \times 2.5 \text{ nm}^2$ ), measured at RT. a) Deposition at RT reveals isolated molecules and the formation of short isolated 1D chains. b) After annealing to 400 K for 5 min and c) 450 K for 10 min, the molecular appearance remains unchanged. The close-up STM images and the high-resolution images reveal individual isolated molecules with two conformations (measured at RT): a quadratic arrangement of four lobes (white circle or frame) and rectangular arrangement with six lobes (colored frames). The latter is assigned to an “inverted” structure and has three different appearances (indicated by different colors). For more details, see text. The white arrows indicate the close-packed Cu(110) substrate directions. The STM images were measured with  $U_{\text{bias}}$  between  $-1.28$  and  $+1.25$  V and  $I_{\text{set}}$  between 195 and 197 pA; for details see Table S1.

have an inverted structure with two pyrrole groups oriented nearly perpendicular to the surface. From this similarity, we propose an inverted structure also for 2H-diTTBP(x)BPs on Cu(110).

From the high-resolution images in Figure 7 (bottom row) and Figure 8a, 8b, and 8c, we can further analyze the two different conformations of the 2H-diTTBP(x)BPs. For the inverted conformation, we observe three different appearances of the two central protrusions (indicated by a red, blue, or yellow frames), which we tentatively can correlate with the number of isoindole groups. The assignment is illustrated in Figure 8, where the STM images are overlaid by scaled molecular models. In all of them, a bright central protrusion is assigned to a vertical isoindole group and a dim protrusion to a vertical pyrrole group (the horizontal isoindole or pyrrole groups cannot

be identified): TWO bright central protrusions (red frame) are assigned to  $x=4$  (a1), 3 (a2), or 2-trans (a3), with two vertical isoindole groups, ONE bright central protrusion (blue frame) to  $x=3$  (b1),  $x=2$ -cis (b2), or  $x=1$  (b3), with one vertical isoindole group, ZERO bright central protrusions (yellow frame) are assigned to  $x=2$ -trans (c1), 1 (c2), or 0 (c3), with no vertical isoindole group; notably for pure 2H-tetrakis(3,5-di-*tert*-butyl)phenylporphyrin (2H-diTTBPP), that is, the molecule without an isoindole group ( $x=0$ ), a different appearance has been observed.<sup>[35]</sup>

The appearance with four (nearly) quadratically arranged protrusions for the individual molecules (white frames) is quite different from the crown-shape appearance with four protrusions in the square phases on Ag(111) and Cu(111), which are attributed to upward bent isoindole or pyrrole groups. Here,

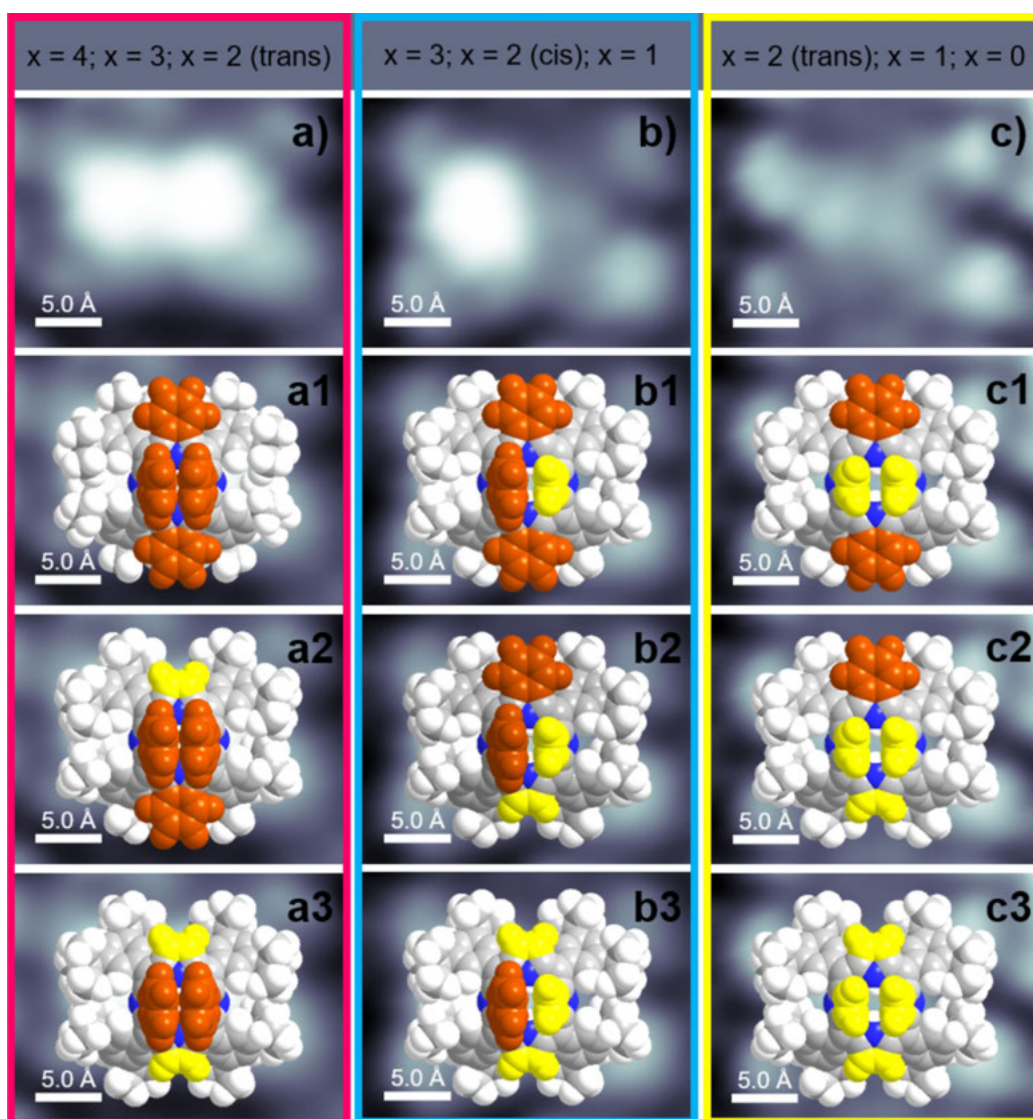


**Figure 8.** Cutouts ( $2.5 \times 1.86 \text{ nm}^2$ ; same high resolution images as in bottom row in Figure 7, measured at RT) of the inverted structures in the STM images of 2H-diTTBP(x)BPs on Cu(110) (a–c), along with superimposed scaled molecular models of individual molecules with TWO bright protrusions (a1–a3: left/red frame;  $x=4$ , 3, or 2-trans), ONE bright protrusion (b1–b3: middle/blue frame;  $x=3$ , 2-cis, or 1), and ZERO bright protrusions (c1–c3: right/yellow frame;  $x=2$ -trans, 1, or 0), to illustrate the different conformations. Isoindole groups are depicted in orange, and pyrrole groups are depicted in yellow. The individual molecules are marked with differently colored frames, with the same color code as used in Figure 7; for more details, see text.

the protrusions are separated by 10 to 12 Å, that is, by about twice the distance than for the “crown-shape” conformation. We thus tentatively assign the structure with four quadratically arranged protrusions to a quite different conformation, in which the isoindole and pyrrole groups are in the plane of the macrocycle and all phenyl groups bent upward and rotated, such that one of the bulky di-*tert*-butyl groups points upward. With this conformation, the four bright protrusions would be due to the upward bent *tert*-butyl phenyl groups. Notably, the appearance of the quadratically arranged protrusions in Figure 7 slightly varies from molecule to molecule. Thus, an unequivocal assignment to the different 2H-diTTBP(x)BPs species is not possible, and our interpretation of the appearance with four quadratically arranged protrusions in the STM images must remain speculative. We also cannot draw conclusions concerning potential self-metalation of the molecule with Cu adatoms: While for Cu(111) self-metalation typically leads to the formation of long-range ordered island of the metalloporphyrins,<sup>[9a,27a,29]</sup> this is not the case on Cu(110), where both 2H-diTTBP and Cu-diTTBP is observed as individual isolated molecules.<sup>[35]</sup>

To probe the stability of conformations and short chains, we annealed the deposited porphyrin films to 400 K for 5 min and to 450 K for 10 min, respectively. Figure 7b and 7c show the corresponding overview and close-up images. Overall, we again observe dispersed short linear 1D chains aligned along the [1  $\bar{1}$  0] direction of the substrate coexisting with individual isolated molecules, with no significant transformations. The molecules in both conformations seem to be intact and thermodynamically stable up to 450 K.

## Conclusions

We investigated the adsorption behavior of the mixture of 2H-tetrakis-(3, 5-di-*tert*-butylphenyl)(x)benzoporphyrins (2H-diTTBP(x)BPs) on Ag(111), Cu(111), and Cu(110) surfaces by scanning tunneling microscopy at room temperature. The mixture contained six different 2H-diTTBP(x)BPs with  $x=0, 1, 2$ -cis, 2-trans, 3, and 4, as obtained from synthesis. For the three surfaces, we obtain a quite different adsorption behavior concerning long-range order and intramolecular conformation of the porphyrins. Notably, on all surfaces, high resolution STM images allow for identifying the different 2H-diTTBP(x)BPs.

On Ag(111), the adsorption of the mixture results in a long-range ordered two-dimensional square phase, which is stable upon heating to 400 K. The individual molecules appear a four quadratically arranged dim or bright protrusions, which are assigned to upward bent isoindole or pyrrole groups in a so-called crown conformation. On Cu(111), the same square phase coexists with a stripe phase; in the latter, the molecules have a rectangular shape with two parallel groups of three protrusion, which reflect a saddle-shape conformation. Heating to 400 K leads to the loss of the stripe phase but leaves the square phase intact. The observation of the same square phase of the mixture of 2H-diTTBP(x)BPs on both surfaces indicates that the long-range order is stabilized by the outer periphery of the

molecules and not by the substrate or the number of isoindole groups.

In contrast, on Cu(110), 2H-diTTBP(x)BPs adsorb as isolated molecules or dispersed short (two to three molecules long) one-dimensional chains along the [1  $\bar{1}$  0] substrate direction that coexist with isolated individual immobile molecules; this structure remains intact up to 450 K. The individual molecules display two conformations. The first is a peculiar rectangular shape with four dim outer protrusions and two dim or bright central protrusions, indicative of an “inverted” conformation of the molecules. The second displays four (nearly) quadratically arranged protrusions for the individual molecules, and is quite different from the crown-shape appearance on Ag(111) and Cu(111); we tentatively attribute it to a structure, in which the isoindole and pyrrole groups are in the plane of the macrocycle and all phenyl groups are bent upward and rotated such that one of the bulky di-*tert*-butyl groups points upward.

The formation and lateral stabilization of 2D supramolecular structures on Ag(111) and Cu(111), as well as 1D short chains on Cu(110) are attributed to van der Waals interactions between the *tert*-butyl possibly phenyl groups of the neighboring molecules. The different conformations observed on the three surfaces are assigned to the different degree of interaction of the iminic nitrogen atoms of the isoindole and pyrrole groups with the substrate atoms. The thermal stability of the crown conformation for the square phases on Ag(111) and Cu(111), and the isolated immobile molecules on Cu(110) indicates the absence of a reaction under the investigated conditions. In contrast, the disappearance of the saddle-shape conformation of the stripe phase on Cu(111) upon longer annealing at 400 K indicates a reaction, the nature of which is, however, difficult to identify. A simple self-metalation of 2H-porphyrins to Cu-porphyrins with substrate adatoms appears unlikely, as metalated porphyrins typically show pronounced island formation, which is not observed after heating. Finally, the stability of the “inverted” structure on Cu(110) proves the absence of a self-metalation, since the inverted structure is not compatible with a central fourfold coordinated metal center of a metalloporphyrin. For the molecules displaying four (nearly) quadratically arranged protrusions metalation cannot be ruled out. Further insights possibly could be obtained by extensive DFT calculations to understand the different structures and conformations on the three surfaces, which is however, out of the scope of this study.

## Experimental

All experiments, sample preparations, and STM measurements were performed in an ultrahigh vacuum (UHV) system with a base pressure in the low  $10^{-10}$  mbar regime. The preparation of the Ag(111), Cu(111), and Cu(110) surfaces was done by sequential cycles of Ar<sup>+</sup> ion bombardment (600 or 700 eV) followed by annealing at 850 K. STM was performed using an RHK UHV VT STM 300 operated at RT, with RHK SPM 100 electronics. All STM images were obtained with a manually cut Pt/Ir tip, in constant current mode. The denoted bias voltages refer to the sample. The STM images were processed with the WSxM software. For noise reduction, moderate filtering (background subtraction, Gaussian

smoothing) was applied.<sup>[24]</sup> The 2H-diTTBP(x)BPs molecules were deposited onto the substrates held at RT using a home-built Knudsen cell with the crucible at 651–662 K. The STM measurements were typically initiated 1–2 h after preparation.

## Notes

The authors declare no competing financial interest.

## Acknowledgements

The authors gratefully acknowledge funding by the German Research Foundation (DFG) through RTG 2861 (project number 491865171) at the Friedrich-Alexander-Universität Erlangen-Nürnberg and the TU Dresden, and SFB 953 (project number 182849149) at the Friedrich-Alexander-Universität Erlangen-Nürnberg. Open Access funding enabled and organized by Projekt DEAL.

## Conflict of Interests

The authors declare no conflict of interest.

## Data Availability Statement

The data that support the findings of this study are available from the corresponding author upon reasonable request.

**Keywords:** benzoporphyrin · isoindole groups · 2H-diTTBP(x)BPs · scanning tunneling microscopy · self-assembly

- [1] a) C. Joachim, J. K. Gimzewski, A. Aviram, *Nature* **2000**, *408*, 541–548; b) M. Ratner, *Nat. Nanotechnol.* **2013**, *8*, 378–381.
- [2] a) J. K. Gimzewski, C. Joachim, *Science* **1999**, *283*, 1683–1688; b) H. Marbach, H.-P. Steinrück, *Chem. Commun.* **2014**, *50*, 9034–9048; c) H. Marbach, *Acc. Chem. Res.* **2015**, *48*, 2649–2658; d) W. Auwärter, D. Ćićija, F. Klappenberger, J. V. Barth, *Nat. Chem.* **2015**, *7*, 105–120; e) K. Diller, A. C. Papageorgiou, F. Klappenberger, F. Allegretti, J. V. Barth, W. Auwärter, *Chem. Soc. Rev.* **2016**, *45*, 1629–1656.
- [3] a) S. Ditze, M. Stark, M. Drost, F. Buchner, H.-P. Steinrück, H. Marbach, *Angew. Chem. Int. Ed.* **2012**, *51*, 10898–10901; b) F. Klappenberger, A. Weber-Bargioni, W. Auwärter, M. Marschall, A. Schiffrin, J. Barth, *J. Chem. Phys.* **2008**, *129*, 214702; c) S. Ditze, M. Stark, F. Buchner, A. Aichert, N. Jux, N. Luckas, A. Görling, W. Hieringer, J. Hornegger, H.-P. Steinrück, H. Marbach, *J. Am. Chem. Soc.* **2014**, *136*, 1609–1616.
- [4] Y. Wada, M. Tsukada, M. Fujihira, K. Matsushige, T. Ogawa, M. Haga, S. Tanaka, *Jpn. J. Appl. Phys.* **2000**, *39*, 3835.
- [5] T. Jung, R. Schlittler, J. Gimzewski, *Nature* **1997**, *386*, 696–698.
- [6] a) I. Fleming, *Nature* **1967**, *216*, 151–152; b) C. E. Castro, *J. Theor. Biol.* **1971**, *33*, 475–490.
- [7] A. R. Battersby, *Nat. Prod. Rep.* **2000**, *17*, 507–526.
- [8] a) A. Zampetti, A. Minotto, F. Cacialli, *Adv. Funct. Mater.* **2019**, *29*, 1807623; b) C. B. Winkelmann, I. Iónica, X. Chevalier, G. Royal, C. Bucher, V. Bouchiat, *Nano Lett.* **2007**, *7*, 1454–1458; c) R. n. Flores-Sánchez, F. Gámez, T. n. Lopes-Costa, J. M. Pedrosa, *ACS Omega* **2020**, *5*, 6299–6308; d) K. Kurlekar, A. Anjali, S. Sonalin, P. M. Imran, S. Nagarajan, *ACS Appl. Electron. Mater.* **2020**, *2*, 3402–3408.
- [9] a) R. Adhikari, G. Sigleithmaier, M. Gurrath, M. Meusel, J. Kuliga, M. Lepper, H. Hölzel, N. Jux, B. Meyer, H.-P. Steinrück, H. Marbach, *Chemistry—A European Journal* **2020**, *26*, 13408–13418; b) M. Lepper, J. Köbl, L. Zhang, M. Meusel, H. Hölzel, D. Lungerich, N. Jux, A. de Siervo, B. Meyer, H.-P. Steinrück, H. Marbach, *Angew. Chem. Int. Ed.* **2018**, *57*, 10074–10079.
- [10] M. Stark, S. Ditze, M. Drost, F. Buchner, H.-P. Steinrück, H. Marbach, *Langmuir* **2013**, *29*, 4104–4110.
- [11] M. Stark, S. Ditze, M. Lepper, L. Zhang, H. Schlott, F. Buchner, M. Röckert, M. Chen, O. Lytken, H.-P. Steinrück, H. Marbach, *Chem. Commun.* **2014**, *50*, 10225–10228.
- [12] J. Kuliga, L. Zhang, M. Lepper, D. Lungerich, H. Hölzel, N. Jux, H.-P. Steinrück, H. Marbach, *Phys. Chem. Chem. Phys.* **2018**, *20*, 25062–25068.
- [13] J. M. Gottfried, *Surf. Sci. Rep.* **2015**, *70*, 259–379.
- [14] C. M. B. Carvalho, T. J. Brocksom, K. T. De Oliveira, *Chem. Soc. Rev.* **2013**, *42*, 3302–3317.
- [15] a) C. Borek, K. Hanson, P. I. Djurovich, M. E. Thompson, K. Aznavour, R. Bau, Y. Sun, S. R. Forrest, J. Brooks, L. Michalski, *Angew. Chem. Int. Ed.* **2007**, *46*, 1109–1112; b) J. R. Sommer, A. H. Shelton, A. Parthasarathy, I. Ghiviriga, J. R. Reynolds, K. S. Schanze, *Chem. Mater.* **2011**, *23*, 5296–5304; c) K. R. Graham, Y. Yang, J. R. Sommer, A. H. Shelton, K. S. Schanze, J. Xue, J. R. Reynolds, *Chem. Mater.* **2011**, *23*, 5305–5312.
- [16] L. Hutter, B. Müller, K. Koren, S. Borisov, I. Klimant, *J. Mater. Chem. C* **2014**, *2*, 7589–7598.
- [17] F. Ménard, V. Sol, C. Ringot, R. Granet, S. Alves, C. Le Morvan, Y. Queneau, N. Ono, P. Krausz, *Bioorg. Med. Chem.* **2009**, *17*, 7647–7657.
- [18] a) S. Aramaki, Y. Sakai, N. Ono, *Appl. Phys. Lett.* **2004**, *84*, 2085–2087; b) P. B. Shea, J. Kanicki, N. Ono, *J. Appl. Phys.* **2005**, *98*, 014503; c) P. B. Shea, J. Kanicki, L. R. Pattison, P. Petroff, M. Kawano, H. Yamada, N. Ono, *J. Appl. Phys.* **2006**, *100*, 034502; d) P. B. Shea, C. Chen, J. Kanicki, L. R. Pattison, P. Petroff, H. Yamada, N. Ono, *Appl. Phys. Lett.* **2007**, *90*, 233107.
- [19] Y. Matsuo, Y. Sato, T. Niinomi, I. Soga, H. Tanaka, E. Nakamura, *J. Am. Chem. Soc.* **2009**, *131*, 16048–16050.
- [20] a) J. Brox, R. Adhikari, M. Shaker, M. Ruppel, N. Jux, H. Marbach, S. Jaekel, H.-P. Steinrück, *Surf. Sci.* **2022**, *720*, 122047; b) R. Adhikari, J. Kuliga, M. Ruppel, N. Jux, H. Marbach, H.-P. Steinrück, *J. Phys. Chem. C* **2021**, *125*, 7204–7212; c) L. Zhang, M. Lepper, M. Stark, T. Menzel, D. Lungerich, N. Jux, W. Hieringer, H.-P. Steinrück, H. Marbach, *Phys. Chem. Chem. Phys.* **2017**, *19*, 20281–20289; d) M. Lepper, L. Zhang, M. Stark, S. Ditze, D. Lungerich, N. Jux, W. Hieringer, H.-P. Steinrück, H. Marbach, *J. Phys. Chem. C* **2015**, *119*, 19897–19905; e) L. Zhang, M. Lepper, M. Stark, D. Lungerich, N. Jux, W. Hieringer, H.-P. Steinrück, H. Marbach, *Phys. Chem. Chem. Phys.* **2015**, *17*, 13066–13073.
- [21] M. Ruppel, D. Lungerich, S. Sturm, R. Lippert, F. Hampel, N. Jux, *Chem. A Eur. J.* **2020**, *26*, 3287–3296.
- [22] M. Ruppel, L.-P. Gazetas, D. Lungerich, F. Hampel, N. Jux, *J. Org. Chem.* **2020**, *85*, 7781–7792.
- [23] M. Lepper, J. Köbl, T. Schmitt, M. Gurrath, A. de Siervo, M. A. Schneider, H.-P. Steinrück, B. Meyer, H. Marbach, W. Hieringer, *Chem. Commun.* **2017**, *53*, 8207–8210.
- [24] I. Horcas, R. Fernández, J. Gomez-Rodríguez, J. Colchero, J. Gómez-Herrero, A. Baro, *Rev. Sci. Instrum.* **2007**, *78*, 013705.
- [25] a) F. Buchner, I. Kellner, W. Hieringer, A. Görling, H.-P. Steinrück, H. Marbach, *Phys. Chem. Chem. Phys.* **2010**, *12*, 13082–13090; b) F. Buchner, V. Schwald, K. Comanici, H.-P. Steinrück, H. Marbach, *ChemPhysChem* **2007**, *8*, 241–243; c) M. Lepper, T. Schmitt, M. Gurrath, M. Raschmann, L. Zhang, M. Stark, H. Hölzel, N. Jux, B. Meyer, M. A. Schneider, H.-P. Steinrück, H. Marbach, *J. Phys. Chem. C* **2017**, *121*, 26361–26371.
- [26] J. Brede, M. Linares, S. Kuck, J. Schwöbel, A. Scarfato, S.-H. Chang, G. Hoffmann, R. Wiesendanger, R. Lensen, P. H. Kouwer, *Nanotechnology* **2009**, *20*, 275602.
- [27] a) F. Buchner, E. Zillner, M. Röckert, S. Gläsel, H.-P. Steinrück, H. Marbach, *Chem. A Eur. J.* **2011**, *17*, 10226–10229; b) F. Buchner, J. Xiao, E. Zillner, M. Chen, M. Röckert, S. Ditze, M. Stark, H.-P. Steinrück, J. M. Gottfried, H. Marbach, *J. Phys. Chem. C* **2011**, *115*, 24172–24177.
- [28] a) A. Weber-Bargioni, W. Auwärter, F. Klappenberger, J. Reichert, S. Lefrançois, T. Strunskus, C. Wöll, A. Schiffrin, Y. Pennec, J. V. Barth, *ChemPhysChem* **2008**, *9*, 89–94; b) K. Diller, F. Klappenberger, M. Marschall, K. Hermann, A. Nefedov, C. Wöll, J. Barth, *J. Chem. Phys.* **2012**, *136*, 014705; c) T. Yokoyama, S. Yokoyama, T. Kamikado, S. Mashiko, *J. Chem. Phys.* **2001**, *115*, 3814–3818.
- [29] J. Xiao, S. Ditze, M. Chen, F. Buchner, M. Stark, M. Drost, H.-P. Steinrück, J. M. Gottfried, H. Marbach, *J. Phys. Chem. C* **2012**, *116*, 12275–12282.

- [30] M. Xi, M. X. Yang, S. K. Jo, B. E. Bent, P. Stevens, *J. Chem. Phys.* **1994**, *101*, 9122–9131.
- [31] G. Di Santo, C. Castellarin-Cudia, M. Fanetti, B. Taleatu, P. Borghetti, L. Sangaletti, L. Floreano, E. Magnano, F. Bondino, A. Goldoni, *J. Phys. Chem. C* **2011**, *115*, 4155–4162.
- [32] M. Oehzelt, L. Grill, S. Berkebile, G. Koller, F. P. Netzer, M. G. Ramsey, *ChemPhysChem* **2007**, *8*, 1707–1712.
- [33] W. Auwärter, A. Weber-Bargioni, A. Riemann, A. Schiffrin, O. Gröning, R. Fasel, J. Barth, *J. Chem. Phys.* **2006**, *124*, 194708.
- [34] J. Kuliga, S. Massicot, R. Adhikari, M. Ruppel, N. Jux, H.-P. Steinrück, H. Marbach, *ChemPhysChem* **2020**, *21*, 423–427.
- [35] L. Zhang, M. Lepper, M. Stark, R. Schuster, D. Lungerich, N. Jux, H.-P. Steinrück, H. Marbach, *Chem. A Eur. J.* **2016**, *22*, 3347–3354.

---

Manuscript received: May 19, 2023  
Revised manuscript received: June 21, 2023  
Accepted manuscript online: June 21, 2023  
Version of record online: July 12, 2023

# ChemPhysChem

Supporting Information

## **Structure and Conformation of Individual Molecules upon Adsorption of a Mixture of Benzoporphyrins on Ag(111), Cu(111), and Cu(110) Surfaces**

Rajan Adhikari, Jan Brox, Stephen Massicot, Michael Ruppel, Norbert Jux, Hubertus Marbach, and Hans-Peter Steinrück\*

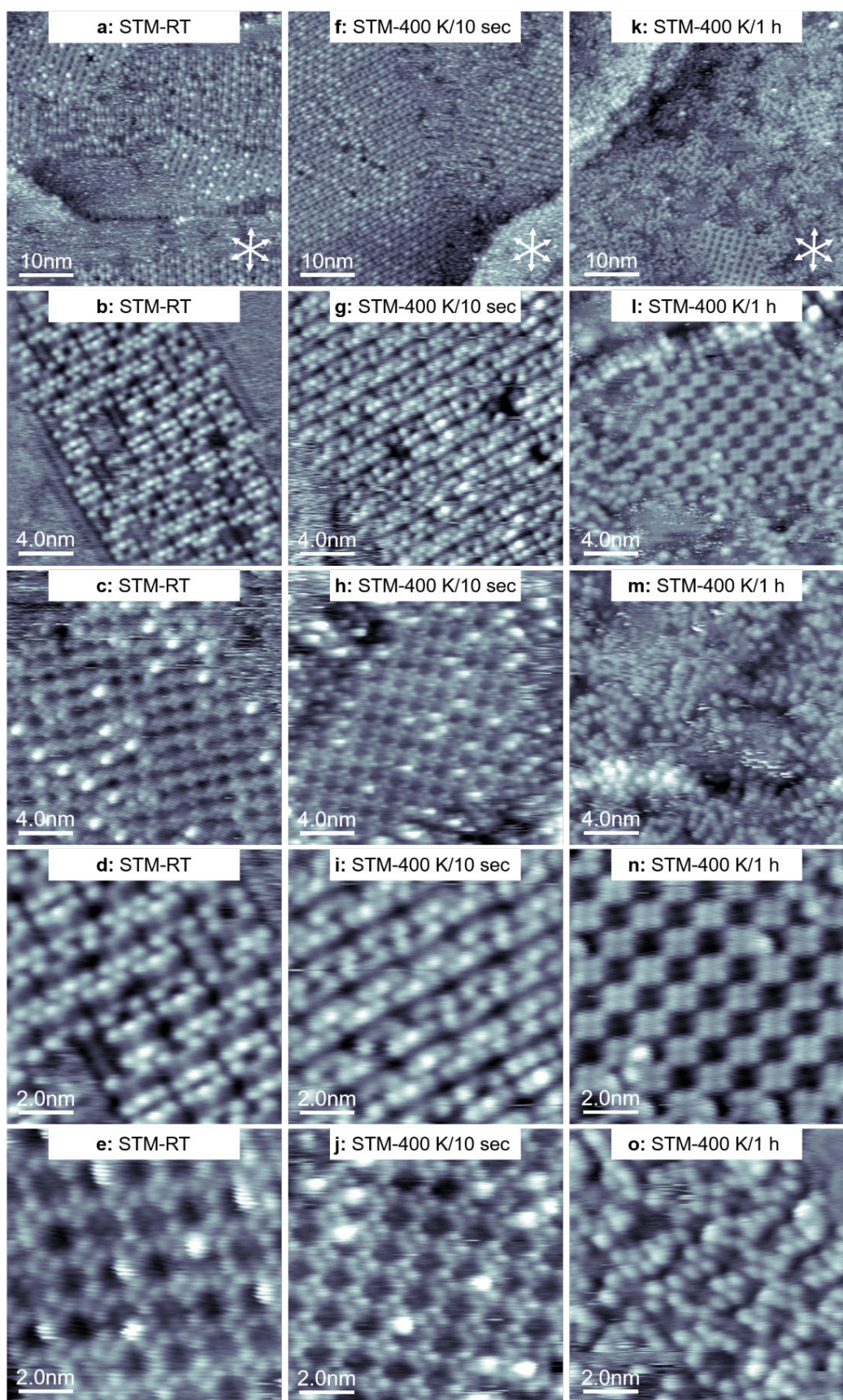


**Figure S1.** Extended version of Figure 4 for 2H-diTTBP(x)BPs on Cu(111) measured at RT. For more details, see text. The white arrows indicate the close-packed Cu(111) substrate directions. The STM images were measured with  $U_{bias}$  between -1.59 and 1.26 V and  $I_{set}$  between 88.9 and 299 pA; for details see Table S1 in the SI.

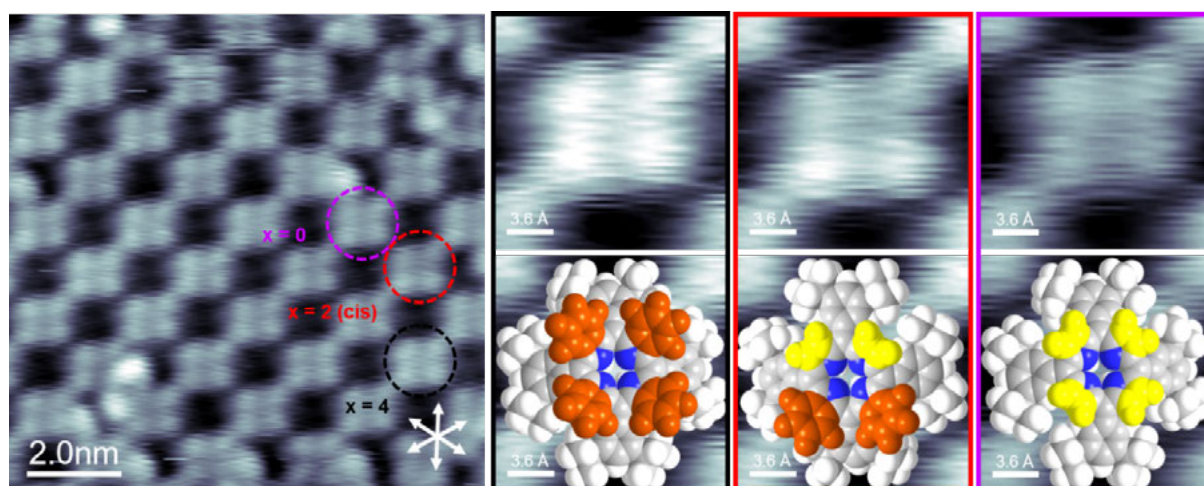


**Figure S2.** High resolution STM image of the square phase of 2H-diTTBP(x)BPs on Cu(111) measured at RT (left, 10 x 10 nm<sup>2</sup>; for details see Figure 4a-c), and cutout STM images (right-top; 1.8 x 1.8 nm<sup>2</sup>) overlaid with the proposed scaled molecular models (right bottom). Each molecule is characterized by four protrusions. The bright protrusions are assigned to upward bent isoindole groups (orange), and the dim protrusions to upward bent pyrrole groups (yellow). Individual molecules ( $x = 0$ , 2-cis, or 4) are marked with different color code (circles and frames). The proposed molecular model depicts a “crown-shape” conformation; for more details, see text. The STM image was measured with  $U_{bias} = -1.58$  V,  $I_{set} = 294$  pA; for details see Table S1 in the SI.

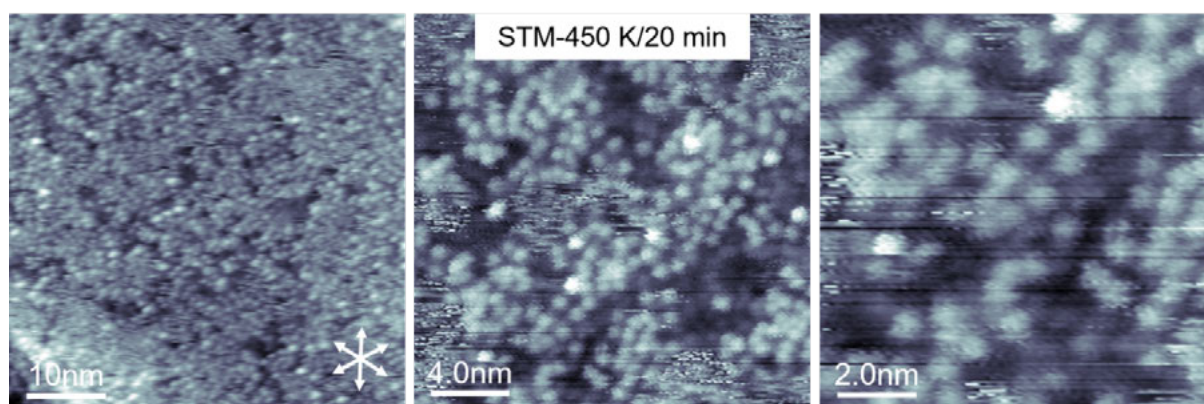


**Figure S3.** STM images of 2H-diTTBP(x)BPs on Cu(111) after annealing at 450 K for 20 min and measured at RT, as overview (left, 50 x 50 nm<sup>2</sup>), close-up (middle, 20 x 20 nm<sup>2</sup>), and with high resolution (right, 10 x 10 nm<sup>2</sup>). The STM images show the conversion of square and stripe phases (observed at lower temperatures – see Figure 4) into a disordered phase. For more details, see text. The white arrows indicate the close-packed Cu(111) substrate directions. The STM images were measured with  $U_{bias} = -1.01$  V and  $I_{set} =$  between 291 and 294 pA; for details see Table S1 in the SI.

**Table S1.** List of STM images in Figures 2-8 and Figures SI1-3, along with their tunneling parameters and File IDs.

Figures	Method	STM $U_{bias}$ [V], $I_{set}$ [pA]	File IDs YYMMDD_##-##
2a L	STM	1.25, 188	190130_28
2a M	STM	1.88, 89.3	190131_39
2a R / (3a)	STM	1.88, 89.3	190131_40
2b L	STM	1.0, 96.5	190201_20
2b M	STM	1.88, 201	190204_48-53
2b R / (3c)	STM	1.88, 201	190204_58-77
4a L	STM	-1.59, 188	190123_01
4a M	STM	-1.0, 299	190122_07
4a R / (6)	STM	-1.0, 297	190121_38
4b L	STM	0.98, 97.7	190124_206
4b M	STM	1.26, 95.7	190109_42
4b R	STM	0.98, 96.1	190124_160
4c L	STM	-1.58, 294	190110_35
4c M / (SI2)	STM	-1.58, 294	190110_30
4c R	STM	-1.54, 200	190109_59
5 L-T	STM	-1.0, 297	190121_38
5 M-T	STM	-1.0, 293	190121_96
5 R-T	STM	-1.0, 293	190121_71
5 L-B	STM	-1.0, 297	190121_38
5 M-B	STM	-1.0, 298	190121_101
5 R-B	STM	-1.0, 297	190121_59
7a L	STM	1.25, 195	190225_08
7a R	STM	-1.0, 195	190222_84
7b L	STM	-1.27, 196	190225_44
7b R	STM	-1.27, 197	190225_46
7c L	STM	-1.28, 195	190226_25
7c R	STM	-1.28, 196	190226_26
7B (B-L-three; B-R) / (8)	STM	1.27, 194; -1.25, 197	190222_70; 190225_25
S 1a	STM	-1.59, 188	190123_01
S 1b	STM	-1.0, 297	190121_38
S 1c	STM	-1.56, 88.9	190122_20
S 1d	STM	-1.0, 296	190121_40
S 1e	STM	-1.0, 299	190122_07
S 1f	STM	0.98, 97.7	190124_206
S 1g	STM	0.98, 96.1	190124_158
S 1h	STM	1.26, 95.7	190109_40
S 1i	STM	0.98, 96.1	190124_160
S 1j	STM	1.26, 95.7	190109_42
S 1k	STM	-1.58, 294	190110_35
S 1l	STM	-1.58, 294	190110_26
S 1m	STM	-1.58, 294	190110_24
S 1n	STM	-1.58, 294	190110_30
S 1o	STM	-1.54, 200	190109_59
S 3 L	STM	-1.01, 294	190128_12
S 3 M / R	STM	-1.01, 291	190128_08
Top = T, Bottom = B, Left = L, Middle = M, and R = Right			